Novel techniques in Free Electron Lasers

A thesis submitted to The Department of Physics

of the University of Strathclyde

for the degree of Doctor of Philosophy.

James Robert Henderson

June 23, 2015

Declaration

This thesis is the result of the author's original research. It has been composed by the author and has not been previously submitted for examination which has led to the award of a degree.

Signed: Date:

Abstract

Free Electron Lasers can generate high power transversely coherent tunable radiation. X-ray radiation can be generated in the Self Amplified Spontaneous Emission regime, however this radiation has poor temporal coherence. The Echo-Enabled Harmonic Generation method can improve the radiation's temporal coherence in x-ray. In this thesis analysis of the Echo-Enabled Harmonic Generation technique reveals that electron pulse has a modal density profile. This density profile when matched to amplification profile of an undulator-chicane lattice generates a train of coherent radiation spikes. The interaction of multiple electron pulses is investigated in this thesis. Propagating multiple electron pulses through an undulator produce a train of radiation spikes. The temporal separation of the radiation spikes can be manipulated using magnetic chicanes. Two new techniques are then proposed to improve FEL performance when the electron pulse has a large energy spread, such as those produced in plasma accelerators. These techniques use seeded-undulators and chicanes to manipulate the electron phase space prior to injection through an undulator-chicane lattice.

Acknowledgements

Thanks must go to my supervisor, Dr Brian M^{c}Neil, for his guidance and patience. I must also thank Dr Lawrence Campbell for his support and kindness. Thanks to EPSRC and STFC for the funding that made this PHD possible. And thanks to my friends and family for their encouragement and support. Love and thanks to Claire.

Contents

List of Figures

Chapter 1

Introduction

1.1 Free Electron Lasers

The Free Electron Laser [1, 2] (FEL) is a unique radiation source offering many advantages over conventional laser systems. Free Electron Lasers produce highly tunable radiation that is 8-10 orders of magnitude brighter [1, 2] than the radiation produced by conventional laser systems. In 1971, John Madey [3] invented the FEL when he published his seminal work on small signal gain theory. Madey was then involved in the first experimental demonstration of the Free Electron Laser [4] at Stanford in 1977. In the FEL an electron beam and radiation field co-propagate through a magnetic undulator. The interaction of electron beam, undulator and radiation field will amplify a small radiation field to saturation after many undulator periods. A number of review articles [1, 2, 5, 6] describe the history of the Free Electron Laser and current FEL projects in greater detail than this thesis. High gain FELs typically operate in the Self Amplified Spontaneous Emission regime [7]. The Self Amplified Spontaneous Emission [7, 8] (SASE) FEL amplifies spontaneous radiation (produced by electron shot-noise) to saturation in a long undulator. The SASE FEL has a wide operational bandwidth, with few practical limitations. However, SASE radiation lacks temporal coherence, its temporal radiation profile containing of a series of uncorrelated coherent radiation spikes.

The FEL process can be initiated with a coherent seed laser, in seeded FELs the output radiation retains the good coherence properties of the seed laser. However, seeding is not an option x-ray FEL as there is lack of high quality seed lasers in the x-ray [1, 2]. Therefore hard x-ray FELs almost exclusively operate in the SASE regime.

The second chapter of this thesis will discuss basic FEL theory and derive a set of simplified differential equations to describe the FEL interaction. Then chapter 3 will discuss the 1D FEL simulation code hpFull [9, 10] and the 3D Puffin [11]. Modifications to Puffin [11, 12] will be described, these modifications allow a more realistic undulator field to be modelled. Novel FEL methods will then be discussed in the fourth chapter, methods that improve the FEL temporal coherence in x-ray have become increasingly important in FEL community. One such scheme Echo-Enabled Harmonic Generation [13, 14] is explored in detail and improvements to the scheme investigated using numerical simulations. The results of this work was published in [15], a copy of this paper can be found in the appendix. In chapter 5 the interaction of multiple electron pulses is investigated. When sufficiently separated in energy, each electron pulse will perform its own FEL interaction, this results in the generation of multiple side-band radiation modes. Delicate manipulation of these side-band radiation modes can be achieved using chicane delay sections. The remaining chapters of this thesis are dedicated to improving performance of the FEL when the electron pulse has a large energy spread. Chapter 6 describes the interaction of multiple chirped electrons pulse [16]. A similar structure can be generated from a single electron pulse, with a large energy spread, and is investigated in chapter 6. By propagating such a structure through an undulator-chicane lattice the FEL radiation power is shown to increase by 2-3 order of magnitude. The beam-by-design [17] manipulation/Fourier-synthesis of electron pulses is studied to increase the FEL efficiency for electron pulses with large energy spread. One such method that uses 'rf-function' [17, 18] rectangular electron pulse is studied in chapter 7, and shows 4-6 orders of magnitude improvement to the FEL radiation power when propagated through an appropriate undulator-chicane lattice.

Chapter 2

Basic FEL physics

2.1 Qualitative description

In the Free Electron Laser (FEL) a magnetic undulator couples a radiation field to a relativistic ($\gamma > 1$) electron pulse. This electron-radiation-field coupling results in a collective instability (a feed-back loop), which exponentially amplifies a small initial radiation field. A planar undulator consists of two rows of alternating polarity dipole magnets, see figure 2.1 where the blue poles are the south poles and the brown the north poles. This arrangement of magnets produces a sinusoidal magnetic field along the undulator axis.

FELs can operate in two distinct regimes. In the low gain regime an undulator is placed inside a cavity and the radiation field is amplified to saturation over many passes of the cavity by the electron pulse. However, in the high gain regime radiation is amplified to saturation in a long undulator

The radiation field creates an energy modulation in the electron pulse. The natural dispersion action of the undulator will convert this energy modulation into a density modulation. This density modulation is known as electron microbunching. The microbunches are periodic at the resonant radiation wavelength, therefore they can emit radiation collectively and coherently at the resonant wavelength. As the radiation field grows the level of microbunching increases in a collective feed-back loop. However, the electron microbunches

form around the zero crossing of the radiation field and as such cannot amplify radiation. In low gain FELs [19] this results in the FEL lasing off-resonance. On the other hand, in high gain FELs [1] the phase of the radiation field evolves, in effect this shifts the electron microbunches to a phase where the radiation field can be further amplified.

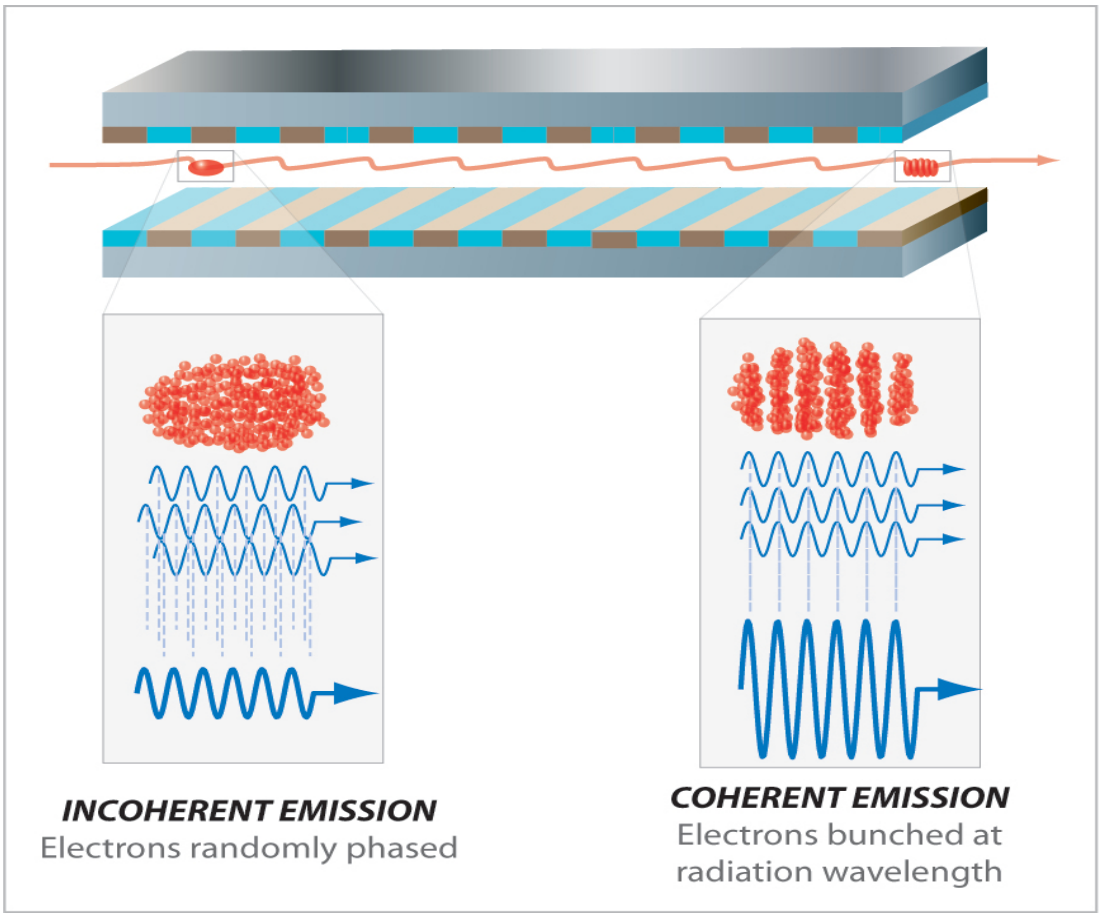

Figure 2.1: An undulator consists of two sets of alternating dipole magnets. The electron pulse propagates through the undulator which combined with a radiation field bunches the beam at the resonant wavelength. These electron bunches then produce coherent emission exponentially amplifying the radiation. This figure is from [1]. This is an example of planar undulator, however an undulator can be constructed with two sinusoidally varying, perpendicular, magnetic field known as a helical undulator.

FEL radiation is centred around the resonant wavelength, which is calculated from the FEL resonance condition. This condition is often stated as,

$$\lambda_r = \frac{\lambda_u}{2\gamma_r^2}(1 + a_u^2), \tag{2.1}$$

where $\gamma_r =< \gamma_j >$, and shows the inherent tunability of the FEL. For example increasing the electron pulse's resonant energy γ_r will decrease the resonant wavelength by a factor $1/\gamma_r^2$. The resonant wavelength can also be tuned by adjusting the undulator period λ_u and the undulator parameter $a_u \propto B_0\lambda_u$, where B_0 is the peak undulator magnetic field.

2.2 Slippage and the resonance condition

As electrons are massive particles their velocity is less than the speed of light. The electrons' longitudinal velocity is further reduced because they take a sinusoidal trajectory through the undulator. Because the radiation pulse propagates faster than the electron pulse, the electrons are seen to slip backwards with respect to the radiation pulse. In the FEL [19], a continuous interaction can be maintained if there is a fixed phase relationship between the radiation pulse and the electron pulse's perpendicular velocity. In other words, if the radiation pulse's electric field and the electron perpendicular velocity are in the same direction in each undulator period then energy can be continuously passed from electron to radiation field. This can be achieved [1] by ensuring that an electron slips an integer number of radiation periods behind the radiation field in one undulator period. This condition is derived using a time of flight argument. The time of flight for a electron and radiation pulse in one undulator period are equated,

$$t_r = t_e \tag{2.2}$$

$$\frac{\lambda_u + n\lambda_{rj}}{c} = \frac{\lambda_u}{\beta_{zj}c} \tag{2.3}$$

here λ_{rj} is the resonant wavelength for the j^{th} electron, n is an integer and $\beta_{zj}c = v_{zj}$ is the electron velocity in z.

$$\frac{\lambda_u + n\lambda_{rj}}{c} - \frac{\lambda_u}{\beta_{zj}c} = 0 \tag{2.4}$$

$$\frac{\lambda_u}{c}\left(\frac{\beta_{zj} - 1}{\beta_{zj}}\right) + \frac{n\lambda_{rj}}{c} = 0 \tag{2.5}$$

$$n\lambda_{rj} = \lambda_u\left(\frac{1 - \beta_{zj}}{\beta_{zj}}\right) \tag{2.6}$$

$$\lambda_{rj} = \frac{\lambda_u}{n}\left(\frac{1 - \beta_{zj}}{\beta_{zj}}\right) \tag{2.7}$$

This is the resonant wavelength for a single electron, in an electron pulse there will be a spread of electron energies (and velocities v_{zj}). Therefore it more useful to consider the average resonant wavelength defined as,

$$\lambda_r = \frac{\lambda_u}{n}\left(\frac{1 - \bar{\beta}_z}{\bar{\beta}_z}\right) \tag{2.8}$$

where $\bar{\beta}_z c = \bar{v}_z$ is the average electron velocity for the electron pulse. For an electron pulse with a correlated energy chirp the electron pulse will have correlated resonant frequency. Equation 2.1 is in fact a useful approximation of the above expression and can be derived by considering the on-axis injection of resonant electron.

2.3 Outline of the 1D FEL equations

In this section a set of simplified 1D FEL differential equations are derived in the classical limit, which is sufficient for most Free Electron Lasers. Most FEL simulation codes are simply integrators of the Lorentz force and Maxwell's wave equations. To understand this we shall first consider the electron motion in the undulator and then derive some simple expressions for the radiation-

electron energy exchange. In the following derivation the on-axis injection of a cold electron pulse is assumed. Furthermore, the electron pulse's perpendicular momentum is assumed to be constant with respect to the radiation field, therefore it can be written as a simple function of the undulator's magnetic field.

2.3.1 Electron trajectory through the undulator

The trajectory of the electron pulse through the undulator is first derived. A helical undulator is assumed, the helical magnetic field will force the electron pulse to take a helical path through the undulator. A 1D approximation to an undulator magnetic field is given by,

$$\mathbf{B}_u = \frac{B_0}{2}\left(\mathbf{u}e^{-ik_u z} + c.c.\right) \tag{2.9}$$

where $\mathbf{u} = u_x\hat{\mathbf{x}} + iu_y\hat{\mathbf{y}}$ describes the undulator polarization, $u_{x,y} = 1$ for a helical undulator.

$$\mathbf{B}_u = \frac{B_0}{2}\left[(u_x\hat{\mathbf{x}} + iu_y\hat{\mathbf{y}})e^{-ik_u z} + (u_x\hat{\mathbf{x}} - iu_y\hat{\mathbf{y}})e^{ik_u z}\right] \tag{2.10}$$

$$\mathbf{B}_u = \frac{B_0}{2}\left[u_x\hat{\mathbf{x}}(e^{ik_u z} + e^{-ik_u z}) - iu_y\hat{\mathbf{y}}(e^{ik_u z} - e^{-ik_u z})\right] \tag{2.11}$$

applying Euler's relations $2\cos x = e^{ix} + e^{-ix}$ and $2i\sin x = e^{ix} - e^{-ix}$.

$$\mathbf{B}_u = B_0\left[u_x\hat{\mathbf{x}}\cos(k_u z) + u_y\hat{\mathbf{y}}\sin(k_u z)\right] \tag{2.12}$$

Now, assume a helical undulator ($u_{x,y} = 1$)

$$\mathbf{B}_u = B_0\left[\hat{\mathbf{x}}\cos(k_u z) + \hat{\mathbf{y}}\sin(k_u z)\right] \tag{2.13}$$

The Lorentz force equation will determine the electron pulse's transverse motion. Consider the force experienced by the j^{th} electron,

$$\mathbf{F}_j = -e(\mathbf{E} + c\boldsymbol{\beta}_j \times \mathbf{B}) \tag{2.14}$$

The electron pulse's transverse motion is calculated in the absence of the radiation pulse's electric and magnetic fields. This assumption allows the FEL equations to be simplified. However, this does assume that the electric field, of the radiation pulse, does not affect the electron pulse's perpendicular momentum ($p_\perp$) which is incorrect but it is a good enough approximation for this 1D model.

$$\mathbf{F}_j = -e(c\boldsymbol{\beta}_j \times \mathbf{B}) \tag{2.15}$$

$$\mathbf{F}_j = -ec\boldsymbol{\beta}_j \times \mathbf{B}_u \tag{2.16}$$

Following Newton's third law, where the relativistic momentum is $\mathbf{p}_j = \gamma_j mc\boldsymbol{\beta}_j$, and $\boldsymbol{\beta}_j c = \boldsymbol{v}_j$,

$$\frac{d\gamma_j mc\boldsymbol{\beta}_j}{dt} = -e(c\boldsymbol{\beta} \times \mathbf{B}_u) \tag{2.17}$$

$$mc\left(\boldsymbol{\beta}_j \frac{d\gamma_j}{dt} + \gamma_j \frac{d\boldsymbol{\beta}_j}{dt}\right) = -e(c\boldsymbol{\beta}_j \times \mathbf{B}_u) \tag{2.18}$$

By neglecting the electric field zero energy exchange can be assumed, i.e., $\frac{d\gamma_j}{dt} = 0$. This assumption comes from the fact that a charged particle's energy cannot be changed by a magnetic field. This fact will be demonstrated later, now equation 2.18 becomes,

$$mc\gamma_j \frac{d\boldsymbol{\beta}_j}{dt} = -e(c\boldsymbol{\beta}_j \times \mathbf{B}_u) \tag{2.19}$$

$$\frac{d\boldsymbol{\beta}_j}{dt} = -\frac{e}{\gamma_j m}\boldsymbol{\beta}_j \times \mathbf{B}_u, \tag{2.20}$$

now calculating the cross product,

$$\boldsymbol{\beta}_j \times \mathbf{B}_u = \begin{vmatrix} \hat{\mathbf{x}} & \hat{\mathbf{y}} & \hat{\mathbf{z}} \\ \beta_{xj} & \beta_{yj} & \beta_{zj} \\ B_x & B_y & B_z \end{vmatrix} = \begin{vmatrix} \hat{\mathbf{x}} & \hat{\mathbf{y}} & \hat{\mathbf{z}} \\ \beta_{xj} & \beta_{yj} & \beta_{zj} \\ B_0\cos(k_u z) & B_0\sin(k_u z) & 0 \end{vmatrix}$$

$$\boldsymbol{\beta} \times \mathbf{B}_u = -\hat{\mathbf{x}}\beta_{zj}B_0\sin(k_u z) + \hat{\mathbf{y}}\beta_{zj}B_0\cos(k_u z) + \hat{\mathbf{z}}(\beta_{xj}B_y - \beta_{yj}B_x)$$

and recombining with the above to give,

$$\frac{d\boldsymbol{\beta}_j}{dt} = -\frac{e}{\gamma_j m}(-\hat{\mathbf{x}}\beta_{zj}B_0\sin(k_u z) + \hat{\mathbf{y}}\beta_{zj}B_0\cos(k_u z) + \hat{\mathbf{z}}(\beta_{xj}B_y - \beta_{yj}B_x)) \tag{2.21}$$

now separating the individual components

$$\begin{aligned} \frac{d\beta_{xj}}{dt} &= \frac{e}{\gamma_j m}\beta_z B_0\sin(k_u z) \\ \frac{d\beta_{yj}}{dt} &= -\frac{e}{\gamma_j m}\beta_z B_0\cos(k_u z) \\ \frac{d\beta_{zj}}{dt} &= -\frac{e}{\gamma_j m}(\beta_{xj}B_y - \beta_{yj}B_x)) \end{aligned}$$

ignoring the z-component for now, and transform the derivatives into z using $\frac{d}{dt} = c\beta_{zj}\frac{d}{dz}$

$$\begin{aligned} \frac{d\beta_{xj}}{dz} &= \frac{e}{\gamma_j mc}B_0\sin(k_u z) \\ \frac{d\beta_{yj}}{dz} &= -\frac{e}{\gamma_j mc}B_0\cos(k_u z) \end{aligned}$$

these equations easily integrate to give,

$$\beta_{xj} = -\frac{e}{\gamma_j mck_u} B_0 \cos(k_u z) \tag{2.22}$$

$$\beta_{yj} = -\frac{e}{\gamma_j mck_u} B_0 \sin(k_u z). \tag{2.23}$$

The scaled undulator parameter can be defined as,

$$a_u = \frac{eB_0}{mck_u} \tag{2.24}$$

therefore,

$$\beta_{xj} = -\frac{a_u}{\gamma_j} \cos(k_u z) \tag{2.25}$$

$$\beta_{yj} = -\frac{a_u}{\gamma_j} \sin(k_u z). \tag{2.26}$$

Restating the above in vector form,

$$\boldsymbol{\beta} = -\frac{a_u}{\gamma_j} \left(\cos(k_u z)\hat{\mathbf{x}} + \sin(k_u z)\hat{\mathbf{y}}\right) + \boldsymbol{\beta}_z \hat{\mathbf{z}} \tag{2.27}$$

2.3.2 Interaction with a co-propagating radiation field

Now, an expression for the interaction of a co-propagating radiation field with the electron pulse is derived. The Lorentz force equation is considered, while remembering that the relativistic momentum is given by $\mathbf{p}_j = \gamma_j mc\boldsymbol{\beta}_j$,

$$\mathbf{F}_j = -e(\mathbf{E} + c\boldsymbol{\beta}_j \times \mathbf{B}) \tag{2.28}$$

$$\frac{d\gamma_j mc\boldsymbol{\beta}_j}{dt} = -e(\mathbf{E} + c\boldsymbol{\beta}_j \times \mathbf{B}) \tag{2.29}$$

$$mc\frac{d\gamma_j\boldsymbol{\beta}_j}{dt} = -e(\mathbf{E} + c\boldsymbol{\beta}_j \times \mathbf{B}) \tag{2.30}$$

multiplying both sides by $\boldsymbol{\beta}$ and rearranging to give,

$$mc\frac{d\gamma_j\boldsymbol{\beta}_j}{dt} \cdot \boldsymbol{\beta}_j = -e(\mathbf{E} + c\boldsymbol{\beta}_j \times \mathbf{B}) \cdot \boldsymbol{\beta} \tag{2.31}$$

$$mc(\gamma_j\frac{d\boldsymbol{\beta}_j}{dt} + \boldsymbol{\beta}_j\frac{d\gamma_j}{dt}) \cdot \boldsymbol{\beta}_j = -e(\mathbf{E} + c\boldsymbol{\beta}_j \times \mathbf{B}) \cdot \boldsymbol{\beta}_j \tag{2.32}$$

$$\gamma_j\frac{d\boldsymbol{\beta}_j}{dt} \cdot \boldsymbol{\beta}_j + \boldsymbol{\beta}_j^2\frac{d\gamma_j}{dt} = -\frac{e}{mc}(\mathbf{E} + c\boldsymbol{\beta}_j \times \mathbf{B}) \cdot \boldsymbol{\beta}_j \tag{2.33}$$

$$\frac{\gamma_j}{2}\frac{d\boldsymbol{\beta}_j^2}{dt} + \boldsymbol{\beta}_j^2\frac{d\gamma_j}{dt} = -\frac{e}{mc}(\mathbf{E} + c\boldsymbol{\beta}_j \times \mathbf{B}) \cdot \boldsymbol{\beta}_j \tag{2.34}$$

γ_j is defined as $\gamma_j^2 = 1/(1-\boldsymbol{\beta}_j^2)$ and should be rearranged $\gamma_j^2 = 1/(1-\boldsymbol{\beta}_j^2) => \gamma_j^2(1-\boldsymbol{\beta}_j^2) = 1 => \gamma_j^2 = 1 + \gamma_j^2\boldsymbol{\beta}^2$. γ_j^2 is now differentiated with respect to

time,

$$\frac{d\gamma_j^2}{dt} = \frac{d}{dt}(1 + \gamma_j^2 \boldsymbol{\beta}_j^2) \tag{2.35}$$

$$2\gamma_j \frac{d\gamma_j}{dt} = \frac{d}{dt}\gamma_j^2 \boldsymbol{\beta}_j^2 \tag{2.36}$$

$$2\gamma_j \frac{d\gamma_j}{dt} = 2\gamma_j \boldsymbol{\beta}_j^2 \frac{d\gamma_j}{dt} + 2\gamma_j^2 \boldsymbol{\beta}_j \frac{d\boldsymbol{\beta}_j}{dt} \tag{2.37}$$

$$\frac{d\gamma_j}{dt} = \boldsymbol{\beta}_j^2 \frac{d\gamma_j}{dt} + \gamma_j \boldsymbol{\beta}_j \frac{d\boldsymbol{\beta}_j}{dt} \tag{2.38}$$

$$\frac{d\gamma_j}{dt} = \frac{\gamma_j}{2} \frac{d\boldsymbol{\beta}_j^2}{dt} + \boldsymbol{\beta}_j^2 \frac{d\gamma_j}{dt} \tag{2.39}$$

The above expression is combined with equation 2.34 to give,

$$\frac{d\gamma_j}{dt} = -\frac{e}{mc}(\mathbf{E} + c\boldsymbol{\beta}_j \times \mathbf{B}) \cdot \boldsymbol{\beta} \tag{2.40}$$

now focus on the $(c\boldsymbol{\beta}_j \times \mathbf{B}) \cdot \boldsymbol{\beta}$ part. The cross product $\boldsymbol{\beta}_j \times \mathbf{B}$ will be perpendicular to both $\boldsymbol{\beta}_j$ and $\mathbf{B}$. Therefore the dot product $(c\boldsymbol{\beta}_j \times \mathbf{B}) \cdot \boldsymbol{\beta}$ must be zero, this tells us that a magnetic field cannot change the energy of a charged particle. Setting $(c\boldsymbol{\beta}_j \times \mathbf{B}) \cdot \boldsymbol{\beta}$ to zero leaves

$$\frac{d\gamma_j}{dt} = -\frac{e}{mc}\mathbf{E} \cdot \boldsymbol{\beta}_j. \tag{2.41}$$

The radiation field is defined as,

$$\mathbf{E} = \frac{1}{\sqrt{2}}\left(\hat{\mathbf{e}}\xi e^{i(k_r z - \omega_r t)} + c.c.\right) \tag{2.42}$$

where ξ is the complex field envelope [11] and the unit vector $\hat{\mathbf{e}}$ is given by $\hat{\mathbf{e}} = \frac{1}{\sqrt{2}}(\hat{\mathbf{x}} + i\hat{\mathbf{y}})$, hence $\hat{\mathbf{e}} \cdot \hat{\mathbf{e}} = \frac{1}{2}(\hat{\mathbf{x}}^2 - \hat{\mathbf{y}}^2) = 0$ and $\hat{\mathbf{e}} \cdot \hat{\mathbf{e}}^* = \frac{1}{2}(\hat{\mathbf{x}}^2 + \hat{\mathbf{y}}^2) = 1$.

The definition of $\hat{\mathbf{e}}$ is useful because, $\boldsymbol{\beta} \cdot \sqrt{2}\hat{\mathbf{e}}^* = \beta_x - i\beta_y = \beta_\perp$ and $\mathbf{E} \cdot \sqrt{2}\hat{\mathbf{e}}^* = E_\perp$, etc.

$$\mathbf{E} = \frac{1}{\sqrt{2}} \left(\frac{1}{\sqrt{2}} (\hat{\mathbf{x}} + i\hat{\mathbf{y}}) \xi e^{i(k_r z - \omega_r t)} + c.c. \right) \tag{2.43}$$

$$\mathbf{E} = \frac{1}{2} \left((\hat{\mathbf{x}} + i\hat{\mathbf{y}}) \xi e^{i(k_r z - \omega_r t)} + (\hat{\mathbf{x}} - i\hat{\mathbf{y}}) \xi^* e^{-i(k_r z - \omega_r t)} \right) \tag{2.44}$$

$$\mathbf{E} = \frac{1}{2} \left(\hat{\mathbf{x}} (\xi e^{i(k_r z - \omega_r t)} + \xi^* e^{-i(k_r z - \omega_r t)}) + i\hat{\mathbf{y}} (\xi e^{i(k_r z - \omega_r t)} - \xi^* e^{-i(k_r z - \omega_r t)}) \right) \tag{2.45}$$

the electron's normalised velocity vector is given by

$$\boldsymbol{\beta} = -\frac{a_u}{\gamma_j} (\cos(k_u z)\hat{\mathbf{x}} + \sin(k_u z)\hat{\mathbf{y}}) + \boldsymbol{\beta}_z \hat{\mathbf{z}} \tag{2.46}$$

now the $\mathbf{E} \cdot \boldsymbol{\beta}_j$ term is calculated, this is simplified since $\hat{\mathbf{x}}$,$\hat{\mathbf{y}}$ and $\hat{\mathbf{z}}$ are unit vectors, i.e., $\hat{\mathbf{x}} \cdot \hat{\mathbf{x}} = 1$ and $\hat{\mathbf{x}} \cdot \hat{\mathbf{y}} = 0$ etc.

$$\mathbf{E} \cdot \boldsymbol{\beta}_j = -\frac{1}{2} \frac{a_u}{\gamma_j} \Big((\xi e^{i(k_r z - \omega_r t)} + \xi^* e^{-i(k_r z - \omega_r t)}) \cos(k_u z) + \tag{2.47}$$

$$i(\xi e^{i(k_r z - \omega_r t)} - \xi^* e^{-i(k_r z - \omega_r t)}) \sin(k_u z) \Big) \tag{2.48}$$

rearranging terms and removing common factors of ξ and ξ^*

$$\mathbf{E} \cdot \boldsymbol{\beta}_j = -\frac{1}{2} \frac{a_u}{\gamma_j} \Big((\xi e^{i(k_r z - \omega_r t)})(\cos(k_u z) + i \sin(k_u z)) + \tag{2.49}$$

$$(\xi^* e^{-i(k_r z - \omega_r t)})(\cos(k_u z) - i \sin(k_u z)) \Big) \tag{2.50}$$

now again using Euler's relations $e^{ix} = \cos x + i \sin x$ and $e^{-ix} = \cos x - i \sin x$,

$$\mathbf{E} \cdot \boldsymbol{\beta}_j = -\frac{1}{2} \frac{a_u}{\gamma_j} \Big((\xi e^{i(k_r z - \omega_r t)}) e^{ik_u z} + (\xi^* e^{-i(k_r z - \omega_r t)}) e^{-ik_u z} \Big) \tag{2.51}$$

$$\mathbf{E}\cdot\boldsymbol{\beta}_j = -\frac{1}{2}\frac{a_u}{\gamma_j}\Big((\xi e^{i(k_r z+k_u z-\omega_r t)}) + (\xi^* e^{-i(k_r z+k_u z-\omega_r t)})\Big) \tag{2.52}$$

defining the pondermotive phase as, $\theta_j = k_r z + k_u z - \omega_r t$

$$\mathbf{E}\cdot\boldsymbol{\beta}_j = -\frac{1}{2}\frac{a_u}{\gamma_j}\Big((\xi e^{i\theta_j}) + (\xi^* e^{-i\theta_j})\Big) \tag{2.53}$$

therefore equation 2.41 becomes,

$$\frac{d\gamma_j}{dt} = \frac{1}{2}\frac{e}{mc}\frac{a_u}{\gamma_j}\Big((\xi e^{i\theta_j}) + (\xi^* e^{-i\theta_j})\Big) \tag{2.54}$$

now change to a derivative in z, i.e., $\frac{d}{dt} = c\beta_{zj}\frac{d}{dz}$

$$\frac{d\gamma_j}{dz} = \frac{1}{2}\frac{e}{mc^2\beta_{zj}}\frac{a_u}{\gamma_j}\Big((\xi e^{i\theta_j}) + (\xi^* e^{-i\theta_j})\Big). \tag{2.55}$$

The gain length is defined as $l_g = 1/2k_u\rho$, where the FEL (Pierce) [1] parameter is given by $\rho = \frac{1}{\gamma_r}\left(\frac{a_u\omega_p}{4ck_u}\right)^{2/3}$, $k_u = \frac{2\pi}{\lambda_u}$ and $\omega_p = \left(\frac{e^2 n_p}{\epsilon_0 m}\right)^{1/2}$ is the non-relativistic plasma frequency. The derivative in z can be transformed into scaled notation using $\frac{d\bar{z}}{dz} = 1/l_g$ where $\bar{z} = z/l_g$,

$$\frac{d\gamma_j}{d\bar{z}} = l_g\frac{1}{2}\frac{e}{mc^2\beta_{zj}}\frac{a_u}{\gamma_j}\Big((\xi e^{i\theta_j}) + (\xi^* e^{-i\theta_j})\Big) \tag{2.56}$$

the scaled energy parameter is defined as, $p_j = \frac{\gamma_j-\gamma_r}{\rho\gamma_r}$ therefore $\rho\gamma_r\frac{dp_j}{d\bar{z}} = \frac{d\gamma_j}{d\bar{z}}$,

$$\frac{dp_j}{d\bar{z}} = l_g\frac{1}{2}\frac{e}{mc^2\beta_{zj}}\frac{a_u}{\gamma_j\gamma_r\rho}\Big((\xi e^{i\theta_j}) + (\xi^* e^{-i\theta_j})\Big) \tag{2.57}$$

now assuming $\frac{\gamma_r-\gamma_j}{\rho\gamma_r} \ll 1$, and setting $\gamma_j = \gamma_r$ and $\beta_{zj} = 1$

$$\frac{dp_j}{d\bar{z}} = l_g \frac{1}{2} \frac{e}{mc^2} \frac{a_u}{\gamma_r^2 \rho} \Big(\xi e^{i\theta_j} + \xi^* e^{-i\theta_j} \Big). \tag{2.58}$$

The scaled electric field is defined by,

$$A(\bar{z}, \bar{z}_1) = \frac{e\xi}{mc\omega_p \sqrt{\rho\gamma_r}} \tag{2.59}$$

where $\rho = \frac{1}{\gamma_r} \left(\frac{a_u \omega_p}{4ck_u} \right)^{2/3}$, now rearranging the definition of ρ

$$\rho = \frac{1}{\gamma_r} \left(\frac{a_u \omega_p}{4ck_u} \right)^{2/3} \tag{2.60}$$

$$(\rho\gamma_r)^{3/2} = \frac{a_u \omega_p}{4ck_u} \tag{2.61}$$

$$\frac{1}{\omega_p} = \frac{a_u}{4ck_u (\rho\gamma_r)^{3/2}} \tag{2.62}$$

$$\frac{e}{mc\omega_p \sqrt{\rho\gamma_r}} = \frac{a_u e}{4mc^2 k_u (\rho\gamma_r)^2} \tag{2.63}$$

using the above expression to rearrange equation 2.59,

$$A(\bar{z}, \bar{z}_1) = \frac{a_u e\xi}{4mc^2 k_u (\rho\gamma)^2} \tag{2.64}$$

the gain length is defined by $l_g = \frac{1}{2k_u\rho}$, which with the above definition of A

is used to rearrange equation 2.58,

$$\frac{dp_j}{d\bar{z}} = \frac{1}{2k_u\rho}\frac{1}{2}\frac{e}{mc^2}\frac{a_u}{\gamma_r^2\rho}\Big(\xi e^{i\theta_j} + \xi^* e^{-i\theta_j}\Big) \tag{2.65}$$

$$\frac{dp_j}{d\bar{z}} = \frac{a_u e}{4mc^2 k_u(\rho\gamma_r)^2}\Big(\xi e^{i\theta_j} + \xi^* e^{-i\theta_j}\Big) \tag{2.66}$$

$$\frac{dp_j}{d\bar{z}} = \Big(Ae^{i\theta_j} + A^* e^{-i\theta_j}\Big) \tag{2.67}$$

$$\frac{dp_j}{d\bar{z}} = \Big(Ae^{i\theta_j} + c.c.\Big) \tag{2.68}$$

this expression describes the change in the electron energy along the undulator.

2.3.3 The pondermotive well equation

An equation describing the evolution of the pondermotive well is now derived. By setting the time derivative of the pondermotive phase θ_j to zero the resonance condition is recovered, this is shown below. The resonance condition is a condition for continuous energy exchange between radiation field and electrons.

$$\theta_j = (k_r + k_u)z - \omega_r t \tag{2.69}$$

$$\frac{d\theta_j}{dt} = (k_r + k_u)\frac{dz}{dt} - \omega_r = 0 \tag{2.70}$$

$$\frac{d\theta_j}{dt} = (k_r + k_u)v_{zj} - k_r c = 0 \tag{2.71}$$

$$(k_r + k_u)\beta_{zj} - k_r = 0 \tag{2.72}$$

$$k_u\beta_{zj} + k_r(\beta_{zj} - 1) = 0 \tag{2.73}$$

$$k_u\beta_{zj} = k_r(1 - \beta_{zj}) \tag{2.74}$$

$$\frac{k_r}{k_u} = \frac{\beta_{zj}}{1 - \beta_{zj}} \tag{2.75}$$

$$\frac{\lambda_r}{\lambda_u} = \frac{1 - \beta_{zj}}{\beta_{zj}} \tag{2.76}$$

The on-axis resonance condition, equation 2.7, for the fundamental is recovered. An equation to describe the pondermotive well's evolution along the undulator is now derived by differentiating equation 2.69 w.r.t z and using $kc = \omega$

$$\theta_j = (k_r + k_u)z - \omega_r t \tag{2.77}$$

$$\frac{d\theta_j}{dz} = (k_r + k_u) - k_r \frac{1}{\beta_{zj}} \tag{2.78}$$

$$\frac{d\theta_j}{dz} = k_u + k_r(1 - \frac{1}{\beta_{zj}}) \tag{2.79}$$

now rearranging γ_j^2

$$\frac{1}{\gamma_j^2} = 1 - \boldsymbol{\beta}_j^2 \tag{2.80}$$

now consider the electron velocity vector $\boldsymbol{\beta}_j$,

$$\boldsymbol{\beta}_j = -\frac{a_u}{\gamma_j}\left(\cos(k_u z)\hat{\mathbf{x}} + \sin(k_u z)\hat{\mathbf{y}}\right) + \beta_{zj}\hat{\mathbf{z}} \tag{2.81}$$

$$\boldsymbol{\beta}_j^2 = \frac{a_u^2}{\gamma_j^2}\left(\cos(k_u z)^2 + \sin(k_u z)^2\right) + \beta_{zj}^2 \tag{2.82}$$

$$\boldsymbol{\beta}_j^2 = \frac{a_u^2}{\gamma_j^2} + \beta_{zj}^2 \tag{2.83}$$

since $\sin(x)^2 + \cos(x)^2 = 1$, now inserting the above expression into equation 2.80 to give,

$$\frac{1}{\gamma_j^2} = 1 - \frac{a_u^2}{\gamma_j^2} - \beta_{zj}^2 \tag{2.84}$$

$$\frac{1}{\gamma_j^2} + \frac{a_u^2}{\gamma_j^2} = 1 - \beta_{zj}^2 \tag{2.85}$$

$$1 - \beta_{zj}^2 = \frac{1 + a_u^2}{\gamma_j^2} \tag{2.86}$$

$$\beta_{zj}^2 = 1 - \frac{1 + a_u^2}{\gamma_j^2} \tag{2.87}$$

$$\frac{1}{\beta_{zj}} = \left(1 - \frac{1 + a_u^2}{\gamma_j^2}\right)^{-1/2} \tag{2.88}$$

performing a Binomial expansion to the first order, i.e., $(1 - x)^{-1/2} = 1 + \frac{1}{2}x$, which assumes $x \ll 1$ i.e., $\gamma_j^2 \gg 1 + a_u^2$

$$\frac{1}{\beta_{zj}} = \left(1 + \frac{1 + a_u^2}{2\gamma_j^2}\right) \tag{2.89}$$

By combining this expression with equation 2.76 and setting $\gamma_j = \gamma_r$ one can derive the approximate resonance condition given by equation 2.1[1]. Now, equation 2.1 is rearranged to give,

$$\gamma_r^2 = \frac{k_r}{2k_u}(1 + a_u^2) \tag{2.90}$$

$$\frac{k_u}{k_r}\gamma_r^2 = \frac{(1 + a_u^2)}{2} \tag{2.91}$$

[1]First take $\frac{1}{\beta_{zj}} = \left(1 + \frac{1+a_u^2}{2\gamma_r^2}\right)$ and rearrange $\frac{1-\beta_{zj}}{\beta_{zj}} = \frac{1+a_u^2}{2\gamma_r^2}$, now combine with $\frac{\lambda_r}{\lambda_u} = \frac{1-\beta_{zj}}{\beta_{zj}}$ to get $\frac{\lambda_r}{\lambda_u} = \frac{1+a_u^2}{2\gamma_r^2} => \lambda_r = \frac{\lambda_u}{2\gamma_r^2}(1 + a_u^2)$ as stated by equation 2.1.

and combining with equation 2.89,

$$\frac{1}{\beta_{zj}} = \Big(1 + \frac{k_u}{k_r}\frac{\gamma_r^2}{\gamma_j^2}\Big) \tag{2.92}$$

Inserting the above expression into equation 2.79.

$$\frac{d\theta_j}{dz} = k_u + k_r(1 - (1 + \frac{k_u}{k_r}\frac{\gamma_r^2}{\gamma_j^2})) \tag{2.93}$$

$$\frac{d\theta_j}{dz} = k_u - k_r(\frac{k_u}{k_r}\frac{\gamma_r^2}{\gamma_j^2}) \tag{2.94}$$

$$\frac{d\theta_j}{dz} = k_u - k_u\frac{\gamma_r^2}{\gamma_j^2} \tag{2.95}$$

$$\frac{d\theta_j}{dz} = k_u\Big(1 - \frac{\gamma_r^2}{\gamma_j^2}\Big) \tag{2.96}$$

now introduce $\Delta\gamma = \gamma_j - \gamma_r => \gamma_j = \Delta\gamma + \gamma_r$ and looking at the γ_r^2/γ_j^2 term

$$\frac{\gamma_r^2}{\gamma_j^2} = \frac{\gamma_r^2}{(\Delta\gamma + \gamma_r)^2} = \frac{\gamma_r^2}{\gamma_r^2}\frac{1}{(\Delta\gamma/\gamma_r + 1)^2} = (1 + \Delta\gamma/\gamma_r)^{-2} \tag{2.97}$$

another Binomial expansion, which assumes $\Delta\gamma \ll \gamma_r$, gives,

$$\frac{\gamma_r^2}{\gamma_j^2} = 1 - \frac{2\Delta\gamma}{\gamma_r} \tag{2.98}$$

$$1 - \frac{\gamma_r^2}{\gamma_j^2} = \frac{2\Delta\gamma}{\gamma_r} \tag{2.99}$$

substituting this expression into equation 2.96 and remembering $\Delta\gamma = \gamma_j - \gamma_r$ yields,

$$\frac{d\theta_j}{dz} = 2k_u\Big(\frac{\gamma_j - \gamma_r}{\gamma_r}\Big). \tag{2.100}$$

Remembering the gain length is defined as $l_g = 1/2k_u\rho$ and using $\frac{d\bar{z}}{dz} = 1/l_g$ to rearrange the above expression

$$\frac{d\theta_j}{d\bar{z}} = 2k_u l_g\Big(\frac{\gamma_j - \gamma_r}{\gamma_r}\Big) \tag{2.101}$$

$$\frac{d\theta_j}{d\bar{z}} = \frac{\gamma_j - \gamma_r}{\rho\gamma_r} \tag{2.102}$$

inserting the scaled energy parameter $p_j = \frac{\gamma_j - \gamma_r}{\rho\gamma_r}$

$$\frac{d\theta_j}{d\bar{z}} = p_j. \tag{2.103}$$

2.3.4 The 1D wave equation

To simulate the evolution of the radiation field, the 1D Maxwell wave equation is introduced,

$$\Big(\frac{\partial^2}{\partial z^2} - \frac{1}{c^2}\frac{\partial^2}{\partial t^2}\Big)\mathbf{E} = \mu_0\frac{\partial \mathbf{J}}{\partial t} \tag{2.104}$$

The radiation field was previously defined as,

$$\mathbf{E} = \frac{1}{\sqrt{2}}\left(\hat{\mathbf{e}}\xi e^{i(k_r z - \omega_r t)} + c.c.\right) \tag{2.105}$$

where $\hat{\mathbf{e}} = \frac{1}{\sqrt{2}}(\hat{\mathbf{x}} + i\hat{\mathbf{y}})$ is defined such that, $\hat{\mathbf{e}}\cdot\hat{\mathbf{e}} = \frac{1}{2}(\hat{\mathbf{x}}^2 - \hat{\mathbf{y}}^2) = 0$ and $\hat{\mathbf{e}}\cdot\hat{\mathbf{e}}^* = \frac{1}{2}(\hat{\mathbf{x}}^2 + \hat{\mathbf{y}}^2) = 1$. The transverse electric field and transverse current are given by $\sqrt{2}\hat{\mathbf{e}}^*\cdot\mathbf{E} = E_\perp = E_x - iE_y = \xi e^{i(k_r z - \omega_r t)}$ and $\sqrt{2}\hat{\mathbf{e}}^*\cdot\mathbf{J} = J_\perp = J_x - iJ_y$ now, projecting equation 2.104 onto $\sqrt{2}\hat{\mathbf{e}}^*$ and integrating over the x-y plane (assuming equal cross sectional areas σ between radiation field and electron

pulse) gives

$$\iint_A dxdy\Big(\frac{\partial^2}{\partial z^2}-\frac{1}{c^2}\frac{\partial^2}{\partial t^2}\Big)\mathbf{E}\cdot\hat{\mathbf{e}}^*\sqrt{2}=\mu_0\iint_A\frac{\partial\mathbf{J}}{\partial t}dxdy\cdot\hat{\mathbf{e}}^*\sqrt{2} \tag{2.106}$$

$$\sigma\Big(\frac{\partial^2}{\partial z^2}-\frac{1}{c^2}\frac{\partial^2}{\partial t^2}\Big)\mathbf{E}\cdot\hat{\mathbf{e}}^*\sqrt{2}=\mu_0\frac{\partial\mathbf{J}}{\partial t}\cdot\hat{\mathbf{e}}^*\sqrt{2} \tag{2.107}$$

$$\Big(\frac{\partial^2}{\partial z^2}-\frac{1}{c^2}\frac{\partial^2}{\partial t^2}\Big)\mathbf{E}\cdot\hat{\mathbf{e}}^*\sqrt{2}=\frac{\mu_0}{\sigma}\frac{\partial\mathbf{J}}{\partial t}\cdot\hat{\mathbf{e}}^*\sqrt{2} \tag{2.108}$$

here $\iint_A\frac{\partial\mathbf{J}}{\partial t}dxdy=\frac{\partial\mathbf{J}}{\partial t}$, because the current vector $\mathbf{J}$ contains implicit factors of $\delta(x-x_j)$ and $\delta(y-y_j)$ which both integrate to unity.

$$\Big(\frac{\partial^2}{\partial z^2}-\frac{1}{c^2}\frac{\partial^2}{\partial t^2}\Big)\xi e^{i(k_rz-\omega_rt)}=\frac{\mu_0}{\sigma}\frac{\partial J_\perp}{\partial t} \tag{2.109}$$

$$\Big(\frac{\partial}{\partial z}-\frac{1}{c}\frac{\partial}{\partial t}\Big)\Big(\frac{\partial}{\partial z}+\frac{1}{c}\frac{\partial}{\partial t}\Big)\xi e^{i(k_rz-\omega_rt)}=\frac{\mu_0}{\sigma}\frac{\partial J_\perp}{\partial t} \tag{2.110}$$

converting to scaled units using, where $\bar{z}_1l_g=\frac{z-c\bar{\beta}_zt}{(1-\bar{\beta}_z)}$ and $\bar{z}l_g=z$,

$$\left(\frac{\partial}{\partial\bar{z}}+\frac{\partial}{\partial\bar{z}_1}\right)=l_g\left(\frac{\partial}{\partial z}+\frac{1}{c}\frac{\partial}{\partial t}\right) \tag{2.111}$$

and

$$2\frac{\bar{\beta}_z}{1-\bar{\beta}_z}\left[\frac{1-\bar{\beta}_z}{2\bar{\beta}_z}\left(\frac{\partial}{\partial\bar{z}_1}+\frac{\partial}{\partial\bar{z}}\right)+\frac{\partial}{\partial\bar{z}_1}\right]=l_g\left(\frac{\partial}{\partial z}-\frac{1}{c}\frac{\partial}{\partial t}\right) \tag{2.112}$$

see appendix B.3 for a derivation of the above expressions. Now,

$$2\frac{\bar{\beta}_z}{1-\bar{\beta}_z}\left[\frac{1-\bar{\beta}_z}{2\bar{\beta}_z}\left(\frac{\partial}{\partial\bar{z}_1}+\frac{\partial}{\partial\bar{z}}\right)+\frac{\partial}{\partial\bar{z}_1}\right]\left(\frac{\partial}{\partial\bar{z}}+\frac{\partial}{\partial\bar{z}_1}\right)\xi e^{i(k_rz-\omega_rt)} \tag{2.113}$$

$$=l_g^2\frac{\mu_0}{\sigma}\frac{\partial J_\perp}{\partial t} \tag{2.114}$$

$\bar{z}_1$ can be rearranged to give[2] $\bar{z}_1 = 2\rho z(k_r + k_u) - 2\rho k_r ct$, combining with $\bar{z} = 2k_u\rho z$, $\bar{z}_1 - \bar{z} = 2\rho k_r z - 2\rho k_r ct$ to give $(\bar{z}_1 - \bar{z})/2\rho = k_r z - \omega_r t$

$$2\frac{\bar{\beta}_z}{1-\bar{\beta}_z}\left[\frac{1-\bar{\beta}_z}{2\bar{\beta}_z}\left(\frac{\partial}{\partial\bar{z}_1}+\frac{\partial}{\partial\bar{z}}\right)+\frac{\partial}{\partial\bar{z}_1}\right]\left(\frac{\partial}{\partial\bar{z}}+\frac{\partial}{\partial\bar{z}_1}\right)\xi e^{i\frac{\bar{z}_1-\bar{z}}{2\rho}} \tag{2.115}$$

$$= l_g^2\frac{\mu_0}{\sigma}\frac{\partial J_\perp}{\partial t} \tag{2.116}$$

expanding the square brackets,

$$\left[\frac{1-\bar{\beta}_z}{2\bar{\beta}_z}\left(\frac{\partial}{\partial\bar{z}_1}+\frac{\partial}{\partial\bar{z}}\right)+\frac{\partial}{\partial\bar{z}_1}\right]\xi e^{i\frac{\bar{z}_1-\bar{z}}{2\rho}} \tag{2.117}$$

$$e^{i\frac{\bar{z}_1-\bar{z}}{2\rho}}\left[\frac{1-\bar{\beta}_z}{2\bar{\beta}_z}\left(\frac{\partial\xi}{\partial\bar{z}_1}+\frac{\partial\xi}{\partial\bar{z}}\right)+\frac{\partial\xi}{\partial\bar{z}_1}+\frac{i}{2\rho}\xi\right] \tag{2.118}$$

the $\frac{1-\bar{\beta}_z}{2\bar{\beta}_z}\left(\frac{\partial\xi}{\partial\bar{z}_1}+\frac{\partial\xi}{\partial\bar{z}}\right)$ term can be ignored if,

$$\left|\frac{1-\bar{\beta}_z}{2\bar{\beta}_z}\left(\frac{\partial\xi}{\partial\bar{z}_1}+\frac{\partial\xi}{\partial\bar{z}}\right)\right| \ll \left|\frac{\partial\xi}{\partial\bar{z}_1}+\frac{i}{2\rho}\xi\right|, \tag{2.119}$$

hence the square brackets are replaced with,

$$\left[\frac{1-\bar{\beta}_z}{2\bar{\beta}_z}\left(\frac{\partial}{\partial\bar{z}_1}+\frac{\partial}{\partial\bar{z}}\right)+\frac{\partial}{\partial\bar{z}_1}\right]\xi e^{i\frac{\bar{z}_1-\bar{z}}{2\rho}} = e^{i\frac{\bar{z}_1-\bar{z}}{2\rho}}\left[\frac{\partial\xi}{\partial\bar{z}_1}+\frac{i}{2\rho}\xi\right] \tag{2.120}$$

$$\left[\frac{1-\bar{\beta}_z}{2\bar{\beta}_z}\left(\frac{\partial}{\partial\bar{z}_1}+\frac{\partial}{\partial\bar{z}}\right)+\frac{\partial}{\partial\bar{z}_1}\right]\xi e^{i\frac{\bar{z}_1-\bar{z}}{2\rho}} = \frac{\partial}{\partial\bar{z}_1}\xi e^{i\frac{\bar{z}_1-\bar{z}}{2\rho}} \tag{2.121}$$

[2] $\bar{z}_1 = 2k_w\rho\frac{z-c\bar{\beta}_z t}{(1-\beta_z)} = \frac{2k_w\rho z}{(1-\beta_z)} - \frac{2k_w\rho c\bar{\beta}_z t}{(1-\beta_z)}$ now $\frac{k_r}{k_w} = \frac{\bar{\beta}_z}{1-\bar{\beta}_z}$ and using $\frac{1-\bar{\beta}_z}{1-\beta_z} = 1$, $\frac{k_r}{k_w} + 1 = \frac{\bar{\beta}_z}{1-\bar{\beta}_z} + \frac{1-\bar{\beta}_z}{1-\bar{\beta}_z} \rightarrow \frac{k_r+k_w}{k_w} = \frac{1}{1-\bar{\beta}_z} \rightarrow k_r + k_w = \frac{k_w}{1-\bar{\beta}_z}$ combining these expressions $\bar{z}_1 = 2(k_w + k_r)\rho z - 2k_r\rho ct$

therefore,

$$2\frac{\bar{\beta}_z}{1-\bar{\beta}_z}\frac{\partial}{\partial\bar{z}_1}\left(\frac{\partial}{\partial\bar{z}}+\frac{\partial}{\partial\bar{z}_1}\right)\xi e^{i\frac{\bar{z}_1-\bar{z}}{2\rho}}=l_g^2\frac{\mu_0}{\sigma}\frac{\partial J_\perp}{\partial t} \tag{2.122}$$

now rewrite the RHS in scaled units, using,

$$\frac{\bar{\beta}_z}{1-\bar{\beta}_z}\frac{\partial}{\partial\bar{z}_1}=-\frac{l_g}{c}\frac{\partial}{\partial t} \tag{2.123}$$

$$2\frac{\bar{\beta}_z}{1-\bar{\beta}_z}\frac{\partial}{\partial\bar{z}_1}\left(\frac{\partial}{\partial\bar{z}}+\frac{\partial}{\partial\bar{z}_1}\right)\xi e^{i\frac{\bar{z}_1-\bar{z}}{2\rho}}=-l_g c\frac{\bar{\beta}_z}{1-\bar{\beta}_z}\frac{\mu_0}{\sigma}\frac{\partial J_\perp}{\partial\bar{z}_1} \tag{2.124}$$

$$\frac{\partial}{\partial\bar{z}_1}\left(\frac{\partial}{\partial\bar{z}}+\frac{\partial}{\partial\bar{z}_1}\right)\xi e^{i\frac{\bar{z}_1-\bar{z}}{2\rho}}=-l_g c\frac{\mu_0}{2\sigma}\frac{\partial J_\perp}{\partial\bar{z}_1} \tag{2.125}$$

$$\frac{\partial}{\partial\bar{z}_1}\left(\frac{\partial}{\partial\bar{z}}+\frac{\partial}{\partial\bar{z}_1}\right)\xi e^{i\frac{\bar{z}_1-\bar{z}}{2\rho}}+l_g c\frac{\mu_0}{2\sigma}\frac{\partial J_\perp}{\partial\bar{z}_1}=0 \tag{2.126}$$

$$\frac{\partial}{\partial\bar{z}_1}\left[\left(\frac{\partial}{\partial\bar{z}}+\frac{\partial}{\partial\bar{z}_1}\right)\xi e^{i\frac{\bar{z}_1-\bar{z}}{2\rho}}+l_g c\frac{\mu_0}{2\sigma}J_\perp\right]=0 \tag{2.127}$$

then assuming energy conservations i.e. the transverse radiation field is driven by the transverse current, and therefore the bracketed terms must equal zero,

$$\left(\frac{\partial}{\partial\bar{z}}+\frac{\partial}{\partial\bar{z}_1}\right)\xi e^{i\frac{\bar{z}_1-\bar{z}}{2\rho}}+l_g c\frac{\mu_0}{2\sigma}J_\perp=0 \tag{2.128}$$

$$\left(\frac{\partial}{\partial\bar{z}}+\frac{\partial}{\partial\bar{z}_1}\right)\xi e^{i\frac{\bar{z}_1-\bar{z}}{2\rho}}=-l_g c\frac{\mu_0}{2\sigma}J_\perp \tag{2.129}$$

the transverse current density can be written as,

$$J_\perp=-ec\sum_{j=1}^{N}\beta_\perp\delta(z-z_j(t)) \tag{2.130}$$

and is combined with the above expression

$$\left(\frac{\partial}{\partial \bar{z}} + \frac{\partial}{\partial \bar{z}_1}\right) \xi e^{i\frac{\bar{z}_1 - \bar{z}}{2\rho}} = e l_g c^2 \frac{\mu_0}{2\sigma} \sum_{j=1}^{N} \beta_\perp \delta(z - z_j(t)) \tag{2.131}$$

where $\beta_\perp$ is defined as, taking $\boldsymbol{\beta}$ from equation 2.27. The Dirac delta function has the useful property $\int_{T-\epsilon}^{T+\epsilon} f(t)\delta(t-T)dt = f(T)$,

$$\sqrt{2}\hat{\mathbf{e}}^* \cdot \boldsymbol{\beta} = (\hat{\mathbf{x}} - i\hat{\mathbf{y}}) \left(-\frac{a_u}{\gamma_j} (\cos(k_u z)\hat{\mathbf{x}} + \sin(k_u z)\hat{\mathbf{y}}) + \boldsymbol{\beta}_z \hat{\mathbf{z}}\right) \tag{2.132}$$

$$\beta_\perp = -\frac{a_u}{\gamma_j}\Big(\cos(k_u z) - i\sin(k_u z)\Big) \tag{2.133}$$

$$\beta_\perp = -\frac{a_u}{\gamma_j} \exp(-ik_u z) \tag{2.134}$$

using this definition of $\beta_\perp$

$$\left(\frac{\partial}{\partial \bar{z}} + \frac{\partial}{\partial \bar{z}_1}\right) \xi e^{i\frac{\bar{z}_1 - \bar{z}}{2\rho}} = -e l_g c^2 \frac{\mu_0}{2\sigma} \sum_{j=1}^{N} \frac{a_u}{\gamma_j} \exp(-ik_u z)\delta(z - z_j(t)) \tag{2.135}$$

$$\left(\frac{\partial}{\partial \bar{z}} + \frac{\partial}{\partial \bar{z}_1}\right) \xi e^{i\frac{\bar{z}_1 - \bar{z}}{2\rho}} = -e l_g c^2 \frac{a_u}{\gamma_j} \frac{\mu_0}{2\sigma} \sum_{j=1}^{N} \exp(-ik_u z)\delta(z - z_j(t)) \tag{2.136}$$

the delta function transforms as $\delta(z - z_j(t)) = \dfrac{\delta(t - t_j)}{\beta_{zj} c} = 2k_r\rho \dfrac{\delta(\bar{z}_1 - \bar{z}_{1j})}{\beta_{zj}}$, since $\bar{z} = 2k_u \rho z$ and $\bar{z}_1 l_g = \frac{z - c\bar{\beta}_z t}{(1-\bar{\beta}_z)} => \bar{z}_1 = -ct/l_c$

$$\left(\frac{\partial}{\partial \bar{z}} + \frac{\partial}{\partial \bar{z}_1}\right) \xi e^{i\frac{\bar{z}_1 - \bar{z}}{2\rho}} = -e l_g c^2 \frac{a_u}{\gamma_j} \frac{\mu_0}{2\sigma} \sum_{j=1}^{N} e^{(-i\frac{\bar{z}}{2\rho})} 2k_r\rho \frac{\delta(\bar{z}_1 - \bar{z}_{1j})}{\beta_{zj}} \tag{2.137}$$

$$\left(\frac{\partial}{\partial \bar{z}} + \frac{\partial}{\partial \bar{z}_1}\right) \xi e^{i\frac{\bar{z}_1 - \bar{z}}{2\rho}} = -e 2k_r \rho l_g c^2 \frac{a_u}{\gamma_j} \frac{\mu_0}{2\sigma} \frac{1}{\beta_{zj}} \sum_{j=1}^{N} e^{-i\frac{\bar{z}}{2\rho}} \delta(\bar{z}_1 - \bar{z}_{1j}) \tag{2.138}$$

$$\left(\frac{\partial}{\partial \bar{z}} + \frac{\partial}{\partial \bar{z}_1}\right) \xi = -e 2k_r \rho l_g c^2 \frac{a_u}{\gamma_j} \frac{\mu_0}{2\sigma} \frac{1}{\beta_{zj}} \sum_{j=1}^{N} e^{-i\frac{\bar{z}_1}{2\rho}} \delta(\bar{z}_1 - \bar{z}_{1j}) \tag{2.139}$$

now using $1/c^2 = \mu_0 \epsilon_0 => \mu_0 = 1/(\epsilon_0 c^2)$

$$\left(\frac{\partial}{\partial \bar{z}} + \frac{\partial}{\partial \bar{z}_1}\right) \xi = -e 2k_r \rho l_g \frac{a_u}{\gamma_j \epsilon_0} \frac{1}{2\sigma} \frac{1}{\beta_{zj}} \sum_{j=1}^{N} e^{-i\frac{\bar{z}_1}{2\rho}} \delta(\bar{z}_1 - \bar{z}_{1j}) \tag{2.140}$$

the plasma frequency ω_p is now rearranged,

$$\omega_p = \left(\frac{e^2 n_p}{\epsilon_0 m}\right)^{1/2} \tag{2.141}$$

$$\omega_p^2 = \left(\frac{e^2 n_p}{\epsilon_0 m}\right) \tag{2.142}$$

$$\frac{\omega_p^2}{n_p} = \frac{e^2}{\epsilon_0 m} \tag{2.143}$$

$$\frac{m}{e}\frac{\omega_p^2}{n_p} = \frac{e}{\epsilon_0} \tag{2.144}$$

now inserting into equation 2.140 and rearranging,

$$\left(\frac{\partial}{\partial\bar{z}}+\frac{\partial}{\partial\bar{z}_1}\right)\xi=-2k_r\rho l_g\frac{m}{e}\frac{\omega_p^2}{n_p}\frac{a_u}{\gamma_j}\frac{1}{2\sigma}\frac{1}{\beta_{zj}}\sum_{j=1}^{N}e^{-i\frac{\bar{z}_1}{2\rho}}\delta(\bar{z}_1-\bar{z}_{1j}) \tag{2.145}$$

$$\left(\frac{\partial}{\partial\bar{z}}+\frac{\partial}{\partial\bar{z}_1}\right)\xi=-2k_r\rho\frac{1}{2k_u\rho}\frac{m}{e}\frac{\omega_p^2}{n_p}\frac{a_u}{\gamma_j}\frac{1}{2\sigma}\frac{1}{\beta_{zj}}\sum_{j=1}^{N}e^{-i\frac{\bar{z}_1}{2\rho}}\delta(\bar{z}_1-\bar{z}_{1j}) \tag{2.146}$$

$$\left(\frac{\partial}{\partial\bar{z}}+\frac{\partial}{\partial\bar{z}_1}\right)\xi=-2k_r\rho\frac{1}{\rho}\frac{m}{e}\frac{\omega_p}{n_p}\frac{1}{\gamma_j}2c\frac{a_u\omega_p}{4ck_u}\frac{1}{2\sigma}\frac{1}{\beta_{zj}}\sum_{j=1}^{N}e^{-i\frac{\bar{z}_1}{2\rho}}\delta(\bar{z}_1-\bar{z}_{1j}) \tag{2.147}$$

now ρ can be rearranged,

$$\rho=\frac{1}{\gamma_r}\left(\frac{a_u\omega_p}{4ck_u}\right)^{2/3} \tag{2.148}$$

$$\left(\rho\gamma_r\right)^{3/2}=\frac{a_u\omega_p}{4ck_u} \tag{2.149}$$

$$\left(\frac{\partial}{\partial\bar{z}}+\frac{\partial}{\partial\bar{z}_1}\right)\xi=-2k_r\rho\frac{1}{\rho}\frac{m}{e}\frac{\omega_p}{n_p}\frac{1}{\gamma_j}2c\left(\rho\gamma_r\right)^{3/2}\frac{1}{2\sigma}\frac{1}{\beta_{zj}}\sum_{j=1}^{N}e^{-i\frac{\bar{z}_1}{2\rho}}\delta(\bar{z}_1-\bar{z}_{1j}) \tag{2.150}$$

now, assuming $\frac{\gamma_r-\gamma_j}{\gamma_r}\ll 1$, then setting $\gamma_j=\gamma_r$ and $\beta_{zj}=1$

$$\left(\frac{\partial}{\partial\bar{z}}+\frac{\partial}{\partial\bar{z}_1}\right)\xi=-2k_r\rho\frac{1}{\rho}\frac{m}{e}\frac{\omega_p}{n_p}\frac{1}{\gamma_r}2c\left(\rho\gamma_r\right)^{3/2}\frac{1}{2\sigma}\sum_{j=1}^{N}e^{-i\frac{\bar{z}_1}{2\rho}}\delta(\bar{z}_1-\bar{z}_{1j}) \tag{2.151}$$

$$\left(\frac{\partial}{\partial\bar{z}}+\frac{\partial}{\partial\bar{z}_1}\right)\xi=-2k_r\rho\frac{m}{e}\frac{\omega_p}{n_p}2c\left(\rho\gamma_r\right)^{1/2}\frac{1}{2\sigma}\sum_{j=1}^{N}e^{-i\frac{\bar{z}_1}{2\rho}}\delta(\bar{z}_1-\bar{z}_{1j}) \tag{2.152}$$

$$\left(\frac{\partial}{\partial\bar{z}}+\frac{\partial}{\partial\bar{z}_1}\right)\frac{e\xi}{mc\omega_p\sqrt{\rho\gamma_r}}=-2k_r\rho\frac{1}{n_p}\frac{1}{\sigma}\sum_{j=1}^{N}e^{-i\frac{\bar{z}_1}{2\rho}}\delta(\bar{z}_1-\bar{z}_{1j}) \tag{2.153}$$

the scaled radiation field was defined as, $A(\bar{z},\bar{z}_1)=\frac{e\xi}{mc\omega_p\sqrt{\rho\gamma_r}}$

$$\left(\frac{\partial}{\partial\bar{z}}+\frac{\partial}{\partial\bar{z}_1}\right)A(\bar{z},\bar{z}_1)=-\frac{2k_r\rho}{n_p\sigma}\sum_{j=1}^{N}e^{-i\frac{\bar{z}_1}{2\rho}}\delta(\bar{z}_1-\bar{z}_{1j}) \tag{2.154}$$

The scaled linear density is defined as, $\bar{n}_p=\frac{n_p\sigma}{2k_r\rho}=l_c n_p\sigma$

$$\left(\frac{\partial}{\partial\bar{z}}+\frac{\partial}{\partial\bar{z}_1}\right)A(\bar{z},\bar{z}_1)=-\frac{1}{\bar{n}_p}\sum_{j=1}^{N}e^{-i\frac{\bar{z}_1}{2\rho}}\delta(\bar{z}_1-\bar{z}_{1j}) \tag{2.155}$$

Now, the wave equation is converted into form suited to numerical integration. This done by integrating the wave equation over one resonant radiation period $(4\pi\rho)$,

$$\int_{\bar{z}_1-2\pi\rho}^{\bar{z}_1+2\pi\rho}\left(\frac{\partial}{\partial\bar{z}}+\frac{\partial}{\partial\bar{z}_1}\right)A(\bar{z},\bar{z}_1)d\bar{z}_1=\int_{\bar{z}_1-2\pi\rho}^{\bar{z}_1+2\pi\rho}-\frac{1}{\bar{n}_p}\sum_{j=1}^{N}e^{-i\frac{\bar{z}_1}{2\rho}}\delta(\bar{z}_1-\bar{z}_{1j})d\bar{z}_1 \tag{2.156}$$

The local radiation field is defined as, over the integration window, $\bar{A}(\bar{z},\bar{z}_1)=[A(\bar{z},\bar{z}_1+2\pi\rho)+A(\bar{z},\bar{z}_1-2\pi\rho)]/2$

$$\left(\frac{\partial}{\partial\bar{z}}+\frac{\partial}{\partial\bar{z}_1}\right)\bar{A}(\bar{z},\bar{z}_1)\int_{\bar{z}_1-2\pi\rho}^{\bar{z}_1+2\pi\rho}d\bar{z}_1=\int_{\bar{z}_1-2\pi\rho}^{\bar{z}_1+2\pi\rho}-\frac{1}{\bar{n}_p}\sum_{j=1}^{N}e^{-i\frac{\bar{z}_1}{2\rho}}\delta(\bar{z}_1-\bar{z}_{1j})d\bar{z}_1 \tag{2.157}$$

$$\left(\frac{\partial}{\partial\bar{z}}+\frac{\partial}{\partial\bar{z}_1}\right)\bar{A}(\bar{z},\bar{z}_1)4\pi\rho=-\frac{1}{\bar{n}_p}\sum_{j=1}^{N_\lambda}e^{-i\frac{\bar{z}_{1j}}{2\rho}} \tag{2.158}$$

$$\left(\frac{\partial}{\partial\bar{z}}+\frac{\partial}{\partial\bar{z}_1}\right)\bar{A}(\bar{z},\bar{z}_1)=-\frac{1}{N_\lambda}\sum_{j=1}^{N_\lambda}e^{-i\frac{\bar{z}_{1j}}{2\rho}} \tag{2.159}$$

however the pondermotive phase was given by $\theta_j = (k_r + k_u)z - \omega_r t_j$ and the scaled coordinate $\bar{z}_{1j} = 2\rho z(k_r + k_u) - 2\rho k_r c t_j$, therefore $\theta_j = \bar{z}_{1j}/2\rho$

$$\left(\frac{\partial}{\partial \bar{z}} + \frac{\partial}{\partial \bar{z}_1}\right) \bar{A}(\bar{z}, \bar{z}_1) = -\frac{1}{N_\lambda} \sum_{j=1}^{N_\lambda} e^{-i\theta_j} \tag{2.160}$$

2.4 1D equations

The 1D FEL equations are restated here,

$$\frac{dp_j}{d\bar{z}} = \left(Ae^{i\theta_j} + c.c.\right) \tag{2.161}$$

$$\frac{d\theta_j}{d\bar{z}} = p_j \tag{2.162}$$

$$\left(\frac{\partial}{\partial \bar{z}} + \frac{\partial}{\partial \bar{z}_1}\right) A(\bar{z}, \bar{z}_1) = -\frac{1}{N_\lambda} \sum_{j=1}^{N_\lambda} e^{-i\theta_j} \tag{2.163}$$

where $p_j = \frac{\gamma_j - \gamma_r}{\rho\gamma_r}$ is scaled energy parameter and $\theta_j = (k_u + k)z - \omega t$ the pondermotive phase. However, now the steady state approximation is made by ignoring the $\frac{d}{d\bar{z}_1}$ derivatives, here we have replaced $A = -A$

$$\frac{dp_j}{d\bar{z}} = -(A\exp[i\theta_j] + c.c.) \tag{2.164}$$

$$\frac{d\theta_j}{d\bar{z}} = p_j \tag{2.165}$$

$$\frac{d}{d\bar{z}}A = < \exp[-i\theta_j] > \tag{2.166}$$

here, $< \exp[-i\theta_j] > = \frac{1}{N_\lambda} \sum_{j=1}^{N_\lambda} e^{-i\theta_j}$.

The complex radiation field can be written as $A = |A| \exp[i\phi]$ with phase ϕ which is allowed to evolve and $|A|$ is the radiation field amplitude. Inserting this definition in equation 2.166 gives,

$$\frac{d}{d\bar{z}}\left(|A| \exp[i\phi]\right) =< \exp[-i\theta_j] > \tag{2.167}$$

$$\exp[i\phi]\frac{d|A|}{d\bar{z}} + i|A| \exp[i\phi]\frac{d\phi}{d\bar{z}} =< \exp[-i\theta_j] > \tag{2.168}$$

$$\frac{d|A|}{d\bar{z}} + i|A|\frac{d\phi}{d\bar{z}} =< \exp[-i\theta_j] > \exp[-i\phi] \tag{2.169}$$

$$\frac{d|A|}{d\bar{z}} + i|A|\frac{d\phi}{d\bar{z}} =< \exp[-i(\theta_j + \phi)] > \tag{2.170}$$

$$\frac{d|A|}{d\bar{z}} + i|A|\frac{d\phi}{d\bar{z}} =< \cos(\theta_j + \phi) > -i < \sin(\theta_j + \phi) > \tag{2.171}$$

now separating the real and imaginary parts,

$$\frac{d|A|}{d\bar{z}} =< \cos(\theta_j + \phi) > \tag{2.172}$$

$$\frac{d\phi}{d\bar{z}} = -\frac{1}{|A|} < \sin(\theta_j + \phi) > \tag{2.173}$$

inserting the new scaled radiation field with phase ϕ into equation 2.164,

$$\frac{dp_j}{d\bar{z}} = -(|A| \exp[i\phi] \exp[i\theta_j] + c.c.) \tag{2.174}$$

$$\frac{dp_j}{d\bar{z}} = -|A|(\exp[i(\theta_j + \phi)] + \exp[-i(\theta_j + \phi)]) \tag{2.175}$$

applying Euler's relations $2\cos x = e^{ix} + e^{-ix}$.

$$\frac{dp_j}{d\bar{z}} = -2|A| \cos(\theta_j + \phi) \tag{2.176}$$

restating the FEL equations once more with the radiation phase equation in

the steady state regime,

$$\frac{dp_j}{d\bar{z}} = -2|A|\cos(\theta_j + \phi) \tag{2.177}$$

$$\frac{d\theta_j}{d\bar{z}} = p_j \tag{2.178}$$

$$\frac{d|A|}{d\bar{z}} = < \cos(\theta_j + \phi) > \tag{2.179}$$

$$\frac{d\phi}{d\bar{z}} = -\frac{1}{|A|} < \sin(\theta_j + \phi) > \tag{2.180}$$

To understand the FEL mechanism, consider the above set of equations and assume initially $\phi = 0$. Electrons in the region $\pi/2 < \theta < 3\pi/2$ will experience a small increase in energy, as can be seen from equation 2.177. However, electrons located between $3\pi/2 < \theta < 2\pi$ will experience a small decrease in energy. This can be seen figure 2.2(a-b), where the $-\cos(\theta_j + \phi)$ part of equation 2.177 is plotted with an initially cold electron pulse. Now, equation 2.178 tells us that the electrons will bunch around $\theta = 3\pi/2$, as can be seen in figure 2.2(c). However, at this phase the electron microbunches cannot increase the radiation field amplitude $|A|$, i.e., for the electrons at $\theta_j = 3\pi/2$, as $\frac{d|A|}{d\bar{z}} = 0$ in accordance with equation 2.179. This can be seen figure 2.2(d), where the $\cos(\theta_j + \phi)$ part of equations 2.179 is plotted with the electron pulse. But, the radiation phase ϕ which is initially zero will increase (see equation 2.180), such that the increased electron density at $3\pi/2$ will result in $\frac{d\phi}{d\bar{z}} > 0$, as seen in figure 2.2(e). Therefore the phase ϕ and argument of equation 2.179 will increase (see figure 2.2(f)). Hence the radiation field amplitude $|A|$ increases $\frac{d|A|}{d\bar{z}} > 0$, see figure 2.2(f). This then increases the bunching, which further amplifies the radiation field, this is basic mechanism of the FEL. This feedback loop will continue until the radiation field saturates. Linear analysis [8] of the 1D FEL equations shows that FEL high gain amplification process is characterised by the gain length l_g, where an initial radiation power P_0 is exponentially amplified as a function of distance through the undulator as $P = P_0 \exp(\sqrt{3}z/l_g)$.

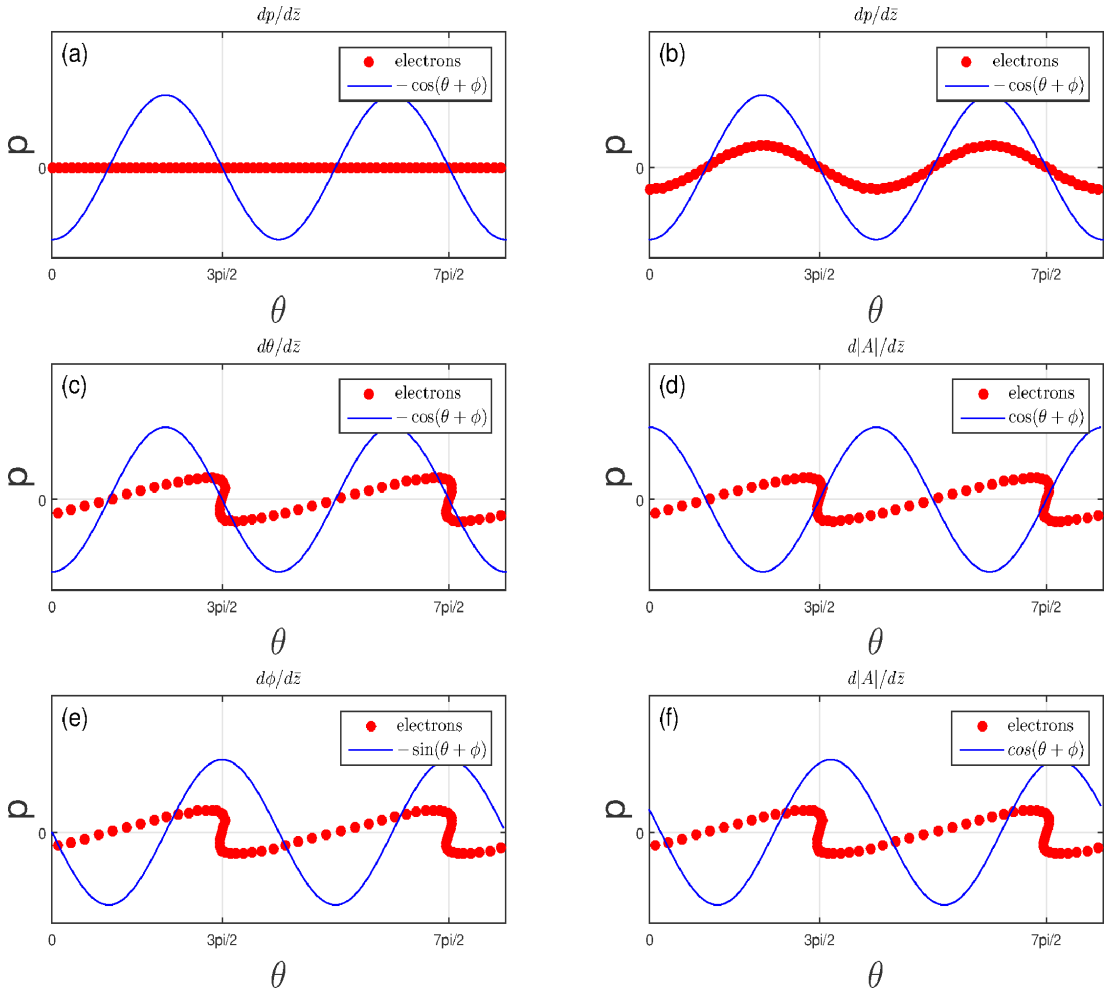

Figure 2.2: The Free Electron Laser mechanism is illustrated above. (a) overlap of the initial cold electron pulse and the functional part of equation 2.177 (b) the electron pulse will experience an energy modulation described by equation 2.177 (c) this energy modulation cause the electron to bunch around $3\pi/2$, $7\pi/2$, etc. (d) electrons bunched around $3\pi/2$ cannot amplify the radiation field i.e. the functional part of equation 2.179 will be zero (e) however the radiation field phase ϕ will increase due the increased electron density around $3\pi/2$ (see equation 2.180) (f) as the radiation phase increases the argument of equation 2.179 will increase such that $\frac{d|A|}{d\bar{z}} > 0$ and radiation field amplitude will increase. Increasing the radiation field amplitude $|A|$ will then increase the bunching which in turn increase the radiation field amplitude in a collective feed back loop.

For the simulations presented in this thesis a larger set of equations, than the simplified equations 2.177-2.180, are integrated numerically. In hpFull [10] for example the electron pulse's transverse trajectory is not assumed to be a simple function of the undulator magnetic field and must be calculated self-consistently. Two different FEL codes are used in the rest of this thesis. The first code is the 1D FEL simulation hpFull, and was used to obtain the results given in section 4.2. The parallelized 3D FEL code Puffin which will be discussed in chapter 3 was used to obtain the results given in chapters 5-7 in the 1D limit. In these codes the slow varying envelope approximation is not made, however the paraxial approximation is and the backwards propagating wave is neglected. These two codes do not apply period averaging in their analytical models unlike more industrious codes, such as Genesis [20]. Genesis is very likely the most popular FEL code in the world. Genesis makes a number of limiting assumptions to reduce the computation time. One of the most important of these assumptions is period averaging. In Genesis the electron pulse and radiation field are discretized at the resonant period, the FEL equations are then solved for each self-contained resonant period/slice. To model slippage effects the radiation field is slipped ahead of the electron pulse by one resonant period/slice after one resonant period of numerical integration. This period averaging gives a large improvement in computational time. Genesis also applies the paraxial and slow varying envelope approximation. Genesis (and any averaged FEL simulator) cannot model sub-period phenomena such as coherent spontaneous emission and is limited in range of frequencies that can be modelled. The simulations presented in this thesis were performed in the unaveraged FEL codes hpFull and Puffin. hpFull combines the unaveraged FEL simulation code of [10] with the macroparticle loading algorithm of [9]. Puffin [11] is reviewed in chapter 3 and the inclusion of physically correct 3D undulator magnetic fields is discussed. The implementation of 3D undulator magnetic field was reported in [12].

Chapter 3

Puffin and the 3D undulator

3.1 Introduction

The equations integrated by hpFull [9, 10] can be derived in a similar fashion to those found in chapter 2. However, the electron transverse momentum and trajectory are not assumed to be simple of functions of the undulator magnetic field. Hence, the electron transverse momentum must be calculated self-consistently. The equation describing the evolution of $p_\perp$, can be derived if the electric field is not ignored in equation 2.14. By including the electric field this equation does not easily integrate and must be solved numerically and self-consistently, with the rest of hpFull's equations. In hpFull the electron longitudinal momentum is calculated self-consistently instead of its energy. Puffin [11] is basically a three dimensional version of hpFull, however the equations are scaled to radiation frame. This allows Puffin to simulate the interaction of 6D electron beams (3 dimensions in momentum space and 3 spatial dimensions) and 3D radiation fields. Puffin is integrating in a 6D phase space, which is very computational intensive. To overcome this, Puffin is implemented in Fortran 90 under the MPI-standard. The MPI-standard (Message Passage Interface) allows Puffin to run on a high performance machine, a supercomputer, across many computational nodes. This can drastically reduce computation time. It is also necessary to run Puffin on a high performance machine, because Puf-

fin's 6D phase space can require a large amounts of local memory (10-100GB), which typically exceeds what is available on desktop machines. Even in the 1D limit it is useful to run Puffin on a cluster to reduce computation time from days to hours and free up local computing power.

Puffin was originally written with a simple 1D dimensional undulator magnetic field. Since, electron pulses' have a non-zero transverse velocity, they expand during propagation through an undulator, therefore Puffin's working equations included an artificial focusing channel [11]. Undulators can be designed to have off-axis parabolic magnetic fields. Such a magnetic field will induce a focusing force in both transverse directions, which counteracts the electron pulse's expansion. Canted pole, those producing parabolic magnetic fields, and plane pole magnetic undulator fields are now included in Puffin's working set of equations [12]. In, doing so the artificial focusing channel was removed, allowing a more physically correct description of the FEL phenomena to emerge in simulations. The inclusion of the 3D undulator magnetic fields is discussed in the proceeding sections of this chapter, with a derivation of the new Puffin equations with the 3D undulator given in appendix A.

3.2 Outline of FEL equations

The derivation of the original FEL system of equations modelled by Puffin is given in [11], using a magnetic undulator field $\mathbf{B}_u = \frac{B_0}{2}(\mathbf{u}e^{ik_u z} + c.c.)$, where $\mathbf{u} = u_x\hat{\mathbf{x}} + iu_y\hat{\mathbf{y}}$ defines the polarization of the undulator. Following a similar derivation, which is given in appendix A, but using a general 3D magnetic field of the form $\mathbf{B} = B_x\hat{\mathbf{x}} + B_y\hat{\mathbf{y}} + B_z\hat{\mathbf{z}}$, one obtains the following system of equations:

$$\frac{dp_{2j}}{d\bar{z}} = \frac{\rho}{\eta}L_j^2\left((\bar{p}^*_{\perp j}A_\perp + c.c)\eta p_{2j} - i\alpha^2(1+\eta p_{2j})(\bar{p}_{\perp j}b^*_{\omega\perp} - c.c.)\right) \tag{3.1}$$

$$\frac{d\bar{p}_{\perp j}}{d\bar{z}} = \frac{1}{2\rho}\left(ib_{w\perp} - \frac{\eta p_{2j}}{\alpha^2}A_\perp\right) - i\alpha\bar{p}_{\perp j}L_j b_z \tag{3.2}$$

the preceding differential equations describe the electron momentum through the undulator, and the field equation is given by,

$$\frac{1}{2}\left(\frac{\partial^2}{\partial\bar{x}^2}+\frac{\partial^2}{\partial\bar{y}^2}\right)A_\perp-\frac{\partial^2}{\partial\bar{z}\partial\bar{z}_2}A_\perp=-\frac{L_j}{\bar{n}_p}\frac{\partial}{\partial\bar{z}_2}\sum_{j=1}^{N}\bar{p}_{\perp j}\delta(\bar{x}_j,\bar{y}_j\bar{z}_{2j}) \tag{3.3}$$

the evolution of electron axial coordinates are described by,

$$\frac{d\bar{z}_{2j}}{d\bar{z}}=p_{2j} \tag{3.4}$$

$$\frac{d\bar{x}_j}{d\bar{z}}=\frac{2\rho\alpha}{\sqrt{\eta}}L_j\Re(\bar{p}_{\perp j}) \tag{3.5}$$

$$\frac{d\bar{y}_j}{d\bar{z}}=-\frac{2\rho\alpha}{\sqrt{\eta}}L_j\Im(\bar{p}_{\perp j}) \tag{3.6}$$

where

$$\begin{aligned}
\bar{p}_\perp&=\frac{p_\perp}{mca_u}, & A_\perp&=\frac{ea_ul_g}{2\gamma_r^2mc^2\rho}E_\perp,\\
\rho&=\frac{1}{\gamma_r}\left(\frac{a_u\omega_p}{4ck_u}\right)^{2/3}, & a_u&=\frac{eB_0}{mck_u},\\
\alpha&=\frac{a_u}{2\rho\gamma_r}, & b_{w\perp}&=b_x-ib_y,\\
L_j&=\frac{\gamma_r}{\beta_{zj}\gamma_j}, & \bar{n}_p&=l_gl_c^2n_p
\end{aligned} \tag{3.7}$$

and $b_{x,y,z}=B_{x,y,z}/B_0$ are the scaled magnetic fields in x, y and z, respectively, and B_0 is the peak on-axis magnetic field. Other parameters are defined in appendix A. In contrast to section 2 and hpFull, these equations are scaled in the radiation frame not the electron pulse frame. The radiation frame is described by $\bar{z}_2=\frac{\bar{\beta}_z}{(1-\bar{\beta}_z)}\frac{(ct-z)}{l_g}$. And the scaled longitudinal velocity is given by $\eta p_{2j}=\frac{1-\beta_{zj}}{\beta_{zj}}$, where $\eta=\frac{1-\bar{\beta}_z}{\bar{\beta}_z}$.

Using the above system of equations, one may use b_x, b_y and b_z to define

a static 3D magnetic field with which to simulate the FEL interaction. The model is still subject to the same limitations as the original Puffin model [11], i.e. the paraxial approximation and the neglect of the backwards propagating wave.

Currently, two 3D undulator fields have been implemented in Puffin using this model, both derived from [21, 22]. The first is an undulator field with canted, or curved, pole faces, providing electron beam focusing in both transverse directions:

$$\begin{aligned} b_x =& \frac{k_{\bar{x}}}{k_{\bar{y}}} \sinh(k_{\bar{x}}\bar{x}) \sinh(k_{\bar{y}}\bar{y}) \sin(\bar{z}/2\rho), \\ b_y =& \cosh(k_{\bar{x}}\bar{x}) \cosh(k_{\bar{y}}\bar{y}) \sin(\bar{z}/2\rho), \\ b_z =& \frac{\sqrt{\eta}}{2\rho k_{\bar{y}}} \cosh(k_{\bar{x}}\bar{x}) \sinh(k_{\bar{y}}\bar{y}) \cos(\bar{z}/2\rho), \end{aligned} \tag{3.8}$$

where $k_{\bar{x},\bar{y}}$ give the hyperbolic variation of the magnetic field in $\bar{x}, \bar{y}$, and must satisfy

$$k_{\bar{x}}^2 + k_{\bar{y}}^2 = \frac{\eta}{4\rho^2}. \tag{3.9}$$

this can be seen by applying Gauss's Law for magnetism to the above magnetic fields.[1]

The second undulator type is a planar undulator with plane pole faces, described by:

$$\begin{aligned} b_x =& 0, \\ b_y =& \cosh(\sqrt{\eta}\bar{y}/2\rho) \sin(\bar{z}/2\rho), \\ b_z =& \sinh(\sqrt{\eta}\bar{y}/2\rho) \cos(\bar{z}/2\rho), \end{aligned} \tag{3.10}$$

which produces a focusing force in one transverse direction.

[1] i.e. $\nabla \cdot \mathbf{B} = \frac{1}{\sqrt{l_g l_c}} \left(\frac{dB_x}{d\bar{x}} + \frac{dB_y}{d\bar{y}} \right) + \frac{1}{l_g} \frac{dB_z}{d\bar{z}} = \frac{B_0}{\sqrt{l_g l_c}} \frac{\bar{k}_x^2}{\bar{k}_y} + \frac{B_0}{\sqrt{l_g l_c}} \bar{k}_y - \frac{B_0}{l_g} \frac{\sqrt{\eta}}{4\rho^2 \bar{k}_y} = 0$ where $\sqrt{\frac{l_c}{l_g}} = \sqrt{\eta}$

3.3 Simulations

The electron transport through both of these undulator types is well known. Some simple tests can therefore be designed to see if the electron motion in Puffin exhibits the correct behaviour.

As described in [21, 22], a natural focusing channel arises from the off-axis variation of the magnetic field in the curved-pole undulator. From this so-called 'natural' focusing, one expects a slow oscillation, shown in figures 3.1-3.2, characterised by betatron wavenumbers and corresponding matched beam radii in $\bar{x}$ and $\bar{y}$, given, in the scaled notation, as:

$$k_{\beta\bar{x}} = \frac{a_u k_{\bar{x}}}{\sqrt{2\eta}\gamma_r}, \qquad k_{\beta\bar{y}} = \frac{a_u k_{\bar{y}}}{\sqrt{2\eta}\gamma_r}, \tag{3.11}$$

$$\bar{\sigma}_x = \sqrt{\frac{\rho\bar{\epsilon}_x}{k_{\beta\bar{x}}}}, \qquad \bar{\sigma}_y = \sqrt{\frac{\rho\bar{\epsilon}_y}{k_{\beta\bar{y}}}}. \tag{3.12}$$

respectively. For the curved pole simulation, $\rho = 0.0017$, $a_u = 4.404$, $\bar{\epsilon}_{x,y} = 1$ and $\gamma_r = 575.63$. The electron pulse hard edges in $\bar{x}$ and $\bar{y}$, matched at injection, are are seen to be oscillating throughout propagation however the radii $\bar{\sigma}_{x,y}$ remains constant. $\bar{\sigma}_x$ is plotted against $\bar{z}$ in figure 3.2. In this case, $k_{\bar{x}} = k_{\bar{y}}$, which, from condition (3.9) and equation (3.11), results in

$$k_{\beta\bar{x}} = k_{\beta\bar{y}} = \frac{a_u}{4\rho\gamma_r}, \tag{3.13}$$

and, from (3.12), matched beam radii of $\bar{\sigma}_{x,y} = 0.039$, giving good agreement with figure 3.2.

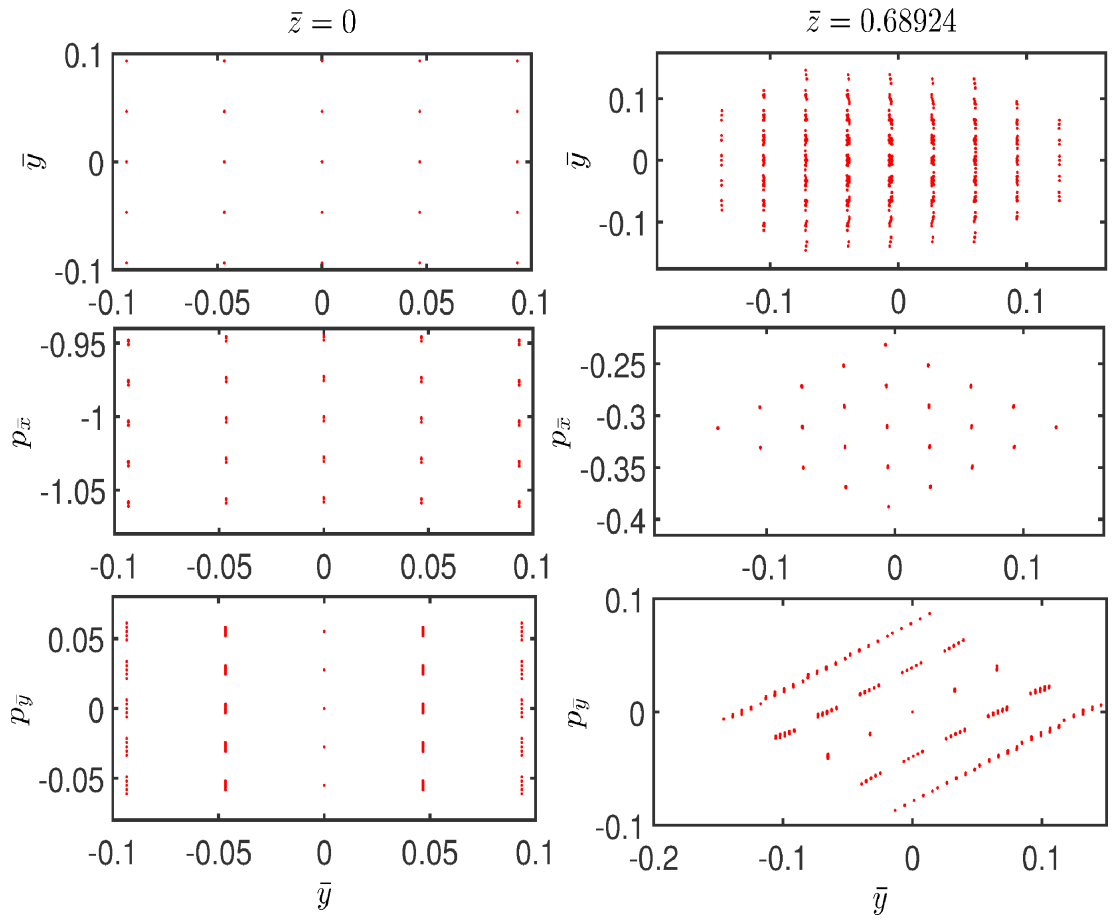

Figure 3.1: Demonstration of the rotation in transverse phase space of a matched electron beam using a curved-pole undulator. Top plots show a transverse plane of the beam at the start of the undulator and at $\bar{z} \approx \bar{\lambda}_\beta/8$, the electron pulse maintains a constant transverse area. The middle plots show the $p_{\bar{x}}$ by $\bar{x}$ phase space, it is seen that the electron pulse has completed a $1/8^{th}$ rotation. In the bottom plots the show the $p_{\bar{y}}$ by $\bar{y}$ phase space, which also demonstrates a rotation of 1/8.

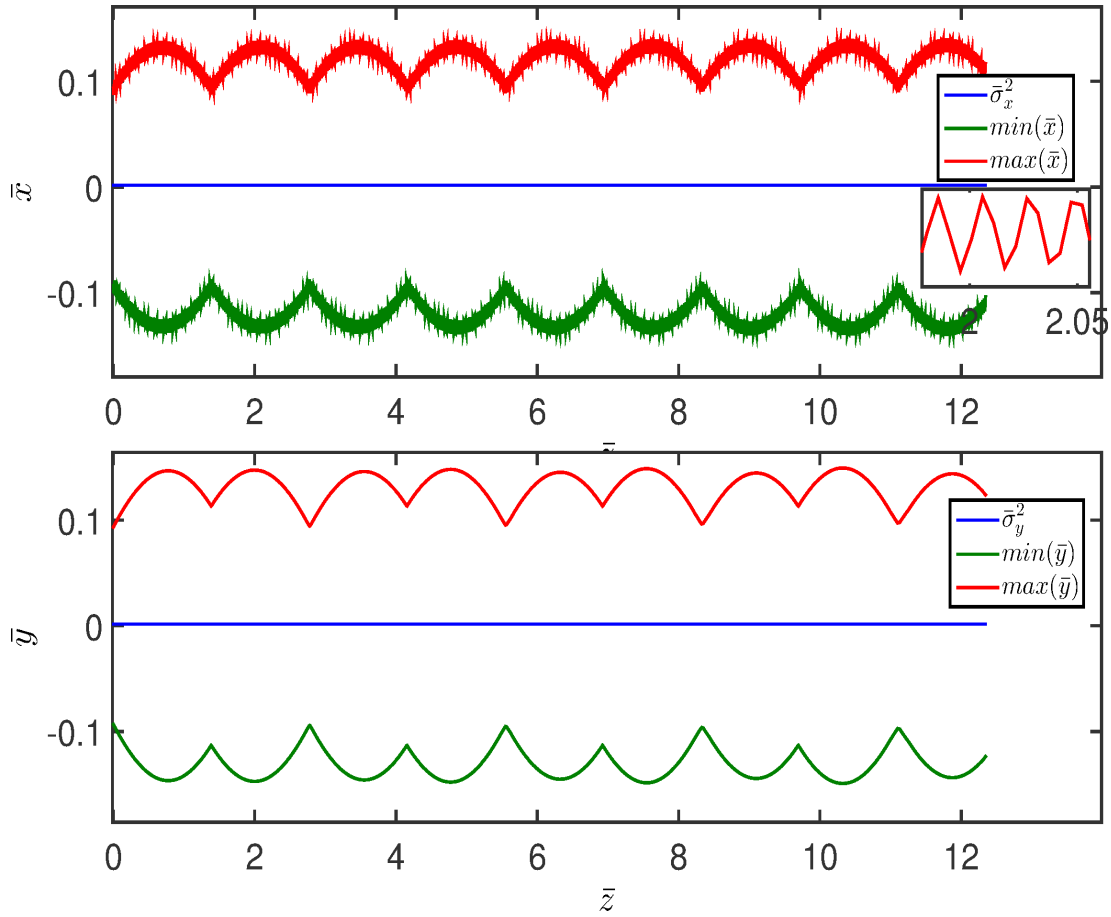

Figure 3.2: The electron pulse rotates in the transverse phase space. This rotation results in an oscillation of the hard edge of the electron beam radius (i.e. maximum and minimum $\bar{x}$ and $\bar{y}$) with a period of $\bar{\lambda}_\beta/4$. In the top plot the wiggle motion of the electron pulse is also seen with a period of $4\pi\rho = 0.0214$. The rms beam radius $\bar{\sigma}_{x,y}$ is approximately constant in $\bar{z}$

Similar to the curved-pole undulator, a natural focusing channel also arises in the plane-pole undulator, this time exclusively in the $\bar{y}$ direction. For this simulation, the parameters used are identical to the curved pole case, except the beam energy and the undulator parameter are adjusted to $\gamma_r = 238.04$ and $a_u = 1.8197$, to give the same transverse radii for comparison to the curved pole case.

The betatron period and matched beam radius in $\bar{y}$ are now:

$$k_{\beta\bar{y}} = \frac{a_u}{2\sqrt{2}\rho\gamma_r}, \tag{3.14}$$

$$\bar{\sigma}_y = \sqrt{\frac{\rho\bar{\epsilon}_y}{k_{\beta\bar{y}}}}, \tag{3.15}$$

and electron motion in the $(\bar{x}, \bar{p}_x)$ dimension should undergo free space dispersion when averaged over an undulator period, resulting in an expansion of the beam in the $\bar{x}$ dimension. The radius in $\bar{x}$ during propagation is plotted in figure 3.4, showing the beam expansion. The initial radius in $\bar{x}$ is here set to the matched radius in $\bar{y}$, so $\bar{\sigma}_x = \bar{\sigma}_y = 0.0327$. The radius in $\bar{y}$ remains constant, as expected.

In figure 3.4 the electron electron pulse expands in x, the expansion can be calculated by considering the evolution of electron axial coordinates as described by,

$$\frac{d\bar{x}_j}{d\bar{z}} = \frac{2\rho\alpha}{\sqrt{\eta}} L_j \Re(\bar{p}_{\perp j}) \tag{3.16}$$

$$\frac{\Delta\bar{x}_j}{\Delta\bar{z}} = \frac{2\rho\alpha}{\sqrt{\eta}} L_j \sigma_{\bar{p}_{xj}} \tag{3.17}$$

where $\sigma_{\bar{p}_{xj}} = \max(\bar{p}_{xj}) - \min(\bar{p}_{xj})$. For these simulations $\rho = 0.0017$, $\eta = 1.6140 \times 10^{-5}$, $\alpha = \frac{a_u}{2\rho\gamma_r}$, $\gamma_r = 238.04$, $a_u = 1.8197$, $L_j \approx 1$, and $\sigma_{\bar{p}_{xj}} = 0.1162$. The increase in $\bar{x}_j$ is given as $\frac{\Delta\bar{x}_j}{\Delta\bar{z}} = 0.2217$ and is in agreement with simulation results presented in figure 3.4. A comparison of the electron pulse radii in x for plane pole and curved pole undulators is made in figure 3.5.

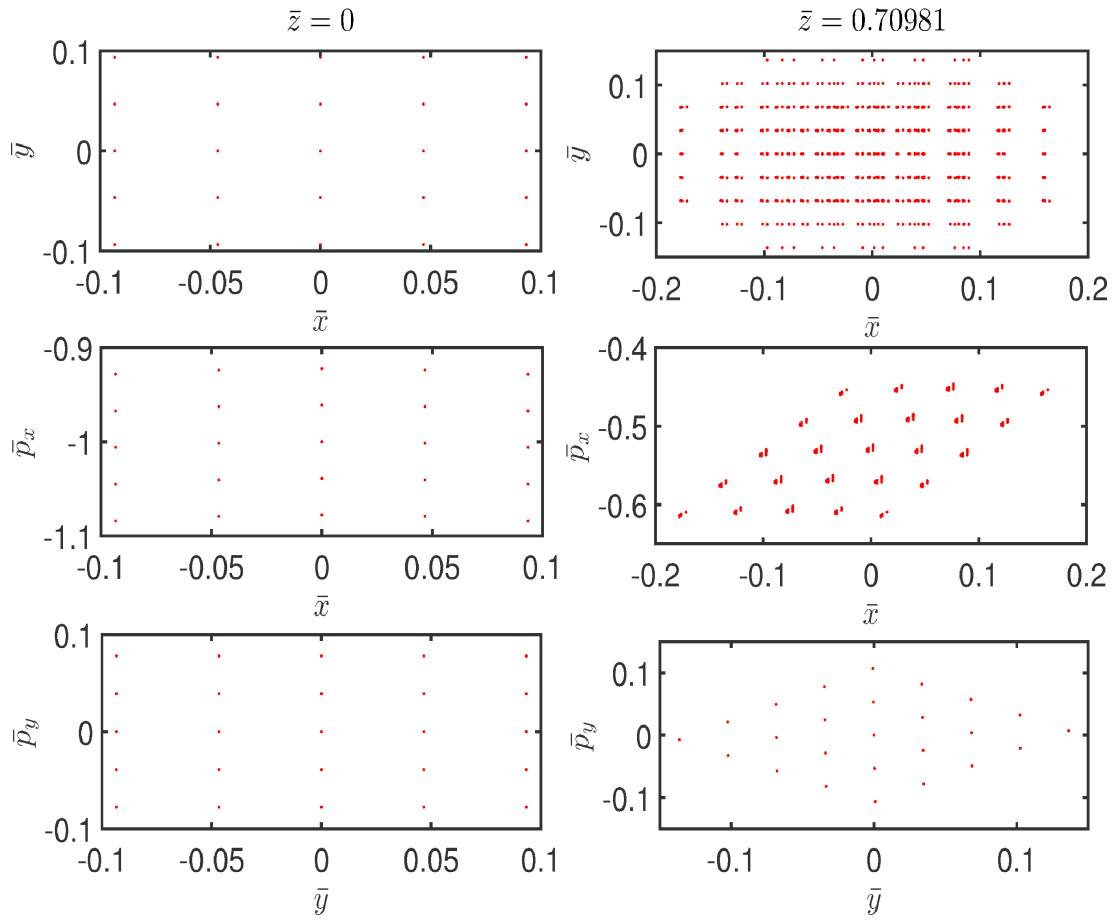

Figure 3.3: Demonstration of the rotation in the $p_{\bar{y}}$ by $\bar{y}$ phase space of a matched electron beam using a plane-pole undulator in the . Top plots show a transverse plane of the beam at the start of the undulator and at $\bar{z} \approx \bar{\lambda}_\beta/8$, the electron pulse maintains a constant transverse area. The middle plots show the $p_{\bar{x}}$ by $\bar{x}$ phase space, that the electron pulse expands as there is no focusing in this direction. In the bottom plots the show the $p_{\bar{y}}$ by $\bar{y}$ phase space, which demonstrates a rotation of 1/8.

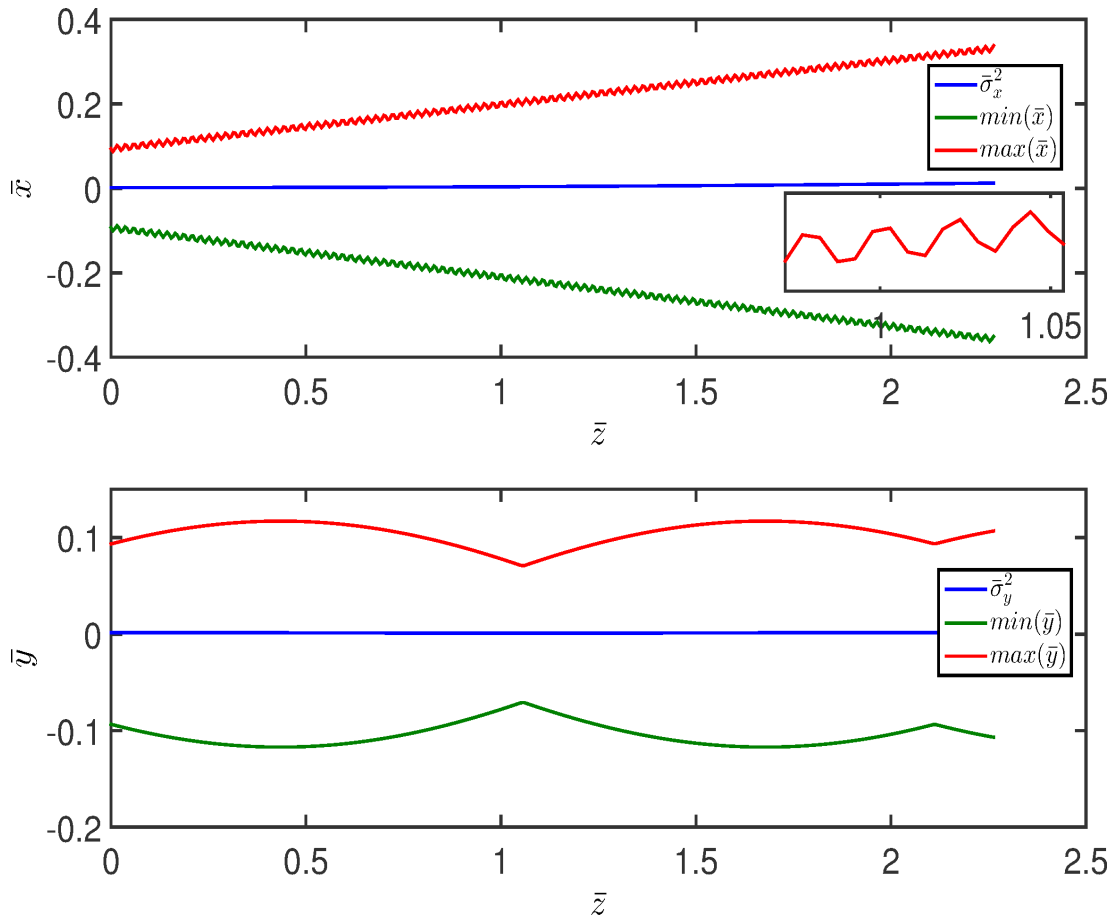

Figure 3.4: The electron pulse rotates in the $p_{\bar{y}}$ by $\bar{y}$ phase space. This rotation results in an oscillation of the hard edge of the electron beam radius (i.e. maximum and minimum $\bar{y}$) with a period of $\bar{\lambda}_\beta/4$ and is seen in the bottom plot. In the top plot the wiggle motion of the electron pulse is also seen with a period of $4\pi\rho = 0.0214$, the emittance driven expansion in $\bar{x}$ is also shown in this plot and is estimated as $\frac{\Delta \bar{x}_j}{\Delta \bar{z}} = 0.2217$. The rms beam radius $\bar{\sigma}_{x,y}$ is approximately constant in $\bar{z}$

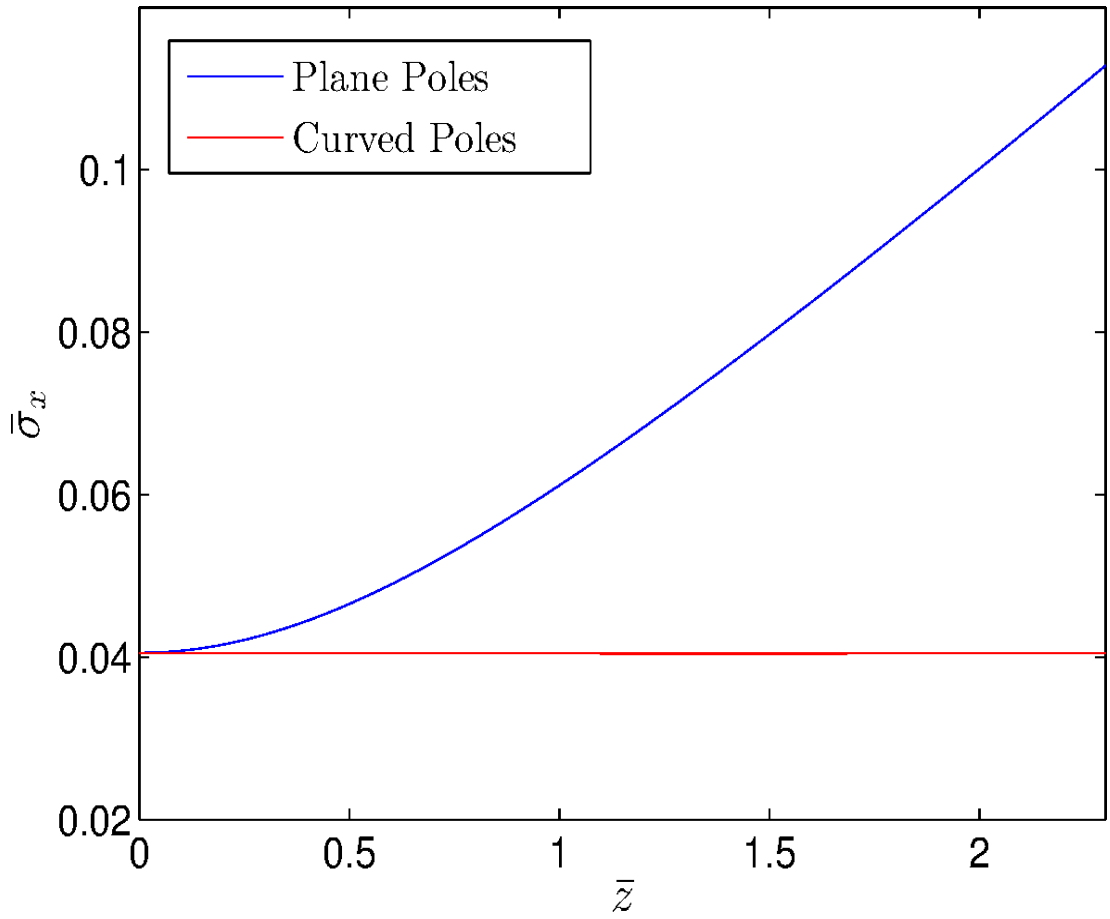

Figure 3.5: The electron pulse radius $\bar{\sigma}_x$ plotted as a function of distance through the undulator. The plane pole undulator does not produce a focussing force in the x direction, however the curved pole undulator does. Therefore, the radius in x when propagated through a plane pole undulator will expand however in the curved pole undulator this expansion is supressed.

Chapter 4

Novel schemes

4.1 Review of novel FEL schemes

Current x-ray Free Electron Lasers lack temporal coherence [6, 13, 14]. Typically Free Electron Lasers operating below the x-ray [1, 6] are either seeded or operate in a cavity configuration. However, conventional seed lasers operating in the x-ray lack the necessary intensity to seed an FEL [1]. Similarly, in the cavity configuration mirrors with a high enough reflectance are not available in the x-ray. Therefore, x-ray FELs operate in Self-Amplified Spontaneous Emission regime (SASE).

In the SASE [23, 24] regime a series of uncorrelated radiation spikes are generated. The SASE FEL requires a long undulator, in which spontaneously emitted radiation is amplified to saturation. Spontaneous radiation is produced because of electron shot-noise [9], i.e., the electrons are randomly distributed in phase. Since the electrons are randomly distributed in phase the radiation spikes generated in SASE do not have a fixed phase relationship.

A number of techniques have been proposed to improve the FEL's temporal coherence in the x-ray. Many of these techniques favour the beam by design [17] approach, where a combination of undulators, long wavelength seed lasers and chicanes are used to precondition the electron pulse. This preconditioning often involves generating a density modulation, at higher frequency, in the electron

pulse.

A chicane [25] is a magnetic device that alters an electron's trajectory in proportion to its energy. In standard chicanes, those with a positive dispersion, higher energy electrons take a shorter path through the chicane than their lower energy counterparts. Therefore, high energy electrons traverse the chicane in a shorter time than low energy electrons, hence the electrons are seen to disperse. i.e. high energy electrons move ahead of low energy electrons. This dispersion is very similar to undulator dispersion. However, chicane dispersion is proportional to the electron energy and for an undulator the electron dispersion is related to the electron velocity (as described by equation 3.5) along the undulator. Undulator dispersion allows electron microbunching to develop, which is key to the FEL interaction, and was discussed in section 2 and illustrated in figure 2.2. Therefore, chicanes can be used to increase the microbunching and improve the FEL interaction when inserted between undulator modules. By, improving FEL efficiency the total undulator length can be reduced and radiation field power increased, such an approach is known as the Optical Klystron (OK) FEL [23]. Just as the radiation pulse slips in front of the electron pulse in an undulator, and since electron velocity must be less than the speed of light, the radiation field will also slip in front of the electron pulse in a chicane section, this distance is known the chicane's slippage length.

Using the correct configuration of magnetic elements, the dispersive strength and slippage length of a chicane section can be precisely controlled [25]. In [25] the design and implementation of isochronous chicanes was described, an isochronous chicane does not disperse the electron pulse however there is still slippage between the radiation field and electron pulse. Isochronous, or slippage-only, chicanes can be desirable when chicanes are required but a delicate phase space structure must be preserved. A negatively dispersed chicane is another possibility [25], in such a chicane low energy electrons will move ahead of high energy electrons, i.e. there is a negative dispersion.

One of first techniques proposed, to improve the FEL's temporal coherence in the x-ray, was the High Gain Harmonic Generation (HGHG) [26] method, shown in figure 4.1. In the HGHG method, the electron beam is energy modulated with a long wavelength seed laser and dispersed in a chicane section.

The chicane section converts this large energy modulation into a density modulation. This density modulation is a form of the electron microbunching phenomena that is key to the FEL mechanism, discussed chapter 2. The electron pulse, which was originally bunched at a long wavelength, also will have bunching components at the high harmonics of this wavelength. In the final section, a radiator (undulator) is tuned to one of these harmonics, and by doing will produce a radiation field with high temporal coherence. However, HGHG [26] has a limited range, such that for harmonics greater than ten the corresponding bunching is very much diminished. The reduced bunching at the higher harmonics will reduce radiation field's temporal coherence at those harmonics.

The Echo Enabled Harmonic Generation [13, 14] technique (figure 4.2) was proposed to overcome this limitation. Echo Enabled Harmonic Generation (EEHG) requires two consecutive modulator(seeded undulator)-chicane sections. The interplay of these sections imprints a fine micro structure on the electron pulse phase space. This microstructure contains bunching components at very high harmonics of the modulator seed lasers. The first modulator-chicane section generates a number of phase-space energy bands. The second modulator-chicane section then converts these energy bands into current bands. These current bands are equispaced and separated by some high harmonic of the seed lasers. The advantage of this scheme is that it can pre-bunch the electron pulse at harmonics greater 10. This allows temporally coherent radiation fields to be generated at very high harmonics of the initial seed laser when passed through a final radiator-undulator.

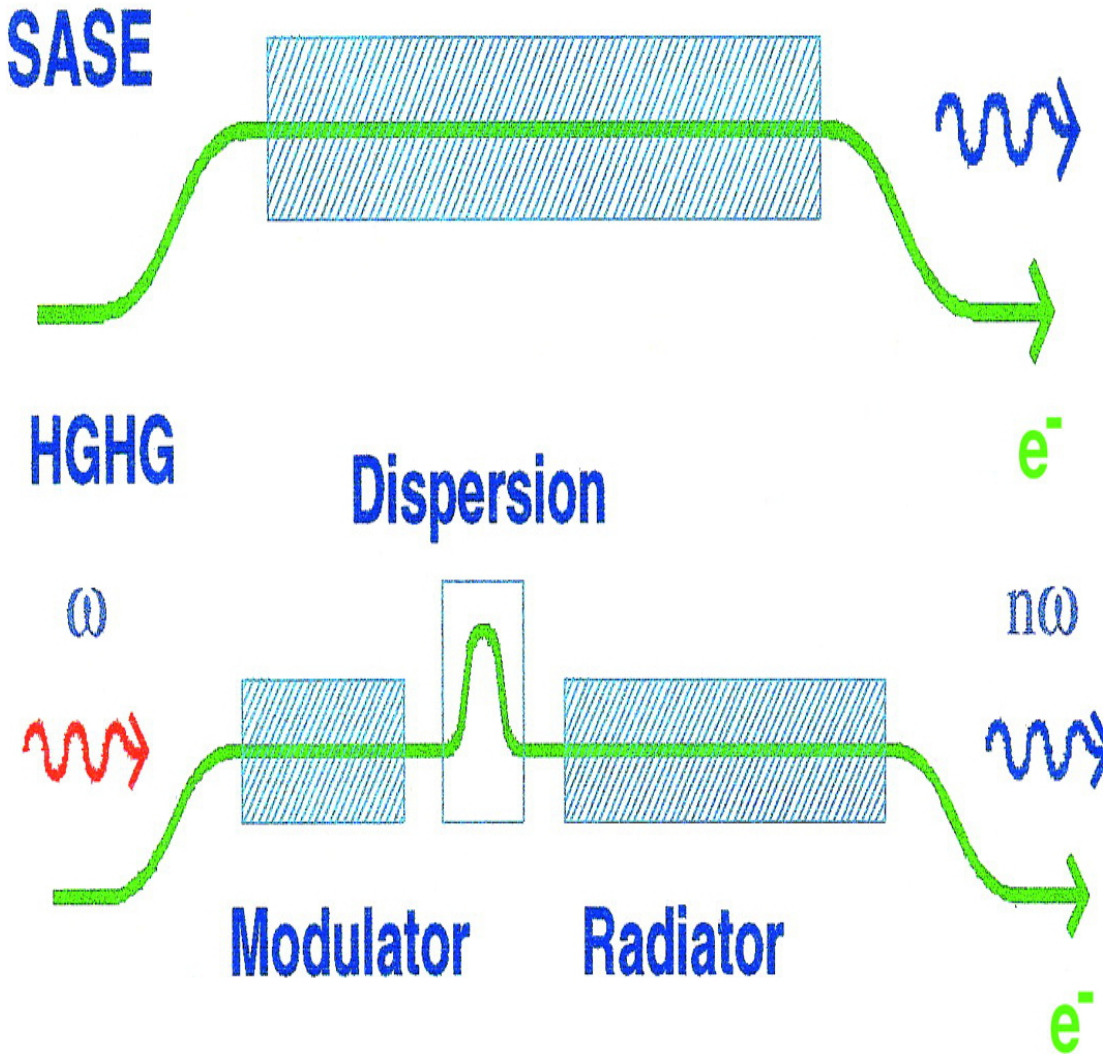

Figure 4.1: Diagram of SASE and HGHG schemes from [26]. In the SASE scheme spontaneous radiation is amplified to saturation in a long undulator. However, in the HGHG method the electron pulse is energy modulated by a long wavelength seed laser. Then, the energy modulation is converted to a density modulation, known as microbunching. A Fourier transform of the electron pulse's density profile will reveal large density modulations at the harmonics of the initial seed laser. A radiator-undulator can be tuned to one these harmonic density modulations, to generate a large temporally coherent radiation field.

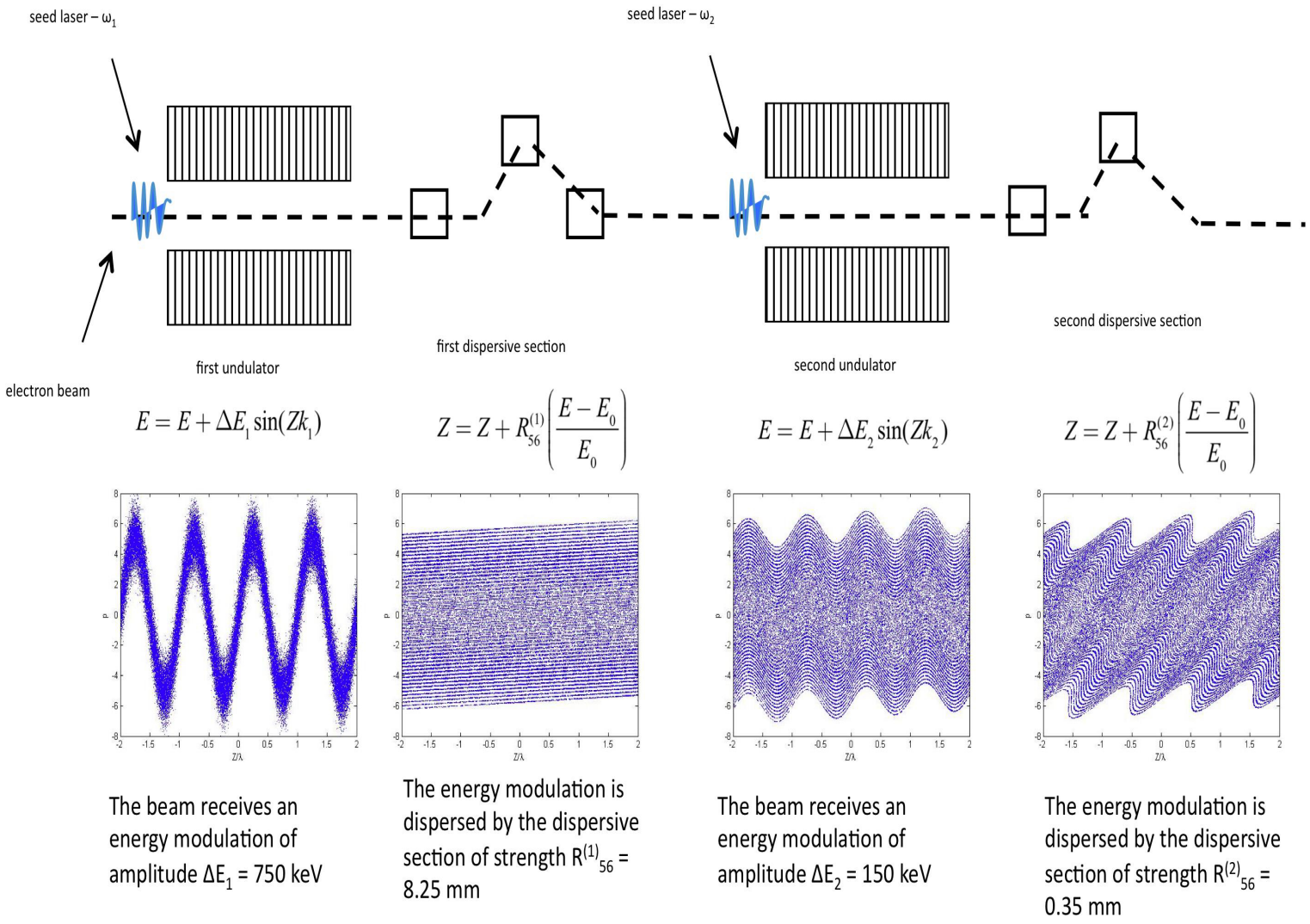

Figure 4.2: Diagram of EEHG scheme: in the EEHG method the electron pulse in energy modulated and dispersed twice in two consecutive undulator-chicane section. The interplay of these modulation and dispersion produces a fine microstructure in phase space.

In conventional laser physics short radiation pulses can be generated by enforcing a fixed phase relationship between cavity radiation modes [27], this is technique is known as mode-locking. The simplest method of mode-locking is to apply a field modulation at a frequency determined by the cavity round trip time, $\omega_L = 2\pi c/2L$, where L is the cavity length. Such a mode-locking set-up will result in a series of temporal radiation spikes separated by $T = 2\pi/\omega_L$. Taking the Fourier transform of such a mode-locked laser pulse reveals a number side-band radiation modes separated by ω_L.

The technique of mode-locking can be applied to the Free Electron Laser [28, 29]. This can be done by sending the electron pulse through an undulator-chicane lattice, constructed from a series of consecutive undulator-chicane modules. Here, the cavity round trip time is equivalent to the slippage length of an undulator-chicane module. An undulator-chicane lattice will amplify side-band radiation modes separated by $\Delta\omega = 2\pi c/s$. s is the total slippage length for an undulator-chicane module, which is constant throughout the lattice.

In the mode-locking technique for free electron lasers, shown in figure 4.1, chicane sections provide a series of periodic slips to the radiation field. Therefore, the only radiation wavelengths that can survive a number of these slips will be an integer divisor of undulator-chicane slippage length, see appendix B.2 for a short derivation. Hence, the undulator-chicane lattice will amplify side-band radiation modes that are separated by,

$$\Delta\omega = \frac{2\pi c}{s}. \tag{4.1}$$

s is the sum of the undulator slippage l and the chicane slippage δ, i.e., $s = l+\delta$. The mode-locking technique will generate a series of temporal radiation spikes. These spikes will be separated by $T = 2\pi/\Delta\omega = s/c$. To fully lock the modes the electron pulse must be premodulated in current or energy at the frequency $\Delta\omega$, otherwise the scheme is known as mode-coupling. Mode-locking can also be achieved when the electron pulse has a density modulation at the frequency $\Delta\omega$, an example of this is discussed in the next section.

Furthermore, undulator-chicane lattices have other uses, such as the High Brightness SASE [30]. In the HB-SASE FEL variable slippage length undulator-

chicane modules are used to extend the FEL instability from localised SASE spikes to encompass the entire electron pulse. By doing so the temporal coherence of the HB-SASE FEL is improved. Another use of an undulator-chicane lattice is the mode-locked afterburner [31] which can be attached to the end of a long undulator to produce mode-locked radiation. Such a technique maybe useful in a pre-existing facility to generate mode-locked radiation without large expense.

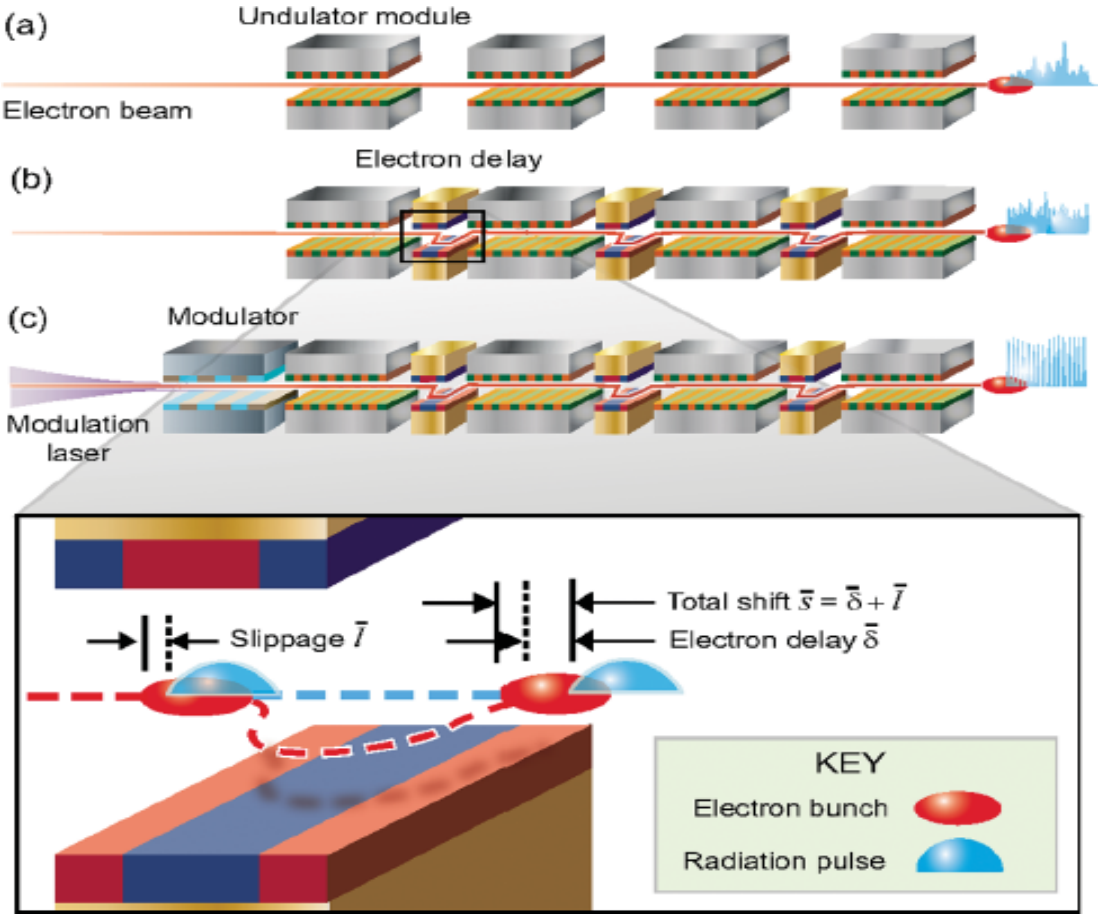

Figure 4.3: This mode-locking diagram was taken from [28]. (a) an illustration of the SASE FEL (b) mode-coupling FEL scheme, a series of chicane slippage sections are used (c) the electron pulse is pre-modulated before injection into the undulator-chicane lattice

4.2 EEHG modelocking

4.2.1 Echo Enabled Harmonic Generation

In this section the technique of Echo Enabled Harmonic Generation is discussed and improvements to the scheme investigated. The results of this work was published in [15]. The EEHG method can be approximated by four simple particle transformations, given by following four equations:

$$\gamma_j^{(1)} = \gamma_j^{(0)} + \Delta\gamma_1 \sin(z_j^{(0)} k_1) \tag{4.2}$$

$$z_j^{(1)} = z_j^{(0)} + R_{56}^{(1)} \left[\frac{\gamma_j^{(1)} - \gamma_r}{\gamma_r} \right], \tag{4.3}$$

$$\gamma_j^{(2)} = \gamma_j^{(1)} + \Delta\gamma_2 \sin(z_j^{(1)} k_2) \tag{4.4}$$

$$z_j^{(2)} = z_j^{(1)} + R_{56}^{(2)} \left[\frac{\gamma_j^{(2)} - \gamma_r}{\gamma_r} \right], \tag{4.5}$$

where the bracketed superscripts $(0, 1, 2)$ referring to the initial conditions, and to the exit from the first and second modulation/dispersive stages respectively; γ is the electron energy in units of the electron rest-mass energy and $\Delta\gamma_{1,2}$ is the energy modulation.

The method of EEHG manipulates electron pulse phase space using two temporally coherent, long wavelength seed lasers, two undulators and two dispersive chicanes, as can be seen in figure 4.2. The electrons are first modulated by a seed laser in an undulator and then dispersed in a chicane, i.e. equations 4.2 and 4.3 are applied to the electron pulse. This process is then repeated (equations 4.4-4.5) and a fine microbunching structure in the electron pulse is generated at a shorter wavelength, this microstructure retains a high level of the temporal coherence from the long wavelength lasers. When propagated through a final radiator undulator, the electron beam emits radiation at the shorter wavelength, of the electron microbunching, and with an improved temporal coherence over that generated by Self Amplified Spontaneous Emission. Previous models of EEHG [13, 14] have applied periodic

boundary conditions to the electron phase space, i.e. electrons leaving the right of the electron pulse window are returned to the left of the window and vice-versa. These simulation codes also average the electron pulse and radiation field over a radiation period, the so-called 'period averaging'. By using the unaveraged FEL code, hpFull [9, 10], these limiting assumptions are removed.

Using this model, simulations of EEHG up to before the final undulator reveal a frequency comb of modes (side-band modes) in the electron microbunching parameter, with adjacent modes being separated by the second seed laser frequency. This frequency comb may then be matched to an undulator-chicane lattice as the final radiator stage to lock the radiation modes as discussed earlier.

4.2.2 EEHG pre-radiator stage

To demonstrate the process, EEHG was simulated with the following parameters for a cold beam with no intrinsic shot-noise. The cold beam approximation refers to an electron pulse of zero energy spread and uniform electron energy. A uniform 'flat top' current profile electron pulse was used with electron energy $E_r = 1.2$GeV, charge $Q = 100$pC and initial pulse length of $12\mu m$ (which is equivalent to a current of 2.5 kA). The first and second seed laser wavelengths are $\lambda_{1,2} = 240$nm with the final radiating resonant wavelength $\lambda_r = 10$nm. The electron energy modulation in the first and second modulating stages are $\Delta E_1 = 750$ keV and $\Delta E_2 = 150$ keV respectively. The dispersive strength of the corresponding chicanes are $R_{56}^{(1)} = 8.25$ mm and $R_{56}^{(2)} = 0.34$ mm. The electrons are modelled by macroparticles [9] each assigned a weight N_j corresponding to the number of electrons the macroparticle represents. A FEL parameter of $\rho = 10^{-3}$ was used as a typical value for the simulations at this resonant wavelength.

Applying the four transforms of equations 4.2-4.5 develops a microstructure in the electron pulse that contains significant microbunching at higher harmonics of the seed radiation fields.

In demonstrating the principle of EEHG, the work of [13, 14] applied periodic boundary conditions in the position of the electrons across a region of

the longitudinal z-axis. Here, no such boundary conditions are applied and the electron positions are transformed according to equations 4.2-4.5. The removal of the boundary condition has little effect around the centre of the electron pulse where the dispersive effects are symmetric. This can be seen figure 4.4 which shows the phase space of the centre of the electron pulse at exit of EEHG scheme and is very similar to that of reported in [13, 14]. However, the higher and lower energy electrons, from the extrema (peaks/troughs) of the energy modulated beam, form tight (single) 'current bands', whereas electrons close to the initially un-modulated beam energy form a looser (double) current band structure. This picture changes towards the head and tail of the electron pulse where dispersion causes predominantly single current bands to form by the higher and lower energy electrons respectively. This effect is seen for the the case of the head of the electron pulse in figure 4.5. In the bottom of figure 4.5 single current bands can be seen in the region 5600-5615 nm whereas the double current bands occupy the region 5620-5830 nm, this patten is repeated longitudinally along the electron pulse as is seen in figure 4.7.

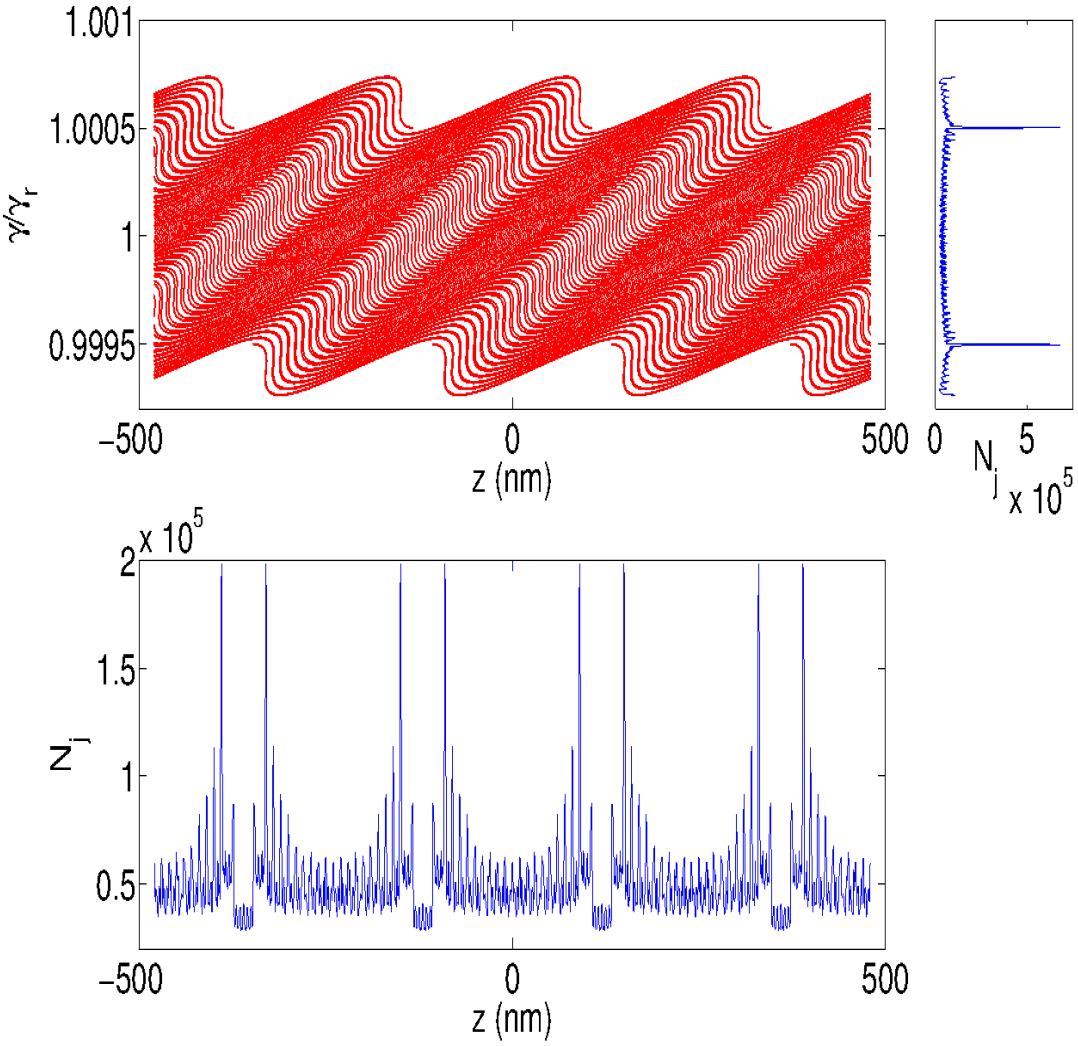

Figure 4.4: Electron phase space (top) and histogram of electron numbers (bottom) about the centre of the electron pulse at $z = 0$. The particle density is increased for the high and low energy electrons as is indicated by the top right plot.

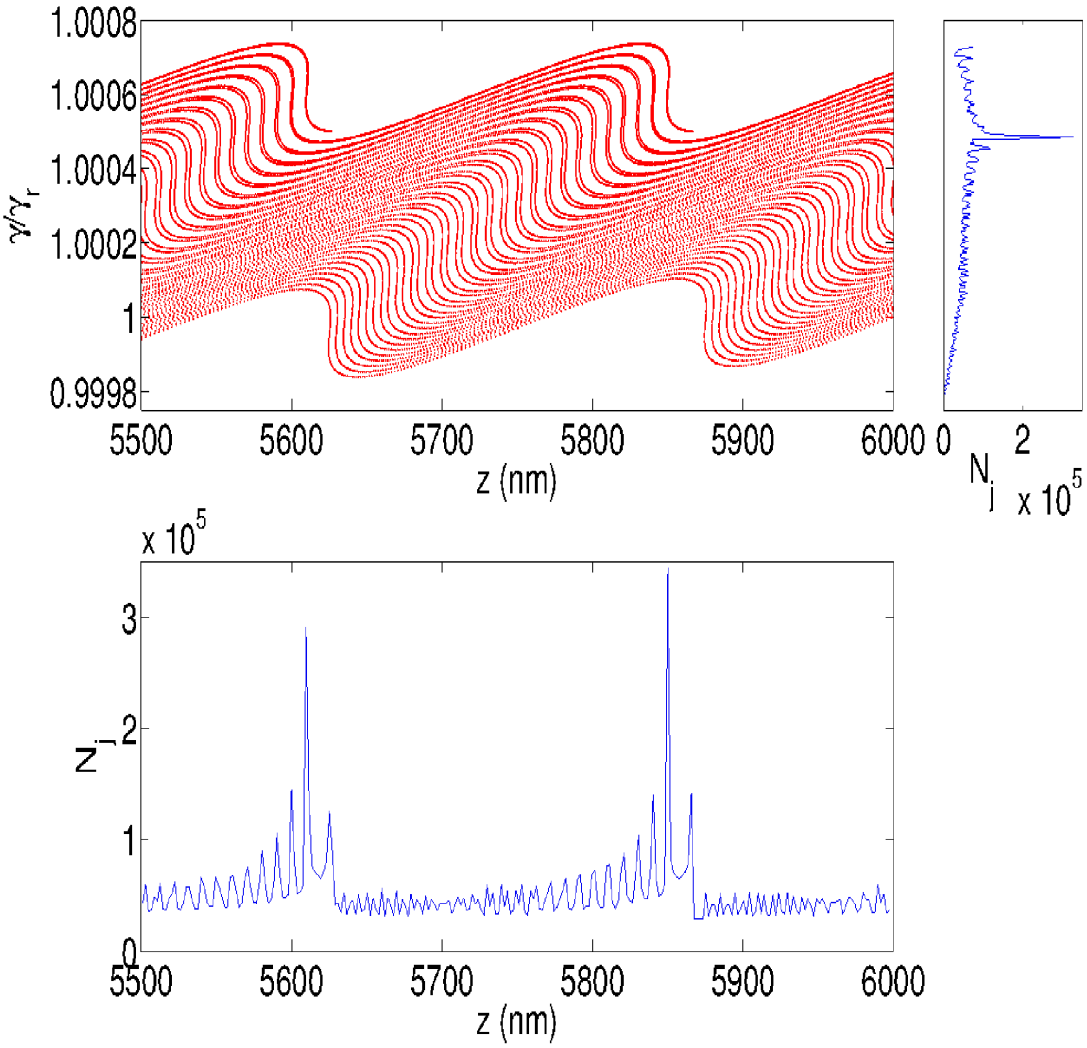

Figure 4.5: Electron phase space (top) and histogram of electron numbers (bottom) at the head of the electron pulse. The particle density is increased for the higher energy electrons as is indicated by the top right plot.

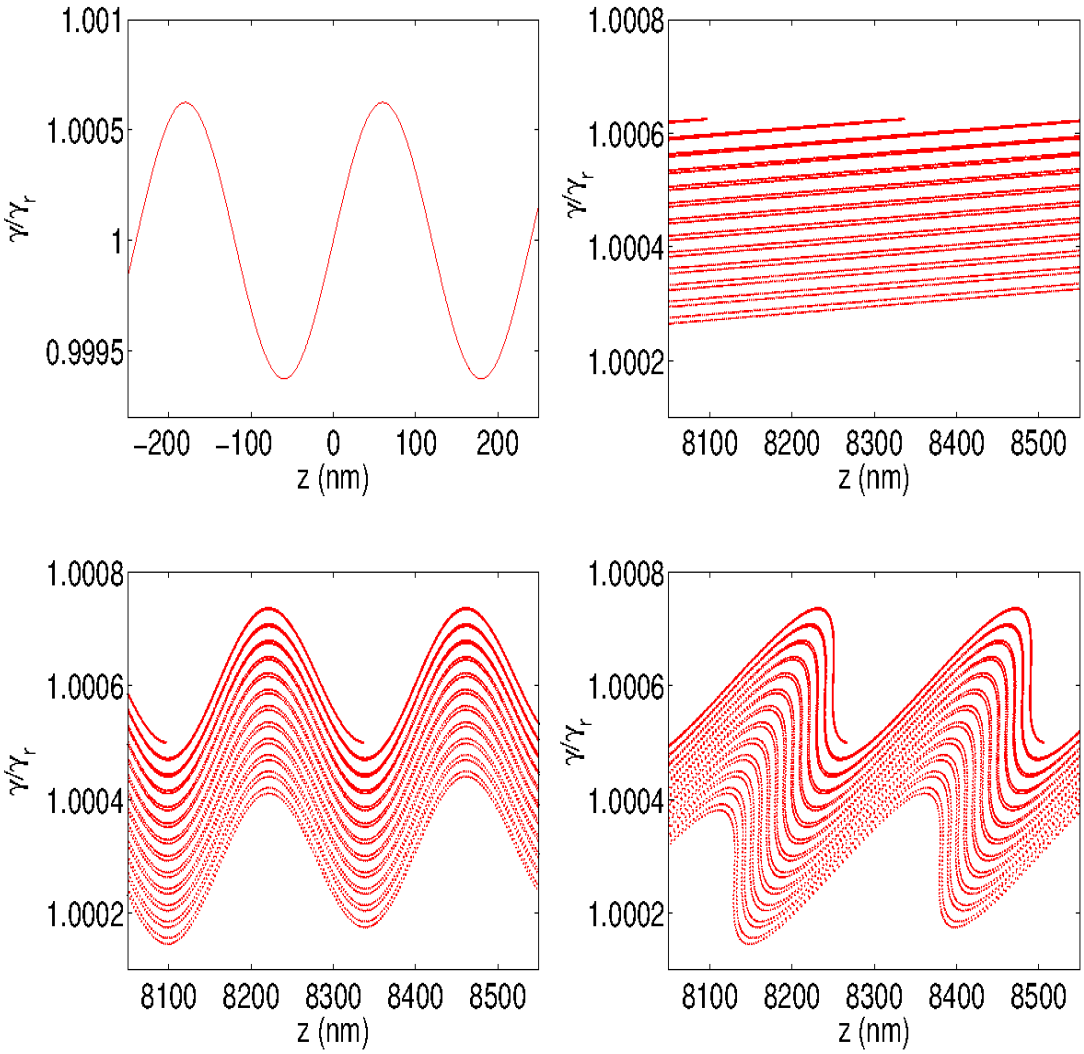

Figure 4.6: The single and double-current bands can be seen to evolve during the pre-radiator EEHG process (top-to-bottom, left-to-right.) The shift in electron positions from left-to-right is due to the chicanes.

The underlying process is detailed in figure 4.6 which shows the effects of the EEHG process upon the higher energy electrons of the initially modulated beam. The higher energy electrons are seen to form relatively tight energy bands which are then transformed into single current bands around the maxima following the second energy modulation. This creates a series of higher energy current bands at the head of the electron pulse separated by the wavelength of the second seed laser. At the tail of the electron pulse, the EEHG process causes similar single current bands to be formed, but around the minima of second energy modulation. Thus, dispersion causes the high (low) energy electrons to be dispersed to the head (tail) of the pulse.

A histogram of the full electron number distribution is shown in figure 4.7 together with a (unitary) Fourier transform of the electron bunching parameter about the resonant frequency ω_r of the final radiator stage. The Fourier bunching parameter is simply derived from the driving term of the scaled wave equation of [9], i.e. the macroparticle version of the wave equation given in basic FEL theory section (see appendix), and may be written:

$$b(z,\omega) = \frac{1}{\sqrt{2\pi}} \frac{1}{n_{p\|}} \sum_{j=1}^{N_m} N_j e^{-iz(k_r+k_u)} e^{i(\omega_r-\omega)t_j}, \tag{4.6}$$

where $n_{p\|}$ is the peak linear electron density, N_m is the total number of macroparticles used in the simulation, k_u is the undulator wavenumber, $t_j = -z_j/c\beta_z$ is the arrival time of the macroparticle at the undulator entrance at $z = 0$ and $\beta_z = v_z/c$ is the mean scaled speed of the electron pulse along the undulator z-axis. It is seen that a well defined modal structure is present in the electron bunching parameter with mode separation given of $\Delta\omega/\omega_r = 10/240 \approx 0.042$ corresponding to the seed modulation frequency. The modes are relatively well phase-matched as seen from the well defined peaked periodic microstructure in the electron density histogram.

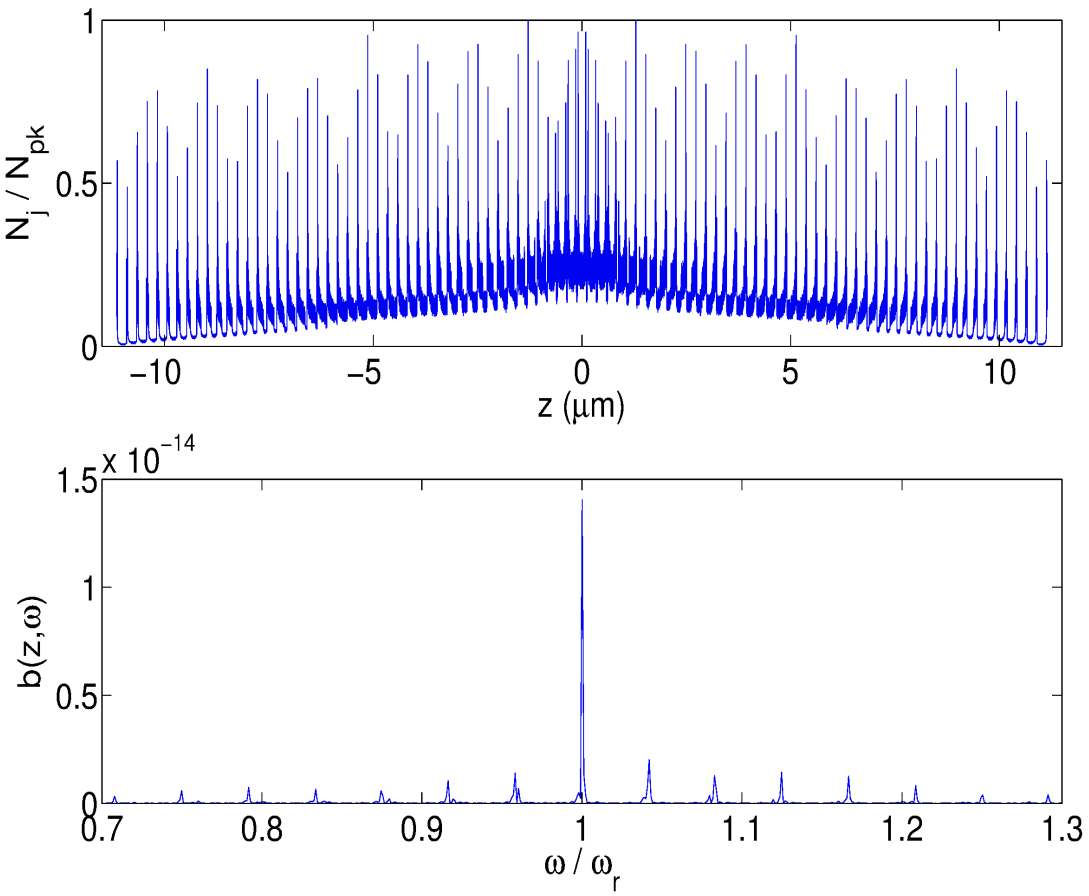

Figure 4.7: Histogram of electron numbers (top) normalised with respect to the peak, and the Fourier transform of the bunching parameter $b(z, \omega)$ for the full electron beam distribution showing the modal structure at the end of the EEHG pre-bunching process.

4.2.3 EEHG radiator

The pre-bunched electron distribution above was propagated through a two different undulator systems, a simple undulator and an undulator-chicane lattice, both tuned to the resonant frequency ω_r using the unaveraged simulation code of [9, 10]. The transformations of (4.2-4.5) may be rewritten in the uni-

versal scaling of [23, 24, 32, 33] as used in the simulations as:

$$p_j^{(1)} = p_j^{(0)} + \Delta p^{(1)} \sin\left(\frac{\bar{z}_{1j}^{(0)}}{2\rho h_1}\right) \tag{4.7}$$

$$\bar{z}_{1j}^{(1)} = \bar{z}_{1j}^{(0)} + 2\rho D^{(1)} p_j^{(1)} \tag{4.8}$$

$$p_j^{(2)} = p_j^{(1)} + \Delta p^{(2)} \sin\left(\frac{\bar{z}_{1j}^{(1)}}{2\rho h_2}\right) \tag{4.9}$$

$$\bar{z}_{1j}^{(2)} = \bar{z}_{1j}^{(1)} + 2\rho D^{(2)} p_j^{(2)} \tag{4.10}$$

where $\Delta p^{(1,2)} = \Delta\gamma^{(1,2)}/\rho\gamma_r$; $D^{(1,2)} = k_r \rho R_{56}^{(1,2)}$; $h_{1,2} = \omega_r/\omega_{1,2}$ and $\bar{\beta}_z \approx 1$ is assumed. At the beginning of the undulator: $\bar{z} \equiv 2\rho k_u z = 0$; $\bar{z}_{1j} = -2k_r \rho c t_j$ and $p_j = (\gamma_j - \gamma_r)/\rho\gamma_r$.

Performing the Fourier transform of the with respect to $\bar{z}_1$ defines the scaled frequency as $\bar{\omega} = -\omega/2\rho\omega_r$ so that:

$$b(\bar{z}, \bar{\omega}) = b(z, \omega)\frac{c}{l_c} \exp\left(i\frac{\omega z}{c}\right). \tag{4.11}$$

4.2.4 Simple undulator

EEHG was first simulated in a simple undulator configuration of scaled length $\bar{z} = 1.1$. The scaled radiation and electron pulse parameters are plotted in figure 4.8. It is seen that while the radiation generated had some temporal structure, no modal structure is present in Fourier space with emission confined to the resonant frequency. This is consistent with the previous results of [13, 14].

4.2.5 undulator-chicane lattice

Here an undulator-chicane lattice is constructed so that the radiation modes amplified by the lattice will match the properties of the electron bunching above. Using the notation of [28], each undulator has four periods so that

a radiation wavefront will propagate four resonant wavelengths through the electron pulse in each undulator. Each chicane delays the electron pulse by a further twenty wavelengths so that the total slippage of a resonant wavefront in traversing one undulator-chicane module is $s = (4 + 20)\lambda_r = 240$nm, which is equal to the second seed laser wavelength. In this way the relative slippage between radiation and electrons in each undulator-chicane module matches the strong periodic electron microbunching. It is seen from figure 4.9 that this matching generates of a periodic train of short radiation pulses ($\sim$106 attoseconds full width at half maximum duration) separated by the second seed laser wavelength $\lambda_2 = 240$nm with a corresponding set of modes equally spaced by the same corresponding frequency $\Delta\omega/\omega_r \approx 0.042$. Note that peak powers generated by the higher energy electrons at the head of the radiation pulse train envelope are greater than those generated at the tail by the lower energy electrons. While the higher energy electrons lose energy and fall into resonance to emit strongly, those at lower energies continually fall away from resonance and strong radiation emission. The visibility of radiation pulse train structure is defined as $V = (|A|^2_{max} - |A|^2_{min})/(|A|^2_{max} + |A|^2_{min})$, were the maximum and minimum values are defined between two adjacent peaks. The effect of introducing an energy spread σ_E in the initial electron pulse energy decreases the visibility gradually from $V = 0.93$ at 1 keV ($\sigma_E/\rho E_r = 0.0008$) to $V = 0.78$ at 150 keV ($\sigma_E/\rho E_r = 0.125$).

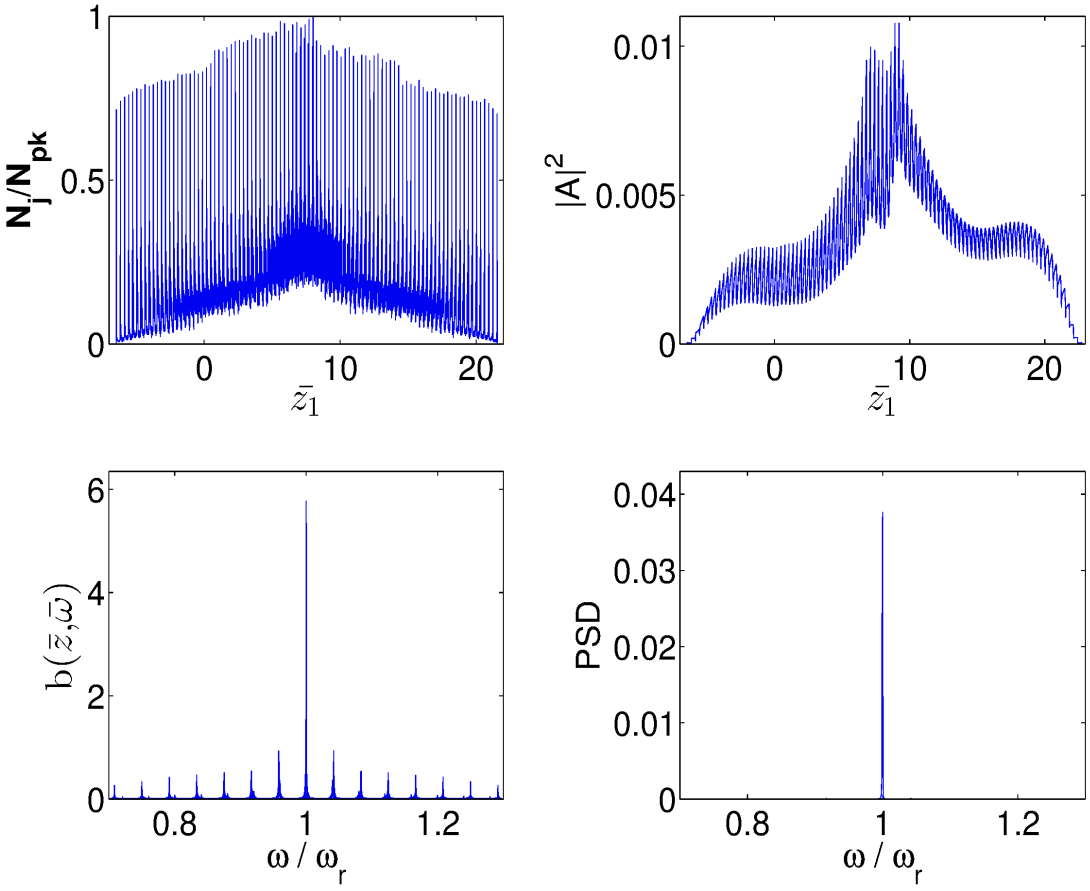

Figure 4.8: Electron and radiation pulse at saturation in a simple undulator at $\bar{z} \approx 1.1$ for the normal EEHG case. Plots on the left are: top - normalised electron number histogram (bin size $= \lambda_r/5$); bottom - Fourier transform of bunching $b(\bar{z}, \bar{\omega})$. On the right: top - radiation field amplitude $|A|^2$ as a function of $\bar{z}_1$; bottom - scaled Power Spectral Density showing emission at resonance dominates.

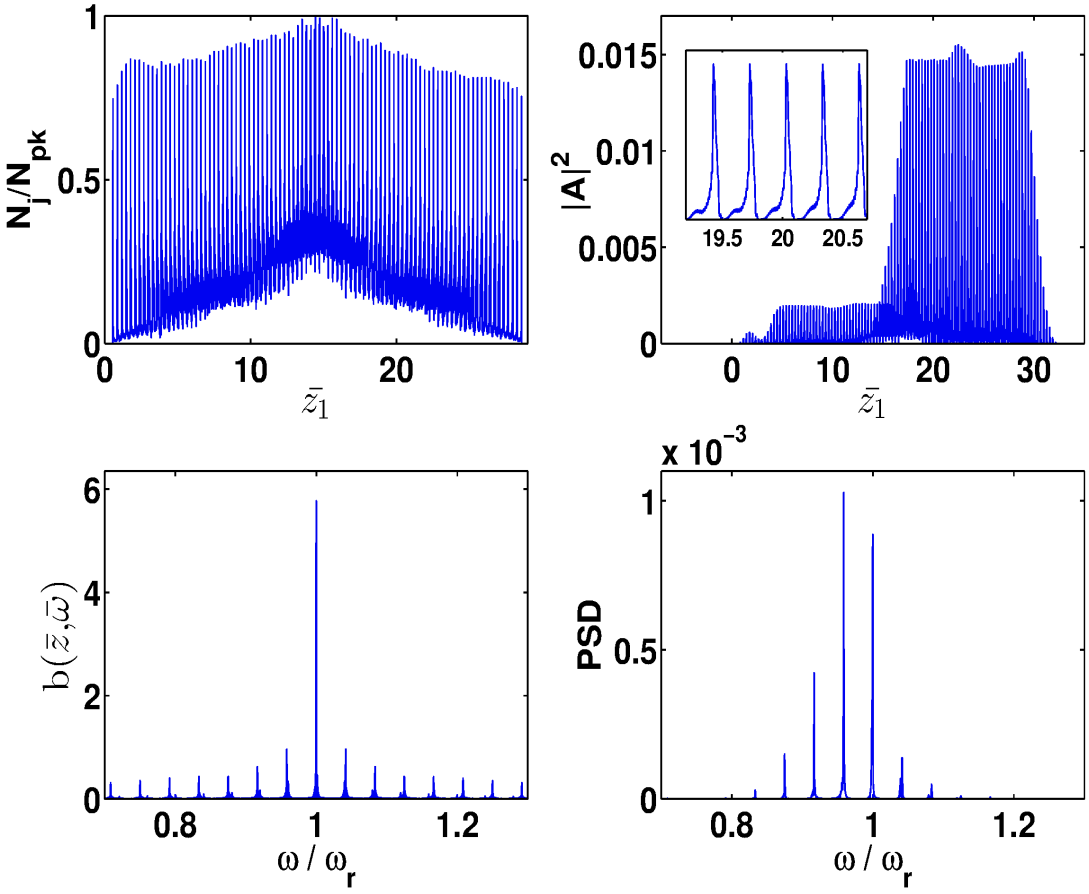

Figure 4.9: As figure 4.8, but for the MLOK undulator at saturation ($\bar{z} \approx 0.6$). Inset top-right shows detail expanded in $\bar{z}_1$. A well defined set of phase-matched radiation modes has developed resulting in a train of short radiation pulses. In unscaled units the individual pulse widths are ∼106 attoseconds (FWHM) and separated by approx. 0.8 femtoseconds.

Chapter 5

Beamlets

5.1 Introduction

In the previous chapter, an FEL technique that produced a train of coherent radiation spikes was discussed. However, there is a demand [31, 34] in the FEL community to produce so-called 'single spike' radiation pulses as opposed to a train of radiation pulses. A few techniques [31, 34] have already been proposed to generate 'single spike' radiation pulses.

In this chapter a method to produce 'single spike' radiation pulses is presented, this method is based on the interaction of multiple short electron pulses or beamlets. The interaction of multiple electron pulses was explored experimentally in [35]. The beamlets investigated here have flat-top current profiles, therefore the large current gradients produced by their hard edges act as coherent radiation sources [36, 37]. This phenomenon is known as coherent spontaneous emission [36, 37] (CSE) and cannot be correctly modelled by averaged FEL codes such as Genesis, hence the need for unaveraged codes such as hpFull and Puffin. Coherent radiation from the head of the beamlet will propagate in free space and receive no amplification. However, coherent radiation generated at the beamlet tail will propagate through and interact [11, 36, 37] with the beamlet. This will amplify the coherent radiation field and increase the electron bunching in the beamlet. This amplification process is known as

Self Amplified Coherent Spontaneous Emission (SACSE) [36, 37].

For these simulations an electron pulse is split into a number of reduced current electron pulses, which are called beamlets. These beamlets are then equispaced in energy and temporally overlapped, as shown in figure 5.3. The system of equations describing the FEL interaction is scaled by the FEL parameter ρ given as,

$$\rho = \frac{1}{\gamma_r}\left(\frac{a_u \omega_p}{4ck_u}\right)^{2/3} \tag{5.1}$$

more importantly the equations are scaled by the plasma frequency,

$$\omega_p = \sqrt{\frac{e^2 n_p}{\epsilon_0 m}}. \tag{5.2}$$

Therefore, the FEL equations are scaled to the peak number density n_p of the electron pulse. Similar to hpFull, that was used in the previous chapter, Puffin uses macroparticles. Puffin's macroparticles are assigned a χ-weighting factor given by,

$$\chi_j = \frac{n_j}{n_p} \tag{5.3}$$

where n_j is the electron number density of the j^{th} macroparticle. For the beamlets, the peak number density n_p, when calculating χ_j, is taken to be the peak number density of the ensemble of beamlets, instead of the individual beamlet. Therefore, the simulations are scaled as if the ensemble of beamlets is just one electron pulse. Effectively each beamlet now has a reduced current. Therefore each beamlet's scaled saturation power is reduced and gain length increased. And since the radiation power in an FEL exponentially amplifies as $P = P_0 \exp(\sqrt{3}z/l_g)$, large increases to the gain length are prohibitive to FEL gain. The change to the beamlet saturation power and gain length can be calculated analytically, and is good agreement with this model. This was done by redefining the FEL parameter for an individual beamlet as $\rho_b = \rho/N_b^{1/3}$,

where N_b is the number of beamlets.

The beamlets have zero energy spread i.e., all electrons have the same energy. When sufficiently separated in energy (see figure 5.3), i.e. the beamlet's energy separation $\Delta\gamma$ satisfies the following condition,

$$\frac{\Delta\gamma}{\gamma_r} \geq 2\rho_b, \tag{5.4}$$

each beamlet will have a distinct resonant frequency or mode. This condition comes from the linear analysis of [32, 33], which shows for an electron to remain part of the FEL interaction it must not deviate from the resonant energy by more than $1.89\rho_b\gamma_r$. Therefore, electrons outside this range can perform their own separate FEL interaction. Here, the condition is approximated to $2\rho_b\gamma_r$ and this condition verified by the work of [35].

When propagated through a simple undulator each beamlet will generate and amplify a radiation field at it's own unique resonant frequency. The interference of these radiation fields will produce a train of temporal radiation spikes. The width of these radiation spikes can be controlled by adjusting the beamlet energy separation or changing the number of beamlets in the system. The temporal separation of the radiation spikes can be manipulated by propagating the beamlets through an undulator-chicane lattice, constructed with slippage-only (isochronous) chicanes. Using slippage-only chicanes, which were discussed in chapter 3, can increase the radiation spikes' temporal separation. The slippage-only chicanes prevent the beamlets from dispersing from each other, while radiation field is still slipped forward. By increasing the temporal separation of the radiation spikes, the frequency separation of the radiation modes is decreased. In other words, the radiation mode separation is frequency compressed. However, the natural side-band mode amplification action of an undulator-chicane lattice will result in the formation of side-band radiation modes for each of the compressed radiation modes. Therefore, for certain undulator-chicane module configurations, packets of compressed radiation modes are formed in frequency space, with two unique mode separations. This leads to the possibility of generating a single radiation pulse. This is achieved by adjusting the relative beamlet positions/phases in a dispersive

chicane section, so that when passed through a short undulator the beamlets will generate coherent radiation fields that interfere to form a single radiation spike.

5.1.1 Beat notes

To understand the interaction of multiple beamlets, it is useful to consider the interaction multiple coherent radiation fields. By representing coherent radiation fields by simple monochromatic sine-waves and using simple trigonometric relations, one can predict the interference of multiple coherent radiation fields. When two frequencies interfere, such as $f_{1,2} = A\sin(\omega_{1,2}t)$, two beat notes are produced,

$$f_T = f_1 + f_2 = A\sin(\omega_1 t) + A\sin(\omega_2 t) \tag{5.5}$$

$$f_T = 2A\cos\left[\frac{\omega_1 - \omega_2}{2}t\right]\sin\left[\frac{\omega_1 + \omega_2}{2}t\right] \tag{5.6}$$

f_T contains a fast oscillation at $\left[\frac{\omega_1+\omega_2}{2}\right]$, the sum frequency, which is modulated by the $2A\cos\left[\frac{\omega_1-\omega_2}{2}t\right]$ term, the difference frequency, and is shown in figure 5.1. However, as seen in figure 5.1 the amplitude of f_T oscillates at a frequency given by $|\omega_1 - \omega_2|$. However, adding many sine waves together that are separated by the same frequency, $\Delta\omega = |\omega_n - \omega_{n+1}|$, leads to an increase of the $|\omega_1 - \omega_{n+1}|$ oscillation as this will be constant for all n. In contrast, there will be a decrease in the $\left|\frac{\omega_n+\omega_{n+1}}{2}\right|$ oscillation, as this oscillation, the sum frequency, is not constant for all n. This is seen is figure 5.2(a), where 10 sine waves for equal frequency separation have been superimposed. The beat note produced takes the form of a series of spikes. Two important effects should be noted, 1 - increasing the frequency difference will decrease the spike width (see figure 5.2(b)) and 2 - increasing the number of sine waves will also decrease the spike width (see figure 5.2(c)).

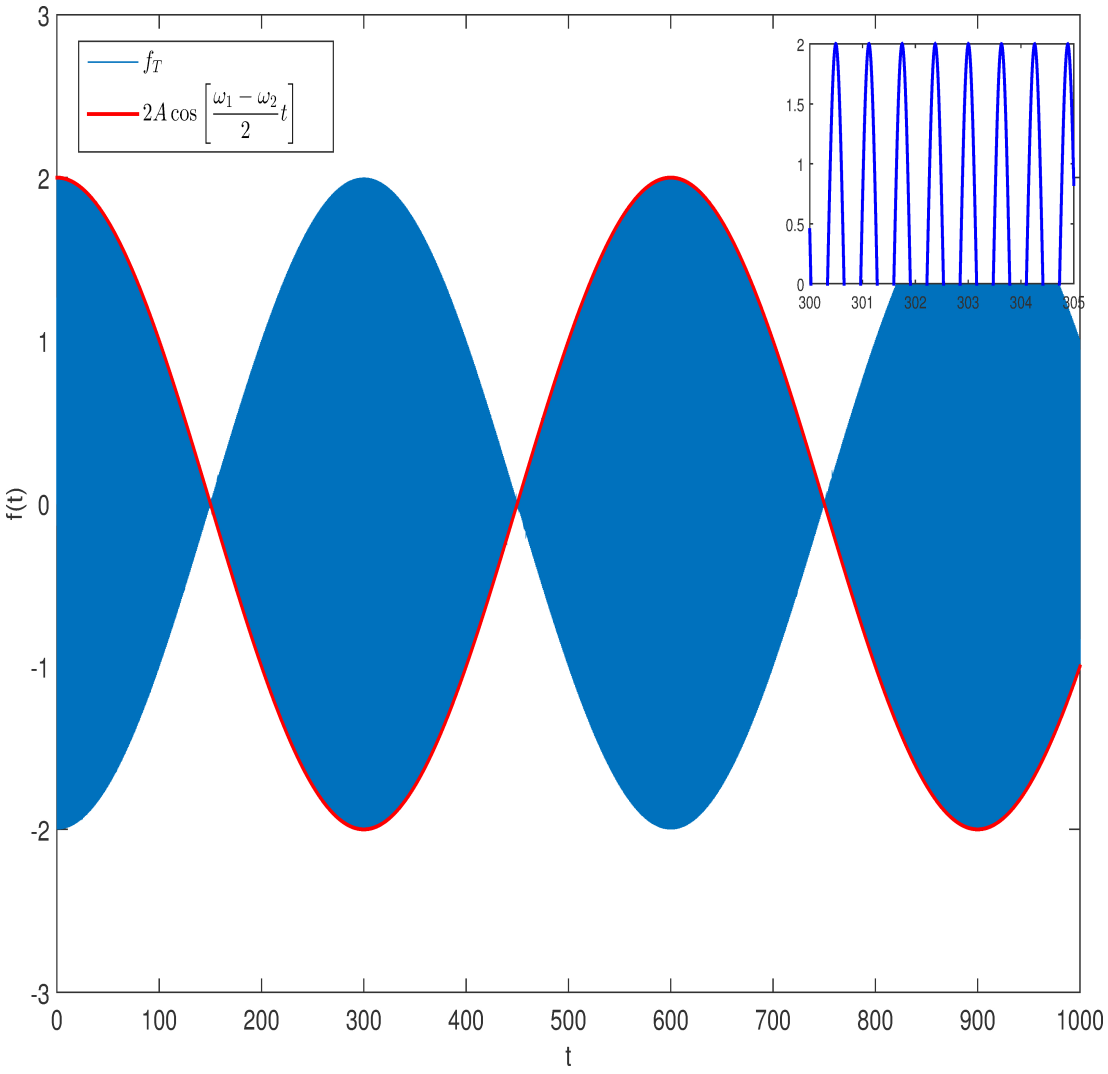

Figure 5.1: An example of a beat note: the fast oscillation is in blue and envelope in red. This is the simplest example of a beat note as it is constructed from two frequency components. The amplitude of y_T oscillates at frequency of $|\omega_1 - \omega_2|$.

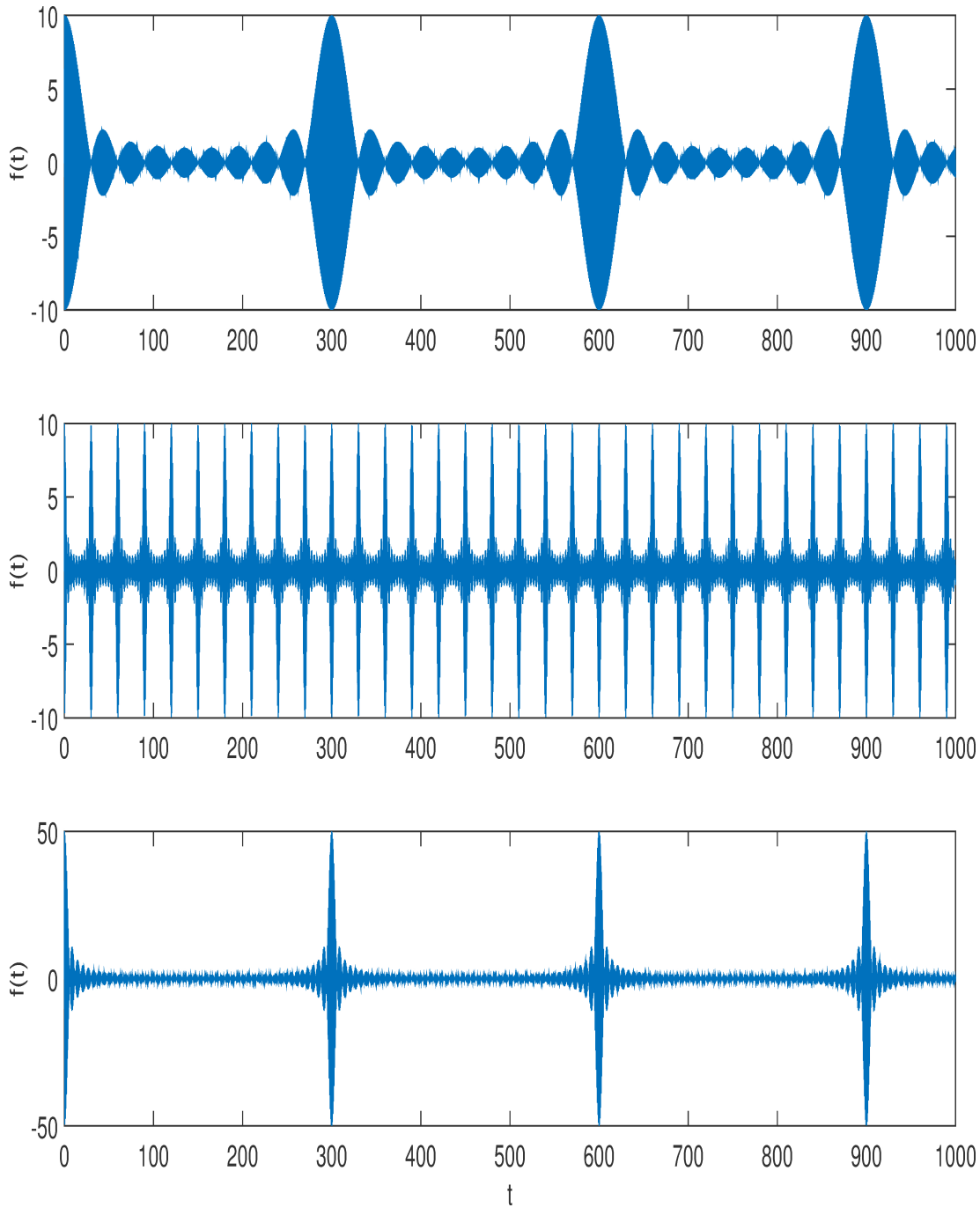

Figure 5.2: (a) An example of beat note produced by the sum of 50 sine waves. The difference frequency between adjacent modes dominates the various sum frequencies of adjacent modes. (b) An example of beat note produced by the sum of 10 sine waves. In this case the frequency difference between the modes is ten times that of (a) this increases the beat note frequency and also decreases the spike (peak) width. (c) An example of beat note produced by the sum of 100 sine waves. The additional modes has the effect of decreasing width of each spike.

5.2 Multiple beamlets

The interaction of multiple beamlets was investigated using the unaveraged FEL simulation code Puffin [11], this code was discussed in chapter 3. In these simulations the FEL parameter was $\rho = 0.001$ and undulator parameter $a_w = 0.0511$. Here, the undulator parameter a_w is uncharacteristically small; however simulations using more feasible parameters produce similar results and will the subject of a future publication. The beamlets had mean resonant energy of $\gamma_r = 176$, a scaled length of 1, and a flat top current profile. In regimes [36, 37] with short electron pulses, flat top current profiles, and long undulators coherent radiation from electron pulse tail will propagate through the electron pulse and be amplified. For this reason it is expected that the amplification of coherent emission will dominate the amplification of spontaneous emission [36, 37] resulting from electron shot-noise [9]. The electron pulse parameters are constant for all simulations presented in this section. Puffin's working equations are solved in the $\bar{z}_2$ radiation rest frame. Hence, the radiation pulse does not propagate in $\bar{z}_2$ instead the electrons slip with respect to the radiation field in $\bar{z}_2$. In $\bar{z}_2$ frame (figure 5.3) the head of the beamlets is the left therefore the electrons are seen to slip to the right.

5.2.1 Simple undulator

Five short beamlets (see figure 5.3), are propagated through a simple undulator lattice. In doing so they generate and amplify coherent radiation fields with five distinct resonant frequencies. The condition placed on the beamlet's energy separation is satisfied, equation 5.4, by setting the energy separation to $\Delta\gamma/\gamma_r = 2\rho$. The interference of these distinct resonant frequencies produce a beat note with a frequency separation of,

$$\Delta\omega_{beat} = |\omega_n - \omega_{n-1}| \tag{5.7}$$

$$\frac{\Delta\omega_{beat}}{\omega_r} \approx 2\frac{\Delta\gamma}{\gamma_r} \tag{5.8}$$

were n = 2,3,4,5, see figure 5.3 and $\Delta\gamma = |\gamma_n - \gamma_{n-1}|$ is the difference of resonant beamlet energies. This can be seen by performing a 1st order expansion of the resonance condition, equation 2.1[1]. In figure 5.4 the results of a simulation are presented where five short beamlets are passed through an undulator. The interference of coherent radiation fields produced by the beamlets create a beat note with a frequency $\Delta\omega_{beat}/\omega_r \approx 0.004$, which is approximately 3 in the scaled units of $\bar{z}_2$. The frequency and spike width of the beat note generated in the undulator by multiple beamlets can be controlled in a similar manner to figure 5.2 (b)-(c). This can achieved by increasing the number of beamlets (figure 5.5) or by increasing the beamlet energy separation $\Delta\gamma$ (figure 5.6).

[1] $\lambda_r = \frac{\lambda_u}{2\gamma_r^2}(1 + a_u^2) \rightarrow \omega_r = \frac{2\gamma_r^2\omega_u}{(1+a_u^2)} \rightarrow \omega_r + \Delta\omega = \frac{2(\gamma_r+\Delta\gamma)^2\omega_u}{(1+a_u^2)} \rightarrow$ expand and ignoring 2nd order terms in $\Delta\gamma$, as $\Delta\gamma \ll \gamma_r$. $\omega_r + \Delta\omega = \frac{2(\gamma_r^2+2\gamma_r\Delta\gamma+\Delta\gamma^2)\omega_u}{(1+a_u^2)} \rightarrow \omega_r + \Delta\omega = \frac{2(\gamma_r^2+2\gamma_r\Delta\gamma)\omega_u}{(1+a_u^2)}$ now cancelling out the initial resonance condition $\Delta\omega = \frac{2(2\gamma_r\Delta\gamma)\omega_u}{(1+a_u^2)}$ again cancelling out the resonance condition $\Delta\omega = \frac{2(2\gamma_r\Delta\gamma)\omega_u}{(1+a_u^2)} \rightarrow \Delta\omega = 2\Delta\gamma\frac{\omega_r}{\gamma_r} \rightarrow \frac{\Delta\omega}{\omega_r} = 2\frac{\Delta\gamma}{\gamma_r}$

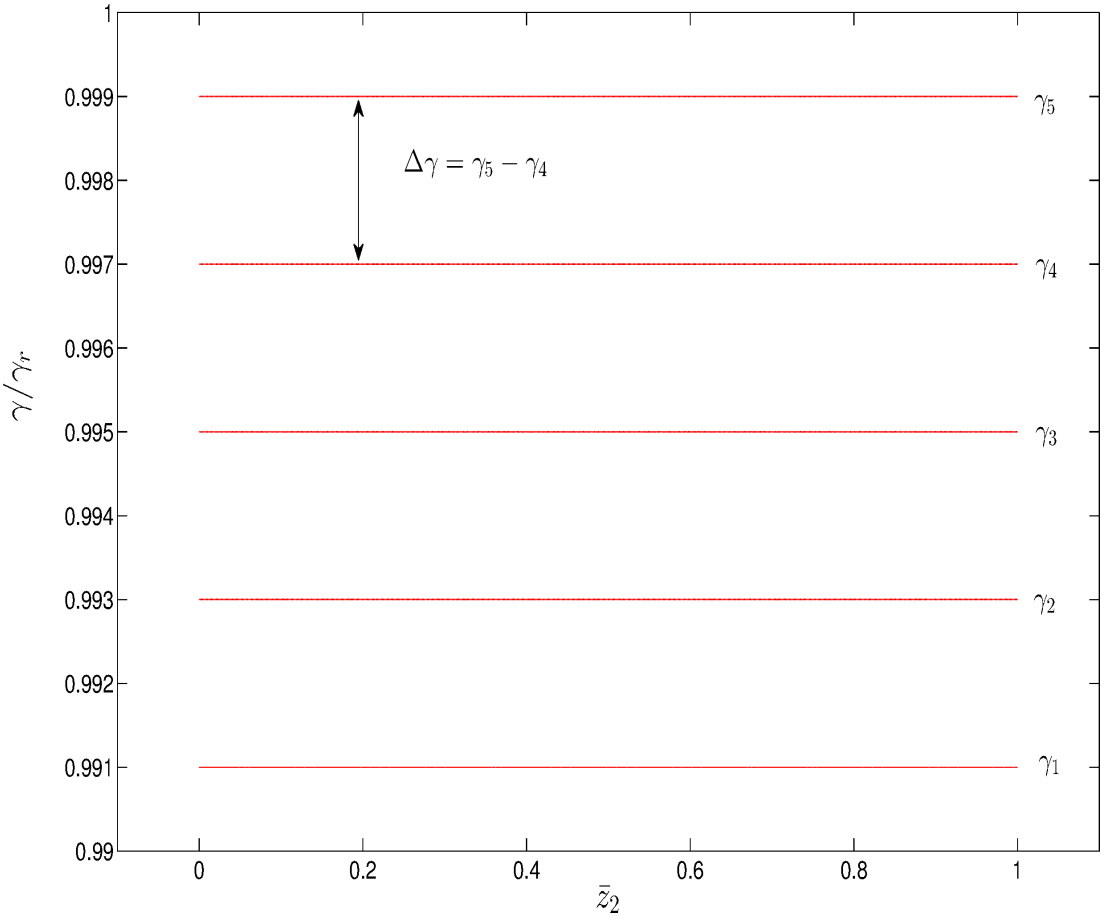

Figure 5.3: Diagram of multiple beamlets. The beamlets are separated by $\Delta\gamma$ in energy. For the simulations presented in this section the energy separation of the beamlets satisfies the condition $\Delta\gamma \geq 2\rho_b\gamma_r$. The beamlets have flat-top current distributions, therefore the discontinuities of a beamlet current profile will generate coherent spontaneous emission.

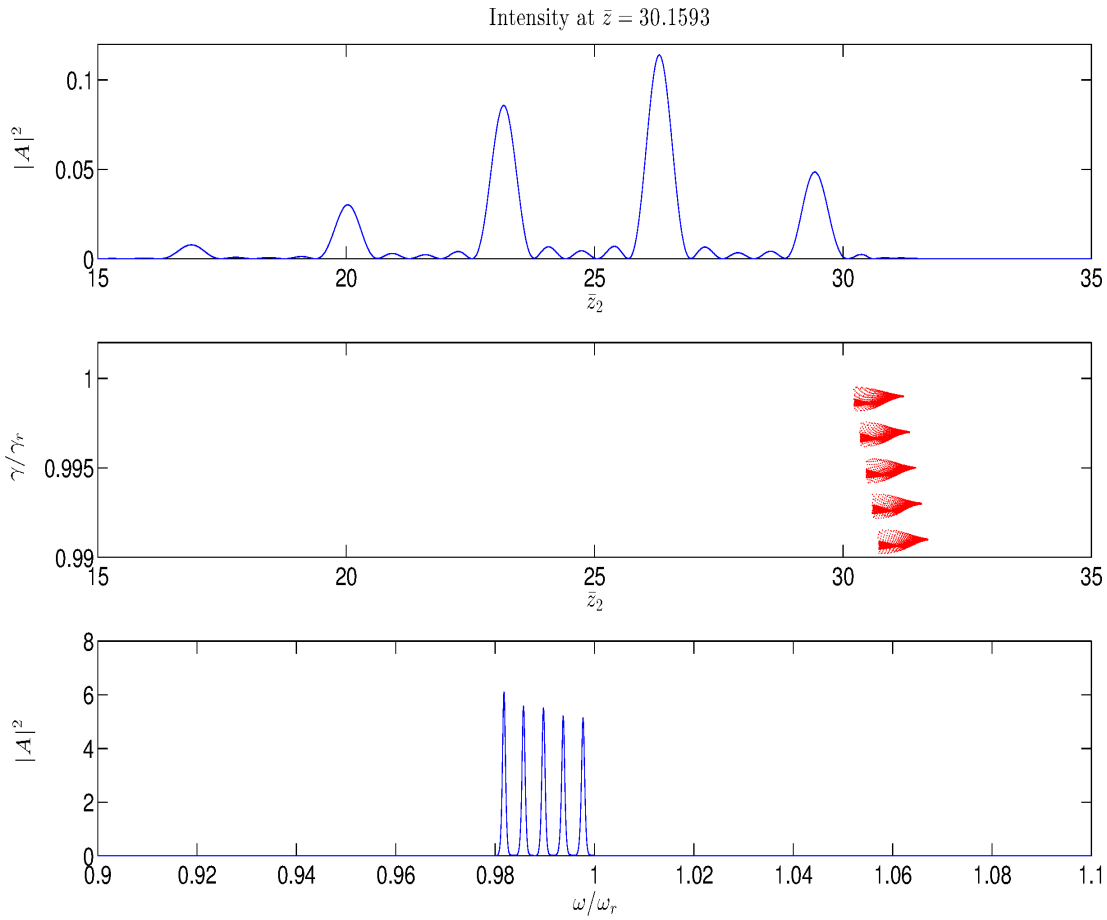

Figure 5.4: Five beamlets equispaced in energy are propagated through a simple undulator. The beamlet have hard edges will act as sources of coherent spontaneous emission. The coherent emission from the beamlet tails will propagate through beamlets and be amplified. In this simulation the beamlets are separated in energy by $\Delta\gamma/\gamma_r = 2\rho$, where $\rho = 0.001$. Therefore, the radiation modes produced should separated by $\Delta\omega/\omega_r \approx 0.004$, see equation 5.8. The radiation modes combine to form a beatnote whose frequency is equal to the frequency separation $\Delta\omega/\omega_r \approx 0.004$. This beatnote has a period of 3 in the scaled units of $\bar{z}_2$.

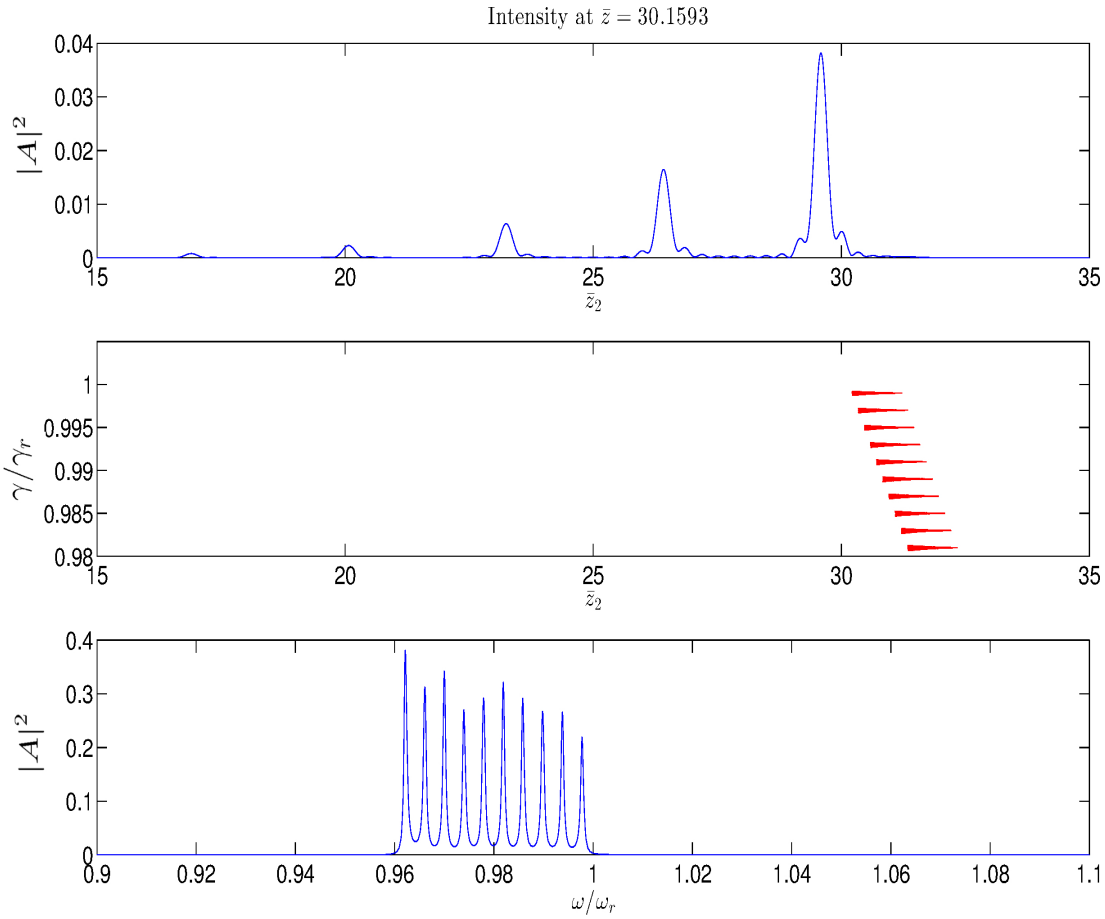

Figure 5.5: Ten beamlets equispaced in energy are propagated through a simple undulator. As beamlet's are sufficiently separated in energy they each produce radiation at their own distinct resonant frequency. Again the difference frequency between adjacent pulses is equal to the beat note produced. In this case the number of beams is increased from 5 to 10 and just as in figure 5.2(c) this reduces the radiation spike width.

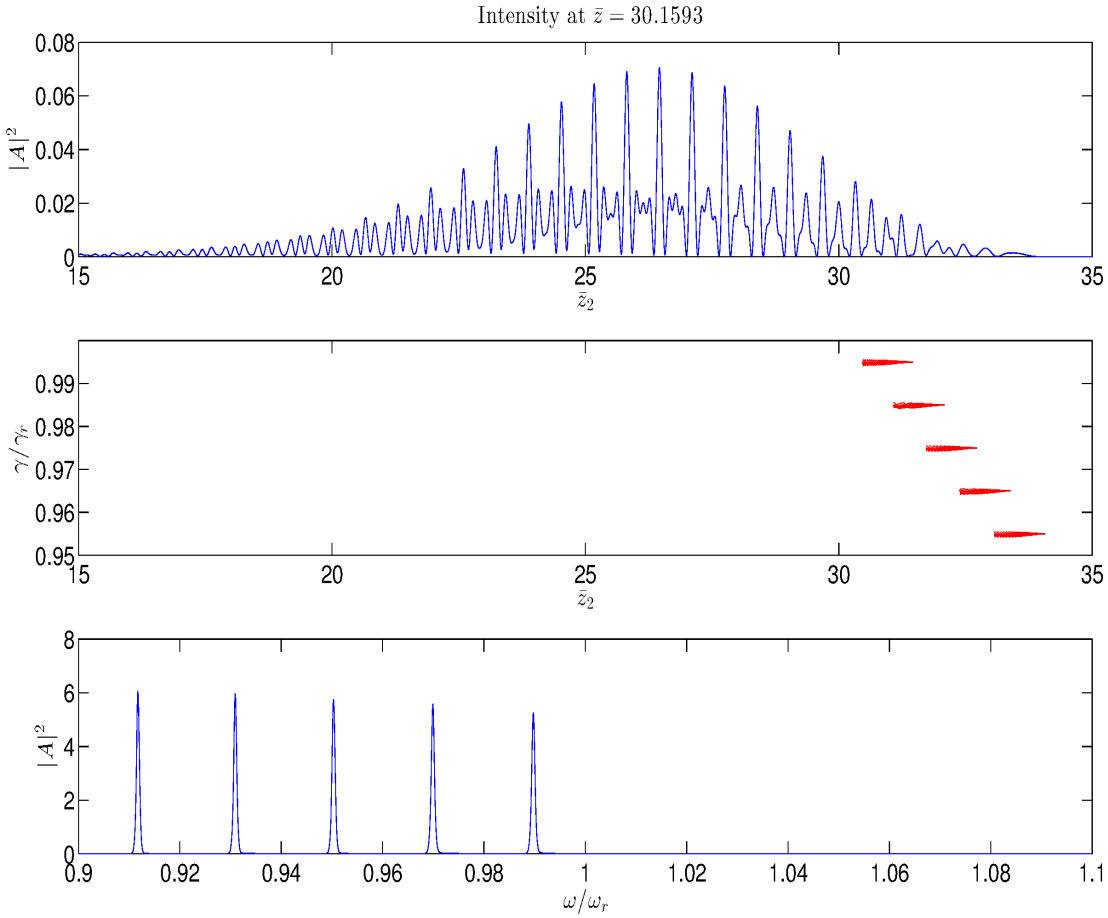

Figure 5.6: Five beamlets equispaced in energy are injected into a simple undulator, each beamlet produces radiation at it's own independent frequency. Just as in figure 5.4 the five radiation fields interfere to produce a beat note whose frequency is given by equation 5.8. However, in this case the beam's separation in energy has been increased by a factor 5, this not only increases the beat note frequency from $0.004\omega_r$ to $0.02\omega_r$ it also decreases the radiation spike width.

5.2.2 An undulator-chicane lattice

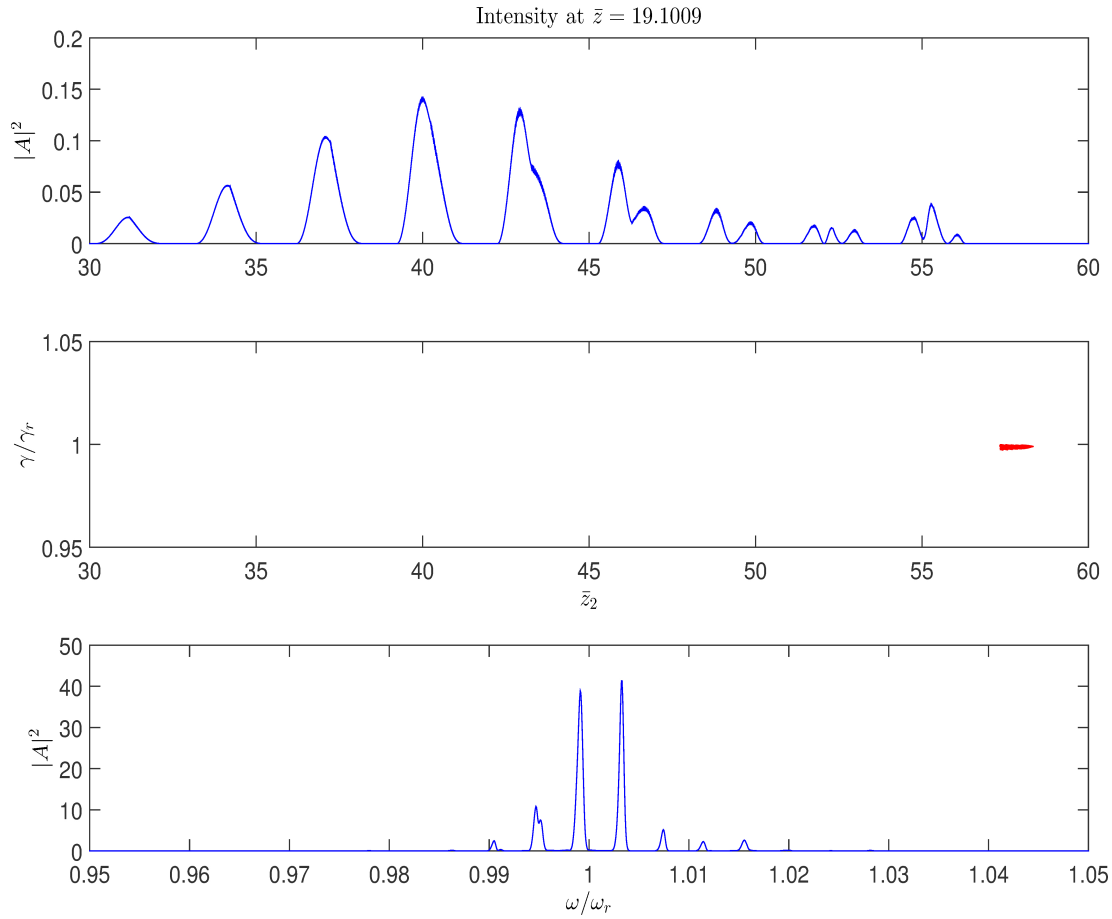

Figure 5.7: An electron pulse injected is through a lattice consisting of undulator-chicane modules. A radiation pulse is generated with side-band radiation modes separated by $\Delta\omega_{modal} = 2\pi c/s$. The electron microbunching has increased the electron pulse energy spread.

Simulations where beamlets are propagated through an undulator-chicane lattice are now discussed. As described in chapter 4 and elsewhere [28, 29], when a single electron pulse sent through an undulator-chicane lattice it will amplify side-band radiation modes, the separation of these side-band radiation

mode is,

$$\Delta\omega_{modal} = \frac{2\pi c}{s}, \tag{5.9}$$

where, is s is the sum of undulator slippage l and chicane slippage δ, i.e. $s = l + \delta$. The chicanes used in these simulations do not apply any electron dispersion, and will be called slippage-only chicanes. Slippage-only or isochronous chicanes have been experimentally demonstrated [25]. In figure 5.7 a single electron pulse has been propagated through an undulator-chicane lattice. The slippage per module of this undulator-chicane was $s = 240\lambda_r$ therefore the lattice amplified side-band radiation mode that are separated by $\Delta\omega_{modal}/\omega_r = 0.0042$.

However, injecting five beamlets (like those in figure 5.4) through the undulator-chicane lattice used in figure 5.7 will generate side-band radiation modes with a 'frequency compressed' separation of,

$$\Delta\omega_c = \Delta\omega_{beat}/S_e \tag{5.10}$$

S_e, the slippage enhancement factor is defined as $S_e = s/l$. For figure 5.8 $s = 240\lambda_r$, $l = 80\lambda_r$ and $S_e = 3$, therefore the modal separation (and corresponding beat note) is given by $\Delta\omega_c/\omega_r \approx 0.0013$ (9 in units of $\bar{z}_2$, i.e., $T = \frac{4\pi\rho\omega_r}{\Delta\omega_c}$)

To understand this modal compression figure 5.4 and figure 5.8 should be compared. In figure 5.4 the radiation spikes have a temporal separation of 3, however in figure 5.8 this separation is now $3 \times S_e = 9$. The undulator-chicane lattice, consisting of slippage-only chicanes, increases the temporal separation of the radiation spikes. The slippage-only chicanes are delaying the electron dispersion of the beamlets. Because the beamlets have different energies they disperse from one another. However, as they are equispaced in energy, they can align periodically to emit radiation that interferes to form a radiation spike (see figure 5.4). Using slippage-only chicanes allows a radiation spike to slip ahead of the beamlets, hence when the next radiation spike is formed the previous spike has been slipped further ahead than would normally happen with a simple undulator, this process is illustrated in figure 5.9. The ratio of

slippage experienced by the radiation field to equivalent beamlet dispersion is given by $S_e = s/l$, commonly known as the slippage enhancement factor. Hence, the temporal separation of radiation spikes is increased by a factor S_e. And, also the side-band radiation mode separation is reduced by a factor $1/S_e$.

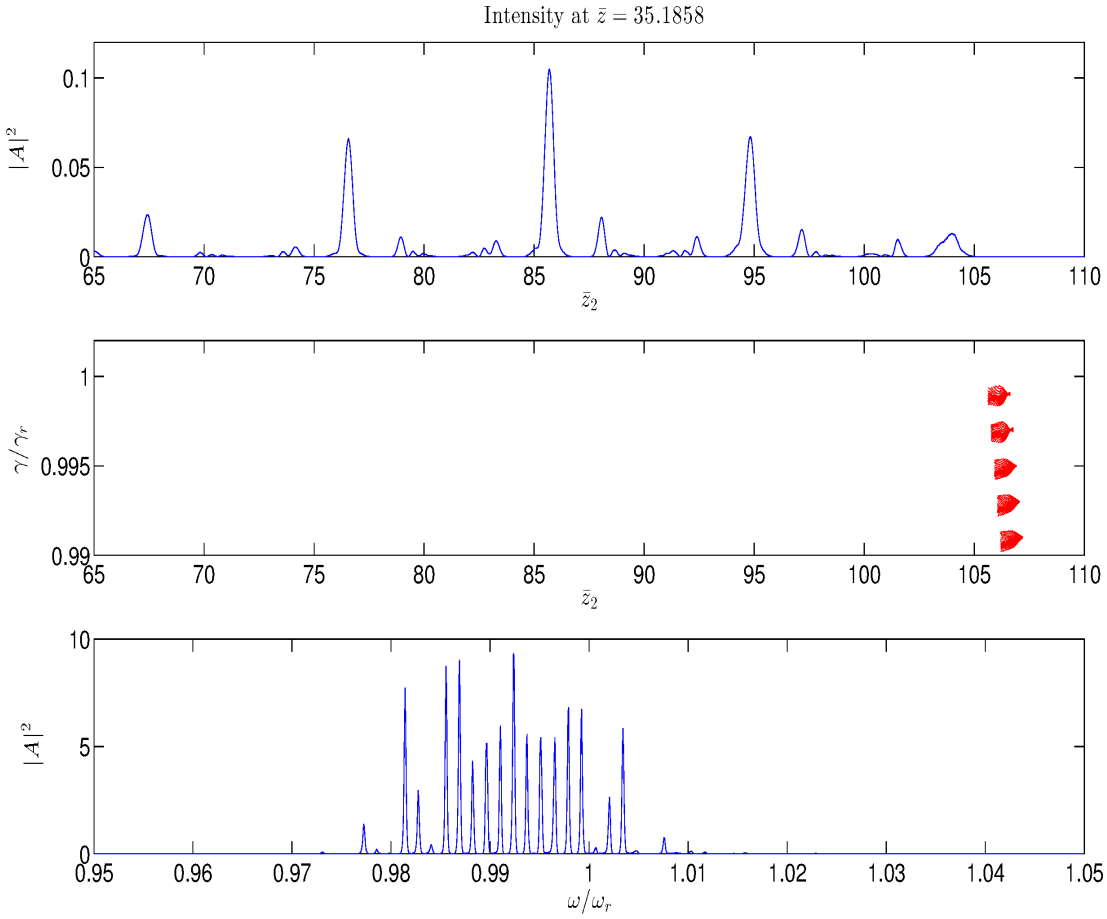

Figure 5.8: Combining five beamlets with an undulator-chicane lattice leads to a new modal structure forming were $\Delta\omega_c = \Delta\omega_{beat}/S_e \approx 0.0013\omega_r$ is the mode separation. In this example the slippage enhancement factor was $S_e = 3$ and the beatnote frequency $\Delta\omega_{beat} \approx 0.004$.

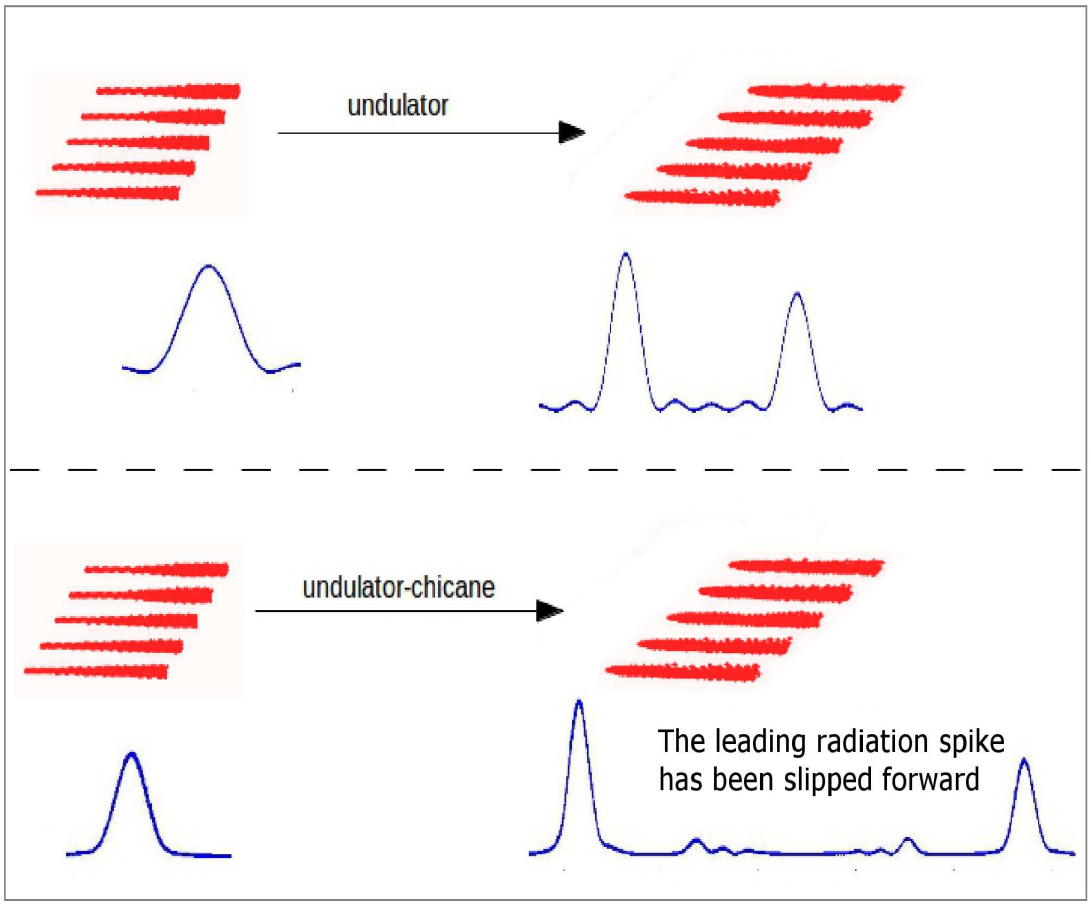

Figure 5.9: The slippage-only chicane causes the lead radiation spike to slip forward while stopping the beamlets from dispersing. This means that when the next radiation spike is generated the previous spike has already been slipped forward. The spike separation is increased by original separation multiplied by the ratio of the total undulator-chicane slippage to the undulator slippage s/l. This increase in the radiation spike separation results in a decrease in the mode separation in frequency space.

Decreasing the slippage per undulator-chicane module s reveals that the modes are actually formed in packets of five, corresponding to the number of beamlets. In each packet the modal separation is $\Delta\omega_c = \Delta\omega_{beat}/S_e$ and the packets are separated by $\Delta\omega_{modal} = 2\pi c/s$, this can be seen in figure 5.10 where $\Delta\omega_c/\omega_r = 0.0014$ and $\Delta\omega_{modal}/\omega_r = 0.0167$, as l = 20 and $\delta = 40$. Therefore, each compressed frequency mode has side-band radiation modes separated by $\Delta\omega_{modal}/\omega_r = 0.0167$. In figure 5.8, these distinct sets of radiation modes overlapped as the range of the compressed side-band modes $4\Delta\omega_c = 0.0052$ was greater than the separation of modes amplified by undulator-chicane lattice $\Delta\omega_{modal} = 0.0042$.

In figure 5.11 five short beamlets are propagated through an undulator-chicane-undulator module, where the chicane section applies a large dispersion to the beamlets. In first undulator, of length $l = 800$, coherent radiation generated at the beamlet's tail is amplified when propagating through the beamlets. This also generates strong electron microbunching in the beamlets. Then the strong chicane section increases the microbunching. The strong chicane also through electron dispersion causes the beamlets to align such that upon passing through the second undulator a large radiation spike is produced. Simulations have shown that the FEL interaction is key to the processes described in this section, i.e. turning off the FEL interaction by forcing $A_\perp = 0$ in the electron equations 3.1-3.2 will produce very different results.

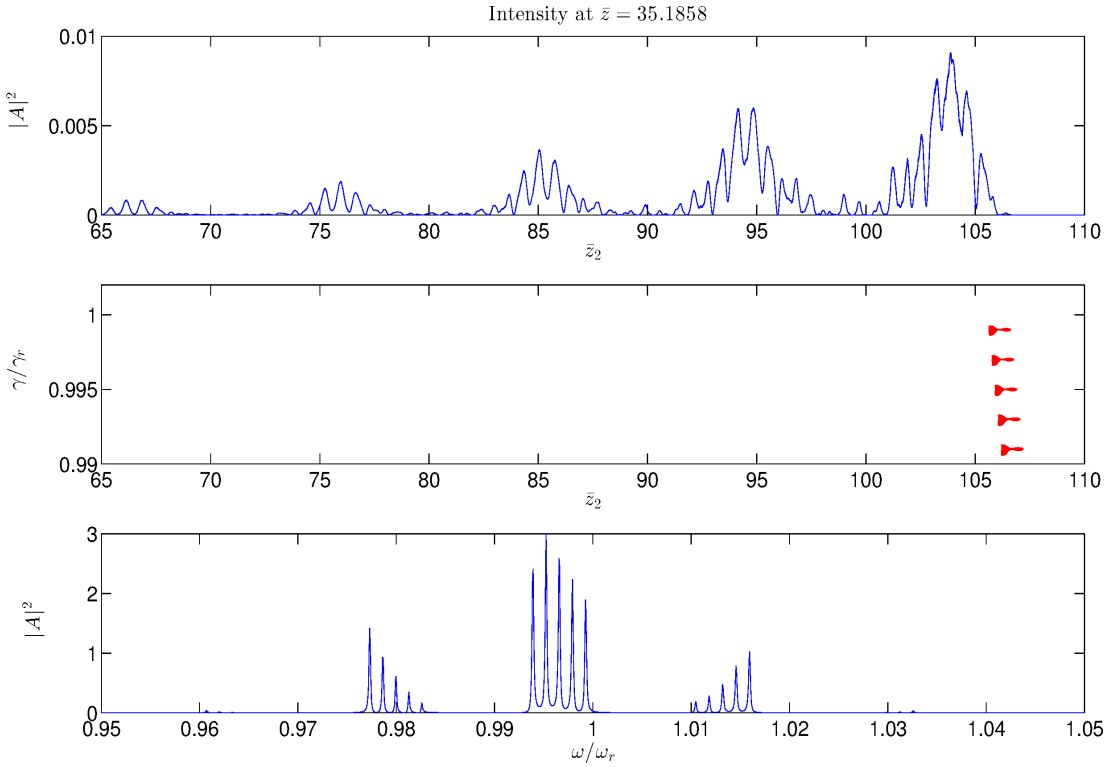

Figure 5.10: Five beamlets injected along an undulator-chicane lattice with a small value of slippage per module. In this case packets of modes (5 per packet) have formed, with the inter packet modal separation given as $\Delta\omega_c = \Delta\omega_{beat}/S_e$ ($= 0.0013\omega_r$) and the packet to packet separation $\Delta\omega_{modal} = 2\pi c/s$ ($= 0.0167\omega_r$). Both modal separations are visible in the temporal domain (top plot) as beat notes. The pulse separation is energy is equivalent to $\Delta\omega_{beat} = 0.004\omega_r$, $S_e = 3$ and $s = 60\lambda_r$

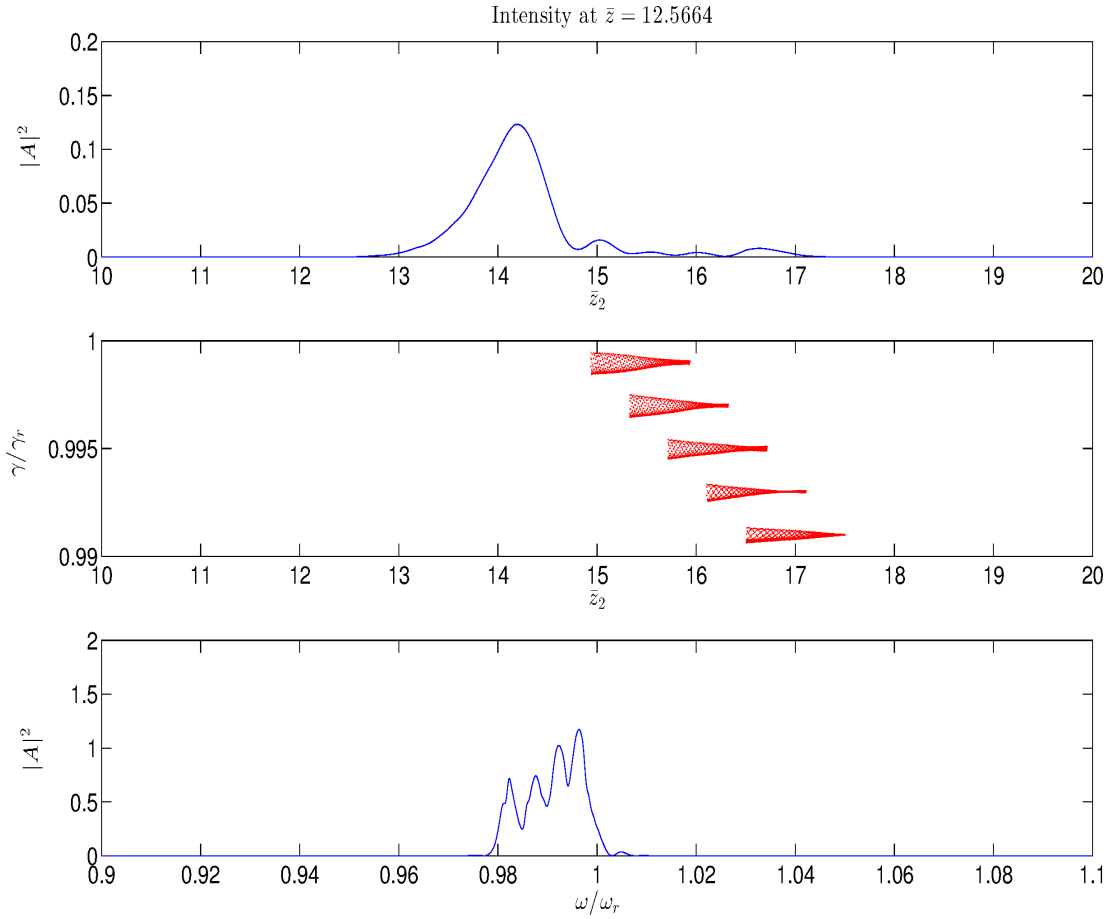

Figure 5.11: Five beamlets injected through one undulator-chicane- undulator module can produce a single radiation pulse. The dispersive chicane shifts the relative phases of the beamlets altering the arrival time of beamlets in the undulator. By altering the arrival time of the beamlets, they can be aligned such their coherent emission will interfere to produce a single radiation spike in the undulator.

Chapter 6

Chirped Beamlets

6.1 Chirped Beamlets

6.1.1 The Model

Now, the interaction of a number of overlapping co-propagating chirped beamlets is investigated [16]. A schematic of the chirped beamlets is shown in figure 6.1. The scheme has been designed so that at an instantaneous position in $\bar{z}_2$ each beamlet has its own distinct FEL bandwidth and equation 5.4 is satisfied. Hence, the separation of the beamlets in energy should satisfy equation 5.4, in this case $\Delta\gamma = 2.5\rho\gamma_r$. The head of the electron pulse is to the left in $\bar{z}_2$ (see figure 6.1), and the electrons slip to the right in $\bar{z}_2$.

Figure 6.1 illustrates the basic principle of this model, a radiation pulse is allowed to propagate through a beamlet in an undulator section. After exiting the undulator section the radiation pulse is passed (or slipped) to the next beamlet in a chicane slippage section. The advantage of this scheme is that the range of electron energies experienced by a radiation pulse can be kept constant throughout the undulator-chicane lattice. The range of electron energies experienced by a radiation pulse is dependent upon the electron pulse's energy gradient and the undulator module slippage length l.

The simulations of this section use the same macroparticle model of the

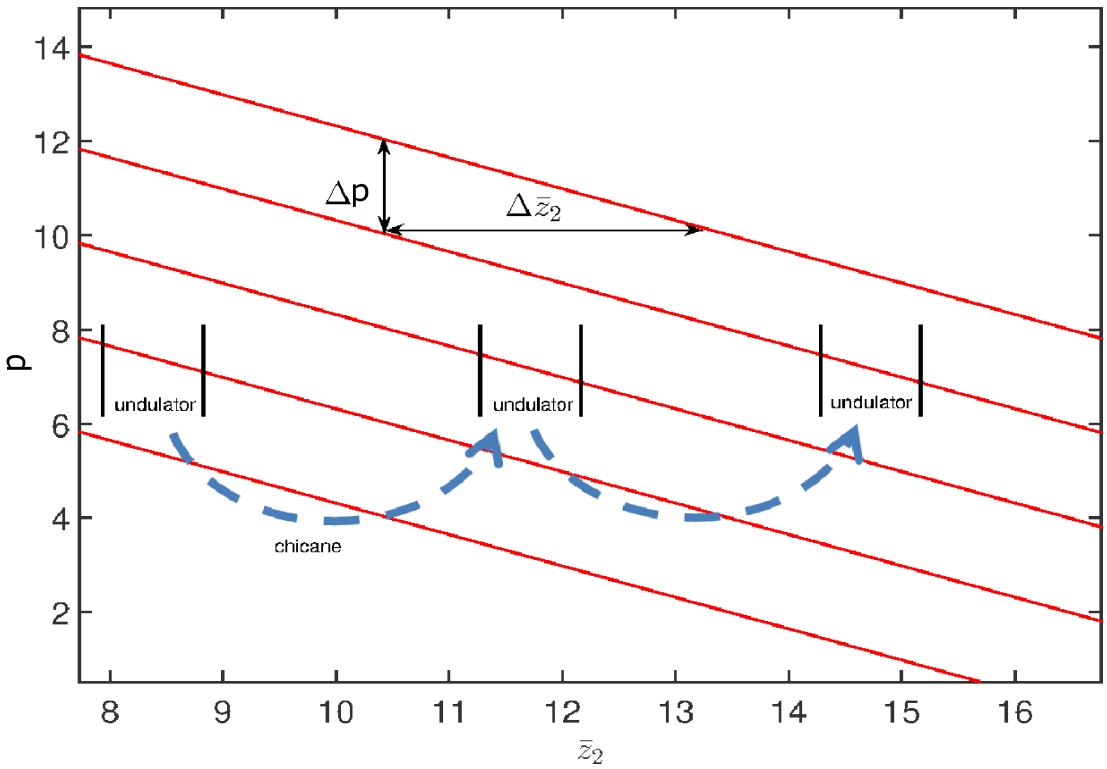

Figure 6.1: Diagram showing the initial electron pulse phase space. Five cold electron pulses (beamlets) with a linear energy chirp are overlapped and separated in energy by $2.5\rho\gamma_r$. The chirp gradient is $\frac{d\gamma}{d\bar{z}_2} = -\gamma_r\rho$ and the temporal separation is 2.5 l_g. Scaled coordinate $\bar{z}_2$ is in the radiation rest frame and the head of the electron pulse is to the left. Electrons slip to the right in $\bar{z}_2$, at a rate of one resonant period per undulator period, as the electron pulse and radiation field co-propagate through the undulator. The scaled energy parameter is defined as $p_j = \frac{\gamma_j - \gamma_r}{\rho\gamma_r}$, and $\Delta p = \frac{\Delta\gamma}{\rho\gamma_r}$. In the undulator a radiation pulse will propagate through a beamlet then the chicane will slip the radiation pulse forward to the next beamlet. By doing so the range of electron energies experienced by a radiation pulse is kept constant.

previous chapter. Therefore these simulations are scaled to the peak number density of the ensemble of beamlets

An electron will slip one resonant wavelength per undulator period in accordance with the resonance condition 2.1. For example in a four period undulator, a resonant electron will slip four resonant wavelengths behind the

radiation field. This quantity is known as the undulator's slippage length l. The resonance condition that determines the resonant wavelength of an electron for a given γ_r, a_u and λ_u is restated here,

$$\lambda_r = \frac{\lambda_u}{2\gamma_r^2}\left(1 + a_u^2\right) \tag{6.1}$$

where λ_u is the undulator period and a_u is the scaled undulator parameter.

In addition to communicating radiation from beamlet to beamlet, an undulator-chicane lattice will amplify side-band radiation modes, as was discussed in chapter 4. The side-band radiation mode separation given by equation 4.1 is rewritten in the scaled notation,

$$\Delta\omega/\omega_r = 4\pi\rho/\bar{s}, \tag{6.2}$$

where $\bar{s}$ is the scaled slippage length in an undulator-chicane module, $\bar{s} = s/l_c$. Where s is slippage length, in real units, of an undulator-chicane module. Here, the undulator-chicane slippage length $\bar{s}$ is equal to the sum of the undulator $\bar{l}$ and chicane $\bar{\delta}$ slippage lengths, i.e., $\bar{s} = \bar{l} + \bar{\delta}$.

In [28] the concept of 'locking' the modes is described, mode-locking is achieved by either energy or current modulating the electron pulse at the mode separation $\Delta\omega$ frequency. However, in this scheme mode-locking is achieved by matching the energy separation of the beamlets to the mode separation $\Delta\omega/\omega_r = 4\pi\rho/\bar{s}$. The energy separation of the beamlets can be rewritten as a difference in resonant frequencies. This is done by performing a perturbative expansion to resonance condition (equation 6.1), as was shown in chapter 5. The following expression results from this expansion; $\Delta\omega/\omega_r \approx 2\Delta\gamma/\gamma_r$, which relates a difference in beamlet energies to a difference in frequency. To lock the modes this frequency difference is equated to equation 6.2 to give $\Delta\gamma/\gamma_r \approx 2\pi\rho/\bar{s}$. As the slippage length $\bar{s}$ is equal to beamlet separation, the electron chirp gradient is given by;

$$\frac{d\gamma}{d\bar{z}_2} = \frac{2\pi\rho\gamma_r}{\bar{s}^2}. \tag{6.3}$$

Note that these expressions limit the choice of beamlet simulation parameters for a mode-locking scheme. For example choosing the beamlet energy separation, determines the beamlet's temporal separation and energy gradient.

The energy chirp of a beamlet can be problematic, because as the beamlet propagates through the undulator it will stretch, reducing the local current density. This stretching can be understood by considering the resonance (equation 6.1) condition. The resonance condition shows that higher energy electrons will have a shorter resonant wavelength, and lower energy electrons a longer resonant wavelength. Therefore high energy electrons will have a shorter undulator slippage length than low energy electrons. Since high energy electrons are at the beamlet head and low energy electrons at the tail, electrons at the beamlet tail slip further behind the radiation field than electrons at the beamlet head. Therefore the beamlet stretches as it propagates through the undulator, this stretching is normally referred to as electron dispersion. The electron pulse's energy chirp will also result in the radiation drifting out of resonance as the radiation propagates into electrons that have a different resonant wavelength. In [34] it was shown that such a electron chirp can be compensated for using a tapered undulator. In a tapered undulator, the undulator parameter will change along the interaction region, in doing so the radiation can kept in resonance with the electrons. Here, in series undulator-chicane modules are used to compensate for the beamlet energy chirp.

A chicane will delay the electrons with respect to the radiation pulse. This delay (or slippage) is proportional to the electron energy. Therefore, electrons at the tail of the beamlet will have a longer slippage length than those at the head, since the beamlet chirp is positive. Hence, the slippage length of an undulator-chicane module will be energy dependent and is given by,

$$\bar{s}_\gamma \approx 2\left(\frac{\gamma_r - \gamma_j}{\gamma_r}\right)(\bar{l} + D) + \bar{s}. \tag{6.4}$$

This expression is an approximation and only valid for small energy deviations, see appendix B.4 for a derivation. The $(\bar{l} + D)$ term is associated with the undulator and chicane dispersion, D was defined in chapter 4 as $D = k_r \rho R_{56}$. The slippage length in an undulator-chicane module is dependent on the electron

energy. Therefore the side-band radiation modes ($\Delta\omega_\gamma/\omega_r = 4\pi\rho/\bar{s}_\gamma$) that can be amplified the undulator-chicane lattice are also energy dependent. Such that the tail of the beamlets will amplify a different set of side-band radiation modes from those amplified at the head. Because of the decreased slippage length, a radiation pulse at head of a beamlet cannot be passed to electrons of the same energy in the next beamlet. Therefore resonant interactions cannot be maintained. This is also the case at the tail of the beamlets. The combination of these effects will disrupt the formation of side-band radiation modes.

These effects will be increased for long undulators, strong chicanes and large energy chirps, as $\bar{s}_\gamma$ will change more rapidly for these cases. It is possible to suppress the energy dependence of the slippage length by applying a negative dispersion in each chicane, when $D = -\bar{l}$ the energy dependence of the slippage length is negated (i.e. $\bar{s}_\gamma = \bar{s}$).

6.1.2 Results

The simulations in this section were performed in Puffin using an electron pulse of charge $3pC$, $\rho = 0.001$, $\gamma_r = 176.2$, and a scaled length of $l_b = 80$. An undulator parameter of $a_w = 0.511$ was selected. Although the electron pulse has a flat-top current profile, since the electron pulse is larger than the total undulator slippage length it is expected the SASE should dominate SACSE [9, 11]. It should be noted that the choice of parameters in this section are purely for demonstrative purposes, and are not intended to represent a real FEL.

For these simulations three distinct types of chicane are required, one of which is a purely theoretical device. (1) a chicane that can provide negative or positive dispersion [25]. (2) an isochronous chicane [25], which has zero electron dispersion, i.e. it will only supply slippage to radiation field, which is referred to as a slippage-only (CS) chicane. (3) a chicane that disperses the electron pulse, but does not slip the radiation field, referred to as a dispersion only (CD) chicane. To the author's knowledge dispersion only (CD) chicanes are purely theoretical devices, here they are only used to demonstrate the importance of dispersion in the energy dependent slippage length, equation 6.4.

The effects of an energy dependent slippage length (see equation 6.4) are demonstrated with long undulators and positive dispersion chicanes. However, the slippage length can be made energy independent by using negatively dispersed chicanes. Slippage-only (isochronous) chicanes can generate an additional set of radiation modes with a separation that is proportional to the chicane slippage length.

In mode-locking Free Electron Lasers [29] increasing the number of undulator periods per undulator-chicane module will increase the average radiation power. Therefore the average power produced in a beamlets simulation should also increase also with increasing number of undulator periods. This is shown in figure 6.2, where five different simulation set-ups are shown. An order of magnitude increase in radiation power is achieved when increasing from 20 to 150 undulator periods per undulator module. To ensure that radiation pulse passed between beamlet sections of the same energy, the total slippage per undulator-chicane module is kept constant for these simulations. The undulator-chicane lattice will amplify side-band radiation modes that are separated by $\Delta\omega/\omega_r = 4\pi\rho/\bar{s}$. An example of this in seen in figure 6.3 where a series of chirped beamlets have been propagated through an undulator-chicane lattice. This undulator-chicane lattice has 20 undulator periods and 180 chicane slippage periods per module, in the scaled notation this can be written as $\bar{l} = 0.2513$ and $\bar{\delta} = 2.2619$. Therefore this lattice will amplify side-band radiation modes with a separation of $\Delta\omega/\omega_r = 0.005$. The energy dependent slippage length s_γ does not vary enough to stop the formation of the side-band radiation modes, because slippage-only (isochronous) chicanes are used and $\bar{l}$ is relatively small.

Now, if the undulator-chicane lattice is composed of (positive) dispersive chicanes, the energy dependent slippage length (equation 6.4) will have a greater variation with energy and as such will be prohibitive to the formation of side-band radiation modes, as shown in figure 6.4.

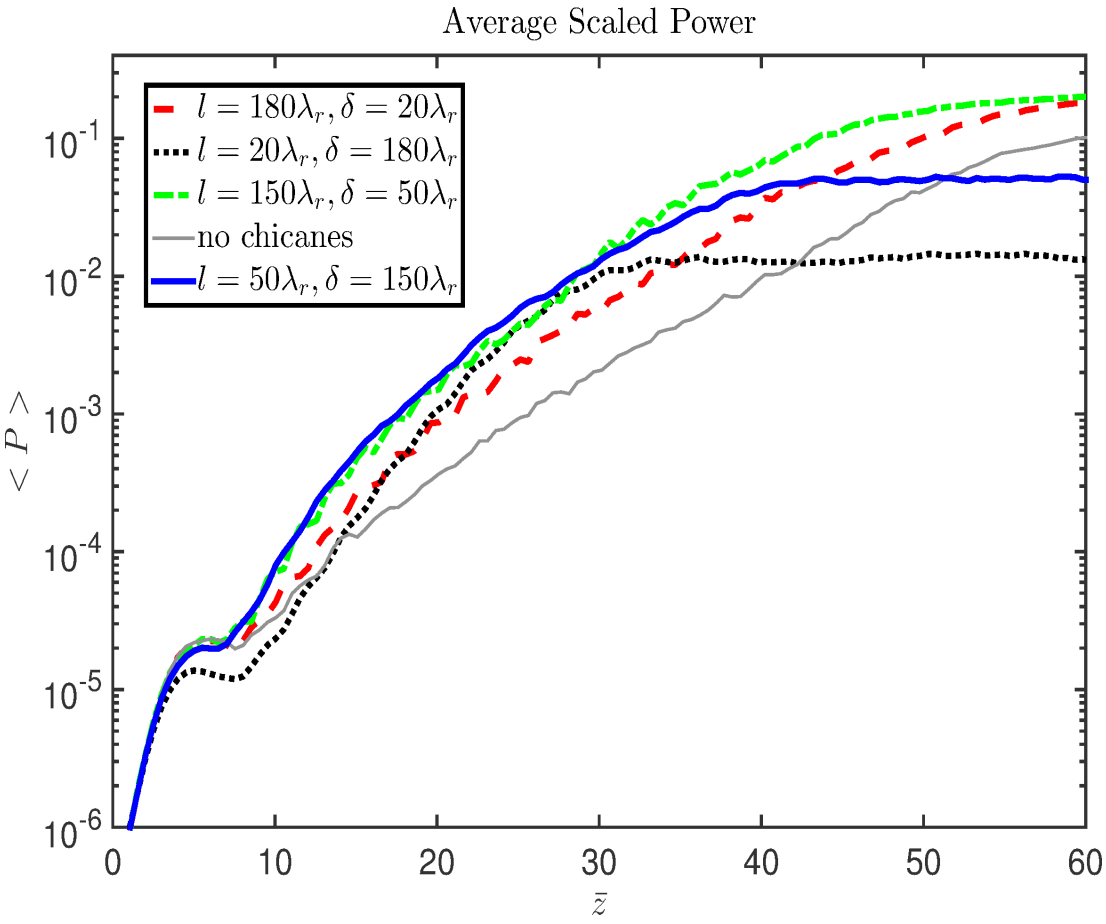

Figure 6.2: Comparison of different simulation setups. The average radiation power is plotted against $\bar{z}$ (i.e. undulator position). For a large section of the FEL interaction the average radiation power is a factor of ten greater when chicane slippage sections are used. Using longer undulator sections will produce higher average radiation powers. For example increasing the undulator length from 20 to 150 undulator periods, increases the average radiation power by an order of magnitude.

The side-band radiation modes are also destroyed when using a long undulator (figure 6.5). As the undulator dispersion over a large number of periods is significant enough to disrupt the formation of side-band radiation modes. However, the slippage-only (isochronous) chicanes generate an extra set of side-band radiation modes separated by $\delta\omega/\omega_r = 4\pi\rho/\bar{\delta} = 0.02$ are generated.

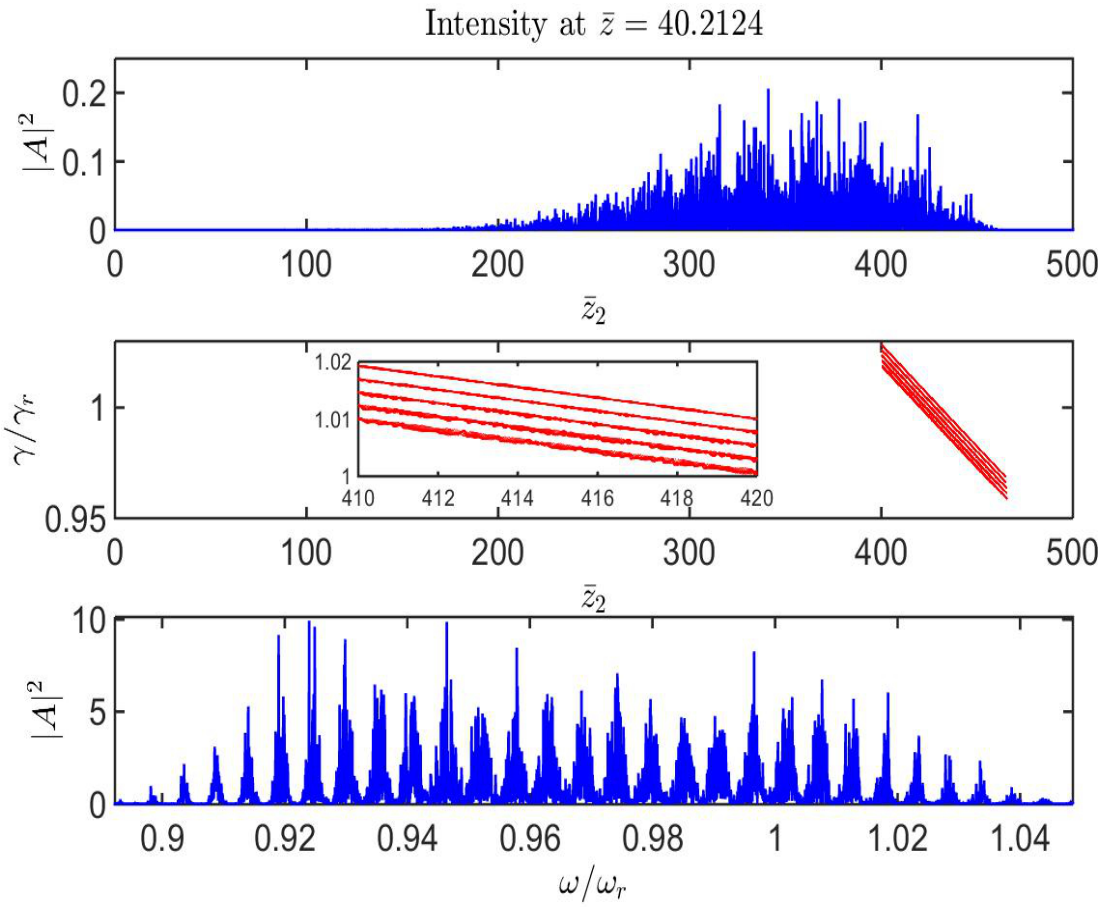

Figure 6.3: At $\bar{z} = 40$ the radiation field is near saturation (top panel), electron microbunching is well developed (middle), and the radiation field spectrum is shown in the bottom panel. In a normal FEL amplifier $\bar{z} = 40$ would be considered post-saturation, however here the macroparticle weight is scaled differently. Such that the simulation is scaled as if only one electron pulse were modelled, instead of multiple electron pulses. Therefore each beamlet has a reduced gain length. In this simulation $\bar{l} = 0.2513$ and $\bar{\delta} = 2.2619$. This gives a modal separation of $\Delta\omega/\omega_r = 4\pi\rho/\bar{s} = 0.005$.

These new radiation modes are generated because the beamlets will produce radiation pulses before and after the slippage-only chicane that are similar (nearly identical). Therefore the only modes that can survive this chicane slip are those separated by $\delta\omega/\omega_r = 4\pi\rho/\bar{\delta} = 0.02$.

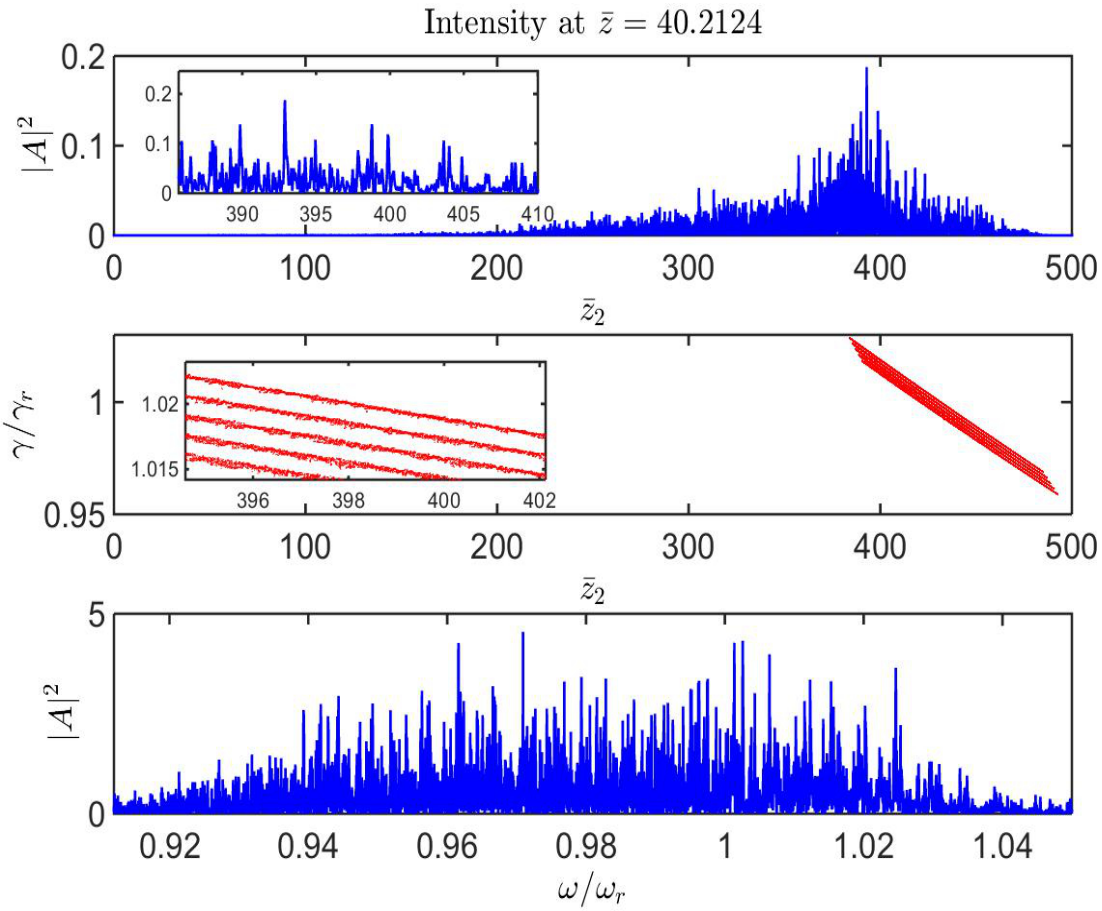

Figure 6.4: This simulation is identical to figure 6.3, except that the chicanes now apply dispersion to the electron pulse. This chicane dispersion is equivalent to the chicane slippage lengthn δ as in normal chicanes. This chicane dispersion prevents the formation of side-band radiation modes. This is because an electron pulse with such a large energy chirp will have an energy dependent slippage length. For example the slippage length of a low energy electron will be greater than that of a high energy electron. Using a dispersive chicane will increase the difference in slippage lengths between high and low energy electrons. Therefore modes generated at the head of the pulse will have different $\bar{s}_\gamma$ than at the tail and a different $\Delta\omega_\gamma/\omega_r = 4\pi\rho/\bar{s}_\gamma$ (see equation 6.4),as such the modes are not matched (locked).

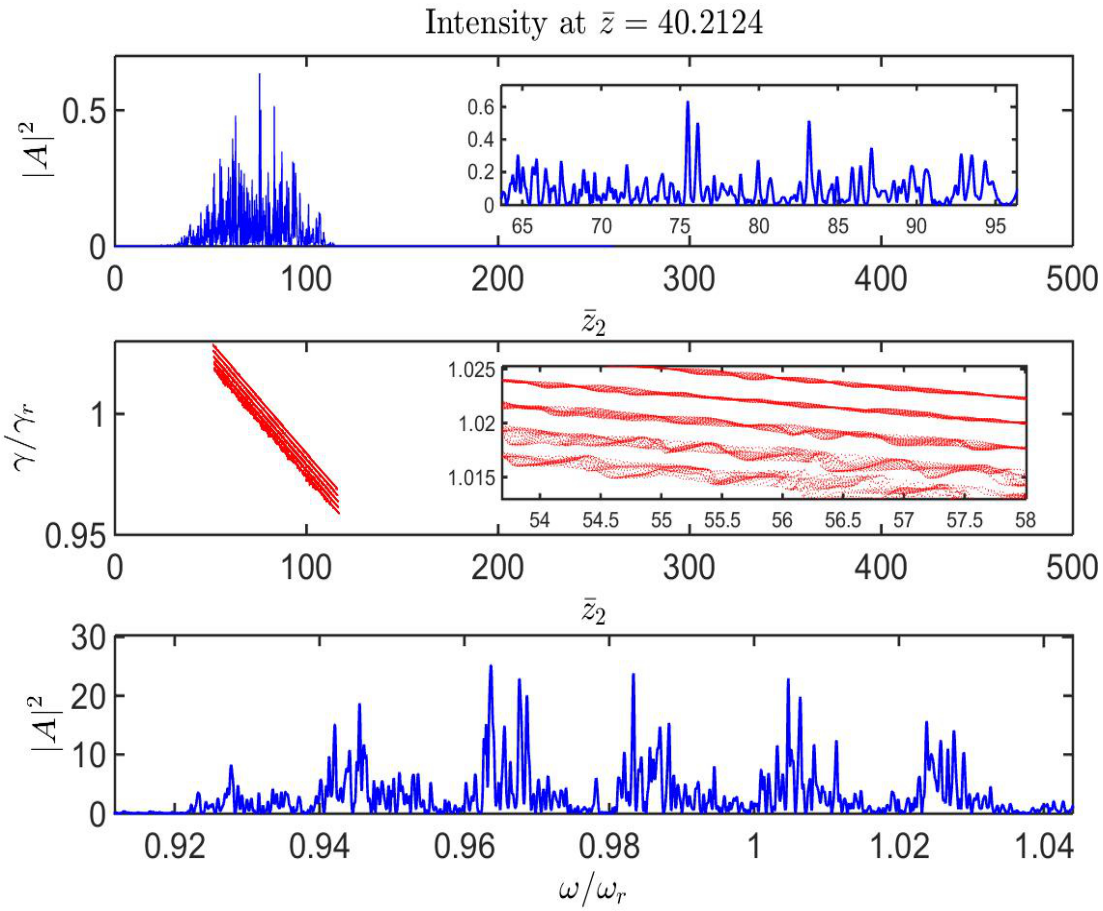

Figure 6.5: In this simulation longer undulator modules are used, $\bar{l} = 1.885$, and slippage-only chicanes $\bar{\delta} = 0.6283$, compared to figure 6.3. Using a longer undulator results more electron dispersion, which makes the difference in slippage lengths between electrons of different energies greater. Therefore, the side-band radiation modes do not form. However, the slippage-only chicanes produce additonal modes separated $\delta\omega/\omega_r = 4\pi\rho/\bar{\delta}$. This is because the electron pulse does not evolve in the slippage-only chicane. And therefore will produce similar (nearly identical) radiation pulses, in the undulator, before and after the slippage-only chicane. Therefore the only modes that can survive the U-CS-U section are given by $\delta\omega/\omega_r = 4\pi\rho/\bar{\delta} = 0.02$.

The slippage-only chicane modes can be replaced by the original undulator-chicane lattice side-band radiation modes, those separated by $\Delta\omega/\omega_r = 4\pi\rho/\bar{s}$,

by using negative dispersion chicanes (figure 6.6). Here, the dispersion in each chicane is such that the total dispersion in an undulator-chicane module is now zero, i.e. $D = \bar{l}$. Having zero-dispersion undulator-chicane modules makes the slippage length energy independent (see equation 6.4). Using zero-dispersion undulator-chicane modules is prohibitive to the development of electron microbunching, reducing the radiation intensity.

Now, the modes of figure 6.5 can also be generated by using a short undulator (U), a dispersion only chicane (CD) and a slippage-only (isochronous) chicane (CS). For this simulation (figure 6.7) an undulator-chicane lattice was constructed from modules of U-CD-U-CS. However, each undulator has half the number of periods (10 periods) compared to the undulators used in figure 6.3. The dispersion only chicane will supply the equivalent of 130 periods of undulator dispersion. This gives a total dispersion of 150 periods per module just as in figure 6.5 and just as in figure 6.5 the slippage-only chicane generates modes separated by $\delta\omega/\omega_r = 4\pi\rho/\bar{\delta} = 0.02$

Finally, the side-band radiation modes amplified by an undulator-chicane lattice and those generated by slippage-only chicanes can be combined, as shown in figure 6.8. For this example it was necessary to double the beamlet length, to increase the energy bandwidth of the beamlets. Here, a similar undulator-chicane lattice was set-up, consisting of U-C-U-CS modules. In each module there are two 5-period undulator sections, a chicane that applies 170 periods of slippage and the equivalent of 10 periods of negative undulator dispersion. Applying a negative dispersion in the chicane will increase the radiation mode visibility, as was shown in figure 6.6. The slippage-only chicane will supply 20 periods of slippage to the radiation field. Therefore the undulator-chicane lattice will amplify side-band radiation modes separated by $\Delta\omega/\omega_r = 0.005$ and the slippage-only chicane will generate radiation modes with a separation of $\delta\omega/\omega_r = 0.05$. There is a significant difference in the mode separation for the two cases, this was done to highlight the different mode types in figure 6.8. This simulation was also performed with a single 'cold' electron pulse and produced these two distinct type of side-band radiation modes (not shown), and is worthy of further investigation.

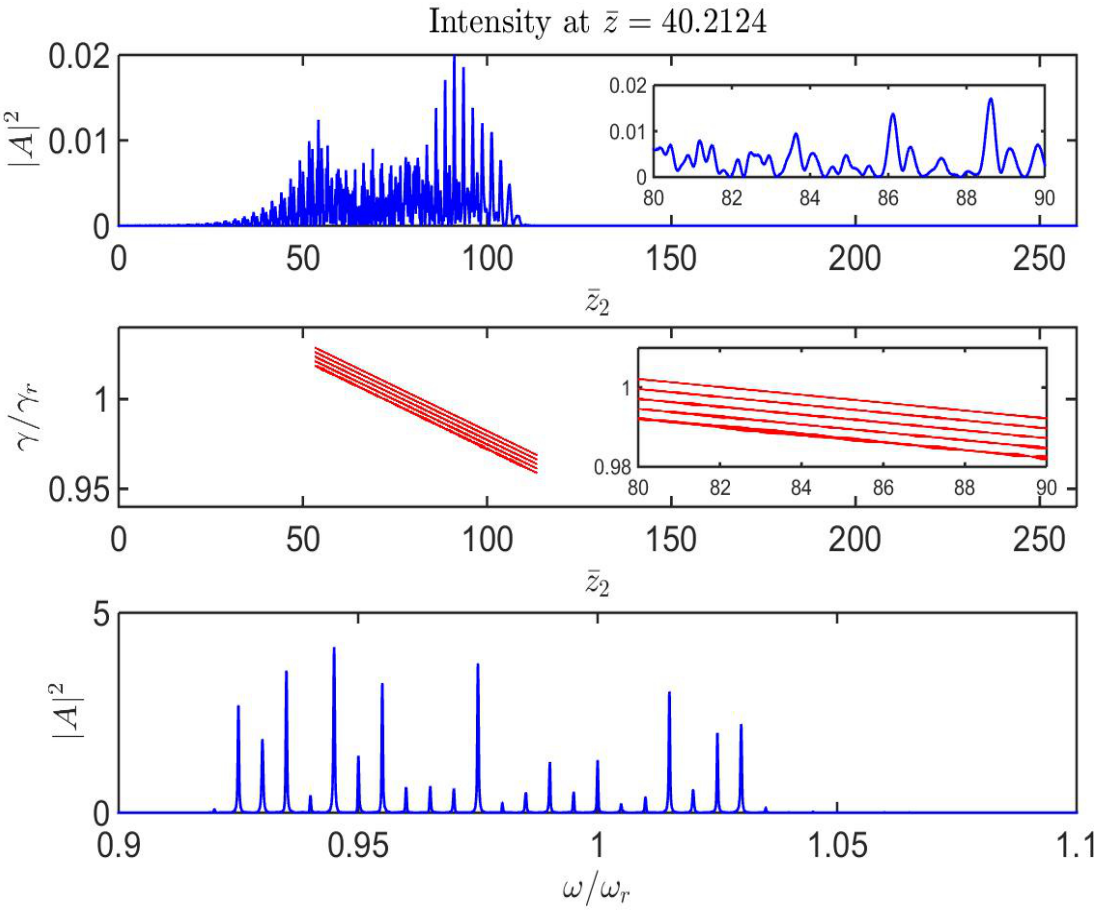

Figure 6.6: The side-band radiation modes that where destroyed in figure 6.5, can be restored by using chicanes that apply negative dispersion. The magnitude of dispersion applied is equal to the amount dispersion experienced in the preceding undulator section. Therefore in each undulator-chicane module there is effectively zero dispersion electron dispersion. In this simulation $\bar{l} = 1.885, \bar{\delta} = 0.6283$. Note the reduced radiation intensities, which is due to the negative dispersion chicanes hindering the formation of microbunches. However, the side-band radiation mode visibility has improved as zero dispersion undulator-chicane modules are being used.

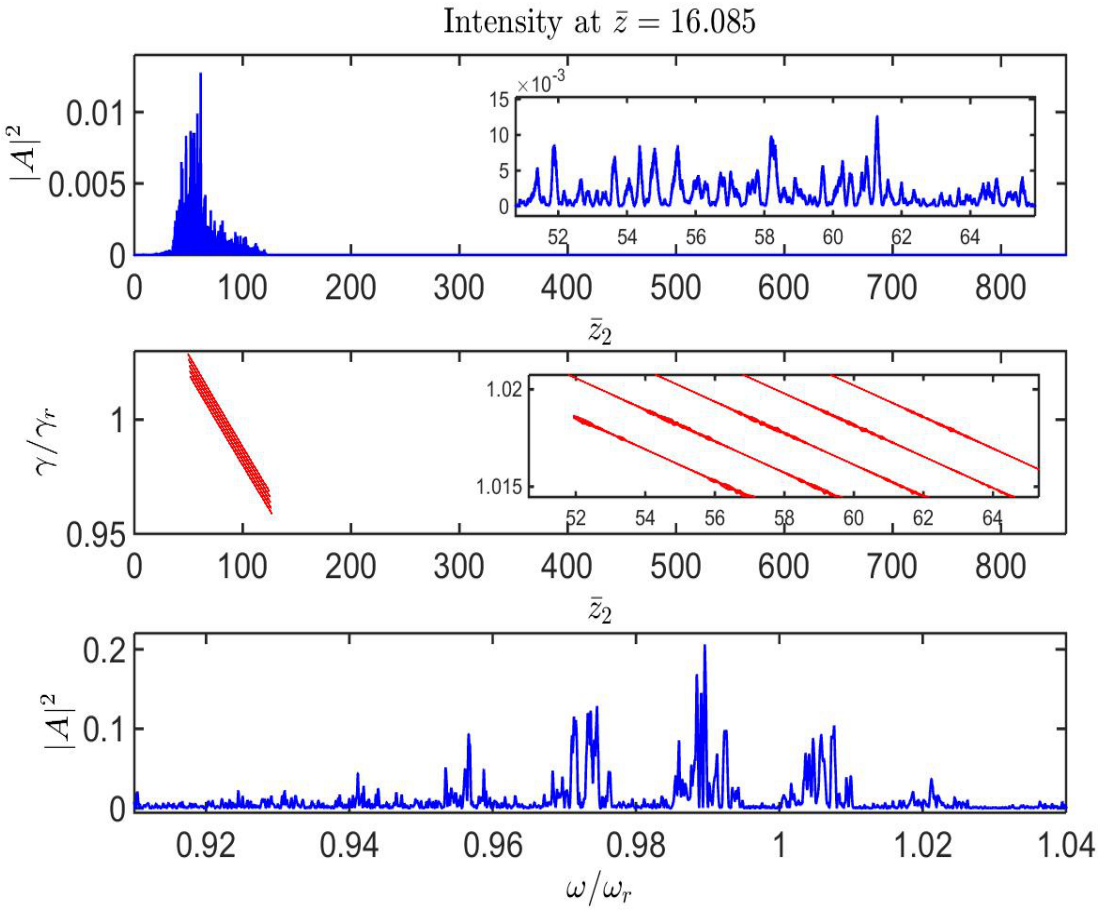

Figure 6.7: The slippage-only chicane side-band radiation modes shown in figure 6.5 can generated using a unique undulator-chicane lattice. This was done to demonstrate the slippage-only chicane modes are due solely to the interplay of slippage-only chicanes and undulators. The lattice was constructed from dispersion only chicanes (CD), slippage-only chicanes (CS), and undulator sections(U). The lattice is constructed from blocks of U-CD-U-CS arranged in series. The following lattice paramers were used; for the undulators $\bar{l} = 0.1257$ (10 periods), in the dispersion only chicane (CD) the equivalent of $\bar{\delta} = 1.6336$ (130 periods) of dispersion is applied and in the slippage-only chicane (CS) a slippage of $\bar{\delta} = 0.6283$ (50 periods) is used. Therefore the dispersion is the same per module as it is in figure 6.5. As in figure 6.5 the slippage-only chicane generates modes given by $\delta\omega/\omega_r = 4\pi\rho/\bar{\delta} = 0.02$.

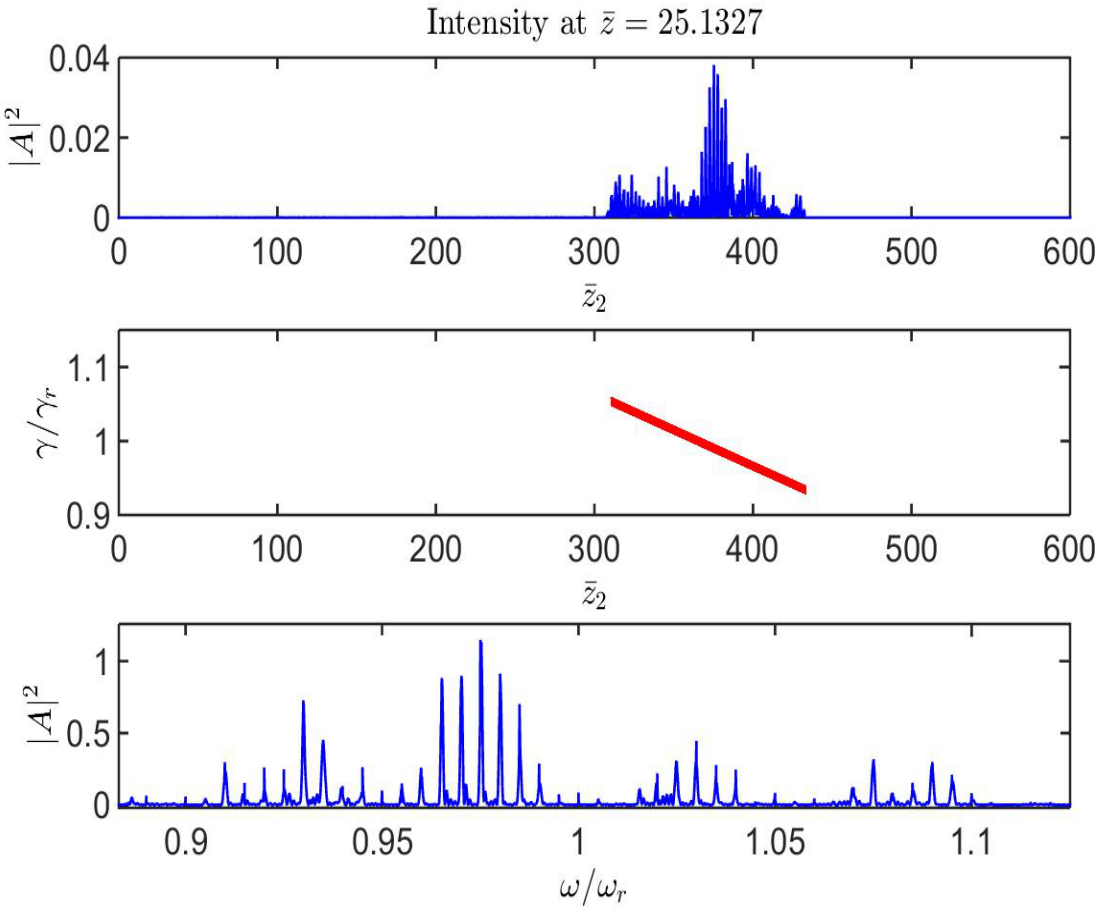

Figure 6.8: The side-band radiation modes generated by slippage-only chicanes and by an undulator-chicane lattice can be combined, i.e., those shown in figures 6.5 and 6.6. In this simulation the electron pulse is doubled in length to accommodate more side-band radiation modes. Here, a similar undulator-chicane lattice was set-up, consisting of U-C-U-CS modules. In each module there are two 5-period undulator sections, a chicane that applies 170 periods of slippage and the equivalent of 10 periods of negative undulator dispersion. Applying a negative dispersion in the chicane will increase the radiation mode visibility, as was shown in figure 6.6. The slippage-only chicane will supply 20 periods of slippage to the radiation field. Therefore the undulator-chicane lattice will amplify side-band radiation modes separated by $\Delta\omega/\omega_r = 0.005$ and slippage-only chicane will generate radiation modes with a separation of $\delta\omega/\omega_r = 0.05$.

6.2 Real Beamlets

A method to generate beamlets from a single electron pulse is now presented. This method is aimed at electron pulses with large energy spreads. More importantly when the electron pulse's energy spread is greater than the FEL bandwidth, $\sigma_\gamma \geq 2\rho\gamma_r$. The beamlet method follows the beam-by-design approach [17]; first the electron pulse receives a large energy modulation in a seed-undulator (modulator), then the electron pulse is dispersed in a chicane. The resulting phase-space structure (figure 6.9) now contains a series of beamlets with reduced local 'slice' energy spreads. For optimum performance the beamlets slice energy spread should be reduced and the slice FEL parameter ρ_b maximised. For useful FEL gain the beamlet 'slice' energy spread should satisfy $\sigma_{\gamma b} < \rho_b\gamma_r$. Now, using an undulator-chicane lattice radiation can be passed between adjacent beamlet sections of the same energy to sustain the FEL interaction.

6.2.1 The Model

The electron pulse is first modulated in a seeded-undulator (modulator) and then dispersed in a chicane section. These transformations can be approximated by the following point-transforms,

$$\gamma = \gamma^0 - \Delta\gamma \sin\left(\frac{\bar{z}_2^0}{2\rho n} + \phi\right) \tag{6.5}$$

$$\bar{z}_2 = \bar{z}_2^0 - 2D\left(\frac{\gamma - \gamma_r}{\gamma_r}\right) \tag{6.6}$$

where $n = \lambda_1/\lambda_r$ is the ratio of the modulation λ_1 and resonant λ_r wavelengths. γ^0 and $\bar{z}_2^0$ are the initial energy and position coordinates. $\Delta\gamma$ is the modulation amplitude and $D = k_r\rho R_{56}$ is the chicane dispersive strength.

In simulations it has been observed for regimes with extreme electron dispersion that the noise statistics in the electron beam can become incorrect. This is due to the fact that, the electron beam has different sampling requirements before and after dispersion which can generate non-physical CSE. The

sampling in the p_2 dimension is translated into a sampling in the $\bar{z}_2$ dimension. Puffin's macroparticle model, for most realistic cases, requires a larger number of macroparticles in the temporal dimension $\bar{z}_2$ than the energy dimension p_2. The macroparticles are generated on a grid, however as the sampling requirements are greater in $\bar{z}_2$ than in p_2 the electron phase space takes the appearance of electron rows separated in energy. This is a physically, and statistically, correct description of the electron pulse. However, when the electron pulse is subject to a large energy modulation and dispersion the rows of electrons are converted to columns of electrons, each of which is a current source producing unphysical CSE.

To overcome this and reduce computational time a functional form of the beamlet phase space is derived. By using a functional form of the beamlet phase space the electron pulse can be correctly sampled after the energy modulation and dispersion transformations have been performed. An initial normalised electron distribution is assumed,

$$f(\bar{z}_2, \gamma) = \frac{1}{2\pi\sigma_\gamma\sigma_{\bar{z}_2}} \exp\left[\frac{-(\gamma-\gamma_r)^2}{2\sigma_\gamma^2}\right] \exp\left[\frac{-(\bar{z}_2-\bar{z}_c)^2}{2\sigma_{\bar{z}_2}^2}\right] \tag{6.7}$$

in the above distribution $\bar{z}_c$ is the electron pulse centre, $\sigma_{\gamma,\bar{z}_2}$ is the standard deviation in γ and $\bar{z}_2$ respectively. By making similar substitutions to those outlined in [13], a final distribution function is arrived at,

$$f(\bar{z}_2, \gamma) = \frac{1}{2\pi\sigma_\gamma\sigma_{\bar{z}_2}} \exp\left[\frac{-1}{2\sigma_\gamma^2}\left(\gamma + \Delta\gamma \sin\left[\frac{1}{2\rho n}\left(\bar{z}_2 \ +2D\left(\frac{\gamma-\gamma_r}{\gamma_r}\right)\right)+\phi\right]-\gamma_r\right)^2\right] \exp\left[\frac{-1}{2\sigma_{\bar{z}_2}^2}\left(\bar{z}_2 + 2D\left(\frac{\gamma-\gamma_r}{\gamma_r}\right) - \bar{z}_c\right)^2\right]. \tag{6.8}$$

Upon exiting the chicane the electron pulse has a unique phase-space structure, which is shown in figure 6.9. In figure 6.9 equation 6.8 is plotted, where the false colour represents normalised electron density. The electron pulse is now composed of a number of beamlets with a reduced energy slice energy spread.

The beamlet's reduced energy spread is now within the FEL bandwidth, .i.e., $\sigma_\gamma < 2\rho_b\gamma_r$. However, the beamlet's slice FEL parameter ρ_b is reduced, which increases the FEL gain length. In figure 6.10 the beamlet slice energy spread σ_{p_b} and slice FEL parameter ρ_b are plotted at the beamlet head and the beamlet centre for the beamlets delineated by the white dashed lines. The beamlet slice FEL parameter is calculated as $\rho_b = \frac{1}{\gamma_r}\left(\frac{a_u\omega_{pb}}{4ck_u}\right)^{2/3}$ where $\omega_{pb} = \left(\frac{e^2 n_{pb}}{\epsilon_0 m}\right)^{1/2}$ and n_{pb} is beamlet slice number density. σ_{p_b} and ρ_b are calculated between the dashed white lines. So called 'single' beamlets are generated at the head (and tail) of the beamlets. At the beamlets centre these single beamlets split into the double beamlets. This can be seen in figure 6.10 where ρ_b and σ_{p_b} are calculated at the beamlet head and centre. The beamlet 'slice' energy spread is $\sigma_{p_b} < 1$ at the beamlet head (and tail) and centre. However, the beamlet ρ_b has also been reduced, this reduction is greater at the centre as only one of the double beamlets is examined. At the beamlet centre the energy separation of the beamlets is not constant and the condition $\Delta\gamma \geq 2\rho_b\gamma_r$ is not always satisfied. However, at the beamlet head and tail the beamlets' energy separation is approximately constant and meets the requirement $\Delta\gamma \geq 2\rho_b\gamma_r$ therefore the FEL gain should be greater at the beamlet heads and tails.

After the modulator-chicane section the beamlets are propagated through an undulator-chicane lattice. This allows radiation to be passed from beamlet to beamlet sustaining the FEL interaction throughout the electron pulse. The slippage in a undulator-chicane module is equal to the energy modulation wavelength, $\lambda_1 = 2\pi/k_1$. In doing so radiation is passed between beamlet sections of the same energy.

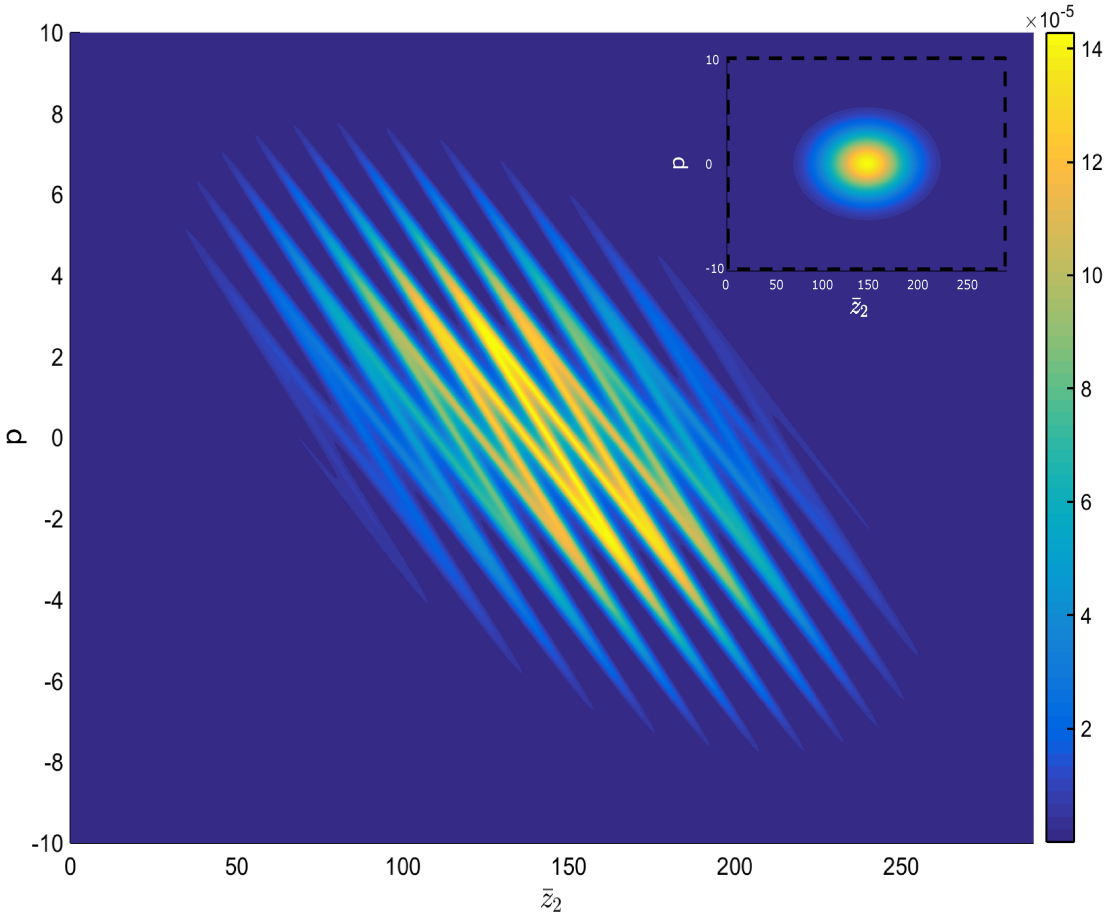

Figure 6.9: An example of the beamlet method shown here by plotting equation 6.8, the false colour indicates normalised electron density. An electron pulse (see inset), with a large energy spread, is energy modulated ($\Delta\gamma = 0.04\gamma_r$) and dispersed ($D = 268.51$) by applying transforms 6.5 and 6.6. This results in the formation of beamlets, that have a reduced local energy spread. Now, radiation can then be passed from beamlet to beamlet sustaining the FEL interaction. The electron pulse has a Gaussian current distribution and Gaussian energy distribution. The macroparticle model of Puffin eliminates marcoparticles whose weight is below a certain threshold, as such the particles at the corners of the pulse (in phase space) have the lowest weight and are eliminated. This leaves the outer beamlets less dense and less able to contribute to the FEL interaction. The initial electron pulse distribution function is shown in the inset.

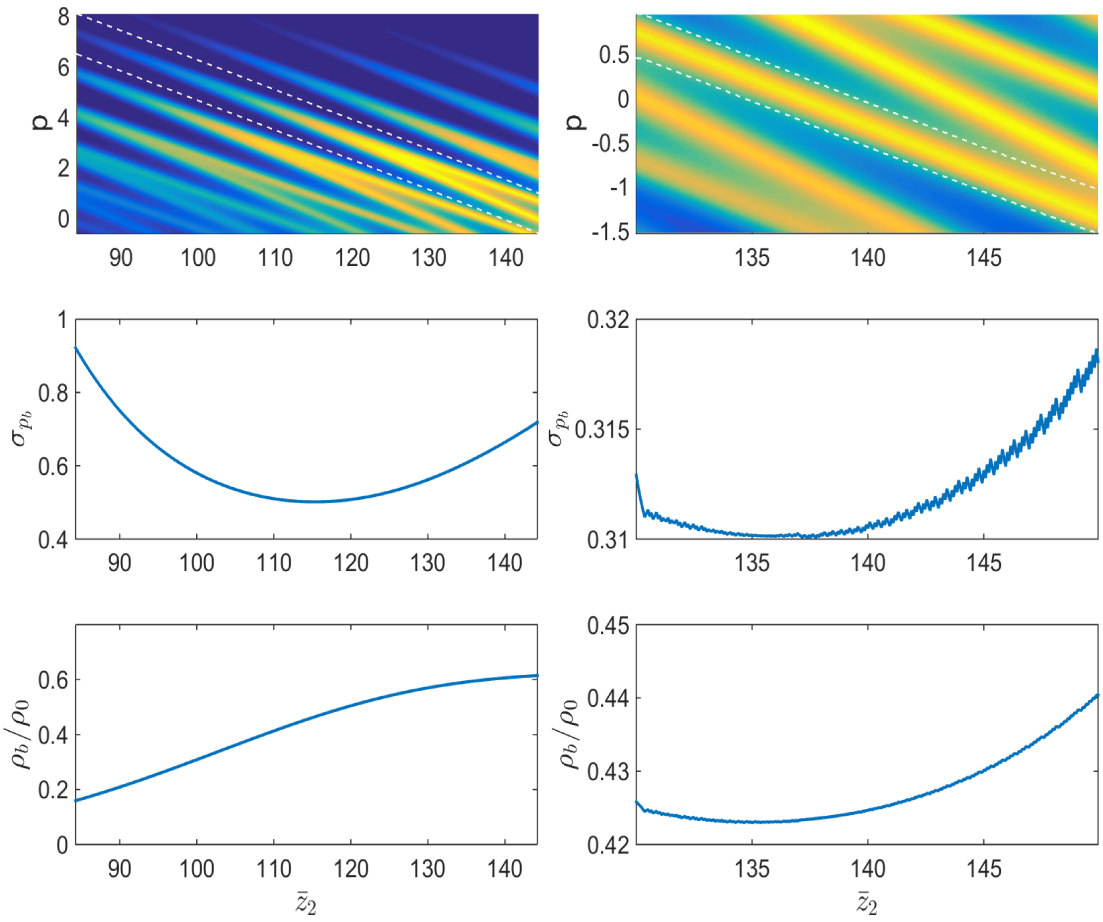

Figure 6.10: Comparison of the beamlet slice ρ_b and energy spread σ_{p_b} at the beamlet head and centre. ρ_b and σ_{p_b} are calculated for the beamlets delineated by white dashed lines in each case. In both cases the condition on the beamlet energy spread is satisfied $\sigma_{p_b} < 1$. And in both cases there is a reduction in ρ_b. Near the beamlet extremities $\bar{z}_2 < 105$ the electron pulse is diffuse which increases the beamlet energy spread and decreases ρ_b. At the centre of the beamlets, where the beamlets spilt, only a single beamlet is considered. The energy spread is much less here but the energy separation of the beamlet is not constant and does always satisfy the condition $\Delta\gamma > 2\rho_b\gamma_r$. Therefore, the FEL gain at the beamlet will be diminished.

.

6.2.2 Results

1D simulations were performed in Puffin which was first modified to read in particle distribution files. Currently particle distribution files can be generated in Matlab or Python. Puffin applies noise statistics to the particle distributions. Therefore one particle distribution file can be used for many simulation runs, where having good noise statistics is important. Two particle files were generated; one using the initial electron beam distribution function (equation 6.7) and one using the beamlet distribution function given by equation 6.8. Macroparticles with low weight are eliminated by Puffin. Consequently the electron pulse's phase space is rounded, as there is a Gaussian distribution in current and energy.

For these simulations an energy spread of $\sigma_r = 2\rho\gamma_r$ was chosen with $\rho = 1.6 \times 10^{-2}$ and $\gamma_r = 1200$. The total beam charge of $Q = 1nC$ with a standard deviation of current in $\bar{z}_2$ of $\sigma_{\bar{z}_2} = 28.97$ was selected. To be consistent with other simulation parameters a scaled undulator parameter of $\bar{a}_u = 3$ was used. A modulation amplitude of $\Delta\gamma = 0.04\gamma_r$ and dispersion of $D = 268.51$ was selected with a modulation period of $\lambda_1 = 68\lambda_r$. In the undulator-chicane lattice there are 20 undulator periods ($\bar{l} = 4.02$) and 48 chicane ($\bar{\delta} = 9.65$) slippage periods per module. This gives a total of 68 slippage periods per undulator-chicane module to match the modulation period. The electron pulse's Gaussian current profile generates coherent emission at the lower frequencies. Therefore, the radiation field filtered around the resonant frequency $0.5 < \omega/\omega_r < 1.5$. Due to the electron pulse's large energy spread it cannot produce and amplify radiation to significant intensities. At $\bar{z} = 30$ in the post saturation regime, significant radiation is not present (figure 6.11). However, the beamlets simulation (at $\bar{z} = 30$) shows an approximately two-three orders of magnitude improvement, as is shown in figure 6.11-6.12. However, the radiation intensity is seen to be higher for radiation frequencies below resonance, see figure 6.11. This can by explained by considering how the 'slice' FEL parameter was calculated $\rho_b = \frac{1}{\gamma_r}\left(\frac{a_u\omega_{pb}}{4ck_u}\right)^{2/3}$. In this expression γ_r is the average energy of the entire electron pulse, therefore this does not take into account variations in the electron pulse energy. Since the electron energy varies

from $0.8\gamma_r$ to $1.2\gamma_r$ the gain length can be up to 50% larger for higher energy electrons compared to lower energy electrons. Therefore, lower energy electrons, those at the beamlet tail, should generate more radiation. As the lower energy beamlets generate more radiation the lower energy beamlet should have a higher degree of microbunching. This can be seen by comparing figures 6.13 and 6.14, where microbunching for low energy beamlet is greater than it is for high energy beamlet.

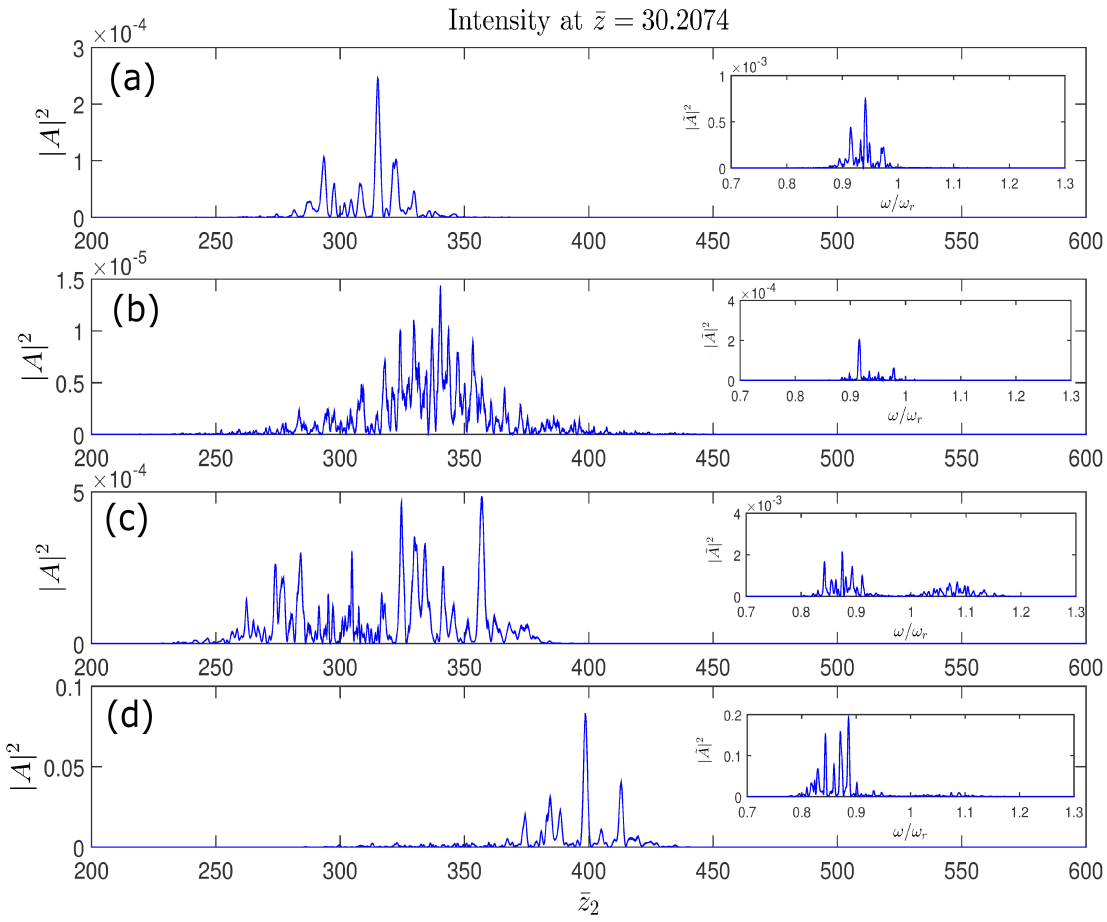

Figure 6.11: A comparison of simulations involving a unmodified beam (a-b) and beamlets (c-d), when propagated through an undulator and an undulator-chicane lattice respectively. The beamlet structure (panel c) when propagated through an undulator gives a small improvement to the output radiation over the unmodified beam (a-b). But this improvement is increased when the beamlets are propagated through an undulator-chicane lattice, shown in panel d. The improvement is seen to be greater when comparing the unmodified beam (b) and beamlets (d) propagated through the same undulator-chicane lattice. The undulator-chicane lattice amplifies side-band radiation modes separated by $\Delta\omega = 0.147$ as shown in panel d's inset. For all results shown in this figure the radiation field has been filtered around the resonant wavelength, to eliminate low frequency coherent emission, i.e. $0.5 < \omega/\omega_r < 1.5$.

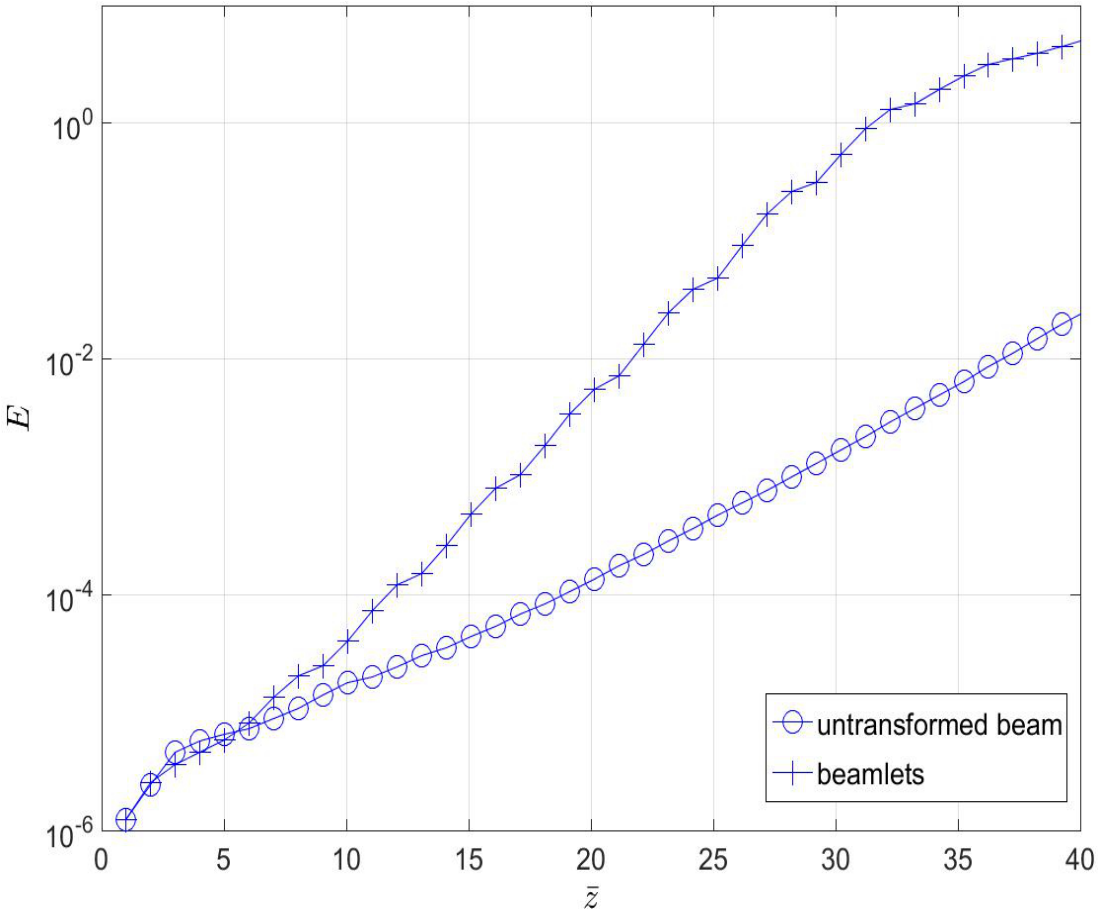

Figure 6.12: Comparison of the radiation field energy for the untransformed beam when propagated through an undulator (figure 6.11(a)) and the beamlets propagated through an undulator-chicane lattice (figure 6.11(d)) is shown here. The radiation field energy has increased by two orders of magnitude using the beamlets scheme.

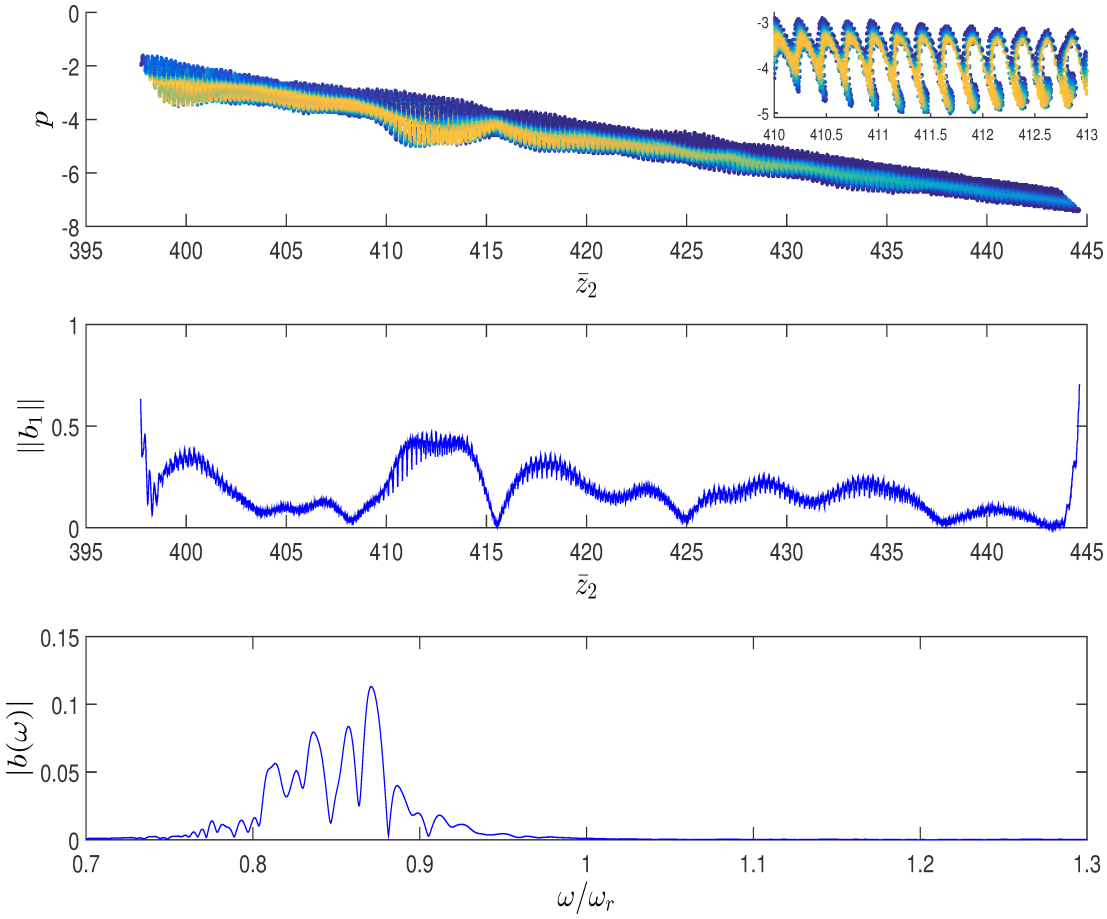

Figure 6.13: Plotted in the top panel is the electron phase-space of a lower energy beamlet section at $\bar{z} = 30$. The bunching factor calculated at the fundamental and the Fourier transform of the electron for a lower energy (tail) beamlet. The instantaneous bunching factor for the resonant (fundamental) frequency is shown in the middle panel indicating strong bunching for this beamlet. The Fourier transform of the electrons, shown in the bottom panel, contains side-band bunching modes as expected. These side-band modes become clearer when taking the Fourier transform of the full electron pulse. The electron microbunching is larger for the lower energy beamlets. And this microbunching occurs at below the resonant frequency.

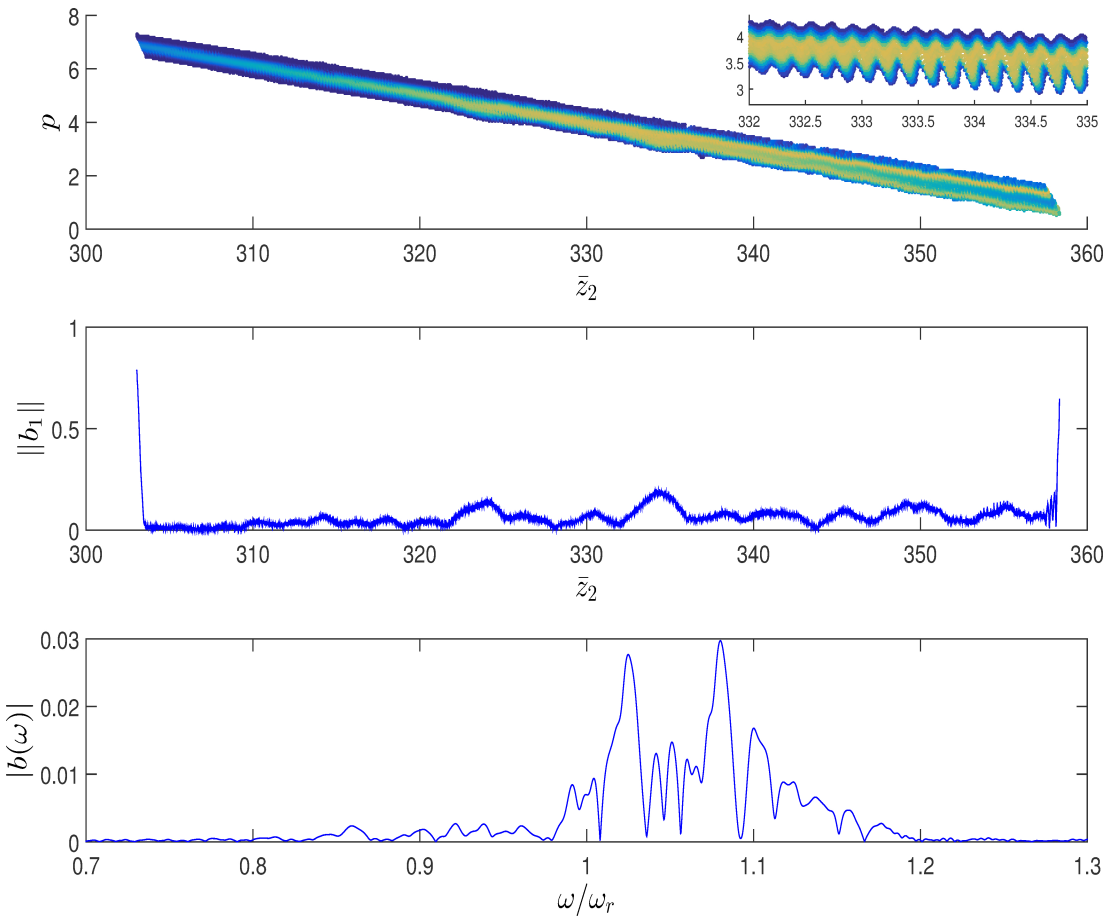

Figure 6.14: Plotted in the top panel is the electron phase-space of an upper beamlet section at $\bar{z} = 30$. The bunching factor calculated at the fundamental and the Fourier of the electron for a upper energy (head) beamlet. The Fourier transform of the electrons contains side-band bunching modes as expected. These side-band modes become clearer when taking the Fourier transform of the full electron pulse. The electron microbunching is smaller for the higher energy beamlets. The microbunching at the higher energy beamlet is generated above the resonant frequency.

Chapter 7

RF function electron beams

7.1 Rectangular electron pulses

The electron pulse's current profile can be altered to improve FEL performance using a combination of seeded-undulators and chicanes. This type of phase space manipulation of the electron pulse is typically called beam-by-design [17]. An electron pulse consisting of a series of rectangular wave forms [18] can be generated. Such an electron pulse will contain a series of current spikes. These current spikes will produce coherent emission which can amplified to saturation by propagating through a series of undulator-chicane modules. The following simulations use the same electron pulse parameters as section 6.2. Therefore the electron pulse's energy spread is prohibitive to FEL gain. The results of this chapter and section 6.2 have been submitted for publication with the arXiv draft included in the appendix.

7.1.1 The Model - Rectangular Electron Pulses

A new approach to produce so-called 'rf-function' electron beams was introduced in [18]. An rf-function generator produces simple repeated wave forms by combining many sine-waves of different frequencies much like a Fourier series. In a similar fashion an electron pulse can be created that consists of

repeated 'waveforms'.

Following the notation of [18] so-called rf-function electron pulses can be modelled in Puffin, these beams are generated in a triple modulator-chicane scheme. Of particular interest here is the case of an electron pulse containing a series of rectangular beams. In [18] a infinity long electron pulse distribution was assumed. However to model the FEL interaction in Puffin, a finite electron beam is required, therefore equation 6.7 is again used. Then, using similar substitutions to those outlined in [18] with equations 6.5 and 6.6 the final distribution function (given in appendix B.5) is arrived at.

To generate a series of rectangular wave-forms in the electron pulse the following parameters were used, $\Delta\gamma_1 = 10\sigma_\gamma, \Delta\gamma_2 = \Delta\gamma_1/4, \Delta\gamma_3 = \Delta\gamma_2/16$, $D_1 = n_1\rho\gamma_r\sqrt{3}\pi/(2\Delta\gamma_1), D_2 = -3D_1, D3 = -3D_2/4$, $n_{1,2,3} = 20$ and $\phi_2 = 0, \phi_3 = \pi$. Discontinuous regions of the rectangular wave-form will produce regions of enhanced current, current spikes. Therefore each rectangular wave-form will contain two current spikes. These current spikes will produce coherent emission [36], however the current spikes will quickly disperse. This dispersion will reduce the amount of coherent emission produced by the current spikes. By using negatively dispersed chicanes the current spike dispersion can be compensated for, allowing for sustained coherent emission throughout the undulator-chicane lattice. The slippage per undulator-chicane module is set equal to the current spike separation so that radiation is passed from current spike to current spike. This allows the coherent radiation to constructively interfere in each new undulator section.

7.1.2 Results - Rectangular Electron Pulses

Puffin was set-up in the manner described in section 6.2. A particle distribution file was first generated in Matlab, using the distribution function found in appendix B.5, and then read into Puffin.

The initial current profile of the electron pulse contains a number of spikes at half the modulation period with larger spikes at the full modulation period. These current spikes (figure 7.1) will act a series of phase correlated coherent emitters producing a train of coherent radiation spikes. Taking the Fourier

transform of this reveals a number of side-band radiation modes. The temporal separation of the radiation spikes is given by half the initial modulation period ($10 \times 4\pi\rho \approx 2$) with larger spikes present at the full modulation period ($20 \times 4\pi\rho \approx 4$).

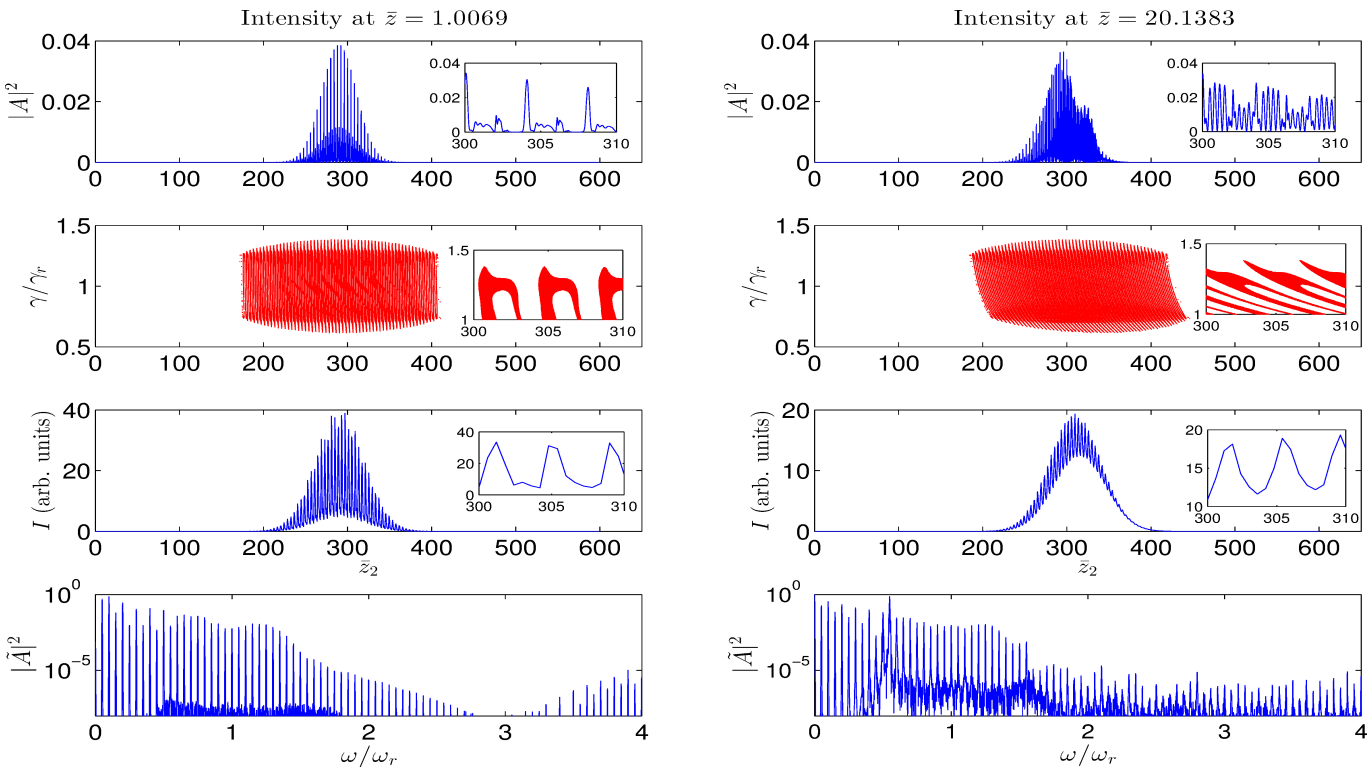

Figure 7.1: An electron pulse with an initially large energy spread has been transformed into an electron pulse that contains a number of rectangular waveforms (see the second plot on the left). The electron pulse structure now contains a train of current spikes. When this electron pulse is passed through an undulator each current spike will act a source of coherent emission. Taking the Fourier transform of this radiation reveals a number of side-band radiation modes that are separated by $\frac{\Delta\omega}{\omega_r} = 0.05$. As the electron pulse propagates along the undulator, the rectangular waveforms will disperse and reduce the current spike widths and amplitudes. As the current spikes' 'sharpness' decrease the coherent radiation produced by the current spikes will decrease. Because of this no amplification is seen when passing such an electron pulse through a long undulator, see r.h.s. of this figure.

The large energy modulation of the rectangular electron beam will cause the electron beam to disperse in the undulator (figure 7.1) which degrades the current spikes. As the current spikes lose their sharpness and decrease in amplitude the coherent emission they produce is diminished.

The electron pulse dispersion can be compensated for, using an undulator-chicane lattice where each chicane [25] has a negative dispersion. In each undulator-chicane module the total dispersion is set to zero, this is achieved by setting the dispersion part of equation 6.4 to zero i.e. $D = -\bar{l}$.

In the following simulation (figure 7.2) an undulator-chicane lattice where $l = 5\lambda_r$ and $\delta = 5\lambda_r$ was chosen to match the separation of the current spikes. Therefore, coherent radiation is passed from current spike to current spike, this allows the coherent radiation fields to constructively interfere. In this lattice the electron pulse will disperse for 5 undulator periods and then this dispersion will be partly reversed by the chicane. Equation 6.4 is only valid for small energy deviations therefore a large energy modulation's dispersion cannot be fully reversed.

In figure 7.2 the effect of using a negative dispersion chicane is shown. After each chicane section the electron current profile is 'effectively reset', therefore these large current spikes can emit more coherent radiation in each new undulator section.

In this simulation each new undulator section simply generates a new coherent radiation field which constructively interferes with the coherent radiation field of the previous undulator section. To produce a coherent radiation field only one undulator period is required, therefore the number of undulator periods per undulator module can be reduced without reducing the output radiation power. Hence, for a smaller number of undulator periods a larger radiation field can be generated (figure 7.3).

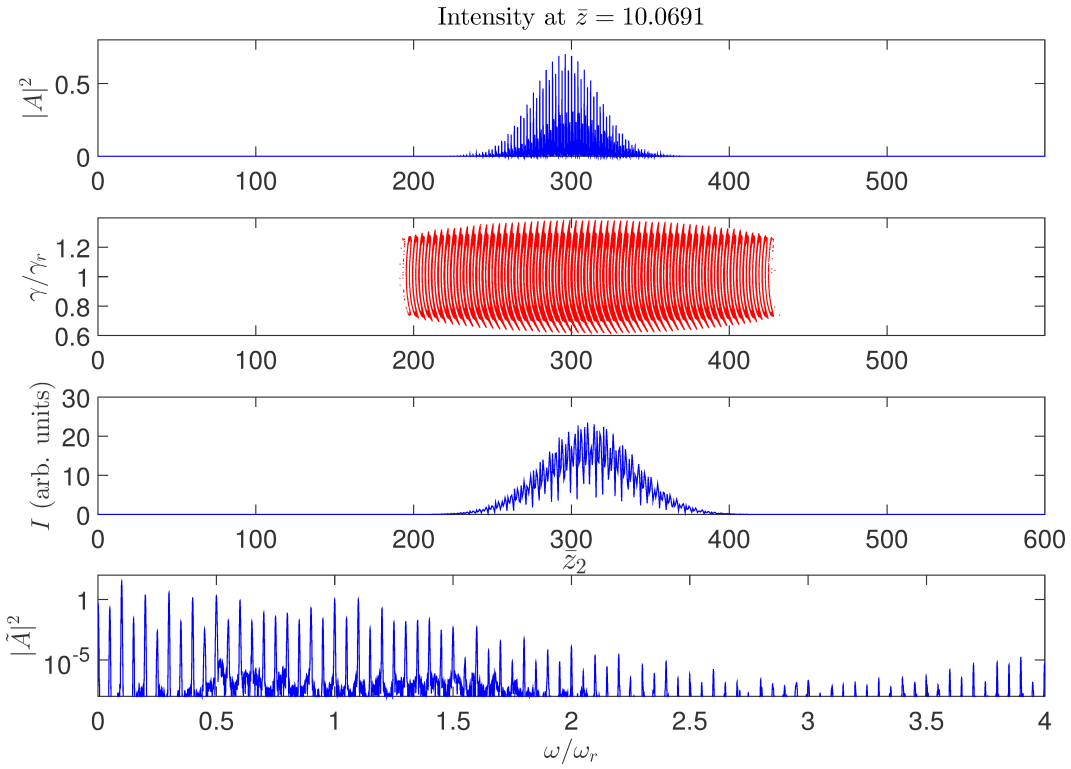

Figure 7.2: By using negatively dispersed chicane sections the undulator dispersion of the rectangular sections of the electron beam can be compensated for. In doing so the electron pulse can continue to emit coherent emission in each new undulator section. Therefore, the radiation field can be amplified to saturation. In this simulation an undulator-chicane lattice is used, where each undulator section has 5 periods and the chicane slippage is 5 resonant periods, to match the current spike separation. However, the chicane applies the equivalent of 5 periods of negative undulator dispersion to counteract the undulator dispersion, i.e., the undulator-chicane modules are dispersionless. This allows the rectangular electron pulses to emit more coherent radiation in each new undulator section. Hence, coherent radiation fields are added, constructively interfered, in each new undulator section until saturation is achieved.

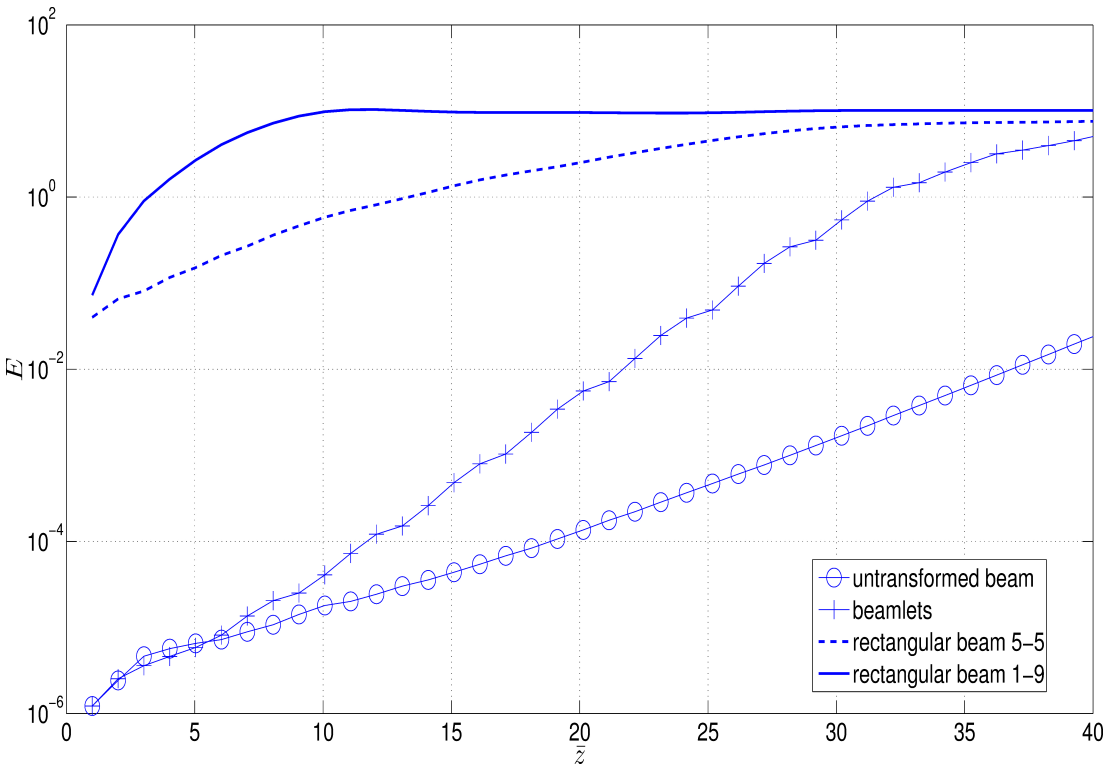

Figure 7.3: A comparison of the total radiation field energy of beamlet, rectangular beams and original beam simulations is given above. The radiation is filtered around the resonant frequency, $0.5 < \omega/\omega_r < 1.5$. Around 2 orders of magnitude improvement has been achieved for beamlets at $\bar{z} = 30$ and about 5-6 orders of magnitude improvement is shown for rectangular beams at $\bar{z} = 10$. Small to no FEL gain is seen for the rectangular beam scheme, and this is due to the prohibitively large energy spread of the electron beam. The numbers listed in the legend refer to the number of undulator periods and chicane slippage period respectively for the rectangular beams case. For example rectangular beams 5-5 refers to a lattice with 5 undulator period and 5 chicane slippage periods per module. The unmodified and beamlet plots are based on the simulations of the previous section. For the unmodified beam case propagating the electron beam through a simple undulator lattice is shown. For the beamlets case the propagation of the beamlets through an undulator-chicane lattice is displayed. To reduce memory requirements of these simulations Puffin was set to produce output data at the end of every undulator-chicane module. Each undulator-chicane module has a length of 1 in $\bar{z}$, therefore no data was written out before $\bar{z} = 1$.

In figure 7.3 a comparison is made of the radiation field's total energy for the simulations of section 6.2 (normal beam and beamlets) and the rectangular beam scheme. In all the simulations shown in figure 7.3, the same initial electron beam parameters have been used. Two rectangular beam simulations are shown in figure 7.3 using two different undulator-chicane lattices; (1) 5 undulator periods and 5 chicane slippage periods, (2) 1 undulator period and 9 chicane slippage periods. In both these simulations the undulator-chicane modules have a total dispersion of zero, i.e. $D = -\bar{l}$. Case (2) which has 1 undulator period per undulator module shows more gain per unit $\bar{z}$. After one undulator period the electron pulse's current distribution is reset in the chicane, allowing coherent emission to be produced again in the next undulator period/section. The scaled coordinate $\bar{z}$ does not take into account the chicane slippage length. Figure 7.3 shows that an improvement of 6 orders magnitude can be achieved with the new rectangular beam scheme when using the single period undulator modules (however impractical) lattice.

The radiation power [1] can be approximated by considering the superposition of multiple coherent radiation fields, the total radiation power is given by,

$$P_{rad} \propto \sum_{i}^{n} A_i^2 = (\sum_{i}^{n} A_{i=j})^2 + 2 \sum_{\substack{i \neq j \\ i,j}}^{n} A_i A_j \tag{7.1}$$

where n is the number of superposition, which in this case is the number of undulator modules. If there is no phase correlation between radiation fields, the cross term $2 \sum_{\substack{i \neq j \\ i,j}}^{n} A_i A_j$ is zero, and the total radiation power would be nA_0^2 assuming $A_0 = A_i$. However, if the radiation fields are fully phase correlated then the total radiation power should scale as $n^2 A_0^2$. In the rectangular beam system with negative chicanes, if radiation fields generated in each undulator are phase correlated the total radiation power should scale as $n^2 A_0^2$. However, if the radiation fields are not phase correlated then the radiation power should scale nA_0^2. This brings up an important point about the chicanes. The electron pulse's undulator dispersion is proportional to p_2 (see equation 3.4). However, the chicanes disperse in γ, and the electron change in position is given by $\Delta \bar{z}_2 = 2 \left(\frac{\gamma_r - \gamma_j}{\gamma_r} \right) D + \bar{\delta}$. Therefore the electron pulse's current structure can't

not be fully restored by the negatively dispersed chicane. Because of this the radiation pulse that is generated in each undulator section is significantly different (uncorrelated in phase) such that the radiation power will scale as $n|A_0|^2$, where n is the number of undulator modules. However, if the chicane could disperse in p_2, i.e. the electron change in position is given by $\Delta\bar{z}_2 = (1 - p_{2j})\, D + \bar{\delta}$, see appendix B.4 for more detail, then the current profile can fully restored. By fully restoring the current spikes, the emitted radiation fields can interfere coherently and the radiation power will scale as square of the undulator-module number, $n^2|A_0|^2$, as demonstrated in figure 7.4.

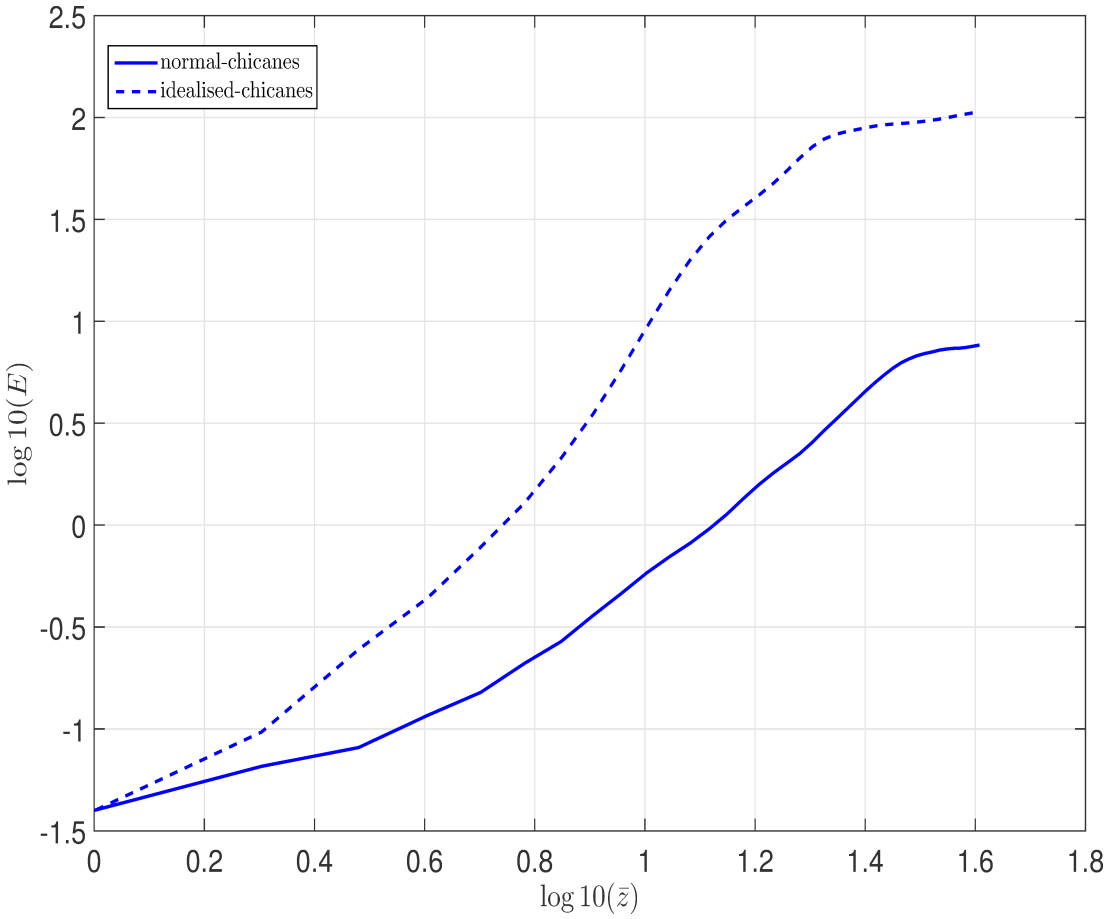

Figure 7.4: A comparison of idealised p_2 and normal γ dispersive chicane. Here, $\log 10(E)$ is plotted against $\log 10(\bar{z})$, therefore gradient of this plot is radiation power scaling factor, i.e. $|A_0|^2 n^m$ where m is the gradient. Here, a transition is observed from a system where the radiation energy scales as the number of undulator-chicane modules $n|A_0|^2$ to one that scales as the square of the number of modules $n^2|A_0|^2$, i.e. the gradient changes from 1 to 2.

The triple modulator-chicane scheme can be simplified to a double modulator-chicane scheme with the following parameters; $\Delta\gamma_1 = 10\sigma_\gamma, \Delta\gamma_2 = \Delta\gamma_1/4$, $D_1 = n_1\rho\gamma_r\sqrt{3}\pi/(2\Delta\gamma_1), D_2 = -D_1$ $n_{1,2} = 20$ and $\phi_2 = 0$. This scheme generates a similar (figure 7.5) rectangular beam profile and does not greatly reduce the radiation field intensity when compared to figure 7.2.

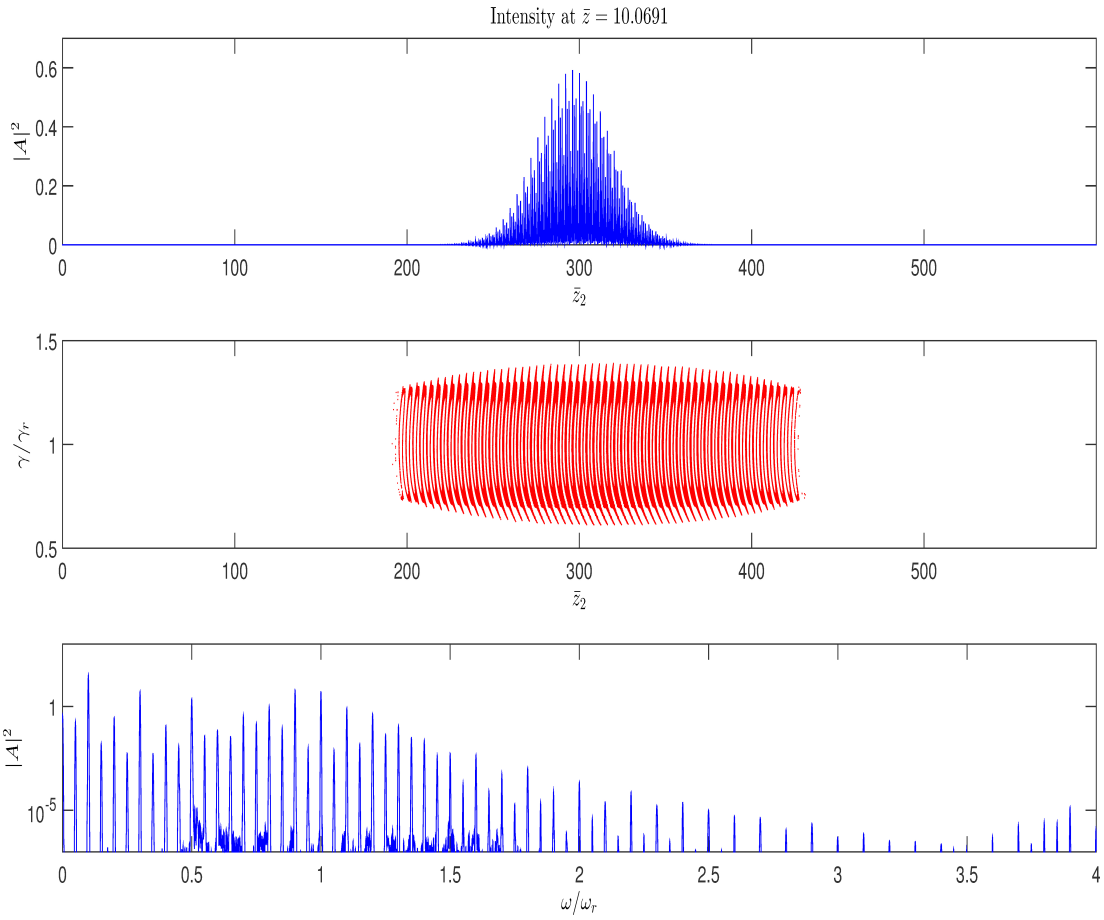

Figure 7.5: A simplified two-stage scheme can produce similar results to the three-stage scheme, shown in figure 7.2. Here, the dispersive strength factor of the second chicane is the negative of the first chicane.

Puffin along with all classical FEL codes, does not simulate spontaneous emission correctly. When spontaneous emission is generated the electrons do not lose the equivalent energy. This limitation may be overcome with a fully quantum description [38] of the FEL process. Part of the issue is believed to be related to momentum recoil i.e., each spontaneously emitted photon must carry away momentum from the electron. This can only be understood in quantum context as there is no physically correct classical description. In the SASE regime this momentum loss by the electrons may be insignificant. For example the FERMI@Elettra [39] FEL operates at $1.2GeV$ and produces resonant radiation at $10nm$. $10nm$ is equivalent to $124eV$ and is approximately 6 orders of magnitude less than the electron energy. However, it is not known that this will be the case for coherent spontaneous emission where the initial radiation field intensity is significantly higher. And, this may prove a limitation of this rectangular beam scheme. Furthermore, the propagation of such an 'exotic' beam structure through undulators and chicanes is not well understood.

Chapter 8

Conclusions and Future Work

Upgrades to the 3D FEL simulation code Puffin have been implemented. Puffin is now able to simulate the Free Electron Laser interaction in the presence of 3D undulator magnetic field. Two 3D undulator magnetic fields are now implemented in Puffin which both have off-axis magnetic field terms, these off-axis terms produce a natural focusing force in either one or both transverse directions. By implementing the 3D undulator the previously applied artificial focusing channel was removed.

Detailed analysis of the Echo Enabled Harmonic Generation scheme, in the absence of boundary conditions, revealed modal structure in the longitudinal density modulation, in the microbunching, of the electron pulse. By matching this bunching profile to amplification profile of an undulator-chicane lattice, mode-locking can be achieved.

The interaction of multiple of short electron pulse has been studied. When sufficiently separated in energy, each electron pulse (beamlet) will generate radiation at its own resonant frequency. The interference of these frequencies results in a series of temporal radiation spikes. The separation of these temporal spikes can be manipulated using isochronous chicanes. Changes to the temporal separation of the radiation spikes produce a similar change in the frequency separation of the radiation modes. By using isochronous chicane packets of radiation modes can be produced which are equispaced in the frequency domain. Furthermore, the manipulation of the beamlets in a

chicane, can force the beamlets to emit a single radiation spike in a radiator undulator. Here, the radiation spike temporal separation is increased which decreases the mode frequency separation. However, an interesting possibility exists of using positive dispersion to decrease temporal separation of the radiation spikes, which would increase the frequency separation. This could possibly be achieved by using longer beamlets and seed lasers to pre bunch the beamlets. In doing so, it may possible, by increasing frequency separation of the radiation modes, to generate x-ray radiation from beamlets that are resonant in uv or gamma-ray radiation from x-ray radiation.

With a view to operating the Free Electron Laser with a large energy spread electron pulse. The interaction of multiple chirped beamlets was then investigated. This revealed the importance of electron energy variation in mode-locking schemes. As such, a new expression for the slippage length in undulator-chicane module was derived. This new slippage length is dependent on electron energy, however this dependence can be eliminated by using negative dispersion chicanes. The importance of negative dispersion chicanes was demonstrated and has proved useful in later work.

A series of chirped beamlets can be generated from an electron pulse with a large energy spread, using a seeded-undulator and chicane. These beamlets when propagated through an undulator-chicane lattice produce radiation powers that are 2-3 orders greater than the radiation power produced by the initial untransformed electron pulse.

Taking advantage of the current spikes present in a series of rectangular beams can significantly (4-6 orders of magnitude) increase the FEL's output radiation power, for electron beams with large energy spreads. Here, negative dispersion chicanes were used to reset the electron pulse current profile after each undulator module. This allows the coherent emission to be emitted in each new undulator module and superimpose to produce a large radiation field. Although chapter 7 focused on rf-function beams for so called 'dirty' electron beams (with large energy spread) such a scheme may have uses for normal 'FEL optimised' electron beams. The next step is simulate the rf-function beams with more realistic electron pulses. For example the electron pulse generated by a plasma accelerator. The intriguing possibility of produc-

ing an rf-function electron pulse in cross-planar two colour undulator should be investigated. The rf-function technique is capable of generating a variety interesting pulse shapes in the electron phase space, such as triangular, saw-tooth etc. and should be investigated using Puffin. It may also possible to produce such an rf-function electron pulse in single planar undulator. This maybe possible by injecting multiple seed lasers at the harmonics of the resonant frequency as in Fourier series.

Bibliography

[1] B. W. J. M^{c}Neil and N. R. Thompson. X-ray Free-Electron Lasers. *Nature Photonics*, 4:814-821, 2010.

[2] C. Pellegrini. The History of X-ray Free-Electron Lasers. *Eur. Phys. J. H.*, 37:659-708, 2012.

[3] J. M. J. Madey. Stimulated Emission of Bremsstrahlung in a Periodic Magnetic Field . *J. Appl. Phys.* 42:1906-1931, 1971.

[4] D. A. G. Deacon *et al.* First Operation of a Free Electron Laser. *Phys. Rev. Let.*, 38:892-894, 1977.

[5] B. M^{c}Neil. A down-sized design. *Nature Photonics*, 2:522-524, 2008.

[6] Z. Huang and K.-J. Kim. Review of X-ray Free-Electron Laser Theory. *Phys. Rev. ST-AB* 10, 034801, 2007.

[7] J. Andruszkow *et al.* First Observation of Self-Amplified Spontaneous Emission in a Free-Electron Laser at 109 nm Wavelength. *Phys. Rev. Let.*, 85:3825, 2000.

[8] R. Bonifacio C. Pellegrini and L. Narducci. Collective instabilities and high-gain regime in a free electron laser. *Opt. Commun.* 50:373-378, 1984.

[9] B. W. J. M^{c}Neil, M. W. Poole, and G. R. M. Robb. Unified Model of Electron Beam Shot Noise and Coherent Spontaneous Emission in the Helical Wiggler Free Electron Laser. *Phys. Rev. ST-Accel. Beams*, 6:070701, 2003.

[10] B. W .J. McNeil, G. R. M. Robb and D. A. Jaroszynski. Self-Amplification of Coherent Spontaneous Emission in the Free Electron Laser. *Opt. Commun.*, 165:65-70, 1999.

[11] L. T. Campbell, and B. W. J. McNeil. Puffin: A Three Dimensional, Unaveraged Free Electron Laser Simulation Code. *Physics of Plasmas*, 19:093119, 2012.

[12] J. R. Henderson, L. T. Campbell, A. R. Maier, and B. W. J. McNeil. The Implementation of 3D Undulator Fields in the Unaveraged FEL Simulation Code Puffin. *Proceedings of FEL 2014, Basel, Switzerland*, TUP022, 2014.

[13] D. Xiang and G. Stupakov. Echo-Enabled Harmonic Generation Free Electron Laser. *Phys. Rev. ST-Accel. Beams*, 12:030702, 2009.

[14] G. Stupakov. Using the Beam-Echo Effect for Generation of Short-Wavelength Radiation. *Phys. Rev. Let.*, 102:074801, 2009.

[15] J. R. Henderson and B. W. J. McNeil. Echo Enabled Harmonic Generation Free Electron Laser in a Mode-Locked Configuration. *EPL*, 100:64001, 2012.

[16] J. R. Henderson, L. T. Campbell and B. W. J. McNeil. Chirped and Modulated Electron Pulse Free Electron Laser Techniques. *Proceedings of FEL 2014, Basel, Switzerland*, MOC04, 2014.

[17] E. Hemsing, G. Stupakov, A. Zholents, and D. Xiang. Beam by design: Laser Manipulation of Electrons in Modern Accelerators. *Rev. Mod. Phys.*, 86:897-941, 2014.

[18] E. Hemsing and D. Xiang. Cascaded Modulator-Chicane Modules for Optical Manipulation of Relativistic Electron Beams. *Phys. Rev. ST-Accel. Beams* 16:010706, 2013.

[19] P. Schmuser, M. Dohlus, J. Rossbach, C. Behrens, Free-Electron Laser in the Ultraviolet and X-Ray Regime, *Springer Tracts in Modern Physics*, 229, 2008.

[20] S. Reichem. GENESIS: A Fully 3D Time-Dependant FEL Simulation Code. *Nucl. Instr. and Meth. in Phys. Res. A*, 429:243-248, 1999.

[21] E. T. Scharlemann. Wiggle Plane Focusing in Near Wigglers. *J. Appl. Phys.*, 58:2154, 1985.

[22] E. T. Scharlemann. Selected Topics In FELs. *High Gain, High Power Free Electron Laser: Physics and Application to TeV Particle Acceleration (edited by R. Bonifacio et al.)*, 95-126, 1989.

[23] R. Bonifacio, R. Corsini and P. Pierini. Theory of the High-Gain Optical Klystron. *Phys. Rev. A*, 45, 6, 1992.

[24] R. Bonifacio, L. De Salvo, P. Pierini, N. Piovella and C. Pellegrini. Spectrum, Temporal Structure, and Fluctuations in a High-Gain Free-Electron Laser Starting from Noise. *Phys. Rev. Let.*, 73:1, 1994.

[25] F. Jackson, D. Angal-Kalinin, J. K. Jones, and P. H. Williams. Longitudinal Beam Transport in the ALICE IR-FEL Facility. *Proceedings of IPAC2013, Shanghai, China*, WEPWA063, 2013.

[26] L.-H Yu, et al., High-Gain Harmonic-Generation Free-Electron Laser. *Science*, 289:932:934, 2000.

[27] A. E. Siegman. Lasers. *University Science Books, Sausalito, USA.*, chapter 27, 1986.

[28] N. R. Thompson and B. W. J. McNeil. Mode Locking in a Free-Electron Laser Amplifier. *Phys. Rev. Let.*, 100:203901, 2008.

[29] B. W. J. M^{c}Neil, N. R. Thompson, D. J. Dunning, and B. Sheehy. Retention of Attosecond Pulse Structure in an HHG Seeded FEL Amplifier. *Proceedings of FEL08, Gyeongju, Korea*, MOCAU04, 2008.

[30] B. W. J. M^{c}Neil, N. R. Thompson and D. J. Dunning. Transform-Limited X-Ray Pulse Generation from a High-Brightness Self-Amplified Spontaneous-Emission Free-Electron Laser. *Phys. Rev. Let.*, 110:134802, 2013.

[31] D. J. Dunning, B. W. J. McNeil and N. R. Thompson. Few-Cycle Pulse Generation in an X-Ray Free-Electron Laser. *Phys. Rev. Let.*, 110:104801, 2013.

[32] R. Bonifacio et al. Physics of the High-Gain FEL and Superradiance. *Rivista Del Nuovo Cimento*, 13:9, 1990.

[33] R. Bonifacio et al. New Effects in the Physics of High-Gain Free-Electron Laser; a Proposed Experiment and Possible Applications. *Rivista Del Nuovo Cimento*, 15:11, 1992.

[34] E. L. Saldin, E. A. Schneidmiller, and M. V. Yurkov. Self-Amplified Spontaneous Emission FEL with Energy-Chirped Electron Beam and its Application for Generation of Attosecond X-ray Pulses. *Phys. Rev. ST-Accel. Beams*, 9:050702, 2006.

[35] V. Petrillo et. al. Observation of Time-Domain Modulation of Free-Electron-Laser Pulses by Multipeaked Electron-Energy Spectrum. *Phys. Rev. Let.* 111:114802, 2013.

[36] B. W. J. M^{c}Neil, G. R. M. Robb, and D. A. Jaroszynski. SACSE in a FEL Amplifier with Energy Spread. *Nucl, Instr. and Meth. in Phys. Res. A* 445:72-76, 2000.

[37] B. W. J. M^{c}Neil, G. R. M. Robb, and D. A. Jaroszynski. Self-Amplification of Coherent Spontaneous Emission in the Free Electron Laser. *Opt. Commun.*, 165:65-70, 1999.

[38] R. Bonifacio, N. Piovella, G. R. M. Robb, and A. Schiavi. Quantum Regime of Free Electron Lasers Starting from Noise. *Phys. Rev. ST-Accel. Beams*, 9:090701, 2006.

[39] Fermi@Elettra conceptual design report,
http://www.elettra.trieste.it/FERMI, Elettre, 2007.

Appendix A

3D undulator derivation

In this appendix the equations governing the electron motion through the undulator are derived in a general way. The equations replace the working equations of Puffin [11], to simulate FEL interaction with various undulator types. The current Puffin electron equations assume a 1D undulator which does not satisfy Gauss's Law because the undulator field does not have a z-component. A 3D undulator field with a z-component will produce in a focusing force perpendicular to z and the electron's transverse wiggle in accordance with Lorentz force equation. The two different undulators will be considered, a plane-pole undulator (i.e. a standard planar undulator that satisfies Gauss's Law) which produces a focusing force in one transverse direction. A curved-pole (decanted poles) undulator shall also be considered as this undulator offers focusing in both transverse directions, and therefore removes the need for external focusing elements (such as quadrupoles).

A.1 Transverse electron momentum

The Lorentz force for the electron pulse is calculated in two parts first the transverse part is derived.

$$\mathbf{F}_j = \frac{d\mathbf{p}_j}{dt} = -e(\mathbf{E}_j + \frac{\mathbf{p}_j}{\gamma_j m} \times \mathbf{B}) \tag{A.1}$$

define a unit vector $\hat{\mathbf{e}} = \frac{1}{\sqrt{2}}(\hat{\mathbf{x}} + i\hat{\mathbf{y}})$ such that $\hat{\mathbf{e}} \cdot \hat{\mathbf{e}} = \hat{\mathbf{e}}^* \cdot \hat{\mathbf{e}}^* = 0$ and $\hat{\mathbf{e}} \cdot \hat{\mathbf{e}}^* = \hat{\mathbf{e}}^* \cdot \hat{\mathbf{e}} = 1$ therefore $\hat{\mathbf{x}} = \frac{1}{\sqrt{2}}(\hat{\mathbf{e}} + \hat{\mathbf{e}}^*)$ and $\hat{\mathbf{y}} = -\frac{i}{\sqrt{2}}(\hat{\mathbf{e}} - \hat{\mathbf{e}}^*)$ hence $\sqrt{2}\hat{\mathbf{e}}^* \cdot \mathbf{p} = p_x - ip_y = p_\perp$ and $\sqrt{2}\hat{\mathbf{e}} \cdot \mathbf{p} = p_x + ip_y = p^*_{\perp j}$. Similarly for the electric field $\sqrt{2}\hat{\mathbf{e}}^* \cdot \mathbf{E} = E_x - iE_y = E_\perp$ and $\sqrt{2}\hat{\mathbf{e}} \cdot \mathbf{E} = E_x + iE_y = E^*_\perp$ now take the scalar product of $\sqrt{2}\hat{\mathbf{e}}^*$ and equation A.1.

$$\sqrt{2}\hat{\mathbf{e}}^* \cdot \frac{d\mathbf{p}_j}{dt} = -e(\mathbf{E}_j + \frac{\mathbf{p}_j}{\gamma_j m} \times \mathbf{B}) \cdot \hat{\mathbf{e}}^* \sqrt{2} \tag{A.2}$$

$$\frac{dp_{\perp j}}{dt} = -e(E_\perp + \sqrt{2}\hat{\mathbf{e}}^* \cdot \left(\frac{\mathbf{p}_j}{\gamma_j m} \times \mathbf{B}\right)) \tag{A.3}$$

now look at the second part of the above equation,

$$\sqrt{2}\hat{\mathbf{e}}^* \cdot \left(\frac{\mathbf{p}_j}{\gamma_j m} \times \mathbf{B}\right) \tag{A.4}$$

using the vector identity $A \cdot (B \times C) = C \cdot (A \times B)$

$$\begin{aligned}
\sqrt{2}\hat{\mathbf{e}}^* \cdot (\mathbf{p}_j \times \mathbf{B}_j) &= \mathbf{B}_j \cdot (\sqrt{2}\hat{\mathbf{e}}^* \times \mathbf{p}_j) \\
\sqrt{2}\hat{\mathbf{e}}^* \cdot (\mathbf{p}_j \times \mathbf{B}_j) &= \mathbf{B}_j \cdot \begin{vmatrix} \hat{\mathbf{x}} & \hat{\mathbf{y}} & \hat{\mathbf{z}} \\ 1 & -i & 0 \\ p_{xj} & p_{yj} & p_{zj} \end{vmatrix} \\
\sqrt{2}\hat{\mathbf{e}}^* \cdot (\mathbf{p}_j \times \mathbf{B}_j) &= \mathbf{B}_j \cdot (\hat{\mathbf{x}}(-ip_z) - \hat{\mathbf{y}}p_z + \hat{\mathbf{z}}(p_y + ip_x))
\end{aligned} \tag{A.5}$$

using $ip_{\perp j} = p_y + ip_x$

$$\sqrt{2}\hat{\mathbf{e}}^* \cdot (\mathbf{p}_j \times \mathbf{B}_j) = \mathbf{B}_j \cdot (-ip_z\hat{\mathbf{x}} - p_z\hat{\mathbf{y}} + ip_{\perp j}\hat{\mathbf{z}}) \tag{A.6}$$

now, the magnetic field takes the form $\mathbf{B}_j = B_{xj}\hat{\mathbf{x}} + B_{yj}\hat{\mathbf{y}} + B_{zj}\hat{\mathbf{z}}$ and is inserted into the above equation to give,

$$\sqrt{2}\hat{\mathbf{e}}^* \cdot (\mathbf{p}_j \times \mathbf{B}_j) = (-ip_z B_{xj} - p_z B_{yj} + ip_{\perp j} B_{zj}) \tag{A.7}$$

the perpendicular magnetic field is given by $B_\perp = B_x - iB_y$ which is rearranged to give $iB_\perp = B_y + iB_x$

$$\sqrt{2}\hat{\mathbf{e}}^* \cdot (\mathbf{p}_j \times \mathbf{B}_j) = (-ip_z B_{\perp j} + ip_{\perp j} B_{zj}) \tag{A.8}$$

$$\sqrt{2}\hat{\mathbf{e}}^* \cdot (\mathbf{p}_j \times \mathbf{B}_j) = ip_{\perp j} B_{zj} - ip_z B_{\perp j} \tag{A.9}$$

$$\sqrt{2}\hat{\mathbf{e}}^* \cdot \left(\frac{\mathbf{p}_j}{\gamma_j m} \times \mathbf{B}\right) = \frac{1}{\gamma_j m}\left(iB_z p_{\perp j} - ip_{zj} B_{\perp j}\right) \tag{A.10}$$

recombine with equation A.3

$$\frac{dp_{\perp j}}{dt} = -e(E_\perp + \sqrt{2}\hat{\mathbf{e}}^* \cdot \left(\frac{\mathbf{p}_j}{\gamma_j m} \times \mathbf{B}\right)) \tag{A.11}$$

$$\frac{dp_{\perp j}}{dt} = -e(E_\perp + \frac{1}{\gamma_j m}\left(iB_z p_{\perp j} - ip_{zj} B_{\perp j}\right)) \tag{A.12}$$

now convert to $\bar{z}$ using $\frac{d}{dt} = 2k_u \rho c \beta_{zj} \frac{d}{d\bar{z}}$

$$\frac{dp_{\perp j}}{d\bar{z}} = \frac{-e}{2k_u \rho c \beta_{zj}}(E_\perp + \frac{1}{\gamma_j m}\left(iB_z p_{\perp j} - ip_{zj} B_{\perp j}\right)) \tag{A.13}$$

separate the perpendicular magnetic field into wiggler and radiation components $B_\perp = B_{w\perp} + B_{r\perp}$ the radiation in z is ignored as the paraxial approxi-

mation is made.

$$\frac{dp_{\perp j}}{d\bar{z}} = \frac{-e}{2k_u\rho c\beta_{zj}}(E_\perp + \frac{1}{\gamma_j m}\left(iB_z p_{\perp j} - ip_{zj}(B_{w\perp} + B_{r\perp j})\right)) \tag{A.14}$$

now $B_{r\perp j} = B_{rxj} - iB_{ryj}$ these component can be rewritten in terms of the electric field $B_{rx} \approx -E_y/c$ and $B_{ry} \approx E_x/c$ by applying Faraday's Law.

$$B_{r\perp j} = B_{rxj} - iB_{ryj} \tag{A.15}$$
$$B_{r\perp j} = -(E_{ryj} + iE_{rxj})/c \tag{A.16}$$
$$B_{r\perp j} = -i(-iE_{ryj} - i^2E_{rxj})/c \tag{A.17}$$
$$B_{r\perp j} = -i(-iE_{ryj} + E_{rxj})/c \tag{A.18}$$
$$B_{r\perp j} = -i(E_{rxj} - iE_{ryj})/c \tag{A.19}$$
$$B_{r\perp j} = -iE_\perp/c \tag{A.20}$$

were $E_\perp = E_{rxj} - iE_{ryj}$

$$\frac{dp_{\perp j}}{d\bar{z}} = \frac{-e}{2k_u\rho c\beta_{zj}}(E_\perp + \frac{1}{\gamma_j m}\left(iB_z p_{\perp j} - ip_{zj}(B_{w\perp} - iE_\perp/c)\right)) \tag{A.21}$$
$$\frac{dp_{\perp j}}{d\bar{z}} = \frac{-e}{2k_u\rho c\beta_{zj}}\left(E_\perp + \frac{1}{\gamma_j m}\left(iB_z p_{\perp j} - ip_{zj}B_{w\perp} - p_{zj}\frac{E_\perp}{c}\right)\right) \tag{A.22}$$
$$\frac{dp_{\perp j}}{d\bar{z}} = \frac{-e}{2k_u\rho}\left(\frac{E_\perp}{c\beta_{zj}} + \frac{1}{\gamma_j mc\beta_{zj}}\left(iB_z p_{\perp j} - ip_{zj}B_{w\perp} - p_{zj}\frac{E_\perp}{c}\right)\right) \tag{A.23}$$

$p_{zj} = \gamma_j mc\beta_{zj}$

$$\frac{dp_{\perp j}}{d\bar{z}} = \frac{-e}{2k_u\rho}\left(\frac{E_\perp}{c\beta_{zj}} + \frac{1}{p_{zj}}\left(iB_z p_{\perp j} - ip_{zj}B_{w\perp} - p_{zj}\frac{E_\perp}{c}\right)\right) \tag{A.24}$$

$$\frac{dp_{\perp j}}{d\bar{z}} = \frac{-e}{2k_u\rho}\left(\frac{E_\perp}{c\beta_{zj}} + \left(iB_z\frac{p_{\perp j}}{p_{zj}} - iB_{w\perp} - \frac{E_\perp}{c}\right)\right) \tag{A.25}$$

$$\frac{dp_{\perp j}}{d\bar{z}} = \frac{-e}{2k_u\rho}\left(\frac{E_\perp}{c\beta_{zj}} + iB_z\frac{p_{\perp j}}{p_{zj}} - iB_{w\perp} - \frac{\beta_{zj}}{\beta_{zj}}\frac{E_\perp}{c}\right) \tag{A.26}$$

$$\frac{dp_{\perp j}}{d\bar{z}} = \frac{-e}{2k_u\rho}\left(\frac{E_\perp}{c}\frac{1-\beta_{zj}}{\beta_{zj}} + iB_z\frac{p_{\perp j}}{p_{zj}} - iB_{w\perp}\right) \tag{A.27}$$

use $\eta p_{2j} = \frac{1-\beta_{zj}}{\beta_{zj}}$

$$\frac{dp_{\perp j}}{d\bar{z}} = \frac{-e}{2k_u\rho}\left(\frac{E_\perp}{c}\eta p_{2j} + iB_z\frac{p_{\perp j}}{p_{zj}} - iB_{w\perp}\right) \tag{A.28}$$

introduce $\bar{p}_{\perp j} = \frac{p_\perp}{mca_u} => p_{\perp j} = mca_u\bar{p}_{\perp j}$,

$$\frac{mca_u}{u}\frac{d\bar{p}_{\perp j}}{d\bar{z}} = \frac{-e}{2k_u\rho}\left(\frac{E_\perp}{c}\eta p_{2j} + i\frac{mca_u}{u}B_z\frac{\bar{p}_{\perp j}}{p_{zj}} - iB_{w\perp}\right) \tag{A.29}$$

use scaled electric field of $A_\perp = \frac{ea_u l_g}{2\gamma_r^2 mc^2\rho}E_\perp$ which rearranged gives, $E_\perp = \frac{2\gamma_r^2 mc^2\rho}{ea_u l_g}A_\perp$

$$mc\bar{a}_u\frac{d\bar{p}_{\perp j}}{d\bar{z}} = \frac{-e}{2k_u\rho}\left(\frac{2\gamma_r^2 mc\rho}{ea_u l_g}A_\perp\eta p_{2j} + imca_u B_z\frac{\bar{p}_{\perp j}}{p_{zj}} - iB_{w\perp}\right) \tag{A.30}$$

$$\frac{d\bar{p}_{\perp j}}{d\bar{z}} = \frac{1}{mc\bar{a}_u}\frac{-e}{2k_u\rho}\left(\frac{2\gamma_r^2 mc\rho}{ea_u l_g}A_\perp\eta p_{2j} + imca_u B_z\frac{\bar{p}_{\perp j}}{p_{zj}} - iB_{w\perp}\right) \tag{A.31}$$

$$\frac{d\bar{p}_{\perp j}}{d\bar{z}} = \frac{-e}{2k_u\rho}\left(\frac{2\gamma_r^2 mc\rho}{ea_u l_g}\frac{1}{mca_u}A_\perp \eta p_{2j} + iB_z\frac{\bar{p}_{\perp j}}{p_{zj}} - i\frac{1}{mca_u}B_{w\perp}\right) \tag{A.32}$$

$$\frac{d\bar{p}_{\perp j}}{d\bar{z}} = \frac{-e}{2k_u\rho}\left(\frac{2\gamma_r^2 \rho}{ea_u^2 l_g}A_\perp \eta p_{2j} + iB_z\frac{\bar{p}_{\perp j}}{p_{zj}} - i\frac{1}{mca_u}B_{w\perp}\right) \tag{A.33}$$

$$\frac{d\bar{p}_{\perp j}}{d\bar{z}} = \frac{-e}{2k_u\rho}\left(\frac{2\gamma_r^2 \rho}{ea_u^2 l_g}A_\perp \eta p_{2j} + iB_z\frac{\bar{p}_{\perp j}}{p_{zj}} - i\frac{1}{mca_u}B_{w\perp}\right) \tag{A.34}$$

$l_g = \frac{1}{2k_u\rho}$

$$\frac{d\bar{p}_{\perp j}}{d\bar{z}} = \frac{-e}{2k_u\rho}\left(\frac{2\gamma_r^2 \rho 2k_u\rho}{ea_u^2}A_\perp \eta p_{2j} + iB_z\frac{\bar{p}_{\perp j}}{p_{zj}} - i\frac{1}{mca_u}B_{w\perp}\right) \tag{A.35}$$

$$\frac{d\bar{p}_{\perp j}}{d\bar{z}} = \frac{-e}{2k_u\rho}\left(\frac{4\gamma_r^2 \rho^2 k_u}{e\bar{a}_u^2}A_\perp \eta p_{2j} + iB_z\frac{\bar{p}_{\perp j}}{p_{zj}} - i\frac{1}{mca_u}B_{w\perp}\right) \tag{A.36}$$

$$\frac{d\bar{p}_{\perp j}}{d\bar{z}} = \frac{-e}{2\rho}\left(\frac{4\gamma_r^2 \rho^2}{ea_u^2}A_\perp \eta p_{2j} + iB_z\frac{\bar{p}_{\perp j}}{p_{zj}}\frac{1}{k_u} - i\frac{1}{mca_u k_u}B_{w\perp}\right) \tag{A.37}$$

define $\alpha = \frac{a_u}{2\rho\gamma_r}$

$$\frac{d\bar{p}_{\perp j}}{d\bar{z}} = \frac{-e}{2\rho}\left(\frac{1}{e\alpha^2}A_\perp \eta p_{2j} + iB_z\frac{\bar{p}_{\perp j}}{p_{zj}}\frac{1}{k_u} - i\frac{1}{mca_u k_u}B_{w\perp}\right) \tag{A.38}$$

$$\frac{d\bar{p}_{\perp j}}{d\bar{z}} = \frac{1}{2\rho}\left(-A_\perp\frac{\eta p_{2j}}{\alpha^2} - ieB_z\frac{\bar{p}_{\perp j}}{p_{zj}}\frac{1}{k_u} + ie\frac{1}{mca_u k_u}B_{w\perp}\right) \tag{A.39}$$

the undulator parameter was given by $a_u = \frac{eB_0}{mck_u}$, now rearranging to give $B_0 = \frac{a_u mck_u}{e} \rightarrow \frac{e}{a_u mck_u} = \frac{1}{B_0}$

$$\frac{d\bar{p}_{\perp j}}{d\bar{z}} = \frac{1}{2\rho}\left(-A_\perp\frac{\eta p_{2j}}{\alpha^2} - e\frac{iB_z\bar{p}_{\perp j}}{k_u p_{zj}} + i\frac{B_{w\perp}}{B_0}\right) \tag{A.40}$$

$L_j \equiv \frac{\gamma_r}{\beta_{zj}\gamma_j} p_{zj} = \gamma_j mc\beta_{zj} => \frac{1}{\gamma_j\beta_{zj}} = \frac{mc}{p_{zj}}$, $L_j = \frac{\gamma_r mc}{p_{zj}} => \frac{L_j}{\gamma_r mc} = \frac{1}{p_{zj}}$

$$\frac{d\bar{p}_{\perp j}}{d\bar{z}} = \frac{1}{2\rho}\left(-A_\perp \frac{\eta p_{2j}}{\alpha^2} - e\frac{iB_z\bar{p}_{\perp j}}{k_u}\frac{L_j}{\gamma_r mc} + i\frac{B_{w\perp}}{B_0}\right) \tag{A.41}$$

again using $\frac{e}{mck_u} = \frac{a_u}{B_0}$

$$\frac{d\bar{p}_{\perp j}}{d\bar{z}} = \frac{1}{2\rho}\left(-A_\perp \frac{\eta p_{2j}}{\alpha^2} - \frac{iB_z}{B_0}a_u\bar{p}_{\perp j}\frac{L_j}{\gamma_r} + i\frac{B_{w\perp}}{B_0}\right) \tag{A.42}$$

define $b_{z,\omega\perp} = B_{z,\omega\perp}/B_0$

$$\frac{d\bar{p}_{\perp j}}{d\bar{z}} = \frac{1}{2\rho}\left(-A_\perp \frac{\eta p_{2j}}{\alpha^2} - ib_z a_u\bar{p}_{\perp j}\frac{L_j}{\gamma_r} + ib_{w\perp}\right) \tag{A.43}$$

$\alpha = \frac{a_u}{2\rho\gamma_r} \rightarrow 2\rho\alpha = \frac{a_u}{\gamma_r}$

$$\frac{d\bar{p}_{\perp j}}{d\bar{z}} = \frac{1}{2\rho}\left(-A_\perp \frac{\eta p_{2j}}{\alpha^2} - ib_z 2\rho\alpha\bar{p}_{\perp j}L_j + ib_{w\perp}\right) \tag{A.44}$$

$$\frac{d\bar{p}_{\perp j}}{d\bar{z}} = \frac{1}{2\rho}\left(ib_{w\perp} - \frac{\eta p_{2j}}{\alpha^2}A_\perp\right) - i\alpha\bar{p}_{\perp j}L_j b_z \tag{A.45}$$

A.2 Longitudinal electron momentum

Now, looking at the longitudinal part of the Lorentz equation,

$$\mathbf{F}_j = \frac{d\mathbf{p}_j}{dt} = -e(\mathbf{E}_j + \frac{\mathbf{p}_j}{\gamma_j m} \times \mathbf{B}) \tag{A.46}$$

the z-component is given by,

$$\frac{dp_{zj}}{dt} = \frac{-e}{\gamma_j m}(p_{xj}B_{yj} - p_{yj}B_{xj}) \tag{A.47}$$

Puffin applies the paraxial approximation, therefore the radiation's electric field in z can be ignored. Now, focus on the $p_{xj}B_{yj} - p_{yj}B_{xj}$ term and use the substitution $p_{\perp j} = p_x - ip_y$, $p_x = \frac{p_{\perp j}+p^*_{\perp j}}{2}$, $p_y = \frac{p^*_{\perp j}-p_\perp}{2i}$ and $B_\perp = B_x - iB_y$

$$p_{xj}B_{yj} - p_{yj}B_{xj} = \frac{p_{\perp j} + p^*_{\perp j}}{2}B_{yj} + \frac{p_{\perp j} - p^*_{\perp j}}{2i}B_{xj} \tag{A.48}$$

$$p_{xj}B_{yj} - p_{yj}B_{xj} = \frac{p_{\perp j} + p^*_{\perp j}}{2}B_{yj} - \frac{i(p_{\perp j} - p^*_{\perp j})}{2}B_{xj} \tag{A.49}$$

$$= \frac{1}{2}[p_{\perp j}(B_{yj} - iB_{xj}) + p^*_{\perp j}((B_{yj} + iB_{xj})] \tag{A.50}$$

$$= \frac{1}{2}[-ip_{\perp j}(iB_{yj} - i^2B_{xj}) + ip^*_{\perp j}((-iB_{yj} - i^2B_{xj})] \tag{A.51}$$

$$= \frac{1}{2}[-ip_{\perp j}(iB_{yj} + B_{xj}) + ip^*_{\perp j}((-iB_{yj} + B_{xj})] \tag{A.52}$$

$$= \frac{1}{2}[-ip_{\perp j}(B_{xj} + iB_{yj}) + ip^*_{\perp j}((B_{xj} - iB_{yj})] \tag{A.53}$$

$$= \frac{1}{2}[-iB^*_{\perp j}p_{\perp j} + iB_{\perp j}p^*_{\perp j}] \tag{A.54}$$

$$= \frac{1}{2}[iB_{\perp j}p^*_{\perp j} - iB^*_{\perp j}p_{\perp j}] \tag{A.55}$$

$$= \frac{1}{2}[iB_{\perp j}p^*_{\perp j} + c.c.] \tag{A.56}$$

separate the perpendicular magnetic field into wiggler and radiation components $B_\perp = B_{w\perp} - iE_\perp/c$

$$p_{xj}B_{yj} - p_{yj}B_{xj} = \frac{1}{2}[(iB_{w\perp} + \frac{E_\perp}{c})p^*_{\perp j} + c.c.] \tag{A.57}$$

$$\frac{dp_{zj}}{dt} = \frac{-e}{2\gamma_j m}[(iB_{w\perp} + \frac{E_\perp}{c})p^*_{\perp j} + c.c.] \tag{A.58}$$

now convert to $\bar{z}$ using $\frac{d}{dt} = 2k_u\rho c\beta_{zj}\frac{d}{d\bar{z}}$

$$\frac{dp_{zj}}{d\bar{z}} = \frac{-e}{4k_u\rho c\beta_{zj}\gamma_j m}[(iB_{w\perp} + \frac{E_\perp}{c})p^*_{\perp j} + c.c.] \tag{A.59}$$

$p_{zj} = \gamma_j mc\beta_{zj}$

$$\frac{dp_{zj}}{d\bar{z}} = \frac{-e}{4k_u\rho p_{zj}}[(iB_{w\perp} + \frac{E_\perp}{c})p^*_{\perp j} + c.c.] \tag{A.60}$$

p_z is defined as $p_{zj} = \gamma_j mc\beta_{zj}$ therefore,

$$\frac{dp_{zj}}{d\bar{z}} = \frac{d}{d\bar{z}}(\gamma_j mc\beta_{zj}) \tag{A.61}$$

$$= mc\gamma_j\frac{d\beta_{zj}}{d\bar{z}} + mc\beta_{zj}\frac{d\gamma_j}{d\bar{z}} \tag{A.62}$$

Now, an expression for the interaction of a co-propagating radiation field with the electron pulse is derived. The Lorentz force equation is considered, while

remembering that the relativistic momentum is given by $\mathbf{p}_j = \gamma_j mc\boldsymbol{\beta}_j$,

$$\mathbf{F}_j = -e(\mathbf{E} + c\boldsymbol{\beta}_j \times \mathbf{B}) \tag{A.63}$$

$$\frac{d\gamma_j mc\boldsymbol{\beta}_j}{dt} = -e(\mathbf{E} + c\boldsymbol{\beta}_j \times \mathbf{B}) \tag{A.64}$$

$$mc\frac{d\gamma_j\boldsymbol{\beta}_j}{dt} = -e(\mathbf{E} + c\boldsymbol{\beta}_j \times \mathbf{B}) \tag{A.65}$$

$$\tag{A.66}$$

multiplying both sides by $\boldsymbol{\beta}$ and rearrange,

$$mc\frac{d\gamma_j\boldsymbol{\beta}_j}{dt} \cdot \boldsymbol{\beta}_j = -e(\mathbf{E} + c\boldsymbol{\beta}_j \times \mathbf{B}) \cdot \boldsymbol{\beta} \tag{A.67}$$

$$mc(\gamma_j\frac{d\boldsymbol{\beta}_j}{dt} + \boldsymbol{\beta}_j\frac{d\gamma_j}{dt}) \cdot \boldsymbol{\beta}_j = -e(\mathbf{E} + c\boldsymbol{\beta}_j \times \mathbf{B}) \cdot \boldsymbol{\beta}_j \tag{A.68}$$

$$\gamma_j\frac{d\boldsymbol{\beta}_j}{dt} \cdot \boldsymbol{\beta}_j + \boldsymbol{\beta}_j^2\frac{d\gamma_j}{dt} = -\frac{e}{mc}(\mathbf{E} + c\boldsymbol{\beta}_j \times \mathbf{B}) \cdot \boldsymbol{\beta}_j \tag{A.69}$$

$$\frac{\gamma_j}{2}\frac{d\boldsymbol{\beta}_j^2}{dt} + \boldsymbol{\beta}_j^2\frac{d\gamma_j}{dt} = -\frac{e}{mc}(\mathbf{E} + c\boldsymbol{\beta}_j \times \mathbf{B}) \cdot \boldsymbol{\beta}_j \tag{A.70}$$

γ_j is defined as $\gamma_j^2 = 1/(1-\boldsymbol{\beta}_j^2)$ and should be rearranged $\gamma_j^2 = 1/(1-\boldsymbol{\beta}_j^2) => \gamma_j^2(1-\boldsymbol{\beta}_j^2) = 1 => \gamma_j^2 = 1 + \gamma_j^2\boldsymbol{\beta}^2$. γ_j^2 is now differentiated with respect to time,

$$\frac{d\gamma_j^2}{dt} = \frac{d}{dt}(1 + \gamma_j^2\boldsymbol{\beta}_j^2) \tag{A.71}$$

$$2\gamma_j\frac{d\gamma_j}{dt} = \frac{d}{dt}\gamma_j^2\boldsymbol{\beta}_j^2 \tag{A.72}$$

$$2\gamma_j\frac{d\gamma_j}{dt} = 2\gamma_j\boldsymbol{\beta}_j^2\frac{d\gamma_j}{dt} + 2\gamma_j^2\boldsymbol{\beta}_j\frac{d\boldsymbol{\beta}_j}{dt} \tag{A.73}$$

$$\frac{d\gamma_j}{dt} = \boldsymbol{\beta}_j^2\frac{d\gamma_j}{dt} + \gamma_j\boldsymbol{\beta}_j\frac{d\boldsymbol{\beta}_j}{dt} \tag{A.74}$$

$$\frac{d\gamma_j}{dt} = \frac{\gamma_j}{2}\frac{d\boldsymbol{\beta}_j^2}{dt} + \boldsymbol{\beta}_j^2\frac{d\gamma_j}{dt} \tag{A.75}$$

The above expression is combined with equation A.70 to give,

$$\frac{d\gamma_j}{dt} = -\frac{e}{mc}(\mathbf{E} + c\boldsymbol{\beta}_j \times \mathbf{B}) \cdot \boldsymbol{\beta} \tag{A.76}$$

now focus on the $(c\boldsymbol{\beta}_j \times \mathbf{B}) \cdot \boldsymbol{\beta}$ part. The cross product $\boldsymbol{\beta}_j \times \mathbf{B}$ will be perpendicular to both $\boldsymbol{\beta}_j$ and $\mathbf{B}$. Therefore the dot product $(c\boldsymbol{\beta}_j \times \mathbf{B}) \cdot \boldsymbol{\beta}$ must be zero, this fact tells us that a magnetic field cannot alter the energy of a charged particle. Setting $(c\boldsymbol{\beta}_j \times \mathbf{B}) \cdot \boldsymbol{\beta}$ to zero leaves

$$\frac{d\gamma_j}{dt} = -\frac{e}{mc}\mathbf{E} \cdot \boldsymbol{\beta}_j \tag{A.77}$$

changing to the scaled $\bar{z}$ using $\frac{d}{dt} = 2k_u\rho c\beta_{zj}\frac{d}{d\bar{z}}$

$$\frac{d\gamma}{dt} = -\frac{e}{mc}\mathbf{E} \cdot \boldsymbol{\beta}_j \tag{A.78}$$

$$\frac{d\gamma}{d\bar{z}} = -\frac{e}{2k_u\rho mc^2\beta_{zj}}\mathbf{E} \cdot \boldsymbol{\beta}_j \tag{A.79}$$

$$\mathbf{E} \cdot \boldsymbol{\beta}_j = \frac{\mathbf{p}_j}{\gamma_j mc} \cdot \mathbf{E}_j \tag{A.80}$$

$$\mathbf{E} \cdot \boldsymbol{\beta}_j = \frac{1}{\gamma_j mc}\mathbf{p}_j \cdot \mathbf{E}_j \tag{A.81}$$

$$\mathbf{E} \cdot \boldsymbol{\beta}_j = \frac{1}{\gamma_j mc}(p_{xj}E_{xj} + p_{yj}E_{yj}) \tag{A.82}$$

$$\tag{A.83}$$

now use $p_{\perp j} = p_x - ip_y$, $p_x = \frac{p_{\perp j}+p^*_{\perp j}}{2}$, $p_y = \frac{p^*_{\perp j}-p_{\perp j}}{2i}$ and $E_\perp = E_x - iE_y$, $E_x = \frac{E_\perp+E^*_\perp}{2}$, $E_y = \frac{E^*_\perp-E_\perp}{2i}$

$$\mathbf{E}\cdot\boldsymbol{\beta}_j = \frac{1}{\gamma_j mc}\left(\frac{p_{\perp j}+p^*_{\perp j}}{2}\frac{E_\perp+E^*_\perp}{2} + \frac{p_{\perp j}-p^*_{\perp j}}{2i}\frac{E_\perp-E^*_\perp}{2i}\right) \tag{A.84}$$

$$\mathbf{E}\cdot\boldsymbol{\beta}_j = \frac{1}{4\gamma_j mc}\left((p_{\perp j}+p^*_{\perp j})(E_\perp+E^*_\perp) - (p_{\perp j}-p^*_{\perp j})(E_\perp-E^*_\perp)\right) \tag{A.85}$$

$$\begin{aligned}\mathbf{E}\cdot\boldsymbol{\beta}_j =& \frac{1}{4\gamma_j mc}(p_{\perp j}E_\perp + p^*_{\perp j}E_\perp + p_{\perp j}E^*_\perp + p^*_{\perp j}E^*_\perp \\ & - p_{\perp j}E_\perp + p^*_{\perp j}E_\perp + p_{\perp j}E^*_\perp - p^*_{\perp j}E^*_\perp)\end{aligned} \tag{A.86}$$

$$\mathbf{E}\cdot\boldsymbol{\beta}_j = \frac{1}{2\gamma_j mc}(p^*_{\perp j}E_\perp + p_{\perp j}E^*_\perp) \tag{A.87}$$

$$\Rightarrow \frac{d\gamma_j}{d\bar{z}} = -\frac{e}{2k_u\rho mc^2\beta_{zj}}\frac{1}{2\gamma_j mc}(p^*_{\perp j}E_\perp + p_{\perp j}E^*_\perp) \tag{A.88}$$

$$\frac{d\gamma_j}{d\bar{z}} = -\frac{e}{4k_u\rho\gamma_j m^2c^3\beta_{zj}}(p^*_{\perp j}E_\perp + p_{\perp j}E^*_\perp) \tag{A.89}$$

now substitute back into equation A.62, shown below

$$\frac{dp_{zj}}{d\bar{z}} = mc\gamma_j\frac{d\beta_{zj}}{d\bar{z}} + mc\beta_{zj}\frac{d\gamma_j}{d\bar{z}}$$

$$\frac{dp_{zj}}{d\bar{z}} = \gamma_j mc\frac{d\beta_{zj}}{d\bar{z}} - mc\beta_{zj}\frac{e}{4k_u\rho\gamma_j m^2c^3\beta_{zj}}(p^*_{\perp j}E_\perp + p_{\perp j}E^*_\perp) \tag{A.90}$$

$$\frac{dp_{zj}}{d\bar{z}} = \gamma_j mc\frac{d\beta_{zj}}{d\bar{z}} - \frac{e}{4k_u\rho\gamma_j mc^2}(p^*_{\perp j}E_\perp + p_{\perp j}E^*_\perp) \tag{A.91}$$

now reintroduce equations A.60, shown below

$$\frac{dp_{zj}}{d\bar{z}} = \frac{-e}{4k_u\rho p_{zj}}[(iB_{w\perp} + \frac{E_\perp}{c})p^*_{\perp j} + c.c.]$$

$$\frac{-e}{4k_u\rho p_{zj}}[(iB_{w\perp} + \frac{E_\perp}{c})p^*_{\perp j} + c.c.] = \gamma_j mc\frac{d\beta_{zj}}{d\bar{z}} - \frac{e}{4k_u\rho\gamma_j mc^2}(p^*_{\perp j}E_\perp + p_{\perp j}E^*_\perp)$$

and rearrange for $\frac{d\beta_{zj}}{d\bar{z}}$

$$\gamma_j mc\frac{d\beta_{zj}}{d\bar{z}} = \frac{e}{4k_u\rho\gamma_j mc^2}(p^*_{\perp j}E_\perp + p_{\perp j}E^*_\perp) - \frac{e}{4k_u\rho\gamma_j mc\beta_{zj}}[(iB_{w\perp} + \frac{E_\perp}{c})p^*_{\perp j} + c.c.] \quad \text{(A.92)}$$

moving the $\frac{c}{\beta_{zj}}$ inside the brackets

$$\gamma_j mc\frac{d\beta_{zj}}{d\bar{z}} = \frac{e}{4k_u\rho\gamma_j mc^2}(p^*_{\perp j}E_\perp + p_{\perp j}E^*_\perp) - \frac{e}{4k_u\rho\gamma_j mc^2}[\frac{c}{\beta_{zj}}(iB_{w\perp} + \frac{E_\perp}{c})p^*_{\perp j} + c.c.] \quad \text{(A.93)}$$

$$\gamma_j mc\frac{d\beta_{zj}}{d\bar{z}} = \frac{e}{4k_u\rho\gamma_j mc^2}\left((p^*_{\perp j}E_\perp + c.c) - [\frac{c}{\beta_{zj}}(iB_{w\perp} + \frac{E_\perp}{c})p^*_{\perp j} + c.c.]\right) \quad \text{(A.94)}$$

$$\gamma_j mc\frac{d\beta_{zj}}{d\bar{z}} = \frac{e}{4k_u\rho\gamma_j mc^2}\left((p^*_{\perp j}E_\perp + c.c) - (\frac{c}{\beta_{zj}}\frac{E_\perp}{c}p^*_{\perp j} + c.c.) - [\frac{c}{\beta_{zj}}(iB_{w\perp}p^*_{\perp j} + c.c.)]\right) \tag{A.95}$$

rearranging the β_{zj}'s

$$\gamma_j mc\frac{d\beta_{zj}}{d\bar{z}} = \frac{e}{4k_u\rho\gamma_j mc^2}\left((p^*_{\perp j}E_\perp + c.c)\frac{\beta_{zj}}{\beta_{zj}} - \frac{1}{\beta_{zj}}(p^*_{\perp j}E_\perp + c.c.) - [\frac{c}{\beta_{zj}}(iB_{w\perp}p^*_{\perp j} + c.c.)]\right) \tag{A.96}$$

$$\gamma_j mc\frac{d\beta_{zj}}{d\bar{z}} = \frac{e}{4k_u\rho\gamma_j mc^2}\left((p^*_{\perp j}E_\perp + c.c)\left(\frac{\beta_{zj}-1}{\beta_{zj}}\right) - [\frac{c}{\beta_{zj}}(iB_{w\perp}p^*_{\perp j} + c.c.)]\right) \tag{A.97}$$

$$\gamma_j mc\frac{d\beta_{zj}}{d\bar{z}} = \frac{-e}{4k_u\rho\gamma_j mc^2}\left((p^*_{\perp j}E_\perp + c.c)\left(\frac{1-\beta_{zj}}{\beta_{zj}}\right) + [\frac{c}{\beta_{zj}}(iB_{w\perp}p^*_{\perp j} + c.c.)]\right) \tag{A.98}$$

use $\eta p_{2j} = \frac{1-\beta_{zj}}{\beta_{zj}}$

$$\gamma_j mc \frac{d\beta_{zj}}{d\bar{z}} = \frac{-e}{4k_u \rho \gamma_j mc^2} \left((p^*_{\perp j} E_\perp + c.c) \eta p_{2j} + [\frac{c}{\beta_{zj}} (iB_{w\perp} p^*_{\perp j} + c.c.)] \right) \tag{A.99}$$

$$\frac{d\beta_{zj}}{d\bar{z}} = \frac{-e}{4k_u \rho \gamma_j^2 m^2 c^3} \left((p^*_{\perp j} E_\perp + c.c) \eta p_{2j} + [\frac{c}{\beta_{zj}} (iB_{w\perp} p^*_{\perp j} + c.c.)] \right) \tag{A.100}$$

now changing to p_{2j}
$p_{2j} = \frac{1}{\eta} \frac{1-\beta_{zj}}{\beta_{zj}} \rightarrow p_{2j} = \frac{1}{\eta} \left(\frac{1}{\beta_{zj}} - 1 \right) \rightarrow \frac{dp_{2j}}{d\bar{z}} = -\frac{1}{\eta \beta_{zj}^2} \frac{d\beta zj}{d\bar{z}}$

$$-\eta \beta_{zj}^2 \frac{dp_{2j}}{d\bar{z}} = \frac{-e}{4k_u \rho \gamma_j^2 m^2 c^3} \left((p^*_{\perp j} E_\perp + c.c) \eta p_{2j} + [\frac{c}{\beta_{zj}} (iB_{w\perp} p^*_{\perp j} + c.c.)] \right) \tag{A.101}$$

$$\frac{dp_{2j}}{d\bar{z}} = \frac{1}{\eta \beta_{zj}^2} \frac{e}{4k_u \rho \gamma_j^2 m^2 c^3} \left((p^*_{\perp j} E_\perp + c.c) \eta p_{2j} + [\frac{c}{\beta_{zj}} (iB_{w\perp} p^*_{\perp j} + c.c.)] \right) \tag{A.102}$$

Since p_{2j} is $p_{2j} = \frac{1}{\eta} \frac{1-\beta_{zj}}{\beta_{zj}} \rightarrow \frac{1}{\beta_{zj}} = 1 + \eta p_{2j} \rightarrow \frac{1}{\beta_{zj}^2} = (1 + \eta p_{2j})^2$

$$\frac{dp_{2j}}{d\bar{z}} = \frac{1}{\eta \beta_{zj}^2} \frac{e}{4k_u \rho \gamma_j^2 m^2 c^3} \left((p^*_{\perp j} E_\perp + c.c) \eta p_{2j} + [(1 + \eta p_{2j})(icB_{w\perp} p^*_{\perp j} + c.c.)] \right) \tag{A.103}$$

introduce $\bar{p}_{\perp j} = \frac{1}{mca_u} p_{\perp j} => p_{\perp j} = mca_u \bar{p}_{\perp j}$, use scaled field $E_\perp = \frac{2\gamma_r^2 mc^2 \rho}{ea_u l_g} A_\perp$

$$p^*_{\perp j} E_\perp = mca_u \bar{p}^*_{\perp j} \frac{2\gamma_r^2 mc^2 \rho}{ea_u l_g} A_\perp$$
$$p^*_{\perp j} E_\perp = \bar{p}^*_{\perp j} \frac{2\gamma_r^2 m^2 c^3 \rho}{el_g} A_\perp$$
$$p^*_{\perp j} E_\perp = \bar{p}^*_{\perp j} \frac{2\gamma_r^2 m^2 c^3 \rho}{el_g} A_\perp$$

the gain length is defined as $l_g = \frac{1}{2k_u \rho}$

$$p^*_{\perp j} E_\perp = \bar{p}^*_{\perp j} A_\perp \frac{4\gamma_r^2 k_u m^2 c^3 \rho^2}{e}$$

now inserting into the above

$$\frac{dp_{2j}}{d\bar{z}} = \frac{1}{\eta \beta_{zj}^2} \frac{e}{4k_u \rho \gamma_j^2 m^2 c^3}$$
$$\left(\frac{4\gamma_r^2 k_u m^2 c^3 \rho^2}{e} (\bar{p}^*_{\perp j} A_\perp + c.c) \eta p_{2j} + [(1 + \eta p_{2j})(icB_{w\perp} p^*_{\perp j} + c.c.)] \right) \quad \text{(A.104)}$$

$$\frac{dp_{2j}}{d\bar{z}} = \frac{1}{\eta \beta_{zj}^2} \frac{e}{4k_u \rho \gamma_j^2 m^2 c^3} \frac{4\gamma_r^2 k_u m^2 c^3 \rho^2}{e}$$
$$\left((\bar{p}^*_{\perp j} A_\perp + c.c) \eta p_{2j} + \frac{e}{4\gamma_r^2 k_u m^2 c^3 \rho^2} [(1 + \eta p_{2j})(icB_{w\perp} p^*_{\perp j} + c.c.)] \right) \quad \text{(A.105)}$$

cancelling terms

$$\frac{dp_{2j}}{d\bar{z}} = \frac{1}{\eta \beta_{zj}^2} \frac{\sqrt{2}\gamma_r^2 \rho}{\gamma_j^2} \left((\bar{p}^*_{\perp j} A_\perp + c.c) \eta p_{2j} + \frac{e}{4\sqrt{2}\gamma_r^2 k_u m^2 c^3 \rho^2} [(1 + \eta p_{2j})(icB_{w\perp} p^*_{\perp j} + c.c.)] \right) \quad \text{(A.106)}$$

$$\frac{dp_{2j}}{d\bar{z}} = \frac{1}{\eta\beta_{zj}^2}\frac{\sqrt{2}\gamma_r^2\rho}{\gamma_j^2}\left((\bar{p}_{\perp j}^* A_\perp + c.c)\eta p_{2j} + \frac{e}{4\sqrt{2}\gamma_r^2 k_u m^2 c^3 \rho^2}[(1+\eta p_{2j})(icB_{w\perp}p_{\perp j}^* + c.c.)]\right) \tag{A.107}$$

$L_j \equiv \frac{\gamma_r}{\beta_{zj}\gamma_j}$

$$\frac{dp_{2j}}{d\bar{z}} = \frac{\rho}{\eta}L_j^2\left((\bar{p}_{\perp j}^* A_\perp + c.c)\eta p_{2j} + \frac{e}{4\gamma_r^2 k_u m^2 c^3 \rho^2}[(1+\eta p_{2j})(icB_{w\perp}p_{\perp j}^* + c.c.)]\right) \tag{A.108}$$

again use $\bar{p}_{\perp j} = \frac{1}{mca_u}p_{\perp j} => p_{\perp j} = mca_u\bar{p}_\perp$

$$\frac{dp_{2j}}{d\bar{z}} = \frac{\rho}{\eta}L_j^2\left((\bar{p}_{\perp j}^* A_\perp + c.c)\eta p_{2j} + \frac{e}{4\gamma_r^2 k_u m^2 c^3 \rho^2}mca_u c[(1+\eta p_{2j})(iB_{w\perp}\bar{p}_{\perp j}^* + c.c.)]\right) \tag{A.109}$$

$$\frac{dp_{2j}}{d\bar{z}} = \frac{\rho}{\eta}L_j^2\left((\bar{p}_{\perp j}^* A_\perp + c.c)\eta p_{2j} + \frac{emc^2 a_u}{4\gamma_r^2 k_u m^2 c^3 \rho^2}[(1+\eta p_{2j})(iB_{w\perp}\bar{p}_{\perp j}^* + c.c.)]\right) \tag{A.110}$$

$$\frac{dp_{2j}}{d\bar{z}} = \frac{\rho}{\eta}L_j^2\left((\bar{p}_{\perp j}^* A_\perp + c.c)\eta p_{2j} + \frac{ea_u}{4\gamma_r^2 k_u mc\rho^2}[(1+\eta p_{2j})(iB_{w\perp}\bar{p}_{\perp j}^* + c.c.)]\right) \tag{A.111}$$

now define $a_u = \frac{eB_0}{mck_u} => a_u\frac{mck_u}{e} = B_0$ therefore $a_u\frac{mck_u}{e} = B_0 \rightarrow \frac{a_u}{B_0}\frac{mck_u}{e} = 1$

$$\frac{dp_{2j}}{d\bar{z}} = \frac{\rho}{\eta}L_j^2\left((\bar{p}_{\perp j}^* A_\perp + c.c)\eta p_{2j} + \frac{ea_u}{4\gamma_r^2 k_u mc\rho^2}\frac{a_u}{B_0}\frac{mck_u}{e}[(1+\eta p_{2j})(iB_{w\perp}\bar{p}_{\perp j}^* + c.c.)]\right) \tag{A.112}$$

$$\frac{dp_{2j}}{d\bar{z}} = \frac{\rho}{\eta} L_j^2 \left((\bar{p}^*_{\perp j} A_\perp + c.c) \eta p_{2j} + \frac{e}{4\gamma_r^2 \rho^2} \frac{a_u^2}{B_0 e} [(1 + \eta p_{2j})(i B_{w\perp} \bar{p}^*_{\perp j} + c.c.)] \right) \tag{A.113}$$

further cancelling of terms

$$\frac{dp_{2j}}{d\bar{z}} = \frac{\rho}{\eta} L_j^2 \left((\bar{p}^*_{\perp j} A_\perp + c.c) \eta p_{2j} + \frac{a_u^2}{4\rho^2 \gamma_r^2} \frac{1}{B_0} [(1 + \eta p_{2j})(i B_{w\perp} \bar{p}^*_{\perp j} + c.c.)] \right) \tag{A.114}$$

again using $\alpha = \frac{a_u}{2\rho\gamma_r}$

$$\frac{dp_{2j}}{d\bar{z}} = \frac{\rho}{\eta} L_j^2 \left((\bar{p}^*_{\perp j} A_\perp + c.c) \eta p_{2j} + \frac{\alpha^2}{B_0} [(1 + \eta p_{2j})(i B_{w\perp} \bar{p}^*_{\perp j} + c.c.)] \right) \tag{A.115}$$

$$\frac{dp_{2j}}{d\bar{z}} = \frac{\rho}{\eta} L_j^2 \left((\bar{p}^*_{\perp j} A_\perp + c.c) \eta p_{2j} + \frac{\alpha^2}{B_0} [(1 + \eta p_{2j})(i B_{w\perp} \bar{p}^*_{\perp j} + c.c.)] \right) \tag{A.116}$$

$$\frac{dp_{2j}}{d\bar{z}} = \frac{\rho}{\eta} L_j^2 \left((\bar{p}^*_{\perp j} A_\perp + c.c) \eta p_{2j} + \alpha^2 [(1 + \eta p_{2j})(i \frac{B_{w\perp}}{B_0} \bar{p}^*_{\perp j} + c.c.)] \right) \tag{A.117}$$

remembering $b_{\omega\perp} = B_{\omega\perp}/B_0$

$$\frac{dp_{2j}}{d\bar{z}} = \frac{\rho}{\eta} L_j^2 \left((\bar{p}^*_{\perp j} A_\perp + c.c) \eta p_{2j} + \alpha^2 (1 + \eta p_{2j})(i b_{w\perp} \bar{p}^*_{\perp j} + c.c.) \right) \tag{A.118}$$

$$\frac{dp_{2j}}{d\bar{z}} = \frac{\rho}{\eta} L_j^2 \left((\bar{p}^*_{\perp j} A_\perp + c.c) \eta p_{2j} + \alpha^2 (1 + \eta p_{2j})(i b_{w\perp} \bar{p}^*_{\perp j} + c.c.) \right) \tag{A.119}$$

using $ib_{\omega\perp}\bar{p}^*_{\perp j} + c.c. = -i(b^*_{\omega\perp}\bar{p}_{\perp j} - c.c.)$

$$\frac{dp_{2j}}{d\bar{z}} = \frac{\rho}{\eta}L_j^2\left((\bar{p}^*_{\perp j}A_\perp + c.c)\eta p_{2j} - i\alpha^2(1+\eta p_{2j})(\bar{p}_{\perp j}b^*_{\omega\perp} - c.c.)\right) \qquad \text{(A.120)}$$

A.3 The Field Equation

The 3D Maxwell wave equation, ignoring space charge, is given by,

$$\nabla^2\mathbf{E} - \frac{1}{c^2}\frac{\partial^2\mathbf{E}}{\partial t^2} = \mu_0\frac{\partial\mathbf{J}}{\partial t} \tag{A.121}$$

Puffin makes the paraxial approximation, therefore ($E_z = 0$) the radiation's electric field is purely transverse. Hence, the above equation is projected over $\sqrt{2}\hat{\mathbf{e}}^* = x - iy$. Here, $\sqrt{2}\hat{\mathbf{e}}^*\mathbf{E} = E_\perp = E_x - iE_y$ and $\sqrt{2}\hat{\mathbf{e}}^*\mathbf{J} = J_\perp = J_x - iJ_y$

$$\left(\nabla^2 E_\perp - \frac{1}{c^2}\frac{\partial^2 E_\perp}{\partial t^2}\right) = \mu_0\frac{\partial J_\perp}{\partial t} \tag{A.122}$$

$$\left(\nabla^2 - \frac{1}{c^2}\frac{\partial^2}{\partial t^2}\right) E_\perp = \mu_0\frac{\partial J_\perp}{\partial t} \tag{A.123}$$

$$\left(\frac{\partial^2}{\partial x^2} + \frac{\partial^2}{\partial y^2} + \frac{\partial^2}{\partial z^2} - \frac{1}{c^2}\frac{\partial^2}{\partial t^2}\right) E_\perp = \mu_0\frac{\partial J_\perp}{\partial t} \tag{A.124}$$

$$\left(\frac{\partial^2}{\partial x^2} + \frac{\partial^2}{\partial y^2} + \left(\frac{\partial^2}{\partial z^2} - \frac{1}{c^2}\frac{\partial^2}{\partial t^2}\right)\right) E_\perp = \mu_0\frac{\partial J_\perp}{\partial t} \tag{A.125}$$

$$\left(\frac{\partial^2}{\partial x^2} + \frac{\partial^2}{\partial y^2} + \left(\frac{\partial}{\partial z} + \frac{1}{c}\frac{\partial}{\partial t}\right)\left(\frac{\partial}{\partial z} - \frac{1}{c}\frac{\partial}{\partial t}\right)\right) E_\perp = \mu_0\frac{\partial J_\perp}{\partial t} \tag{A.126}$$

converting to scaled units using, where $\bar{z}_2 = \frac{\bar{\beta}_z}{(1-\bar{\beta}_z)}\frac{(ct-z)}{l_g}$ and $\bar{z} = \frac{z}{l_g}$,

$$\frac{\partial}{\partial\bar{z}} = l_g\left(\frac{\partial}{\partial z} + \frac{1}{c}\frac{\partial}{\partial t}\right) \tag{A.127}$$

and

$$\frac{\partial}{\partial\bar{z}} - \frac{2\bar{\beta}_z}{1-\bar{\beta}_z}\frac{\partial}{\partial\bar{z}_2} = l_g\left(\frac{\partial}{\partial z} - \frac{1}{c}\frac{\partial}{\partial t}\right) \tag{A.128}$$

see appendix B.3 for a derivation of the above expressions.

$$\left(\frac{\partial^2}{\partial x^2}+\frac{\partial^2}{\partial y^2}+\frac{1}{l_g^2}\frac{\partial}{\partial \bar{z}}\left(\frac{\partial}{\partial \bar{z}}-\frac{2\bar{\beta}_z}{1-\bar{\beta}_z}\frac{\partial}{\partial \bar{z}_2}\right)\right)E_\perp=\mu_0\frac{\partial J_\perp}{\partial t} \tag{A.129}$$

now using $\frac{\bar{\beta}_z}{1-\bar{\beta}_z}\frac{\partial}{\partial \bar{z}_2}=\frac{l_g}{c}\frac{\partial}{\partial t}$

$$\left(\frac{\partial^2}{\partial x^2}+\frac{\partial^2}{\partial y^2}+\frac{1}{l_g^2}\frac{\partial}{\partial \bar{z}}\left(\frac{\partial}{\partial \bar{z}}-\frac{2\bar{\beta}_z}{1-\bar{\beta}_z}\frac{\partial}{\partial \bar{z}_2}\right)\right)E_\perp=\frac{\bar{\beta}_z}{1-\bar{\beta}_z}\frac{c}{l_g}\mu_0\frac{\partial J_\perp}{\partial \bar{z}_2} \tag{A.130}$$

Here, the backwards propagating wave is neglected i.e. $\left|\frac{\partial E_\perp}{\partial \bar{z}}\right| \ll \left|\frac{\bar{\beta}_z}{1-\bar{\beta}_z}\frac{\partial E_\perp}{\partial \bar{z}_2}\right|$

$$\left(\frac{\partial^2}{\partial x^2}+\frac{\partial^2}{\partial y^2}-\frac{1}{l_g^2}\frac{2\bar{\beta}_z}{1-\bar{\beta}_z}\frac{\partial}{\partial \bar{z}}\frac{\partial}{\partial \bar{z}_2}\right)E_\perp=\frac{\bar{\beta}_z}{1-\bar{\beta}_z}\frac{c}{l_g}\mu_0\frac{\partial J_\perp}{\partial \bar{z}_2} \tag{A.131}$$

$$\left(\frac{\partial^2}{\partial x^2}+\frac{\partial^2}{\partial y^2}-\frac{1}{l_g^2}\frac{2\bar{\beta}_z}{1-\bar{\beta}_z}\frac{\partial^2}{\partial \bar{z}\partial \bar{z}_2}\right)E_\perp=\frac{\bar{\beta}_z}{1-\bar{\beta}_z}\frac{c}{l_g}\mu_0\frac{\partial J_\perp}{\partial \bar{z}_2} \tag{A.132}$$

using $l_g=\frac{\bar{\beta}_z}{1-\bar{\beta}_z}l_c$

$$\left(\frac{\partial^2}{\partial x^2}+\frac{\partial^2}{\partial y^2}-\frac{1}{l_g l_c}\frac{2\partial^2}{\partial \bar{z}\partial \bar{z}_2}\right)E_\perp=\frac{c}{l_c}\mu_0\frac{\partial J_\perp}{\partial \bar{z}_2} \tag{A.133}$$

now using a 3D perpendicular current density

$$J_\perp=-ec\sum_{j=1}^{N}\beta_{\perp j}\delta(x_j,y_j,z_j) \tag{A.134}$$

where $\delta(x_j, y_j, z_j) = \delta(x - x(t)_j)\delta(y - y(t)_j)\delta(z - z(t)_j)$

$$\left(\frac{\partial^2}{\partial x^2} + \frac{\partial^2}{\partial y^2} - \frac{1}{l_g l_c}\frac{2\partial^2}{\partial \bar{z}\partial \bar{z}_2}\right) E_\perp =$$

$$-\mu_0 \frac{ec^2}{l_c}\frac{\partial}{\partial \bar{z}_2}\sum_{j=1}^{N} \beta_{\perp j}\delta(x - x(t)_j)\delta(y - y(t)_j)\delta(z - z(t)_j) \tag{A.135}$$

the dirac delta function is transformed into scaled variables using

$$\delta(z - z_j) = \frac{1}{\beta_{zj}}\frac{1}{l_g}\frac{\bar{\beta}_z}{1 - \bar{\beta}_z}\delta(\bar{z}_2 - \bar{z}_{2j}) \tag{A.136}$$

$$\delta(x - x_j) = \frac{1}{\sqrt{l_g l_c}}\delta(\bar{x} - \bar{x}_j) \tag{A.137}$$

$$\delta(y - y_j) = \frac{1}{\sqrt{l_g l_c}}\delta(\bar{y} - \bar{y}_j) \tag{A.138}$$

therefore

$$\delta(x - x_j)\delta(y - y_j)\delta(z - z_j) = \frac{1}{\sqrt{l_g l_c}}\delta(\bar{x} - \bar{x}_j)\frac{1}{\sqrt{l_g l_c}}\delta(\bar{y} - \bar{y}_j)\frac{1}{\beta_{zj}}\frac{1}{l_g}\frac{\bar{\beta}_z}{1 - \bar{\beta}_z}\delta(\bar{z}_2 - \bar{z}_{2j}) \tag{A.139}$$

$$\delta(x - x_j)\delta(y - y_j)\delta(z - z_j) = \frac{1}{l_g^2 l_c}\delta(\bar{x} - \bar{x}_j)\delta(\bar{y} - \bar{y}_j)\frac{1}{\beta_{zj}}\frac{\bar{\beta}_z}{1 - \bar{\beta}_z}\delta(\bar{z}_2 - \bar{z}_{2j}) \tag{A.140}$$

$$\delta(x - x_j)\delta(y - y_j)\delta(z - z_j) = \frac{1}{l_g^2 l_c}\frac{1}{\beta_{zj}}\frac{\bar{\beta}_z}{1 - \bar{\beta}_z}\delta(\bar{x} - \bar{x}_j)\delta(\bar{y} - \bar{y}_j)\delta(\bar{z}_2 - \bar{z}_{2j}) \tag{A.141}$$

using $l_g = \frac{\bar{\beta}_z}{1-\bar{\beta}_z} l_c$

$$\delta(x - x_j)\delta(y - y_j)\delta(z - z_j) = \frac{1}{l_g l_c^2}\frac{1}{\beta_{zj}}\delta(\bar{x} - \bar{x}_j)\delta(\bar{y} - \bar{y}_j)\delta(\bar{z}_2 - \bar{z}_{2j}) \quad \text{(A.142)}$$

now inserting into equation 136

$$\left(\frac{\partial^2}{\partial x^2} + \frac{\partial^2}{\partial y^2} - \frac{1}{l_g l_c}\frac{2\partial^2}{\partial \bar{z}\partial \bar{z}_2}\right) E_\perp =$$

$$-\mu_0 \frac{ec^2}{l_c}\frac{\partial}{\partial \bar{z}_2}\sum_{j=1}^{N} \beta_{\perp j}\frac{1}{l_g l_c^2}\frac{1}{\beta_{zj}}\delta(\bar{x} - \bar{x}_j)\delta(\bar{y} - \bar{y}_j)\delta(\bar{z}_2 - \bar{z}_{2j}) \quad \text{(A.143)}$$

now $\delta(\bar{x}_j, \bar{y}_j \bar{z}_{2j}) = \delta(\bar{x} - \bar{x}_j)\delta(\bar{y} - \bar{y}_j)\delta(\bar{z}_2 - \bar{z}_{2j})$

$$\left(\frac{\partial^2}{\partial x^2} + \frac{\partial^2}{\partial y^2} - \frac{1}{l_g l_c}\frac{2\partial^2}{\partial \bar{z}\partial \bar{z}_2}\right) E_\perp = -\mu_0 \frac{ec^2}{l_c}\frac{\partial}{\partial \bar{z}_2}\sum_{j=1}^{N} \beta_{\perp j}\frac{1}{l_g l_c^2}\frac{1}{\beta_{zj}}\delta(\bar{x}_j, \bar{y}_j \bar{z}_{2j}) \quad \text{(A.144)}$$

$$\left(\frac{\partial^2}{\partial x^2} + \frac{\partial^2}{\partial y^2} - \frac{1}{l_g l_c}\frac{2\partial^2}{\partial \bar{z}\partial \bar{z}_2}\right) E_\perp = -\mu_0 \frac{ec^2}{l_c^3 l_g}\frac{1}{\beta_{zj}}\frac{\partial}{\partial \bar{z}_2}\sum_{j=1}^{N} \beta_{\perp j}\delta(\bar{x}_j, \bar{y}_j \bar{z}_{2j}) \quad \text{(A.145)}$$

$$\text{(A.146)}$$

now change the partial derivatives in x and y to scaled notation using $\frac{\partial^2}{\partial x^2} = \frac{1}{l_g l_c}\frac{\partial^2}{\partial \bar{x}^2}$ and $\frac{\partial^2}{\partial y^2} = \frac{1}{l_g l_c}\frac{\partial^2}{\partial \bar{y}^2}$

$$\left(\frac{1}{l_g l_c}\frac{\partial^2}{\partial \bar{x}^2} + \frac{1}{l_g l_c}\frac{\partial^2}{\partial \bar{y}^2} - \frac{1}{l_g l_c}\frac{2\partial^2}{\partial \bar{z}\partial \bar{z}_2}\right) E_\perp = -\mu_0 \frac{ec^2}{l_c^3 l_g}\frac{1}{\beta_{zj}}\frac{\partial}{\partial \bar{z}_2}\sum_{j=1}^{N} \beta_{\perp j}\delta(\bar{x}_j, \bar{y}_j \bar{z}_{2j}) \quad \text{(A.147)}$$

$$\left(\frac{\partial^2}{\partial \bar{x}^2} + \frac{\partial^2}{\partial \bar{y}^2} - \frac{2\partial^2}{\partial \bar{z}\partial \bar{z}_2}\right) E_\perp = -\mu_0 \frac{ec^2}{l_c^2}\frac{1}{\beta_{zj}}\frac{\partial}{\partial \bar{z}_2}\sum_{j=1}^{N} \beta_{\perp j}\delta(\bar{x}_j, \bar{y}_j \bar{z}_{2j}) \quad \text{(A.148)}$$

use scaled electric field of $A_\perp = \frac{ea_u l_g}{2\gamma_r^2 mc^2\rho}E_\perp$ which rearranged gives, $E_\perp = \frac{2\gamma_r^2 mc^2\rho}{ea_u l_g}A_\perp$

$$\frac{2\gamma_r^2 mc^2\rho}{ea_u l_g}\left(\frac{\partial^2}{\partial\bar{x}^2}+\frac{\partial^2}{\partial\bar{y}^2}-\frac{2\partial^2}{\partial\bar{z}\partial\bar{z}_2}\right)A_\perp = \mu_0\frac{ec^2}{l_c^2}\frac{1}{\beta_{zj}}\frac{\partial}{\partial\bar{z}_2}\sum_{j=1}^{N}\beta_{\perp j}\delta(\bar{x}_j,\bar{y}_j\bar{z}_{2j}) \tag{A.149}$$

the perpendicular momentum is given by $p_{\perp j} = \gamma_j mc\beta_{\perp j}$, $\beta_{\perp j} = \frac{p_{\perp j}}{\gamma_j mc}$,

$$\frac{2\gamma_r^2 mc^2\rho}{ea_u l_g}\left(\frac{\partial^2}{\partial\bar{x}^2}+\frac{\partial^2}{\partial\bar{y}^2}-\frac{2\partial^2}{\partial\bar{z}\partial\bar{z}_2}\right)A_\perp = -\mu_0\frac{ec^2}{l_c^2}\frac{1}{\beta_{zj}}\frac{\partial}{\partial\bar{z}_2}\sum_{j=1}^{N}\frac{p_{\perp j}}{\gamma_j mc}\delta(\bar{x}_j,\bar{y}_j\bar{z}_{2j}) \tag{A.150}$$

$$\frac{2\gamma_r^2 mc^2\rho}{ea_u l_g}\left(\frac{\partial^2}{\partial\bar{x}^2}+\frac{\partial^2}{\partial\bar{y}^2}-\frac{2\partial^2}{\partial\bar{z}\partial\bar{z}_2}\right)A_\perp = -\mu_0\frac{ec^2}{l_c^2}\frac{1}{\gamma_j mc\beta_{zj}}\frac{\partial}{\partial\bar{z}_2}\sum_{j=1}^{N}p_{\perp j}\delta(\bar{x}_j,\bar{y}_j\bar{z}_{2j}) \tag{A.151}$$

again use $\bar{p}_{\perp j} = \frac{1}{mca_u}p_{\perp j} => p_{\perp j} = mca_u\bar{p}_{\perp j}$

$$\frac{2\gamma_r^2 mc^2\rho}{ea_u l_g}\left(\frac{\partial^2}{\partial\bar{x}^2}+\frac{\partial^2}{\partial\bar{y}^2}-\frac{2\partial^2}{\partial\bar{z}\partial\bar{z}_2}\right)A_\perp = -\mu_0\frac{ec^2}{l_c^2}\frac{1}{\gamma_j mc\beta_{zj}}\frac{\partial}{\partial\bar{z}_2}\sum_{j=1}^{N}mca_u\bar{p}_{\perp j}\delta(\bar{x}_j,\bar{y}_j\bar{z}_{2j}) \tag{A.152}$$

$$\frac{2\gamma_r^2 mc^2\rho}{ea_u l_g}\left(\frac{\partial^2}{\partial\bar{x}^2}+\frac{\partial^2}{\partial\bar{y}^2}-\frac{2\partial^2}{\partial\bar{z}\partial\bar{z}_2}\right)A_\perp = -\mu_0\frac{ec^2}{l_c^2}\frac{a_u}{\gamma_j\beta_{zj}}\frac{\partial}{\partial\bar{z}_2}\sum_{j=1}^{N}\bar{p}_{\perp j}\delta(\bar{x}_j,\bar{y}_j\bar{z}_{2j}) \tag{A.153}$$

$$\left(\frac{\partial^2}{\partial\bar{x}^2}+\frac{\partial^2}{\partial\bar{y}^2}-\frac{2\partial^2}{\partial\bar{z}\partial\bar{z}_2}\right)A_\perp = -\frac{ea_u l_g}{2\gamma_r^2 mc^2\rho}\mu_0\frac{ec^2}{l_c^2}\frac{a_u}{\gamma_j\beta_{zj}}\frac{\partial}{\partial\bar{z}_2}\sum_{j=1}^{N}\bar{p}_{\perp j}\delta(\bar{x}_j,\bar{y}_j\bar{z}_{2j}) \tag{A.154}$$

$$\left(\frac{\partial^2}{\partial\bar{x}^2}+\frac{\partial^2}{\partial\bar{y}^2}-\frac{2\partial^2}{\partial\bar{z}\partial\bar{z}_2}\right)A_\perp = -\frac{e^2c^2a_u^2 l_g}{2\gamma_r^2 mc^2\rho l_c^2}\mu_0\frac{1}{\gamma_j\beta_{zj}}\frac{\partial}{\partial\bar{z}_2}\sum_{j=1}^{N}\bar{p}_{\perp j}\delta(\bar{x}_j,\bar{y}_j\bar{z}_{2j}) \tag{A.155}$$

$1/c^2 = \mu_0\epsilon_0 => \mu_0 = 1/(\epsilon_0 c^2)$

$$\left(\frac{\partial^2}{\partial\bar{x}^2} + \frac{\partial^2}{\partial\bar{y}^2} - \frac{2\partial^2}{\partial\bar{z}\partial\bar{z}_2}\right) A_\perp = \frac{e^2c^2a_u^2l_g}{2\gamma_r^2 m\epsilon_0 c^4\rho l_c^2}\frac{1}{\gamma_j\beta_{zj}}\frac{\partial}{\partial\bar{z}_2}\sum_{j=1}^{N}\bar{p}_{\perp j}\delta(\bar{x}_j, \bar{y}_j\bar{z}_{2j}) \tag{A.156}$$

from this ω_p is rearranged,

$$\omega_p = \left(\frac{e^2 n_p}{\epsilon_0 m}\right)^{1/2} \tag{A.157}$$

$$\omega_p^2 = \left(\frac{e^2 n_p}{\epsilon_0 m}\right) \tag{A.158}$$

$$\frac{\omega_p^2}{n_p} = \frac{e^2}{\epsilon_0 m} \tag{A.159}$$

$$\left(\frac{\partial^2}{\partial\bar{x}^2} + \frac{\partial^2}{\partial\bar{y}^2} - \frac{2\partial^2}{\partial\bar{z}\partial\bar{z}_2}\right) A_\perp = -\frac{\omega_p^2}{n_p}\frac{c^2a_u^2l_g}{2\gamma_r^2c^4\rho l_c^2}\frac{1}{\gamma_j\beta_{zj}}\frac{\partial}{\partial\bar{z}_2}\sum_{j=1}^{N}\bar{p}_{\perp j}\delta(\bar{x}_j, \bar{y}_j\bar{z}_{2j}) \tag{A.160}$$

using $l_g = \frac{1}{2k_u\rho}$

$$\left(\frac{\partial^2}{\partial\bar{x}^2} + \frac{\partial^2}{\partial\bar{y}^2} - \frac{2\partial^2}{\partial\bar{z}\partial\bar{z}_2}\right) A_\perp = -\frac{\omega_p^2}{n_p}\frac{a_u^2}{4k_u\rho\gamma_r^2c^2\rho l_c^2}\frac{1}{\gamma_j\beta_{zj}}\frac{\partial}{\partial\bar{z}_2}\sum_{j=1}^{N}\bar{p}_{\perp j}\delta(\bar{x}_j, \bar{y}_j\bar{z}_{2j}) \tag{A.161}$$

now ρ can be rearranged,

$$\rho = \frac{1}{\gamma_r}\left(\frac{a_u\omega_p}{4ck_u}\right)^{2/3} \tag{A.162}$$

$$(\rho\gamma_r)^3 = \left(\frac{a_u\omega_p}{4ck_u}\right)^2 \tag{A.163}$$

$$(\rho\gamma_r)^3 4k_u = \left(\frac{a_u^2\omega_p^2}{4c^2k_u}\right) \tag{A.164}$$

$$\left(\frac{\partial^2}{\partial\bar{x}^2} + \frac{\partial^2}{\partial\bar{y}^2} - \frac{2\partial^2}{\partial\bar{z}\partial\bar{z}_2}\right) A_\perp = (\rho\gamma_r)^3 4k_u \frac{1}{n_p}\frac{1}{\gamma_r^2\rho^2 l_c^2}\frac{1}{\gamma_j\beta_{zj}}\frac{\partial}{\partial\bar{z}_2}\sum_{j=1}^{N}\bar{p}_{\perp j}\delta(\bar{x}_j, \bar{y}_j\bar{z}_{2j}) \tag{A.165}$$

$$\left(\frac{\partial^2}{\partial\bar{x}^2} + \frac{\partial^2}{\partial\bar{y}^2} - \frac{2\partial^2}{\partial\bar{z}\partial\bar{z}_2}\right) A_\perp = 4k_u \frac{1}{n_p}\frac{1}{l_c^2}\frac{\rho\gamma_r}{\gamma_j\beta_{zj}}\frac{\partial}{\partial\bar{z}_2}\sum_{j=1}^{N}\bar{p}_{\perp j}\delta(\bar{x}_j, \bar{y}_j\bar{z}_{2j}) \tag{A.166}$$

$$\left(\frac{\partial^2}{\partial\bar{x}^2} + \frac{\partial^2}{\partial\bar{y}^2} - \frac{2\partial^2}{\partial\bar{z}\partial\bar{z}_2}\right) A_\perp = 2\frac{1}{n_p}\frac{2k_u\rho}{l_c^2}\frac{\gamma_r}{\gamma_j\beta_{zj}}\frac{\partial}{\partial\bar{z}_2}\sum_{j=1}^{N}\bar{p}_{\perp j}\delta(\bar{x}_j, \bar{y}_j\bar{z}_{2j}) \tag{A.167}$$

the gain length is defined $l_g = 1/2k_u\rho$

$$\frac{1}{2}\left(\frac{\partial^2}{\partial\bar{x}^2} + \frac{\partial^2}{\partial\bar{y}^2}\right) A_\perp - \frac{\partial^2}{\partial\bar{z}\partial\bar{z}_2}A_\perp = -\frac{1}{n_p}\frac{1}{l_g l_c^2}\frac{\gamma_r}{\gamma_j\beta_{zj}}\frac{\partial}{\partial\bar{z}_2}\sum_{j=1}^{N}\bar{p}_{\perp j}\delta(\bar{x}_j, \bar{y}_j\bar{z}_{2j}) \tag{A.168}$$

the scaled peak number density is $\bar{n}_p = l_g l_c^2 n_p$ and $L_j = \frac{\gamma_r}{\gamma_j\beta_{zj}}$

$$\frac{1}{2}\left(\frac{\partial^2}{\partial\bar{x}^2} + \frac{\partial^2}{\partial\bar{y}^2}\right) A_\perp - \frac{\partial^2}{\partial\bar{z}\partial\bar{z}_2}A_\perp = -\frac{L_j}{\bar{n}_p}\frac{\partial}{\partial\bar{z}_2}\sum_{j=1}^{N}\bar{p}_{\perp j}\delta(\bar{x}_j, \bar{y}_j\bar{z}_{2j}) \tag{A.169}$$

A.4 electron positions

A.4.1 longitudinal coordinate

The electron scaled coordinate $\bar{z}_2$ is given by,

$$\bar{z}_{2j} = 2k_r\rho(ct_j - z) \tag{A.170}$$

this is differentiated with respect to z,

$$\frac{d\bar{z}_{2j}}{dz} = 2k_r\rho(c\frac{dt_j}{dz} - 1) \tag{A.171}$$

$$\frac{d\bar{z}_{2j}}{dz} = 2k_r\rho(c\frac{1}{v_{zj}} - 1) \tag{A.172}$$

$$\frac{d\bar{z}_{2j}}{dz} = 2k_r\rho(\frac{1}{\beta_{zj}} - 1) \tag{A.173}$$

$$\frac{d\bar{z}_{2j}}{dz} = 2k_r\rho(\frac{1-\beta_{zj}}{\beta_{zj}}) \tag{A.174}$$

$$\tag{A.175}$$

now changing to $\bar{z}$ using $\frac{d}{dz} = 2k_u\rho\frac{d}{d\bar{z}}$

$$\frac{d\bar{z}_{2j}}{d\bar{z}} = \frac{k_r}{k_u}(\frac{1-\beta_{zj}}{\beta_{zj}}) \tag{A.176}$$

$$\tag{A.177}$$

using $\frac{1}{\eta} = \frac{\bar{\beta}_z}{1-\bar{\beta}_z} = \frac{k_r}{k_u}$

$$\frac{d\bar{z}_{2j}}{d\bar{z}} = \frac{1}{\eta}(\frac{1-\beta_{zj}}{\beta_{zj}}) \tag{A.178}$$

$$\tag{A.179}$$

now $p_{2j} = \frac{1}{\eta}(\frac{1-\beta_{zj}}{\beta_{zj}})$

$$\frac{d\bar{z}_{2j}}{d\bar{z}} = p_{2j} \tag{A.180}$$

A.4.2 transverse coordinates

The momentum in x is given by,

$$p_{xj} = \gamma_j mc\beta_{xj} \tag{A.181}$$

converting to scaled units $\bar{p}_{\perp j} = \frac{1}{mca_u} p_{\perp j} => p_{\perp j} = mca_u \bar{p}_{\perp j}$

$$\bar{p}_{xj} = \frac{\gamma_j v_{xj}}{a_u c} \tag{A.182}$$

$$\bar{p}_{xj} = \frac{\gamma_j}{a_u c}\frac{dx_j}{dt} \tag{A.183}$$

now changing to $\bar{z}$ using $\frac{d}{dt} = 2k_u\rho c\beta_{zj}\frac{d}{d\bar{z}}$

$$\bar{p}_{xj} = 2k_u\rho c\beta_{zj}\frac{\gamma_j}{a_u c}\frac{dx_j}{d\bar{z}} \tag{A.184}$$

$$\bar{p}_{xj} = 2k_u\rho\beta_{zj}\frac{\gamma_j}{a_u}\frac{dx_j}{d\bar{z}} \tag{A.185}$$

$$\frac{dx_j}{d\bar{z}} = \frac{a_u}{2k_u\rho\beta_{zj}\gamma_j}\bar{p}_{xj} \tag{A.186}$$

changing to a scaled x, i.e. $\frac{d\bar{x}}{dx} = \frac{1}{\sqrt{l_g l_c}}$

$$\sqrt{l_g l_c}\frac{d\bar{x}_j}{d\bar{z}} = \frac{a_u}{2k_u\rho\beta_{zj}\gamma_j}\bar{p}_{xj} \tag{A.187}$$

$$\frac{d\bar{x}_j}{d\bar{z}} = \frac{1}{\sqrt{l_g l_c}}\frac{a_u}{2k_u\rho\beta_{zj}\gamma_j}\bar{p}_{xj} \tag{A.188}$$

$$\frac{d\bar{x}_j}{d\bar{z}} = \sqrt{4k_r k_u\rho^2}\frac{a_u}{2k_u\rho\beta_{zj}\gamma_j}\bar{p}_{xj} \tag{A.189}$$

$$\frac{d\bar{x}_j}{d\bar{z}} = \sqrt{k_r k_u}\frac{a_u}{k_u\beta_{zj}\gamma_j}\bar{p}_{xj} \tag{A.190}$$

$$\frac{d\bar{x}_j}{d\bar{z}} = \frac{a_u\sqrt{k_r}}{\sqrt{k_u}\beta_{zj}\gamma_j}\bar{p}_{xj} \tag{A.191}$$

using $\frac{1}{\eta} = \frac{\bar{\beta}_z}{1-\bar{\beta}_z} = \frac{k_r}{k_u}$

$$\frac{d\bar{x}_j}{d\bar{z}} = \frac{a_u\bar{p}_{xj}}{\sqrt{\eta}\beta_{zj}\gamma_j} \tag{A.192}$$

now using $L_j = \frac{\gamma_r}{\gamma_j\beta_{zj}}$

$$\frac{d\bar{x}_j}{d\bar{z}} = L_j\frac{a_u\bar{p}_{xj}}{\sqrt{\eta}\gamma_r} \tag{A.193}$$

again using $\alpha = \frac{a_u}{2\rho\gamma_r}$

$$\frac{d\bar{x}_j}{d\bar{z}} = \frac{2\rho\alpha}{\sqrt{\eta}}L_j\bar{p}_{xj} \tag{A.194}$$

now since $\bar{p}_{\perp j} = \bar{p}_{xj} - i\bar{p}_{yj}$ therefore $\Re(\bar{p}_{\perp j}) = \bar{p}_{xj}$

$$\frac{d\bar{x}_j}{d\bar{z}} = \frac{2\rho\alpha}{\sqrt{\eta}}L_j\Re(\bar{p}_{\perp j}) \tag{A.195}$$

The momentum in y is given by,

$$p_{yj} = \gamma_j mc\beta_{yj} \tag{A.196}$$

converting to scaled units $\bar{p}_{\perp j} = \frac{1}{mca_u} p_{\perp j} => p_{\perp j} = mca_u \bar{p}_{\perp j}$

$$\bar{p}_{yj} = \frac{\gamma_j v_{yj}}{a_u c} \tag{A.197}$$

$$\bar{p}_{yj} = \frac{\gamma_j}{a_u c} \frac{dy_j}{dt} \tag{A.198}$$

now changing to $\bar{z}$ using $\frac{d}{dt} = 2k_u \rho c \beta_{zj} \frac{d}{d\bar{z}}$

$$\bar{p}_{yj} = 2k_u \rho c \beta_{zj} \frac{\gamma_j}{a_u c} \frac{dy_j}{d\bar{z}} \tag{A.199}$$

$$\bar{p}_{yj} = 2k_u \rho \beta_{zj} \frac{\gamma_j}{a_u} \frac{dy_j}{d\bar{z}} \tag{A.200}$$

$$\frac{dy_j}{d\bar{z}} = \frac{a_u}{2k_u \rho \beta_{zj} \gamma_j} \bar{p}_{yj} \tag{A.201}$$

changing to a scaled x, i.e. $\frac{d\bar{y}}{dy} = \frac{1}{\sqrt{l_g l_c}}$

$$\sqrt{l_g l_c} \frac{d\bar{y}_j}{d\bar{z}} = \frac{a_u}{2k_u \rho \beta_{zj} \gamma_j} \bar{p}_{yj} \tag{A.202}$$

$$\frac{d\bar{y}_j}{d\bar{z}} = \frac{1}{\sqrt{l_g l_c}} \frac{a_u}{2k_u \rho \beta_{zj} \gamma_j} \bar{p}_{yj} \tag{A.203}$$

$$\frac{d\bar{y}_j}{d\bar{z}} = \sqrt{4k_r k_u \rho^2} \frac{a_u}{2k_u \rho \beta_{zj} \gamma_j} \bar{p}_{yj} \tag{A.204}$$

$$\frac{d\bar{y}_j}{d\bar{z}} = \sqrt{k_r k_u} \frac{a_u}{k_u \beta_{zj} \gamma_j} \bar{p}_{yj} \tag{A.205}$$

$$\frac{d\bar{y}_j}{d\bar{z}} = \frac{a_u \sqrt{k_r}}{\sqrt{k_u} \beta_{zj} \gamma_j} \bar{p}_{yj} \tag{A.206}$$

using $\frac{1}{\eta} = \frac{\bar{\beta}_z}{1-\bar{\beta}_z} = \frac{k_r}{k_u}$

$$\frac{d\bar{y}_j}{d\bar{z}} = \frac{a_u \bar{p}_{yj}}{\sqrt{\eta}\beta_{zj}\gamma_j} \tag{A.207}$$

now using $L_j = \frac{\gamma_r}{\gamma_j \beta_{zj}}$

$$\frac{d\bar{y}_j}{d\bar{z}} = L_j \frac{a_u \bar{p}_{yj}}{\sqrt{\eta}\gamma_r} \tag{A.208}$$

again using $\alpha = \frac{a_u}{2\rho\gamma_r}$

$$\frac{d\bar{y}_j}{d\bar{z}} = \frac{2\rho\alpha}{\sqrt{\eta}} L_j \bar{p}_{yj} \tag{A.209}$$

now since $\bar{p}_{\perp j} = \bar{p}_{xj} - i\bar{p}_{yj}$ therefore $\Im(\bar{p}_{\perp j}) = -\bar{p}_{yj}$

$$\frac{d\bar{y}_j}{d\bar{z}} = -\frac{2\rho\alpha}{\sqrt{\eta}} L_j \Im(\bar{p}_{\perp j}) \tag{A.210}$$

A.5 final equations

The final set of Puffin equation are given as

$$\frac{dp_{2j}}{d\bar{z}} = \frac{\rho}{\eta} L_j^2 \left((\bar{p}^*_{\perp j} A_\perp + c.c)\eta p_{2j} - i\alpha^2 (1 + \eta p_{2j})(\bar{p}_{\perp j} b^*_{\omega\perp} - c.c.) \right) \tag{A.211}$$

and

$$\frac{d\bar{p}_{\perp j}}{d\bar{z}} = \frac{1}{2\rho} \left(i b_{w\perp} - \frac{\eta p_{2j}}{\alpha^2} A_\perp \right) - i\alpha \bar{p}_{\perp j} L_j b_z \tag{A.212}$$

And the field equation is given by,

$$\frac{1}{2} \left(\frac{\partial^2}{\partial \bar{x}^2} + \frac{\partial^2}{\partial \bar{y}^2} \right) A_\perp - \frac{\partial^2}{\partial \bar{z} \partial \bar{z}_2} A_\perp = -\frac{L_j}{\bar{n}_p} \frac{\partial}{\partial \bar{z}_2} \sum_{j=1}^{N} \bar{p}_{\perp j} \delta(\bar{x}_j, \bar{y}_j \bar{z}_{2j}) \tag{A.213}$$

the electron axial coordinates are described by,

$$\frac{d\bar{z}_{2j}}{d\bar{z}} = p_{2j} \tag{A.214}$$

$$\frac{d\bar{x}_j}{d\bar{z}} = \frac{2\rho\alpha}{\sqrt{\eta}} L_j \Re(\bar{p}_{\perp j}) \tag{A.215}$$

and

$$\frac{d\bar{y}_j}{d\bar{z}} = -\frac{2\rho\alpha}{\sqrt{\eta}} L_j \Im(\bar{p}_{\perp j}) \tag{A.216}$$

A.5.1 electron energy conservation

The equations describing the electron motion in the FEL are now checked for energy conservation. Taking the unscaled versions of the electron equations we can apply conservation of energy when the radiation field is neglected. Using the unscaled version of the equations A.60 and A.28

$$p_{zj}\frac{dp_{zj}}{d\bar{z}} = \frac{-e}{4k_u\rho}[p^*_{\perp j}(iB_{w\perp} + \frac{E_\perp}{c}) + c.c.)] \tag{A.217}$$

now neglecting the radiation field $E_\perp = 0$

$$p_{zj}\frac{dp_{zj}}{d\bar{z}} = \frac{-el_g}{2}[p^*_{\perp j}iB_{w\perp} + c.c.] \tag{A.218}$$

$$\frac{dp_{\perp j}}{d\bar{z}} = \frac{-e}{2k_u\rho}(\frac{E_\perp}{c}\left(\frac{1-\beta_{zj}}{\beta_{zj}}\right) + \frac{iB_z p_{\perp j}}{p_{zj}} - iB_{w\perp}) \tag{A.219}$$

again neglecting the radiation field $E_\perp = 0$

$$\frac{dp_{\perp j}}{d\bar{z}} = -el_g(\frac{iB_z p_{\perp j}}{p_{zj}} - iB_{w\perp}) \tag{A.220}$$

now taking the definition of relativistic momentum $\mathbf{p} = \boldsymbol{\gamma} m \boldsymbol{\beta} c \rightarrow \boldsymbol{\beta} = \mathbf{p}/\boldsymbol{\gamma} mc$. γ is defined as,

$$1/\boldsymbol{\gamma}^2 = 1 - \boldsymbol{\beta}^2 \tag{A.221}$$

$$1/\boldsymbol{\gamma}^2 = 1 - \left(\frac{\mathbf{p}}{\boldsymbol{\gamma} mc}\right)^2 \tag{A.222}$$

$$1 = \boldsymbol{\gamma}^2 - \left(\frac{\mathbf{p}}{mc}\right)^2 \tag{A.223}$$

$$\boldsymbol{\gamma}^2 = 1 + \left(\frac{\mathbf{p}}{mc}\right)^2 \tag{A.224}$$

$$\boldsymbol{\gamma}^2 = 1 + \frac{\mathbf{p} \cdot \mathbf{p}}{m^2 c^2} \tag{A.225}$$

$$\boldsymbol{\gamma}^2 = 1 + \frac{p_x^2 + p_y^2 + p_z^2}{m^2 c^2} \tag{A.226}$$

now rearranging the perpendicular momentum, $p_\perp = p_x - i p_y \rightarrow |p_\perp|^2 = (p_x - i p_y)(p_x + i p_y) = p_x^2 + p_y^2$

$$\boldsymbol{\gamma}_j^2 = 1 + \frac{|p_{\perp j}|^2 + p_{zj}^2}{m^2 c^2} \tag{A.227}$$

as there is no field in these equations we can apply conservation of energy to the electron equations ($\frac{d\gamma_j}{d\bar{z}} = 0$) $\boldsymbol{\gamma}_j^2 = 1 + \frac{|p_{\perp j}|^2 + p_{zj}^2}{m^2 c^2}$ use $|p_{\perp j}|^2 = p_{\perp j}^* p_{\perp j}$

$$\frac{d\boldsymbol{\gamma}_j^2}{d\bar{z}} = 2\gamma_j \frac{d\gamma_j}{d\bar{z}} = 0 \tag{A.228}$$

$$\frac{d|p_{\perp j}|^2}{d\bar{z}} + \frac{dp_{zj}^2}{d\bar{z}} = 0 \tag{A.229}$$

$$\frac{dp_{\perp j}^* p_{\perp j}}{d\bar{z}} + \frac{dp_{zj}^2}{d\bar{z}} = 0 \tag{A.230}$$

$$p_{\perp j}^* \frac{dp_{\perp j}}{d\bar{z}} + p_{\perp j} \frac{dp_{\perp j}^*}{d\bar{z}} + 2p_{zj} \frac{dp_{zj}}{d\bar{z}} = 0 \tag{A.231}$$

now insert equations A.218 and A.220

$$-p^*_{\perp j} el_g(\frac{iB_z p_{\perp j}}{p_{zj}} - iB_{w\perp}) - p_{\perp j} el_g(\frac{-iB_z p^*_{\perp j}}{p_{zj}} + iB^*_{w\perp}) \\ -el_g[p^*_{\perp j} iB_{w\perp} + c.c.] = 0 \tag{A.232}$$

$$p^*_{\perp j}(\frac{iB_z p_{\perp j}}{p_{zj}} - iB_{w\perp}) + p_{\perp j}(\frac{-iB_z p^*_{\perp j}}{p_{zj}} + iB^*_{w\perp}) + [p^*_{\perp j} iB_{w\perp} + c.c.] = 0 \tag{A.233}$$

$$(\frac{iB_z p_{\perp j}}{p_{zj}} p^*_{\perp j} - iB_{w\perp} p^*_{\perp j}) + (\frac{-iB_z p^*_{\perp j}}{p_{zj}} p_{\perp j} + iB^*_{w\perp} p_{\perp j}) + \\ p^*_{\perp j} iB_{w\perp} - p_{\perp j} iB^*_{w\perp} = 0 \tag{A.234}$$

$$-iB_{w\perp} p^*_{\perp j} + iB^*_{w\perp} p_{\perp j} + p^*_{\perp j} iB_{w\perp} - p_{\perp j} iB^*_{w\perp} = 0 \tag{A.235}$$

All of the terms cancel therefore $\frac{d\gamma_j^2}{d\bar{z}} = 0$ and energy conservation is satisfied.

Appendix B

Useful FEL derivations

B.1 Rescaling of EEHG

In Stupakov's notation p is defined differently from the scaled notation. Four coordinate transformations are made two modulation and two dispersive transformations. E_0 is replaced by E_r and p is defined as,

$$p = \frac{E - E_r}{\sigma_E} \tag{B.1}$$

$$p' = p + A_{1,2}\sin(zk_{1,2}) \tag{B.2}$$

$$z' = z + p\frac{R_{56}^{(1,2)}\sigma_E}{E_r} \tag{B.3}$$

E_r - mean energy (resonant) σ_E r.m.s. energy spread and $A = \frac{\Delta E}{\sigma_E}$. E is in eV. inserting equation B1 into equation B2

$$\frac{E' - E_r}{\sigma_E} = \frac{E - E_r}{\sigma_E} + \frac{\Delta E_{1,2}}{\sigma_E}\sin(zk_{1,2}) \tag{B.4}$$

$$E' = E + \Delta E_{1,2}\sin(zk_{1,2}) \tag{B.5}$$

equation 1 into equation 3

$$z' = z + \frac{E - E_0}{\sigma_E} \frac{R_{56}^{(1,2)} \sigma_E}{E_r} \tag{B.6}$$

$$z' = z + R_{56}^{(1,2)} \frac{E - E_r}{E_0} \tag{B.7}$$

assume compton limit $\rho \ll 1$ and $\beta_z \approx 1$ therefore $z = ct$ getting rid of the primes introduce E_0 and t_0, then equations 4 and 5 become.

$$E = E_0 + \Delta E_{1,2} \sin(\omega_{1,2} t) \tag{B.8}$$

$$t = t_0 + \frac{R_{56}^{(1,2)}}{c} \frac{E - E_r}{E_r} \tag{B.9}$$

redefine in terms of $\gamma = \frac{Ee}{mc^2}$, introduce j for the j^{th} electron.

$$\gamma_j = \gamma_{j0} + \Delta E_{1,2} \frac{e}{mc^2} \sin(\omega_{1,2} t) \tag{B.10}$$

$$t_j = t_{j0} + \frac{R_{56}^{(1,2)}}{c} \frac{\gamma_j - \gamma_r}{\gamma_r} \tag{B.11}$$

introduce scaled variables

$$\bar{z}_{1j} = \frac{z - c\bar{\beta}_z t_j}{\bar{\beta}_z l_c} \tag{B.12}$$

$$p_j = \frac{\gamma_j - \gamma_r}{\rho \gamma_r} \tag{B.13}$$

taking $z = 0$ and rearranging to give,

$$\bar{z}_{1j} = -\frac{ct_j}{l_c} \tag{B.14}$$

$$\bar{z}_{1j} = -2k_r\rho ct_j \tag{B.15}$$

$$\gamma_j = \rho\gamma_r p_j - \gamma_r \tag{B.16}$$

equation B.8 becomes

$$\rho\gamma_r p_j = \rho\gamma_r p_{j0} + \Delta E^{(1,2)}\frac{e}{mc^2} sin\left(\frac{-\omega_{1,2}\bar{z}_{1j}}{2k_r c\rho}\right) \tag{B.17}$$

$$p_j = p_{j0} - \frac{\Delta E^{(1,2)}}{\rho\gamma_r}\frac{e}{mc^2}\sin\left(\frac{\bar{z}_{1j}}{2\rho n_{1,2}}\right) \tag{B.18}$$

where $n_{1,2} = \frac{\omega_r}{\omega_{1,2}}$ equation B.9 become

$$\frac{\bar{z}_{1j}}{-2k_r c\rho} = \frac{\bar{z}_{1j0}}{-2k_r c\rho} + p_j\rho\frac{R_{56}^{(1,2)}}{c} \tag{B.19}$$

$$\bar{z}_{1j} = \bar{z}_{1j0} - 2k_r\rho R_{56}^{(1,2)}\rho p_j \tag{B.20}$$

define new variables,

$$p_{amp}^{(1,2)} = \frac{\Delta E^{(1,2)}}{\rho}\frac{e}{\gamma_r mc^2} \tag{B.21}$$

or as

$$p_{amp}^{(1,2)} = \frac{\Delta E^{(1,2)}}{\rho E_r} \tag{B.22}$$

or

$$p_{amp}^{(1,2)} = \frac{\Delta\gamma^{(1,2)}}{\gamma_r \rho} \tag{B.23}$$

and

$$\bar{R}_{56}^{(1,2)} = 2k_r \rho R_{56}^{(1,2)} \tag{B.24}$$

$$D^{(1,2)} = k_r \rho R_{56}^{(1,2)} \tag{B.25}$$

finally we are left with

$$p_j = p_{j0} - p_{amp}^{(1,2)} \sin\left(\frac{\bar{z}_{1j}}{2\rho n_{1,2}}\right) \tag{B.26}$$

$$\bar{z}_{1j} = \bar{z}_{1j0} - \rho p_j \bar{R}_{56}^{(1,2)} \tag{B.27}$$

$$\bar{z}_{1j} = \bar{z}_{1j0} - 2\rho p_j D^{(1,2)} \tag{B.28}$$

Which are written as four transformations

$$p_j = p_{j0} - p_{amp}^{(1)} \sin\left(\frac{\bar{z}_{1j}}{2\rho n_1}\right) \tag{B.29}$$

$$\bar{z}_{1j} = \bar{z}_{1j0} - 2\rho p_j D^{(1)} \tag{B.30}$$

$$p_j = p_{j0} - p_{amp}^{(2)} \sin\left(\frac{\bar{z}_{1j}}{2\rho n_2}\right) \tag{B.31}$$

$$\bar{z}_{1j} = \bar{z}_{1j0} - 2\rho p_j D^{(2)} \tag{B.32}$$

B.2 Undulator-chicane modes

Assume that the slippage in an undulator chicane module will be an integer multiple of the wavelengths, (i.e the only wavelength that survive are integer divisors of s),

$$s = n\lambda \tag{B.33}$$

$$\lambda = \frac{s}{n} \tag{B.34}$$

Now $\Delta\omega$, difference between adjacent side-band radiation modes, is calculated as,

$$\Delta\omega_{modal} = \omega_n - \omega_{n-1} \tag{B.35}$$

as $\omega = 2\pi c/\lambda = n2\pi c/s$,

$$\Delta\omega_{modal} = \frac{2\pi c}{s}(n - (n-1)) \tag{B.36}$$

$$\Delta\omega_{modal} = \frac{2\pi c}{s}. \tag{B.37}$$

B.3 Converting wave equations derivatives to scaled notation

The 1D wave equation's partial derivatives in time and space are converted to scaled notation. First of all using the scaling of $\bar{z}_1$. Rearranging the definition of $\bar{z}_1$ and using the definition of $z = l_g\bar{z}$,

$$\bar{z}_1 = \frac{z - c\bar{\beta}_z t}{\bar{\beta}_z l_c} \tag{B.38}$$

$$\bar{z}_1 = \frac{l_g\bar{z} - c\bar{\beta}_z t}{\bar{\beta}_z l_c} \tag{B.39}$$

$$\bar{\beta}_z l_c \bar{z}_1 = l_g\bar{z} - c\bar{\beta}_z t \tag{B.40}$$

$$t = \frac{l_g}{c\bar{\beta}_z}\bar{z} - \frac{l_c}{c}\bar{z}_1 \tag{B.41}$$

now differentiating t and z w.r.t $\bar{z}$ and $\bar{z}_1$

$$\frac{\partial t}{\partial \bar{z}} = \frac{l_g}{c\bar{\beta}_z} \tag{B.42}$$

$$\frac{\partial t}{\partial \bar{z}_1} = -\frac{l_c}{c} \tag{B.43}$$

$$\frac{\partial z}{\partial \bar{z}} = l_g \tag{B.44}$$

$$\frac{\partial z}{\partial \bar{z}_1} = 0 \tag{B.45}$$

Now using the chain rule for partial derivatives,

$$\frac{\partial}{\partial \bar{z}} = \frac{\partial t}{\partial \bar{z}}\frac{\partial}{\partial t} + \frac{\partial z}{\partial \bar{z}}\frac{\partial}{\partial z} \tag{B.46}$$

$$\frac{\partial}{\partial \bar{z}} = \frac{l_g}{c\bar{\beta}_z}\frac{\partial}{\partial t} + l_g\frac{\partial}{\partial z} \tag{B.47}$$

and

$$\frac{\partial}{\partial \bar{z}_1} = \frac{\partial t}{\partial \bar{z}_1}\frac{\partial}{\partial t} + \frac{\partial z}{\partial \bar{z}_1}\frac{\partial}{\partial z} \tag{B.48}$$

$$\frac{\partial}{\partial \bar{z}_1} = -\frac{l_c}{c}\frac{\partial}{\partial t} + 0 \tag{B.49}$$

Now using $\frac{l_g}{\bar{\beta}_z} = l_g + l_c$;[1]

$$\frac{\partial}{\partial \bar{z}} + \frac{\partial}{\partial \bar{z}_1} = \frac{l_g + l_c}{c}\frac{\partial}{\partial t} + l_g\frac{\partial}{\partial z} - \frac{l_c}{c}\frac{\partial}{\partial t} \tag{B.50}$$

$$\left(\frac{\partial}{\partial \bar{z}} + \frac{\partial}{\partial \bar{z}_1}\right) = l_g\left(\frac{\partial}{\partial z} + \frac{1}{c}\frac{\partial}{\partial t}\right) \tag{B.51}$$

now take $\frac{\partial}{\partial \bar{z}_1} = -\frac{l_c}{c}\frac{\partial}{\partial t}$ and use $\frac{l_c}{l_g} = \frac{1-\bar{\beta}_z}{\bar{\beta}_z}$ to give, $\frac{\partial}{\partial \bar{z}_1} = -\frac{l_g}{c}\frac{1-\bar{\beta}_z}{\bar{\beta}_z}\frac{\partial}{\partial t}$. Now combining with the above expression,

$$\left(\frac{\partial}{\partial \bar{z}} + \frac{\partial}{\partial \bar{z}_1}\right) + 2\frac{\bar{\beta}_z}{1-\bar{\beta}_z}\frac{\partial}{\partial \bar{z}_1} = l_g\left(\frac{\partial}{\partial z} + \frac{1}{c}\frac{\partial}{\partial t}\right) - 2\frac{l_g}{c}\frac{\partial}{\partial t} \tag{B.52}$$

$$\left(\frac{\partial}{\partial \bar{z}} + \frac{\partial}{\partial \bar{z}_1}\right) + 2\frac{\bar{\beta}_z}{1-\bar{\beta}_z}\frac{\partial}{\partial \bar{z}_1} = l_g\left(\frac{\partial}{\partial z} - \frac{1}{c}\frac{\partial}{\partial t}\right) \tag{B.53}$$

$$2\frac{\bar{\beta}_z}{1-\bar{\beta}_z}\left[\frac{1-\bar{\beta}_z}{2\bar{\beta}_z}\left(\frac{\partial}{\partial \bar{z}} + \frac{\partial}{\partial \bar{z}_1}\right) + \frac{\partial}{\partial \bar{z}_1}\right] = l_g\left(\frac{\partial}{\partial z} - \frac{1}{c}\frac{\partial}{\partial t}\right) \tag{B.54}$$

[1]This comes from rearranging the resonance condition $\frac{k_w}{k_r} = \frac{l_c}{l_g} = \frac{1-\bar{\beta}_z}{\bar{\beta}_z}$, $\frac{l_c}{l_g} + 1 = \frac{1-\bar{\beta}_z}{\bar{\beta}_z} + 1 \rightarrow \frac{l_c+l_g}{l_g} = \frac{1}{\bar{\beta}_z} \rightarrow l_c + l_g = \frac{l_g}{\bar{\beta}_z}$

Now looking at the partial derivatives in $\bar{z}_2$,

$$\bar{z}_2 = \frac{\bar{\beta}_z}{(1-\bar{\beta}_z)}\frac{(ct-z)}{l_g} \tag{B.55}$$

$$\bar{z}_2 = \frac{(ct-z)}{l_c} \tag{B.56}$$

$$\bar{z}_2 l_c = ct - z \tag{B.57}$$

$$\bar{z}_2 l_c = ct - \bar{z} l_g \tag{B.58}$$

$$ct = \bar{z}_2 l_c + \bar{z} l_g \tag{B.59}$$

$$t = \bar{z}_2 \frac{l_c}{c} + \bar{z}\frac{l_g}{c} \tag{B.60}$$

now differentiating w.r.t $\bar{z}$ and $\bar{z}_2$

$$\frac{\partial t}{\partial \bar{z}} = \frac{l_g}{c} \tag{B.61}$$

$$\frac{\partial t}{\partial \bar{z}_2} = \frac{l_c}{c} \tag{B.62}$$

and

$$\frac{\partial z}{\partial \bar{z}} = l_g \tag{B.63}$$

$$\frac{\partial z}{\partial \bar{z}_2} = 0 \tag{B.64}$$

again using the chain rule for partial derivatives

$$\frac{\partial}{\partial \bar{z}} = \frac{\partial t}{\partial \bar{z}}\frac{\partial}{\partial t} + \frac{\partial z}{\partial \bar{z}}\frac{\partial}{\partial z} \tag{B.65}$$

$$\frac{\partial}{\partial \bar{z}} = l_g\left(\frac{\partial}{\partial z} + \frac{1}{c}\frac{\partial}{\partial t}\right) \tag{B.66}$$

and

$$\frac{\partial}{\partial \bar{z}_2} = \frac{\partial t}{\partial \bar{z}_2}\frac{\partial}{\partial t} + \frac{\partial z}{\partial \bar{z}_2}\frac{\partial}{\partial z} \tag{B.67}$$

$$\frac{\partial}{\partial \bar{z}_2} = \frac{l_c}{c}\frac{\partial}{\partial t} + 0 \tag{B.68}$$

now using $\frac{l_c}{l_g} = \frac{1-\bar{\beta}_z}{\bar{\beta}_z}$

$$\frac{\partial}{\partial \bar{z}_2} = \frac{1-\bar{\beta}_z}{\bar{\beta}_z}\frac{l_g}{c}\frac{\partial}{\partial t} \tag{B.69}$$

$$2\frac{\bar{\beta}_z}{1-\bar{\beta}_z}\frac{\partial}{\partial \bar{z}_2} = 2\frac{l_g}{c}\frac{\partial}{\partial t} \tag{B.70}$$

now combining equation B.70 with B.66

$$\frac{\partial}{\partial \bar{z}} - 2\frac{\bar{\beta}_z}{1-\bar{\beta}_z}\frac{\partial}{\partial \bar{z}_2} = l_g\left(\frac{\partial}{\partial z} + \frac{1}{c}\frac{\partial}{\partial t}\right) - 2\frac{l_g}{c}\frac{\partial}{\partial t} \tag{B.71}$$

$$\left(\frac{\partial}{\partial \bar{z}} - 2\frac{\bar{\beta}_z}{1-\bar{\beta}_z}\frac{\partial}{\partial \bar{z}_2}\right) = l_g\left(\frac{\partial}{\partial z} - \frac{1}{c}\frac{\partial}{\partial t}\right) \tag{B.72}$$

B.4 undulator dispersion compensation

The dispersion in the undulator can compensated for by using a chicane with a negative dispersion. To show this the energy dependent slippage length is derived. To begin, in the undulator the electron pulse's longitudinal coordinate evolves according to,

$$\frac{d\bar{z}_2}{d\bar{z}} = p_{2j} \tag{B.73}$$

therefore an electron will change its position in proportion to p_2,

$$\Delta\bar{z}_{2u} = p_{2j}\Delta\bar{z} \tag{B.74}$$

hence if the slippage in an undulator is $\bar{l}$ then $\Delta\bar{z}_{2u} = p_{2j}\bar{l}$, in a chicane the change in position of an electron is given by

$$\Delta\bar{z}_{2c} = -(1-p_2)D + \bar{\delta} \tag{B.75}$$

therefore the combining the undulator and chicane slippages gives,

$$\Delta\bar{z}_{2u+c} = \Delta\bar{z}_{2u} + \Delta\bar{z}_{2c} \tag{B.76}$$
$$\Delta\bar{z}_{2u+c} = p_{2j}\bar{l} - (1-p_{2j})D + \bar{\delta} \tag{B.77}$$
$$\Delta\bar{z}_{2u+c} = p_{2j}\bar{l} - D + p_{2j}D + \bar{\delta} \tag{B.78}$$
$$\Delta\bar{z}_{2u+c} = p_{2j}(\bar{l}+D) - D + \bar{\delta} \tag{B.79}$$

if $D = -l$

$$\Delta\bar{z}_{2u+c} = \bar{l} + \bar{\delta} \tag{B.80}$$
$$\Delta\bar{z}_{2u+c} = \bar{s} \tag{B.81}$$

then the p_2 dependence of slippage in undulator-chicane module is suppressed, i.e. the slippage is $\bar{s}$ regardless of the electron energy. The undulator-chicane module slippage can be written in terms of γ by using the approximation

$p_{2j} = 1 - 2\left(\frac{\gamma_j - \gamma_r}{\gamma_r}\right)$, however this only valid for small energy variations

$$\Delta\bar{z}_{2u+c} = \left(1 - 2\left(\frac{\gamma_j - \gamma_r}{\gamma_r}\right)\right)(\bar{l} + D) - D + \bar{\delta} \tag{B.82}$$

$$\Delta\bar{z}_{2u+c} = (\bar{l} + D) - \left(2\left(\frac{\gamma_j - \gamma_r}{\gamma_r}\right)\right)(\bar{l} + D) - D + \bar{\delta} \tag{B.83}$$

$$\Delta\bar{z}_{2u+c} = \bar{l} - \left(2\left(\frac{\gamma_j - \gamma_r}{\gamma_r}\right)\right)(\bar{l} + D) + \bar{\delta} \tag{B.84}$$

$$\Delta\bar{z}_{2u+c} = -\left(2\left(\frac{\gamma_j - \gamma_r}{\gamma_r}\right)\right)(\bar{l} + D) + \bar{l} + \bar{\delta} \tag{B.85}$$

$$\Delta\bar{z}_{2u+c} = 2\left(\frac{\gamma_r - \gamma_j}{\gamma_r}\right)(\bar{l} + D) + \bar{s} \tag{B.86}$$

$$\bar{s}_\gamma = 2\left(\frac{\gamma_r - \gamma_j}{\gamma_r}\right)(\bar{l} + D) + \bar{s} \tag{B.87}$$

if $D = -\bar{l}$ then

$$\bar{s}_\gamma = \bar{s} \tag{B.88}$$

therefore the energy dependence of the slippage in undulator chicane modules has been suppressed. The above expression of chicane slippage in p_2 is an approximation which is only valid for small energy deviations. Real chicanes apply a dispersion in γ i.e. the change in $\bar{z}_2$ for a chicane is given by

$$\Delta\bar{z}_{2c} = 2\left(\frac{\gamma_r - \gamma_j}{\gamma_r}\right)D + \bar{\delta} \tag{B.89}$$

therefore the change in $\bar{z}_2$ for an undulator-chicane module is given by,

$$\Delta\bar{z}_{2u+c} = \Delta\bar{z}_{2u} + \Delta\bar{z}_{2c} \tag{B.90}$$

$$\Delta\bar{z}_{2u+c} = p_{2j}\bar{l} + 2\left(\frac{\gamma_r - \gamma_j}{\gamma_r}\right)D + \bar{\delta} \tag{B.91}$$

now if $D = -\bar{l}$

$$\Delta\bar{z}_{2u+c} = p_{2j}\bar{l} - 2\left(\frac{\gamma_r - \gamma_j}{\gamma_r}\right)\bar{l} + \bar{\delta} \tag{B.92}$$

in order to eliminate the energy dependence of the undulator-chicane slippage length here, the following approximation must hold $p_{2j} = 1 - 2\left(\frac{\gamma_j - \gamma_r}{\gamma_r}\right)$

$$\Delta\bar{z}_{2u+c} = \left(1 - 2\left(\frac{\gamma_j - \gamma_r}{\gamma_r}\right)\right)\bar{l} - 2\left(\frac{\gamma_r - \gamma_j}{\gamma_r}\right)\bar{l} + \bar{\delta} \tag{B.93}$$

$$\Delta\bar{z}_{2u+c} = \left(1 + 2\left(\frac{\gamma_r - \gamma_j}{\gamma_r}\right)\right)\bar{l} - 2\left(\frac{\gamma_r - \gamma_j}{\gamma_r}\right)\bar{l} + \bar{\delta} \tag{B.94}$$

$$\Delta\bar{z}_{2u+c} = \bar{l} + \bar{\delta} = \bar{s} \tag{B.95}$$

however the above approximation only holds for small variations in energy. But in expression B.79 the p_2 dependence can always be eliminated by setting $D = -\bar{l}$ regardless of variations in p_2. Therefore using a chicane that disperse in p_2 can fully reverse the dispersion of an undulator regardless of energy variation, however a chicane that disperses in γ can not. This fact is illustrated in figure 7.4 where to produce coherent phase-correlated radiation in each new undulator section, the chicane must fully reverse the undulator dispersion. By doing so, the coherent radiation fields can coherently superimpose and the radiation field power scales as the square of the number of undulator-chicane modules. If the radiation fields do not coherently superimpose, e.g. the chicane disperses in γ, the radiation field power scales as the number of undulator-chicane modules.

B.5 rf-func beam distribution function

The final distribution function of a triple-modulator-chicane scheme is given below.

$$f(\bar{z}_2,\gamma) = \frac{1}{2\pi}\frac{1}{\sigma_\gamma}\frac{1}{\sigma_{\bar{z}_2}}\exp\left(\frac{-1}{2\sigma_\gamma^2}\left([((\gamma+\Delta\gamma_3\sin(\frac{1}{2n_3\rho}(\bar{z}_2+2D_3(\gamma-\gamma_r)/\gamma_r)+\phi_3))\right.\right.$$
$$+\Delta\gamma_2\sin(\frac{1}{2n_2\rho}((\bar{z}_2+2D_3(\gamma-\gamma_r)/\gamma_r)+2D_2((\gamma+\Delta\gamma_3\sin(\frac{1}{2n_3\rho}(\bar{z}_2+2D_3(\gamma-\gamma_r)/\gamma_r)+\phi_3))-\gamma_r)/\gamma_r)+\phi_2))$$
$$+\Delta\gamma_1\sin(\frac{1}{2n_1\rho}(((\bar{z}_2+2D_3(\gamma-\gamma_r)/\gamma_r)+2D_2((\gamma+\Delta\gamma_3\sin(\frac{1}{2n_3\rho}(\bar{z}_2+2D_3(\gamma-\gamma_r)/\gamma_r)+\phi_3))-\gamma_r)/\gamma_r)$$
$$+2D_1(((\gamma+\Delta\gamma_3\sin(\frac{1}{2n_3\rho}(\bar{z}_2+2D_3(\gamma-\gamma_r)/\gamma_r)+\phi_3))+\Delta\gamma_2\sin(\frac{1}{2n_2\rho}((\bar{z}_2+2D_3(\gamma-\gamma_r)/\gamma_r)$$
$$\left.\left.+2D_2((\gamma+\Delta\gamma_3\sin(\frac{1}{2n_3\rho}(\bar{z}_2+2D_3(\gamma-\gamma_r)/\gamma_r)+\phi_3))-\gamma_r)/\gamma_r)+\phi_2))-\gamma_r)/\gamma_r)+\phi_1)]-\gamma_r\right)^2\right)$$
$$\exp\left(\frac{-1}{2\sigma_{\bar{z}_2}^2}\left([((\bar{z}_2+2D_3(\gamma-\gamma_r)/\gamma_r)+2D_2((\gamma+\Delta\gamma_3\sin(\frac{1}{2n_3\rho}(\bar{z}_2+2D_3(\gamma-\gamma_r)/\gamma_r)+\phi_3))-\gamma_r)/\gamma_r)\right.\right.$$
$$+2D_1(((\gamma+\Delta\gamma_3\sin(\frac{1}{2n_3\rho}(\bar{z}_2+2D_3(\gamma-\gamma_r)/\gamma_r)+\phi_3))+\Delta\gamma_2\sin(\frac{1}{2n_2\rho}((\bar{z}_2+2D_3(\gamma-\gamma_r)/\gamma_r)$$
$$\left.\left.+2D_2((\gamma+\Delta\gamma_3\sin(\frac{1}{2n_3\rho}(\bar{z}_2+2D_3(\gamma-\gamma_r)/\gamma_r)+\phi_3))-\gamma_r)/\gamma_r)+\phi_2))-\gamma_r)/\gamma_r]-\bar{z}_c\right)^2\right)$$

The energy modulation parameters $\Delta\gamma_{1,2,3}$, modulation frequencies $n_{1,2,3} = k_{1,2,3}/k_w$ and modulation phases $\phi_{1,2,3}$ are associated with first, second and third modulator sections respectively. Similarly $D_{1,2,3}$ are the dispersion factors for chicane 1,2 and 3. $\sigma_{\gamma,\bar{z}_2}$ is the standard deviations in γ and $\bar{z}_2$. The resonant energy is defined as $\gamma_r =< \gamma > |_{\bar{z}=0}$ and the electron pulse centre is given by $\bar{z}_c$.

Appendix C

Publications

- New Journal of Physics Paper (submitted on 24/04/15)
- FEL 2014 Paper 1 (presented as poster)
- FEL 2014 Paper 2 (presented as talk)
- Europhysics Letters Paper

Free Electron Lasers using 'Beam by Design'

J. R. Henderson[1,2], L.T. Campbell[1,2] and B.W.J. M^{c}Neil[1]

1 SUPA, Department of Physics, University of Strathclyde, Glasgow, G4 0NG, UK
2 ASTeC, STFC Daresbury Laboratory and Cockcroft Institute, Warrington, WA4 4AD, UK

E-mail: j.r.henderson@strath.ac.uk, lawrence.campbell@strath.ac.uk, b.w.j.mcneil@strath.ac.uk

Submitted to: *New J. Phys.*

Abstract. Several methods have been proposed in the literature to improve Free Electron Laser output by transforming the electron phase-space before entering the FEL interaction region. By utilising 'beam by design' with novel undulators and other beam changing elements, the operating capability of FELs may be further usefully extended. This paper introduces two new such methods to improve output from electron pulses with large energy spreads and the results of simulations of these methods in the 1D limit are presented. Both methods predict orders of magnitude improvements to output radiation powers.

PACS numbers: 41.60.Cr

1. Introduction

The Free Electron Laser (FEL) is an important scientific research tool that uses a relativistic electron beam to generate coherent radiation from the microwave through to the hard X-ray. At shorter wavelengths into the X-ray, this is unlocking many new areas of science in diverse fields such as: Warm-Dense matter studies [1]; short pulse protein diffraction [2] and medicine/surgery [3]. Current X-ray FELs [4, 5] and those under construction [6], are unique laboratory sources of high power coherent X-rays. They are driven by electron beams generated from Radio-Frequency linear accelerators, which can be up to a few kilometres long.

Many ideas are now being proposed to enhance and improve FEL output, towards shorter wavelengths, shorter output pulse durations, improved temporal coherence [7] and multi-colour operation [8]. These improvements extend the original high-gain FEL design where the electron beam from an accelerator is simply injected into a long undulator where the collective FEL interaction generates coherent output. The new methods rely upon manipulation of the electron beam in phase-space, using laser modulators and magnetic chicanes, either prior to injection into the FEL, or sequentially along the undulator as the FEL interaction progresses.

Proposals also exist to reduce the overall lengths of FEL facilities by replacing the RF-linacs with plasma-wakefield accelerators [9, 10]. These accelerators have large accelerating gradients about 10^3-10^4 times larger than RF-linacs. However, the electron bunches generated so far are limited by a relatively large energy spread which inhibits any useful FEL interaction. As with the above proposed enhancements, methods that manipulate the electron beams have been proposed that may help mitigate the detrimental effects of energy spread. These include stretching the beam longitudinally before injection into the FEL to reduce the localised energy spread [11], or transversely dispersing the electron beam to give a correlated transverse energy distribution and then matching this into a transverse gradient undulator [12].

Using a combination of modulators and chicanes, it is also possible to fourier-compose electron pulses of simple geometric shapes in longitudinal electron beam phase space e.g. rectangular, triangular, and sawtooth [13]. Such waveform synthesis of the electron beam can also be utilised to generate phase-correlated harmonic beam

structures that can then perform analogous waveform synthesis of the coherent light emission from the beam structures.

The electron beam parameters and manipulations described above can be very difficult, if not impossible, to model using conventional FEL simulation codes, which average the FEL interaction over a resonant radiation wavelength limiting both the radiation bandwidth that can be modelled and the range of electron energies, correlated or uncorrelated, within the beam.

In this paper the un-averaged FEL simulation code PUFFIN [14] is used to simulate potentially useful electron beam undulator emission that would not be possible using conventional averaged FEL simulation codes.

Firstly, a new method using electron beam phase-space manipulation is investigated, that may allow a FEL to operate with larger electron beam energy spreads which, for example, may assist the drive towards plasma-accelerator driven FELs. The method constructs a series of energy-chirped electron pulses (beamlets), each of different mean energy, vertically stacked in energy in phase space. The localised, or 'slice', energy spread of each beamlet is smaller than the original, unmodified beam from which the beamlets are constructed. Previous work has used multiple beams generated individually by a photocathode illuminated by multiple light pulses to generate different colour pulses from a FEL [15]. Here, however, the beamlets are generated from a single electron pulse.

Secondly, an example is presented of what may be possible using fourier-synthesised electron beams [13]. This is the first simulation of the output from such waveforms in a FEL-type system. A fourier-synthesised electron pulse with a rectangular wave structure in phase space is used to generate radiation in a series of undulator-chicane modules similar to those used in a mode-locked FEL amplifier [16]. The 'discontinuous' regions of the square electron pulse form larger current regions that can emit significant coherent spontaneous emission (see e.g. [17]). This coherent emission is periodically superimposed using a sequence of undulator-chicane modules and is shown to be able to generate significant output powers. This cannot strictly be called a FEL as little FEL interaction takes place.

The methods simulated here are clearly not to be considered as specific FEL design proposals, rather they are intended to demonstrate future possibilities and potential as electron beam generation advances beyond that of a simple linear beam model.

2. Beamlets

2.1. Beamlets - Description of Method

In the Free Electron Laser (FEL), a relativistic electron beam of mean electron energy $\gamma_r m_e c^2$ amplifies radiation in an undulator of period λ_u and rms magnetic field strength B_u. The resonant radiation wavelength amplified is given by $\lambda_r = \lambda_u(1 + a_u^2)/2\gamma_r^2$. The high-gain amplification process is characterised by the gain length l_g, where an initial radiation power P_0 is amplified exponentially as a function of the distance z through

the undulator as $P(z) = P_0 \exp(\sqrt{3}z/l_g)$ [18]. With an electron beam energy of γ_r, the gain length may be written, neglecting radiation diffraction and for no electron beam energy spread $\sigma_\gamma = 0$, as:

$$l_g = \frac{\lambda_u}{4\pi\rho} = \frac{1}{2k_u\rho}, \tag{1}$$

where: $k_u = 2\pi/\lambda_u$,

$$\rho = \frac{1}{\gamma_r}\left(\frac{\bar{a}_u\omega_p}{4ck_u}\right)^{2/3} \propto I_{pk}^{1/3}, \tag{2}$$

is the is the FEL (or Pierce) parameter, $\bar{a}_u \propto B_u k_u$ is the undulator parameter, ω_p is the peak (non-relativistic) plasma frequency of the beam, and I_{pk} is the peak current. For good amplification, the electron beam energy spread σ_γ must satisfy the 'cold beam' limit of:

$$\sigma_p = \frac{\sigma_\gamma}{\rho\gamma_r} \ll 1. \tag{3}$$

Optimal FEL gain is seen to occur when I_{pk} is maximised and σ_γ minimised. The method described below uses electron beam phase space manipulation to modify both of these parameters in an attempt to improve the FEL output potential of beams with large energy spreads ($\sigma_p \gtrsim 1$).

The method first generates a series of energy chirped beamlets stacked vertically in longitudinal phase space before they are injected into the FEL amplifier. As the FEL interaction occurs within the undulator further manipulation is required to ensure the radiation interaction with the chirped electron beamlets maintains a resonant interaction.

In the first stage before injection into the FEL, the electron beam is passed through a modulating undulator and dispersive chicane, resulting in the beam phase space shown in figure 1. This phase space is similar to the first modulator-chicane section used in the Echo Enhanced Harmonic Gain method [19]. The modulator-chicane sections perform the following consecutive transforms on the electron beam phase space coordinates:

$$\gamma = \gamma_0 - \Delta\gamma \sin\left(\frac{\bar{z}_{20}}{2\rho n} + \phi\right) \tag{4}$$

$$\bar{z}_2 = \bar{z}_{20} - 2D\left(\frac{\gamma - \gamma_r}{\gamma_r}\right), \tag{5}$$

where the subscript 0 denotes the initial, untransformed coordinates, $\bar{z}_2 = (ct - z)/l_c$ is the coordinate in a window travelling at the speed of light scaled with respect to the cooperation length $l_c = \lambda_r/4\pi\rho$ of the FEL interaction, $\Delta\gamma$ is the energy modulation amplitude, $n = \lambda_1/\lambda_r$ is the modulation period scaled with respect to the resonant wavelength and $D = k_r\rho R_{56}$ is the scaled dispersive strength of the chicane. With this scaling, a resonant electron of energy γ_r will fall behind a resonant radiation wavefront a distance l_c on propagating one gain length l_g through the undulator [20].

It has been observed that in regimes where large dispersion is applied that the noise statistics of the macroparticles that simulate the electrons in the dispersed beam can become incorrect. This occurs as the beam sampling in $\bar{z}_2$ is transformed into the γ dimension when rotated in phase space, and vice-versa. To ensure the correct noise is modelled, the functional form of the final electron beam phase space is used to initialize the beam before application of the noise algorithm [21] and simulation using Puffin.

A gaussian distribution for both dimensions of the initial beam phase space is assumed:

$$f(\bar{z}_2,\gamma) = \frac{1}{2\pi\sigma_\gamma\sigma_{\bar{z}_2}} \exp\left[-\frac{(\gamma-\gamma_r)^2}{2\sigma_\gamma^2}\right] \exp\left[-\frac{(\bar{z}_2-\bar{z}_c)^2}{2\sigma_{\bar{z}_2}^2}\right], \tag{6}$$

where: $\bar{z}_c$ is the electron pulse centre and $\sigma_{\gamma,\bar{z}_2}$ are the standard deviations in γ and $\bar{z}_2$ respectively.

By applying similar modulation and dispersive transforms to those outlined in [19], the final beam distribution function obtained is:

$$f(\bar{z}_2,\gamma) = \frac{1}{2\pi\sigma_\gamma\sigma_{\bar{z}_2}} \exp\left[-\frac{1}{2\sigma_\gamma^2}\left(\gamma + \Delta\gamma \sin\left[\frac{1}{2\rho n}\left(\bar{z}_2 \ +2D\left(\frac{\gamma-\gamma_r}{\gamma_r}\right)\right)+\phi\right] - \gamma_r\right)^2\right]$$
$$\times \exp\left[-\frac{1}{2\sigma_{\bar{z}_2}^2}\left(\bar{z}_2 + 2D\left(\frac{\gamma-\gamma_r}{\gamma_r}\right) - \bar{z}_c\right)^2\right]. \tag{7}$$

Figure 1 plots the scaled longitudinal phase space distribution function of the electrons after the modulation-dispersive section and before injection into the FEL undulator using the scaled energy parameter $p_j = (\gamma_j - \gamma_r)/\rho\gamma_r$ with the following parameters: $\Delta\gamma = 0.04\gamma_r$, $D = 268.51$, $n = 68$, $\phi = 0$, $\sigma_\gamma = 2\rho\gamma_r$ (or $\sigma_p = 2$), $\gamma_r = 1200$, $\rho = 1.6\times10^{-2}$ and $\sigma_{\bar{z}_2} = 28.97$. The modulation and dispersion of the beam is seen to create a stacked structure of energy chirped 'beamlets', slice sections of which are seen to have an energy spread which is reduced from the initial un-transformed beam with $\sigma_p = 2$. Under certain conditions, each beamlet may then emit and amplify radiation independently of the other beamlets. The combined output from each of the beamlets may then give improved radiation output over the un-transformed beam.

To illustrate how the method functions in the FEL undulator, a simplified version of the beamlet phase space is shown in figure 2, which consists of a series of chirped, zero energy spread, electron beamlets of different mean energies stacked in phase space. The chirp causes the radiation from one section of the chirped beam to drift out of resonance as it propagates into electrons which are resonant at a different wavelength. This impedes the FEL gain process. This effect may be successfully counteracted by using an appropriate undulator tapering to maintain the electron-radiation resonance [22]. (These results have been reproduced using the simulation methods used here and are in very good agreement [23].) Here, a different approach is demonstrated using a periodic series of undulator-chicane modules with multiple beamlets. The beamlets are periodically delayed by the chicanes so as to maintain a resonant interaction with the radiation generated by electrons of the same energy from the other beamlets.

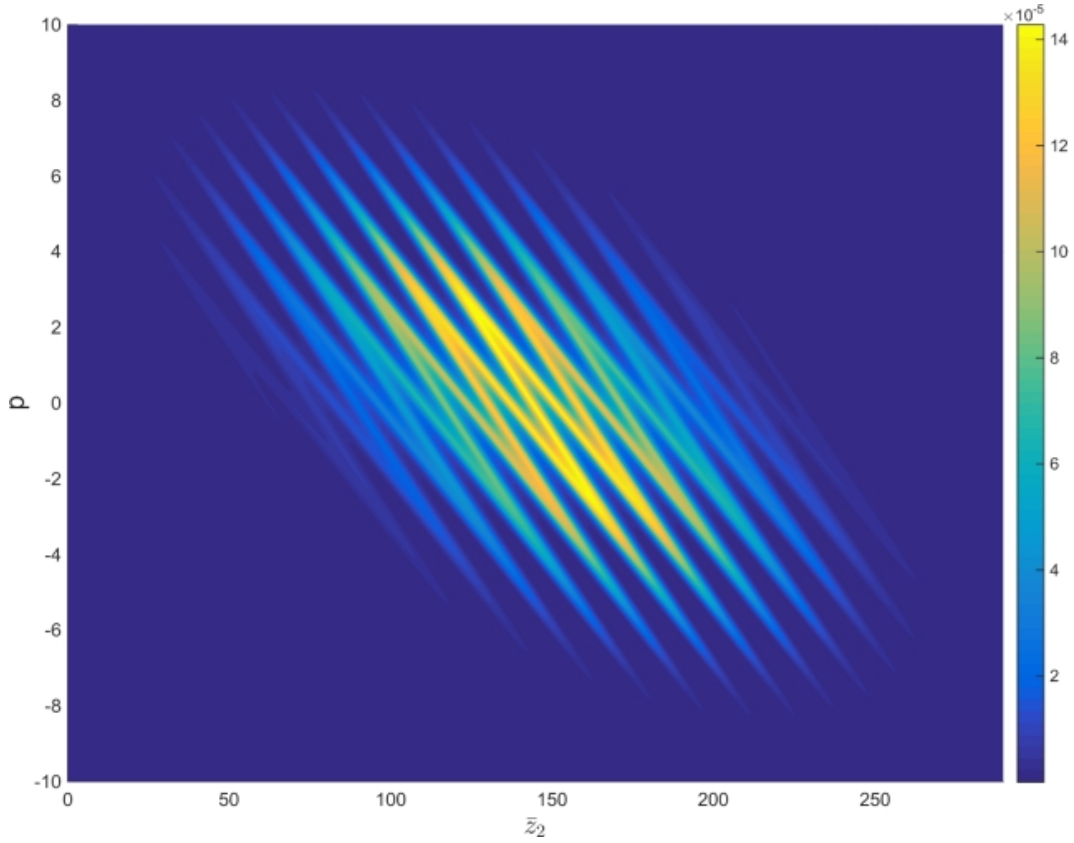

Figure 1. The scaled longitudinal electron beam phase space distribution function given by equation (7) $f(\bar{z}_2, p)$ (using p rather than γ) after transformation by a beam modulator and dispersive chicane.

(Simulations using this method on the simple beamlet structure of figure 2 have been performed and presented elsewhere [23].) In the electron beam frame therefore, the radiation is passed from beamlet to beamlet so that it always interacts with electrons of a similar energy so maintaining a resonant interaction and giving an improved FEL interaction. This is achieved by making the slippage of a radiation wavefront through the electrons in each undulator-chicane module equal to the spatial separation of the beamlets. The enhanced slippage can also be expected to result in the generation of a series of modes in the radiation spectrum similar to that of [16] which demonstrated that an undulator-chicane lattice will amplify side-band radiation modes that are separated by:

$$\Delta\omega/\omega_r = 4\pi\rho/\bar{s}, \tag{8}$$

where $\bar{s}$ is the slippage length in scaled units of $\bar{z}_2$ in one undulator-chicane module [16].

The FEL parameter $\rho \propto I_{pk}^{1/3}$, where I_{pk} is the electron pulse peak current, and is a measure of FEL efficiency. When considering individual beamlets a FEL parameter may also be defined for each beamlet: $\rho_b \propto I_b^{1/3}$ where I_b is localised (slice) current of the beamlet. (Note that as the beamlet energy is chirped, the mean pulse energy γ_r, is used in the definition of ρ_b.) Other beamlet parameters are also defined as $p_b = (\gamma_j - \gamma_r)/\rho_b\gamma_r$

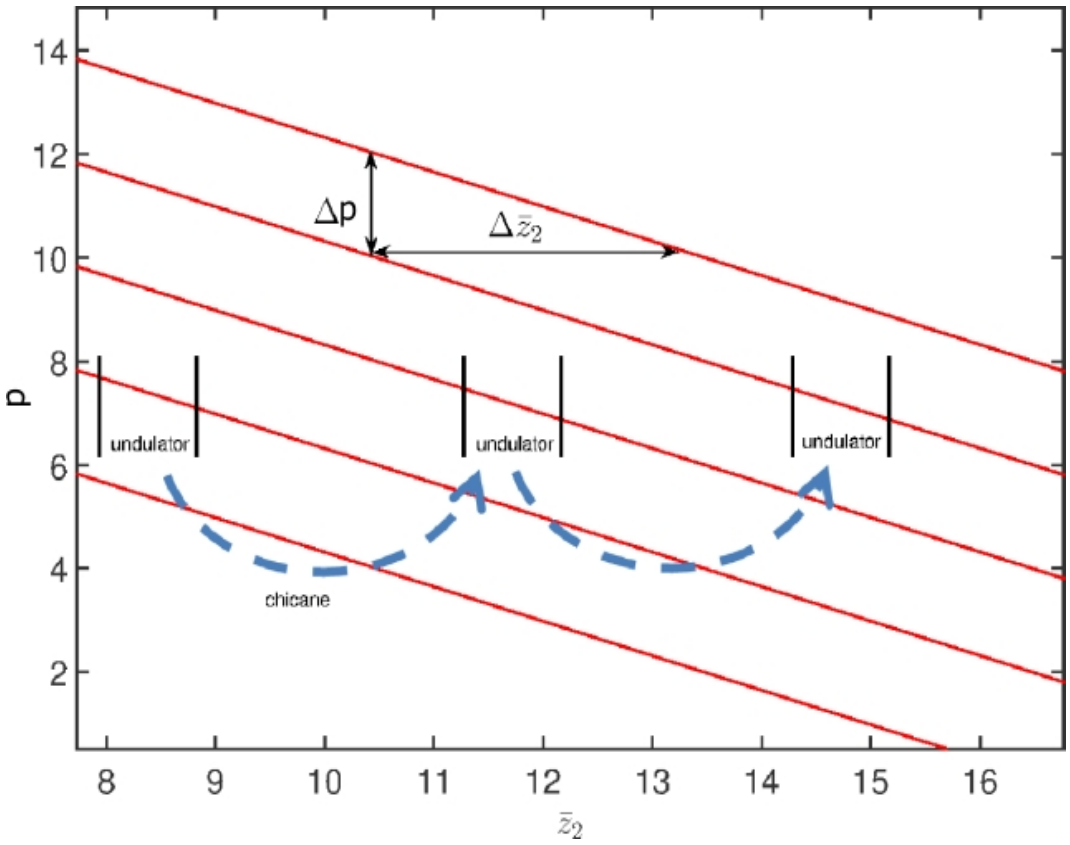

Figure 2. Scaled longitudinal phase space of the electrons for the simplified beamlet model. For a given energy the beamlets are separated spatially by $\Delta\bar{z}_2$ and for a given $\bar{z}_2$ the beamlets are separated by $\Delta p = \Delta\gamma/\rho\gamma_r$. A chicane delay of the electrons corresponds to a positive shift in $\bar{z}_2$. A series of chicanes slip the electrons forward in $\bar{z}_2$ so that they interact with the same resonant wavelength as emitted by the previous beamlet.

and a beamlet scaled slice energy σ_{p_b}. For a beamlet to lase independently its slice energy spread must then satisfy:

$$\sigma_{p_b} = \frac{\sigma_{\gamma_b}}{\rho_b \gamma_r} < 1. \tag{9}$$

(Note here, that the mean pulse energy γ_r is used in the definition of σ_{p_b} rather than a local 'slice' value γ_b. This can be considered a reasonable approximation for the inequality (9), so long as γ_b does not differ significantly from γ_r.) The beamlet slice energy spread σ_{p_b} and instantaneous fractional FEL parameter ρ_b/ρ_0, where ρ_0 is the FEL parameter of the un-transformed beam, can be calculated and are shown in figures 3 and 4 towards the higher energy and mid-sections of the electron pulse respectively.

The energy spread condition for FEL lasing of equation (9) may be used with the FEL radiation bandwidth saturation $\Delta\omega/\omega_r \approx 2\rho$ [24] to define the minimum energy separation $\Delta\gamma$ of the beamlets so that the gain bandwidths of each beamlet do not

overlap:

$$\frac{\Delta\gamma}{\rho_b\gamma_r} \gtrsim 2. \tag{10}$$

At the centre of the electron pulse the beamlets split into pairs [25], i.e. two per half modulation period, while for the electron pulse higher and lower energies, formed by the modulation extrema, the beamlet pairs merge into single beamlets as seen in figures 3 and 4.

Both the energy spread condition (9) and beamlet separation condition (10) are seen in figure 3 to be satisfied for the higher energy regions of the beamlets. (These conditions are also satisfied at the lower energy regions of the beamlets, but are not shown.) However, the condition placed on the beamlets' energy separation (10) is not always satisfied at the pulse centre where the beamlets are formed in pairs, as seen in figure 4. Hence, the undulator-chicane slippage length is set equal to the beamlet separation for the higher and lower energy regions of the pulse where the energy separation of the beamlets is approximately a constant.

Results of a FEL interaction using an un-transformed (no beamlets) pulse with large energy spread $\sigma_p = 2$ and of the transformed (beamlet) pulse are shown in figure 5. As expected, for the pulse without beamlets and the large energy spread, only small scaled peak powers of $|A|^2 \sim 10^{-4}$ are observed in the simulation. However, for the transformed pulse with beamlets that have smaller energy spread, $\sigma_{p_b} < 1$, and that are matched to the undulator-chicane modules, powers 2-3 orders of magnitude greater are observed. For the modulation period of $68\lambda_r$ used here ($n = 68$), matching was achieved using undulator modules of 20 periods and isochronous chicane slippages of $48\lambda_r$. It is seen that the FEL lasing is greater for the lower energy beamlets of the pulse around $\bar{z}_2 \sim 400$. This preferential FEL interaction and amplification of the lower frequency is consistent with the scaling of the FEL parameter $\rho \propto \gamma^{-1}$ which gives greater values and so strength of interaction, for lower beam energies. In the simulations here, the gain length of the higher to lower energy beamlets is up to ∼50% larger. Evidence of the modal structure in the spectrum is also observed in the scaled power spectrum (inset), consistent with the undulator-chicane system which from (8) gives a mode spacing of $\Delta\omega = 0.0147$.

Significant bunching of the electrons in one of the lower energy beamlets, with a mean value of scaled energy $< p >= (< \gamma > -\gamma_r)/\rho\gamma_r \approx -5$, is also observed as shown in figure 6. Note from the lower plot for the spectrum that the electrons are bunched at a lower frequency $\omega/\omega_r \approx 0.85$ than the mean resonant frequency of the electron pulse. This frequency shift from resonance is consistent with the lower mean energy of the electrons as $\Delta\omega/\omega_r \approx 2\rho < p >= 0.16$ and is in agreement with the radiation frequency spectrum of figure 5. Electron bunching is also observed in a higher energy beamlet of mean scaled energy $< p > \approx 4$, shown in figure 7. Here, the bunching is seen to be at a less advanced stage, but can be expected to reach saturation on further propagation through the undulater-chicane lattice.

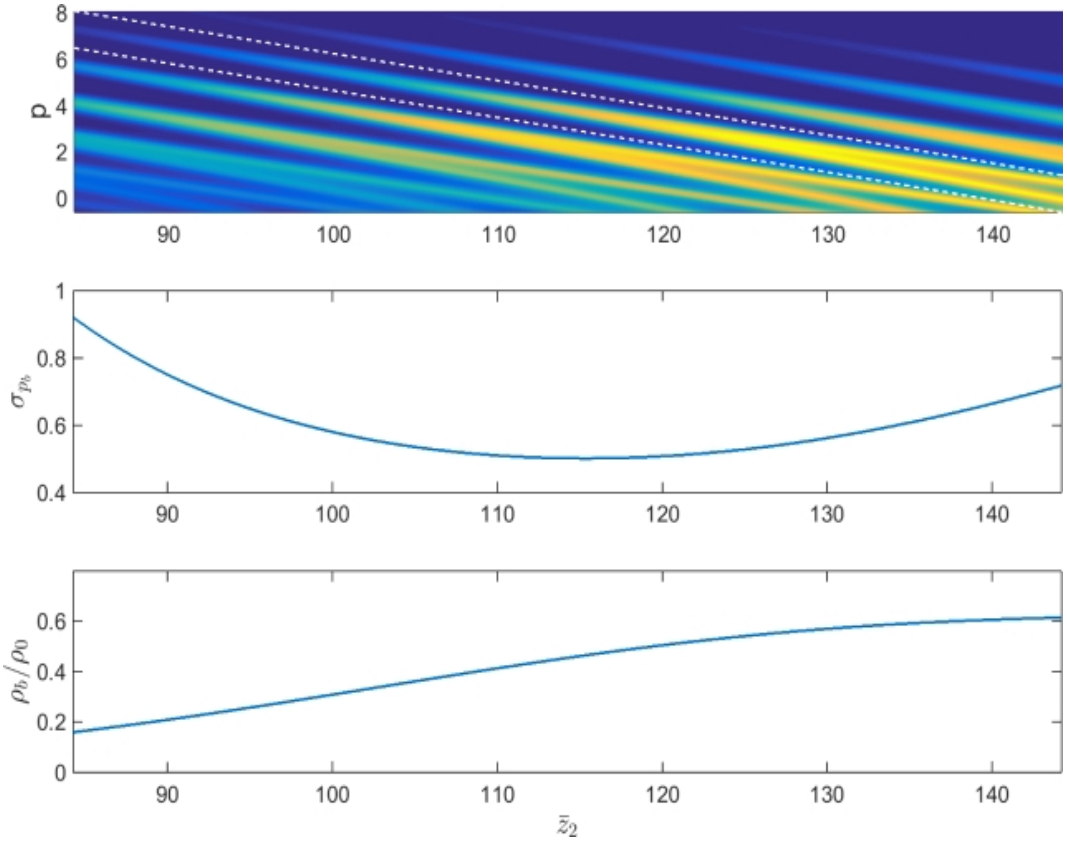

Figure 3. Top panel: Detail of the higher energy beamlet phase space distribution function of equation 7 with a single beamlet delineated by white dashed lines. The values of the scaled energy spread σ_{p_b} (middle) and ρ_b/ρ_0 (bottom) were calculated for the single beamlet as a function of $\bar{z}_2$. Towards the pulse head ($\bar{z}_2 < 105$) the electron pulse is diffuse with a larger energy spread σ_{p_b} and smaller ρ_b. Nearer the centre of the pulse ($105 < \bar{z}_2 < 125$), the scaled energy spread decreases as the local density, and ρ_b increase. However, further towards the pulse centre $\bar{z}_2 > 125$ the energy spread increases further as the beamlet spilts into two identifiably separate beamlets, while the value of ρ_b tends towards a more constant value. The condition for lasing of the beamlet of $\sigma_{p_b} < 1$ is seen to be satisfied within this the head of the pulse (and is also satisfied at the lower energy beamlets of the tail). The energy separation between beamlets is also seen to satisfy condition (10) so that each beamlet can lase independently. The energy separation between beamlets does not change significantly with $\bar{z}_2$, as neither does the longitudinal separation of beamlet regions with the same energy. Towards the centre of the pulse however, the beamlet structures have a more complicated phase space structure.

3. Fourier Synthesised Electron Beams

Further types of phase-space transformation of an electron pulse prior to generating radiation have been proposed and called 'beam-by-design' [7]. An example is investigated here to demonstrate the potential of such beam transformation prior to injection into the FEL and the subsequent transformation in the FEL emission stage using a series of undulator-chicane modules. An electron pulse consisting of a series

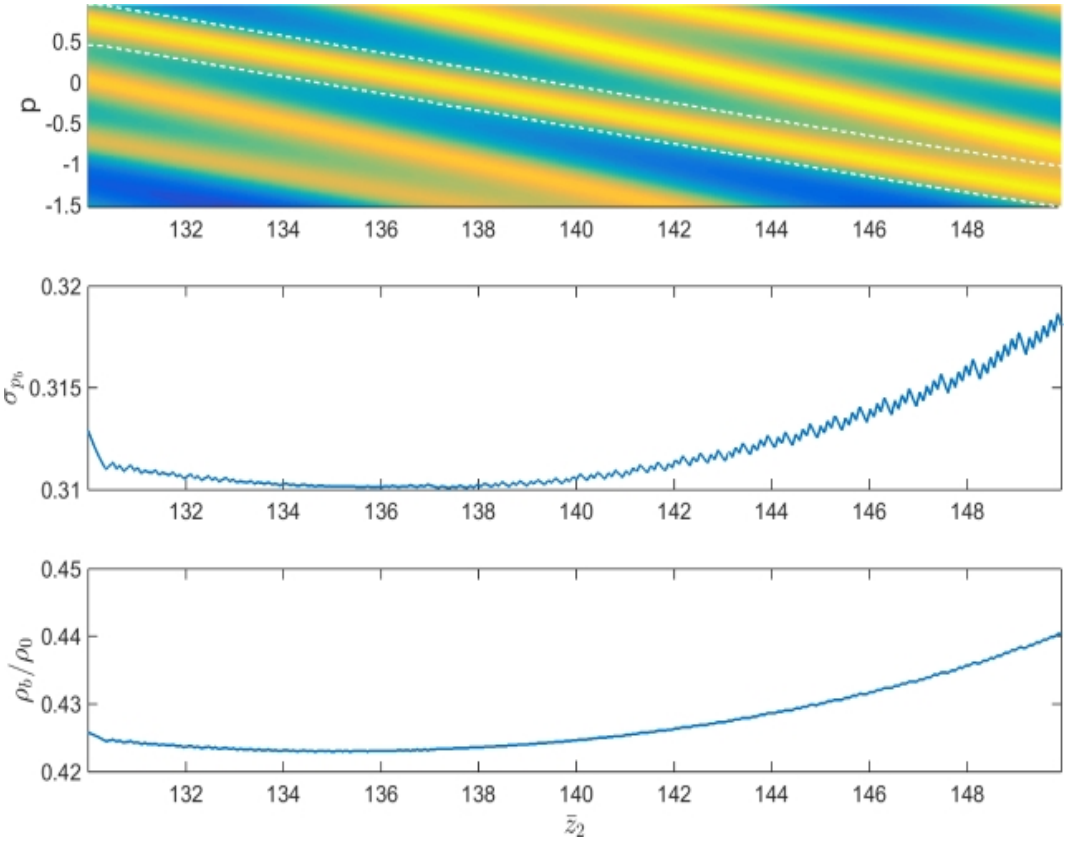

Figure 4. As figure 3, but around the centre of the electron pulse about the mean pulse energy. The beamlets are seen to 'spilt' into two separate beamlets. While the scaled energy spread requirement for lasing $\sigma_{p_b} < 1$, is satisfied, the beamlet energy separation condition (10) is only satisfied for a small region of beamlets about the pulse centre. The beamlets are therefore unlikely lase independently with non-overlapping bandwidths, so that the effective energy spread for the interaction is increased, decreasing the ability of achieving significant FEL lasing.

rectangular shaped distributions in phase-space can be generated [13] and contains a periodic series of current 'spikes'. These current spikes are a source of coherent spontaneous emission which may, through a series of periodic superpositions enabled by chicanes, generate significant radiation output from an undulator-chicane lattice. We note that other methods can generate similar beam structures, e.g. the E-SASE approach [26], however the methods of [13] are used here to demonstrate the types of more exotic interaction that may be modelled using non-averaged simulation codes such as PUFFIN.

3.1. The Model - Coherent Emission from Rectangular Electron Pulses

A new approach to produce so-called 'RF-function' electron beams was introduced in [13]. An RF-function generator produces a series of repeated wave forms by combining sine-waves of different frequencies as in a Fourier series. In a similar fashion, an electron pulse can be created with a phase-space that consists of repeated 'waveforms'

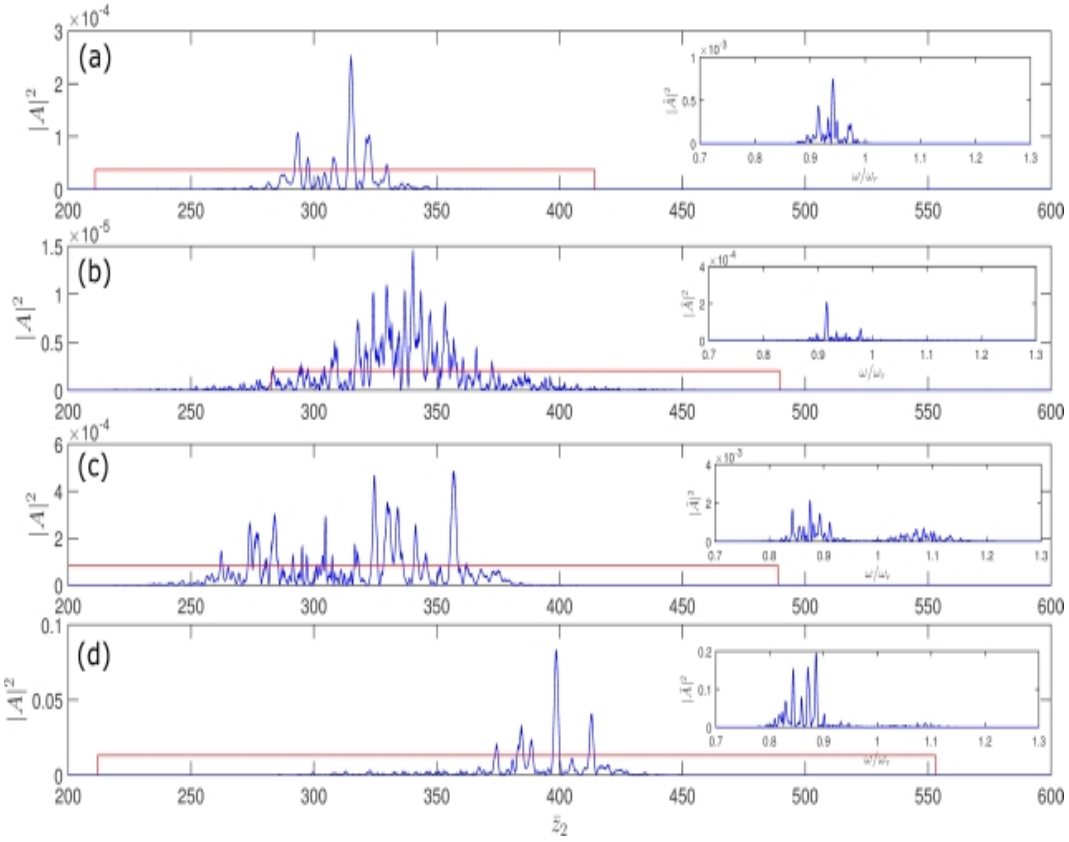

Figure 5. A comparison of the scaled radiation temporal power and spectral power (insets) for an un-transformed electron pulse (panels a and b) and transformed pulse of beamlets (panels c and d), when propagated through an simple undulator and an undulator-chicane lattice respectively and interaction length of $\bar{z} \approx 30$. The (red) box shows the position of the electron pulse relative to the radiation (the head of the pulse is to the left.) Note the different lengths of the electron pulses due to differing dispersive effects of the chicanes. The beamlets propagating through a simple undulator (panel c) is seen to give a small improvement to the output from the un-transformed beam through both an simple undulator and an undulator-chicane system (a and b respectively.) The improvement in output from the beamlets is increased significantly when they are propagated through the matched undulator-chicane lattice as shown in panel d. The undulator-chicane lattice amplifies side-band radiation modes generated by the undulator-chicane modules and are separated by $\Delta\omega = 0.0147$ as seen from the panel d inset and in agreement with the mode-spacing relation of (8). For all results shown in this figure the radiation field has been filtered about the resonant frequency $0.5 < \omega/\omega_r < 1.5$ to eliminate low frequency coherent spontaneous emission.

by modulation the electron beam using a series of seeded undulator modulators using different seed wavelengths, amplitudes and phases. Following the notation of [13], here a rectangular beam shape in phase space using a triple modulator-chicane lattice is synthesized and subsequent radiation generation following injection into an undulator chicane-lattice is modelled using PUFFIN.

While in [13] an infinity long electron beam was assumed, here, a finite electron pulse with an initial Gaussian distribution in both $\bar{z}_2$ and γ is assumed, as given by

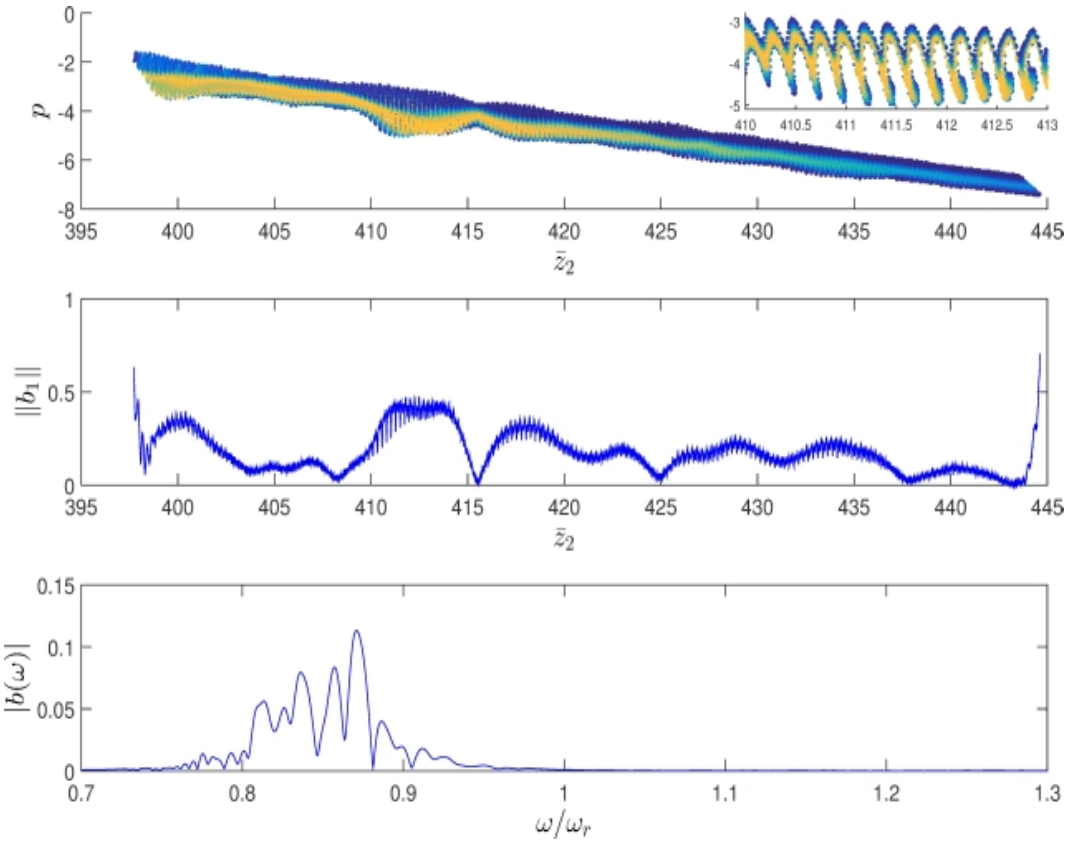

Figure 6. Electron bunching in a lower energy beamlet at $\bar{z} \approx 30$. The top panel plots the charge-weighted electron phase space distribution ; the middle plots the bunching parameter of the beamlet at the fundamental radiation frequency, and the bottom plots the bunching spectrum of the beamlet.

equation (6). As detailed in the Appendix, the same Fourier synthesis as outlined in [13] is applied using the beam modulation transforms given by equation (4) and the energy dispersion transforms of equation (5).

In electron phase-space, the vertical segments of the rectangular waveform generate regions of enhanced current, albeit with a larger energy spread. Each period therefore contains two current 'spikes' which can generate significant coherent spontaneous emission when their width is of a similar scale to a resonant wavelength [17]. However, due to electron beam dispersion in the undulator, the sharpness of the current spikes reduce on propagation, resulting in diminishing coherent emission. This dispersion of the current spikes may be compensated for by the use of chicane systems with a negative dispersion to allow for more prolonged coherent emission. The design of chicane delay systems with negative dispersion have been previously designed and tested as part of an accelerator lattice [27] and are also necessary for generating the RF-function beam shapes [7, 13]. If the slippage per undulator-chicane module is also made equal to the current spike separation, then the radiation is propagated from spike to spike and, if correctly phased, can facilitate the constructive interference of the coherent emission from each current spike in each new undulator module.

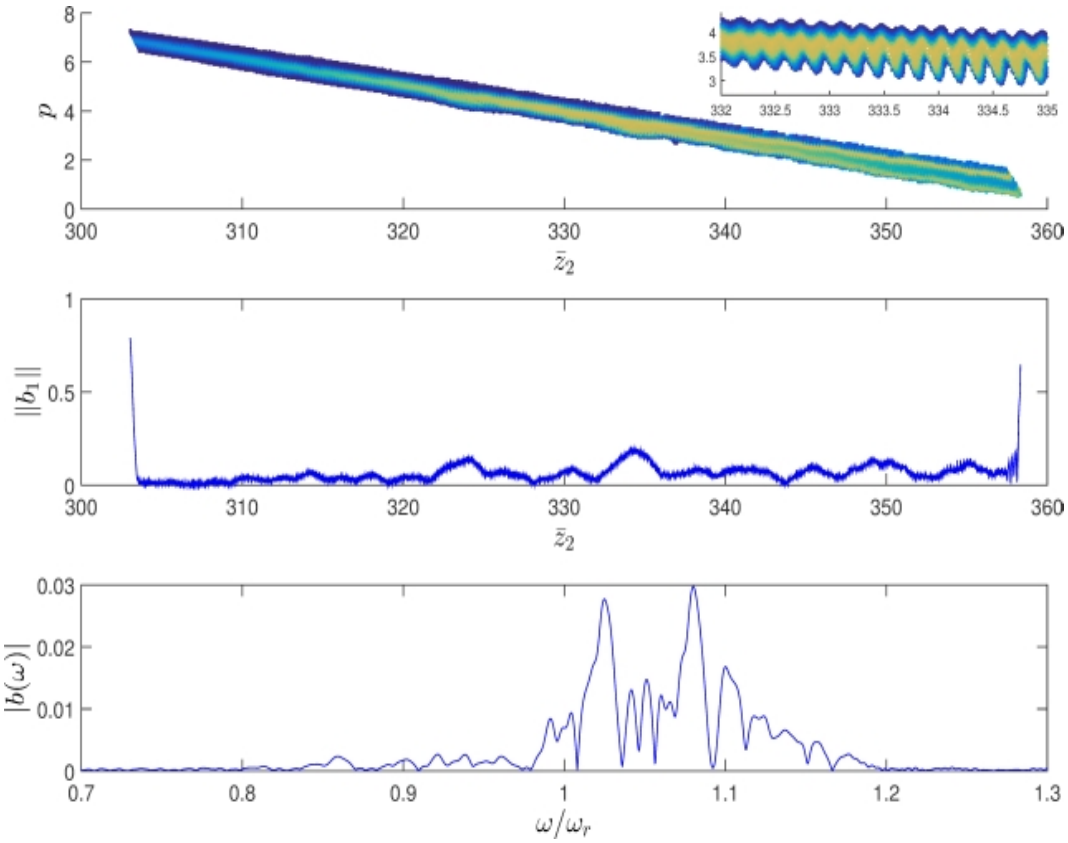

Figure 7. Electron bunching in a higher energy beamlet at $\bar{z} \approx 30$. The top panel plots the charge-weighted electron phase space distribution; the middle plots the bunching parameter of the beamlet at the fundamental radiation frequency; and the bottom plots the bunching spectrum of the beamlet.

3.2. Results - Coherent Emission from Rectangular Electron Pulses

The following simulations use the same electron pulse parameters as the previous section, i.e., the electron pulse's large energy spread is prohibitive to FEL gain. The phase-space distribution of the electron beam for the rectangular waveform was constructed from the analysis of the Appendix for three undulator-chicane modules using the following parameters in $[\Delta\gamma, D]$: $[\Delta\gamma_1 = 10\sigma_\gamma; D_1 = n_1\rho\gamma_r\sqrt{3}\pi/(2\Delta\gamma_1)]$; $[\Delta\gamma_2 = \Delta\gamma_1/4; D_2 = -3D_1]$; $[\Delta\gamma_3 = \Delta\gamma_2/16; D_3 = -3D_2/4 = 9D_1/4]$, with $n_{1,2,3} = 20$, $\phi_{1,2} = 0$ and $\phi_3 = \pi$.

The initial current profile of the electron pulse contains a series of current spikes at half the modulation period corresponding to 10 resonant radiation wavelengths or $10 \times 4\pi\rho \approx 2$ in units of $\bar{z}_2$. On injection into an undulator, these spikes act as a periodic series of phase correlated coherent emitters which, for a relatively short interaction length of $\bar{z} \approx 1$), generate a broad modal radiation spectrum as seen figure 8. However, it is seen that alternate current spikes have dispersed to leave a series of more prominent current spikes at twice the initial spacing of $\Delta\bar{z}_2 \approx 4$. This is reflected in the temporal separation of the larger radiation spikes separated by $\Delta\bar{z}_2 \approx 4$). This also agrees with to

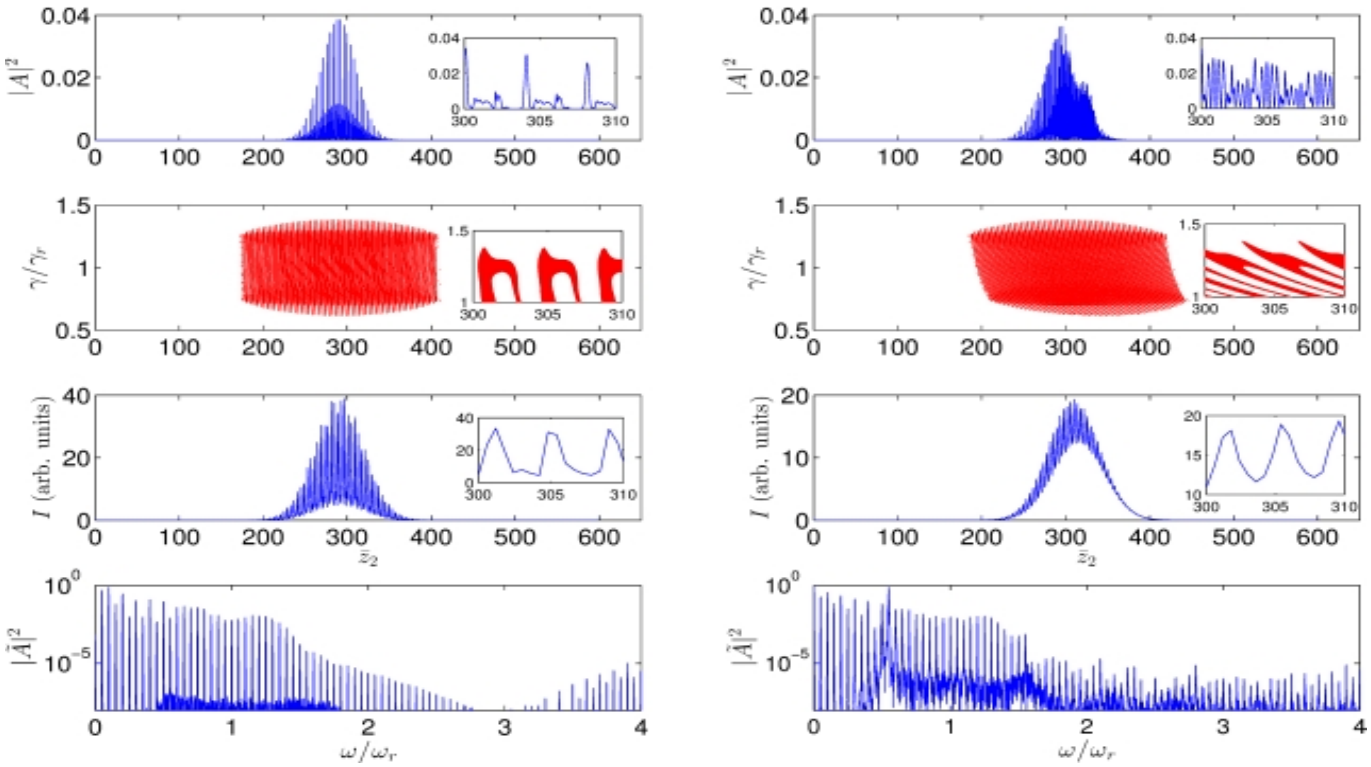

Figure 8. The evolution of a rectangular electron beam in an undulator showing top-to-bottom, the scaled radiation power $|A|^2$ as a function of $\bar{z}_2$, electron phase space $(\gamma/\gamma_r, \bar{z}_2)$ with detail inset, the scaled electron current as a function of $\bar{z}_2$ and the logarithm of the scaled radiation power spectrum $|\tilde{A}|^2$ as a function of the scaled frequency ω/ω_r. The series on the left plot the output for a scaled distance through the undulator of $\bar{z} \approx 1$ and on the right for $\bar{z} \approx 20.1$ An electron pulse with an initially large energy spread has been transformed into an electron pulse that contains a number of rectangular waveforms (see second plot on the left). The electron pulse structure now contains a series of current spikes of spacing $\Delta\bar{z}_2 \approx 4$. When this electron pulse is passes through an undulator each current spike acts as a source of coherent spontaneous emission. The radiation spectrum (bottom panels) show a broad bandwith modal structure with modes separation $\Delta\omega/\omega_r \approx 0.05$. As the electron pulse propagates along the undulator, the rectangular waveforms will disperse, and increase the current spike widths and reduce current spike amplitudes. As the current spikes' 'sharpness' decrease the coherent radiation produced by the current spikes will decrease. Because of this no amplification is seen when passing such an electron pulse through a long undulator, as shown in the r.h.s. of this figure.

the spectrum in which a series of modes are generated with separation, from equation (8), of $\Delta\omega/\omega_r \approx 0.05$ about the resonant frequency.

On propagating further through the interaction region to larger values of $\bar{z} \approx 20$, the right hand panels of figure 8 show that the energy modulation of the rectangular electron beam causes the electron beam to disperse in the undulator degrading the visibility of the current spikes and so decreasing the coherent spontaneous emission generated. Clearly, these dispersive effects mean that there is no benefit in increasing the interaction length over that of $\bar{z} = 20\pi\rho \approx 1$.

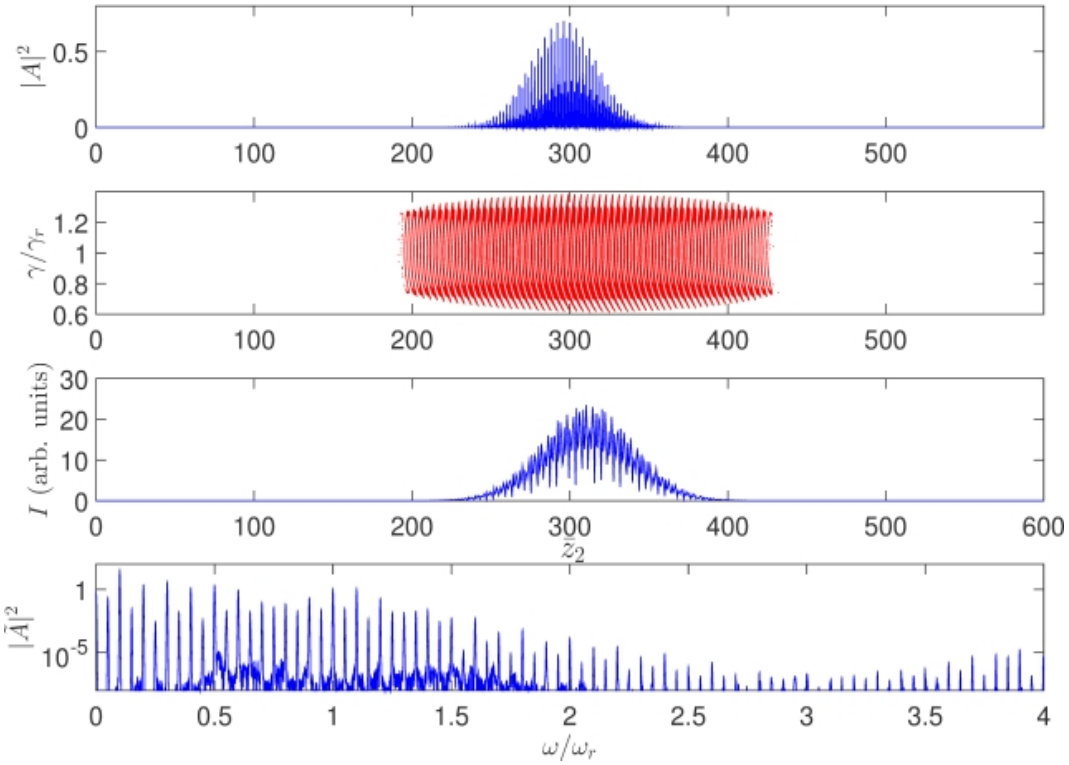

Figure 9. By using chicanes with a negative dispersion, the undulator dispersion of the rectangular sections of the electron beam can be partially compensated for as seen here for $\bar{z} \approx 10$. In doing so the electron pulse can continue to emit coherent emission in each undulator module. Here, each undulator module has 5 periods and each chicane delays the electron pulse by approximately 5 resonant periods, to match the current spike separation. Note that there is small FEL interaction as evidence by electron microbunching (not shown).

By using chicanes with a negative dispersion it is possible to partially compensate for the undulator dispersion and maintain a spiked current profile that can continue to emit CSE over a larger number of modules. An example of this is shown in figure 9 were the chicane dispersion is set equal the negative of the undulator dispersion, i.e. $D = -\bar{l}$ [23]. The total undulator-chicane slippage for the radiation was again set equal to the current-spike separation, $\bar{s} = 10 \times 4\pi\rho$. For this case, undulator-chicane modules of 5 undulator periods and 5 chicane slippage periods were used. In this way, the CSE from successive undulator-chicane modules superimpose and constructively interfere increasing the radiation power emitted.

However, the radiation fields from each undulator-chicane do not superimpose coherently and the radiation energy is seen (not shown) to scale approximately as the number of undulator-chicane modules - a phase-matched coherent superposition would give a radiation energy which scales as the square of the number of undulator-chicane modules. The reason for this non-coherent superposition is that the dispersion of the large energy modulated beam in the undulators cannot be perfectly compensated for by the negative dispersion in the chicanes. (Phase space dispersion of electrons in the

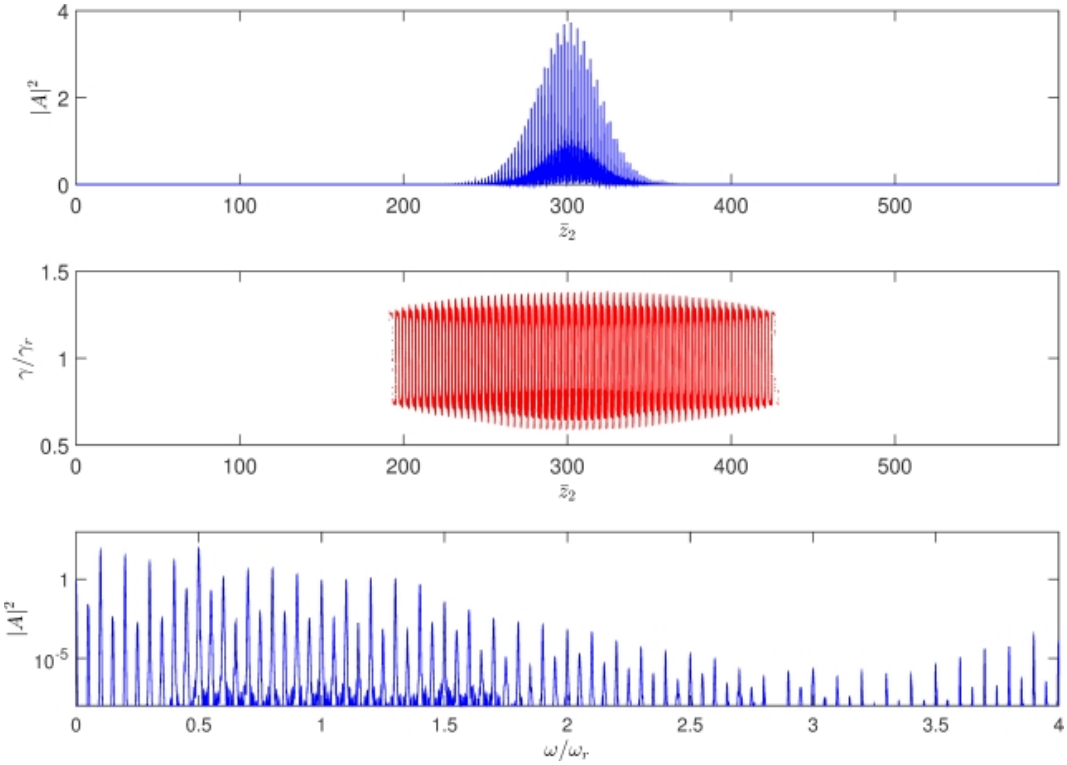

Figure 10. As figure 9, but now using an optimised chicane which maintains the rectangular waveform electron pulse structure in phase space as it propagates through the undulator-chicane lattice. The rectangular electron waveform emits coherent radiation in each new undulator module which constructively interferes with the radiation in subsequent undulator modules.

undulator is due to differences in the axial speed v_z, while electron dispersion in the chicanes is due to differences in the electron energy, γ.) This is observed from the slight 'bowing' of the rectangular structure of the electrons in phase space in figure 9. Two possible methods to improve this are to reduce the initial energy modulation of the rectangular wave (the results here are for a relatively large energy modulation) or to use a (hypothetical) optimised chicane design which has a non-linear dispersive strength as a function of γ. Here the latter is used and the results shown in figure 10. Now, the bowing of the rectangular structure of the electrons in phase space is seen to be removed and the power of the radiation increased. The coherent radiation from each undulator-chicane module is now phase matched and is superimposing coherently after each module. The radiation energy is now also observed to increase in proportion to the square of the number of modules.

A comparison of a normal (untransformed beam) FEL amplifier with the methods of beamlets of the previous Section and that of the fourier synthesised rectangular beam of this section is given in figure 11 which plots how the scaled energy E of the radiation

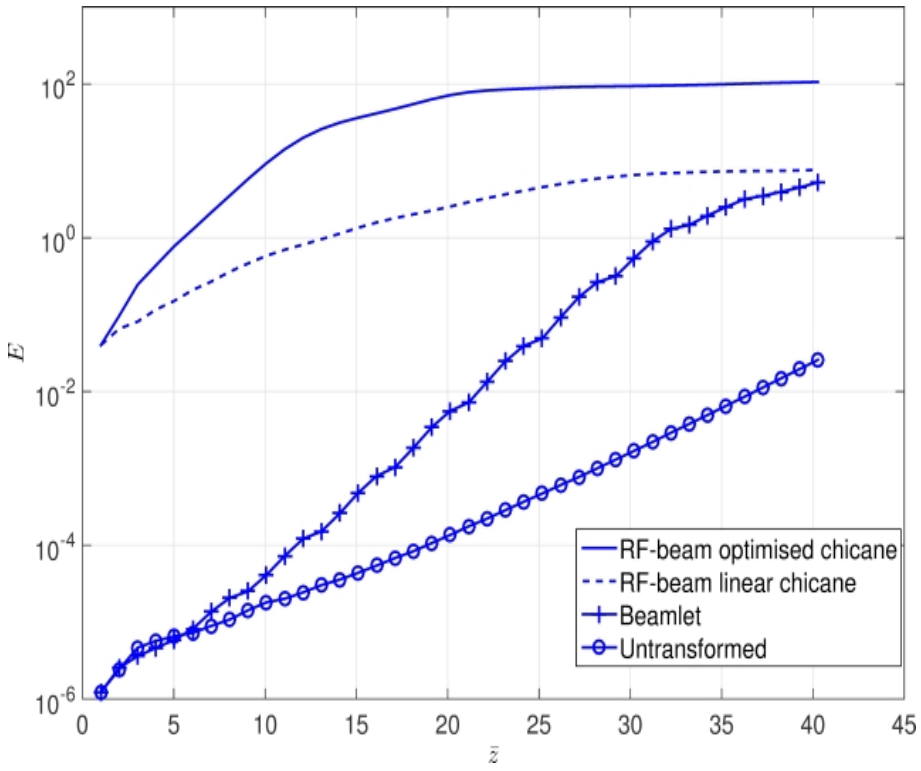

Figure 11. The total radiation field energy $E(\bar{z})$ of the normal (untransformed, no chicanes) FEL, beamlet FEL, and rectangular beams with linear and optimised chicanes. The radiation is filtered around the resonant frequency, $0.5 < \omega/\omega_r < 1.5$.

pulses evolves with the interaction length $\bar{z}$, where:

$$E(\bar{z}) = \int_{-\infty}^{+\infty} |A(\bar{z}, \bar{z}_2)| d\bar{z}_2. \tag{11}$$

Before performing the integral in (11) the field was first fourier bandpass filtered so that only contributions about resonance in the interval $0.5 < \omega/\omega_r < 1.5$ are considered (this removes the significant low-frequency CSE content.) The introduction of the phase=space transform to generate electron beamlets is seen to increase the exponential growth rate over the normal FEL interaction by a factor of approximately two. While the rectangular electron beams are seen not to have an exponential gain, it is essentially a Coherent Spontaneous Emission process, the starting powers are much greater than the FEL processes which start from spontaneous shot noise. It should be noted that when the CSE simulations predict radiation powers that are a significant fraction of the electron beam energy, that the effects of photon recoil should be included in the model. These effects are not included in the classical simulations presented here.

4. Conclusion

This paper has sought to demonstrate what may be possible when electron beams are transformed to alter their properties before injection into an FEL-type system. It is

stressed that the methods demonstrated here are not proposals for any specific design or operational wavelength. Rather, they are used to demonstrate possible research directions towards future light sources, some of which have already been envisaged [7].

Here, the focus was to generate significant radiation output from electron beams that have insufficient beam quality to lase under normal FEL operation. These methods may be developed further and made more specific e.g. to the electron beams generated from plasma accelerator sources which, to date, tend to have relatively high energy spreads. Other possibilities, such as multiple frequency generation, ultra-short pulses, chirped pulses (possibly shorter wavelengths) and others, are potential research areas. One topic that is apparent, but has not been explored here, is the introduction of tapered undulators into the design process. For example, the introduction of tapered undulators, matched to compensate for the chirped beamlets of above, instead of using chicanes, can be expected to produce interesting radiation output.

It is noted that the simulations presented here cannot be modelled effectively, or at all, using simulation codes that are used to successfully model the 'normal' types of FEL interactions. Unaveraged FEL codes, such as the PUFFIN code used here, are required.

Acknowledgments

We gratefully acknowledge support of Science and Technology Facilities Council Agreement Number 4163192 Release #3; ARCHIE-WeSt HPC, EPSRC grant EP/K000586/1; EPSRC Grant EP/M011607/1; and John von Neumann Institute for Computing (NIC) on JUROPA at Jlich Supercomputing Centre (JSC), under project HHH20

Appendix

The final distribution function of a triple-modulator-chicane scheme is given below.

$$f(\bar{z}_2,\gamma) = \frac{1}{2\pi}\frac{1}{\sigma_\gamma}\frac{1}{\sigma_{\bar{z}_2}}\exp\left(\frac{-1}{2\sigma_\gamma^2}\left([((\gamma+\Delta\gamma_3\sin(\frac{1}{2n_3\rho}(\bar{z}_2+2D_3(\gamma-\gamma_r)/\gamma_r)+\phi_3))\right.\right.$$
$$+\Delta\gamma_2\sin(\frac{1}{2n_2\rho}((\bar{z}_2+2D_3(\gamma-\gamma_r)/\gamma_r)+2D_2((\gamma+\Delta\gamma_3\sin(\frac{1}{2n_3\rho}(\bar{z}_2+2D_3(\gamma-\gamma_r)/\gamma_r)+\phi_3))-\gamma_r)/\gamma_r)+\phi_2))$$
$$+\Delta\gamma_1\sin(\frac{1}{2n_1\rho}(((\bar{z}_2+2D_3(\gamma-\gamma_r)/\gamma_r)+2D_2((\gamma+\Delta\gamma_3\sin(\frac{1}{2n_3\rho}(\bar{z}_2+2D_3(\gamma-\gamma_r)/\gamma_r)+\phi_3))-\gamma_r)/\gamma_r)$$
$$+2D_1(((\gamma+\Delta\gamma_3\sin(\frac{1}{2n_3\rho}(\bar{z}_2+2D_3(\gamma-\gamma_r)/\gamma_r)+\phi_3))+\Delta\gamma_2\sin(\frac{1}{2n_2\rho}((\bar{z}_2+2D_3(\gamma-\gamma_r)/\gamma_r)$$
$$\left.\left.+2D_2((\gamma+\Delta\gamma_3\sin(\frac{1}{2n_3\rho}(\bar{z}_2+2D_3(\gamma-\gamma_r)/\gamma_r)+\phi_3))-\gamma_r)/\gamma_r)+\phi_2))-\gamma_r)/\gamma_r)+\phi_1)]-\gamma_r\right)^2\right)$$
$$\exp\left(\frac{-1}{2\sigma_{\bar{z}_2}^2}\left([((\bar{z}_2+2D_3(\gamma-\gamma_r)/\gamma_r)+2D_2((\gamma+\Delta\gamma_3\sin(\frac{1}{2n_3\rho}(\bar{z}_2+2D_3(\gamma-\gamma_r)/\gamma_r)+\phi_3))-\gamma_r)/\gamma_r)\right.\right.$$
$$+2D_1(((\gamma+\Delta\gamma_3\sin(\frac{1}{2n_3\rho}(\bar{z}_2+2D_3(\gamma-\gamma_r)/\gamma_r)+\phi_3))+\Delta\gamma_2\sin(\frac{1}{2n_2\rho}((\bar{z}_2+2D_3(\gamma-\gamma_r)/\gamma_r)$$
$$\left.\left.+2D_2((\gamma+\Delta\gamma_3\sin(\frac{1}{2n_3\rho}(\bar{z}_2+2D_3(\gamma-\gamma_r)/\gamma_r)+\phi_3))-\gamma_r)/\gamma_r)+\phi_2))-\gamma_r)/\gamma_r]-\bar{z}_c\right)^2\right)$$

The energy modulation parameters $\Delta\gamma_{1,2,3}$, modulation frequencies $n_{1,2,3} = k_{1,2,3}/k_w$ and modulation phases $\phi_{1,2,3}$ are associated with first, second and third modulator sections respectively. Similarly $D_{1,2,3}$ are the dispersion factors for chicane 1,2 and 3. $\sigma_{\gamma,\bar{z}_2}$ is the standard deviations in γ and $\bar{z}_2$. The resonant energy is defined as $\gamma_r =< \gamma >|_{\bar{z}=0}$ and the electron pulse centre is given by $\bar{z}_c$.

References

[1] Vinko S M *et al* 2012 Nature **482** 59
[2] Barends R M T *et al* 2014 Nature **505** 244
[3] Edwards G S *et al* 2003 Rev. Sci. Instrum. **74** 3207
[4] Emma P *et al* 2010 Nat. Photonics **4** 641
[5] Ishikawa T *et al* 2012 Nat. Photonics **6** 540
[6] M^{c}Neil B W J and Thompson N R 2010 Nat. Photonics **4** 814
[7] Hemsing E, Stupakov G, and Xiang D 2014 Rev. Mod. Phys. **86** 897
[8] Campbell L T, McNeil B W J and Reiche S 2014 New J. Phys. **16** 103019
[9] Couprie M E, Loulergue A, Labat M, Lehe R, and Malka V 2014 J. Phys. B: At. Mol. Opt. Phys. **47** 234001
[10] Nakajima K 2014 High Power Laser Science and Engineering / Volume 2 / December 2014 / e31
[11] Maier A R *et al* 2012 Phys. Rev. X **2** 031019
[12] Huang Z, Ding Y, and Schroeder C B 2012 Phys. Rev. Lett. **109** 204801
[13] Hemsing E and Xiang D 2013 Phys. Rev. ST-Accel. Beams **16** 010706
[14] Campbell L T and M^{c}Neil B W J 2012 Physics of Plasmas **19** 093119
[15] Ronsivalle C *et al.* 2014 New J. Phys. **16** 033018
[16] Thomson NR and M^{c}Neil BWJ 2008 Phys. Rev. Lett. **100** 203901
[17] M^{c}Neil B W J, Robb G R M, and Jaroszynski D A 2000 Nuclear Instruments and Methods in Physics Research A **445** 72
[18] Bonifacio R, Pellegrini C and Narducci L M 1984 Opt. Comm. **50** 373

[19] Xiang D and Stupakov G 2009 Phys. Rev. ST-Accel. Beams **12** 030702
[20] Bonifacio R, M^{c}Neil B W J and Pierini P 1989 Phys. Rev. A **40** 4467
[21] M^{c}Neil B W J, Poole M W and Robb G R M 2003 Phys. Rev. ST-Accel. Beams **6** 070701
[22] Saldin E, Schneidmiller E, and Yurkov M 2006 Phys. Rev. ST-Accel. Beams **9**, 050702
[23] Henderson J R, Campbell L T and M^{c}Neil B W J 2014 Proceedings of FEL2014, Basel, Switzerland MOC04 303
[24] Bonifacio R, De Salvo L, Pierini P, Piovella N and Pellegrini C 1994 Phys. Rev. Lett. **73** 70
[25] Henderson J R and M^{c}Neil B W J, 2012 EPL **100** 64001
[26] Zholents A A 2005 Phys. Rev. ST-AB **8** 040701
[27] Jackson F, Angal-Kalinin D, Jones J K, and Williams P H 2013 4th International Particle Accelerator Conference (IPAC13) Shanghai, China WEPWA063 2262

THE IMPLEMENTATION OF 3D UNDULATOR FIELDS IN THE UNAVERAGED FEL SIMULATION CODE Puffin

J. R. Henderson[1], L.T. Campbell[1,2,3,4], A.R. Maier[3,4] and B.W.J. McNeil[1]
[1]SUPA, Department of Physics, University of Strathclyde, Glasgow, UK
[2]ASTeC, STFC Daresbury Laboratory and Cockcroft Institute, Warrington, UK
[3]Center for Free-Electron Laser Science, Notkestrasse 85, Hamburg, Germany
[4]Institut für Experimentalphysik, Universität Hamburg, Hamburg, Germany

Abstract

The FEL simulation code Puffin is modified to include 3D magnetic undulator fields. Puffin, having previously used a 1D undulator field, is modified to accommodate general 3D magnetic fields. Both plane and curved pole undulators have been implemented. The electron motion for both agrees with analytic predictions.

INTRODUCTION

Puffin [1] is an unaveraged 3D FEL code which does not make the Slowly Varying Envelope Approximation (SVEA) or period averaging in its analytical model. As such, it is capable of modelling the a broad radiation field spectrum, full longitudinal broadband electron beam transport through the undulator, and Coherent Spontaneous Emission (CSE) emerging from current gradients in the beam.

However, although Puffin models a 6D electron beam and 3D radiation field, it does not employ a 3D magnetic undulator field. Instead, it implements a 1D undulator field with no off-axis variation. Superimposed, is an external focusing channel which is an approximation of the natural focusing found in a helical undulator. This focusing channel may be strengthened or weakened through the use of a 'focusing factor' [2] to obtain a desired betatron frequency.

Such a model does not simulate the detuning of the resonance condition in the transverse dimensions. Nor does it allow the focusing to emerge naturally from the off-axis variation of the magnetic fields. The resulting electron motion is an approximation in the case of a helical or curved-pole undulator; it is inaccurate in the case of an undulator with plane poles. Furthermore, the betatron motion as derived in Puffin is only valid when the electron beam is close to mono-energetic.

There is a need to model more realistic undulator fields; in particular, plane pole and curved pole undulators are more common than helical undulators for UV/X-ray FELs. There is therefore a requirement that various 3D planar undulator types be implemented in Puffin.

In the following, the Puffin model is first generalized to include general undulator magnetic fields. This model also allows a helical field description to be developed. Note also that this general magnetic field description need not be limited to undulators, and may allow future alternative applications of the Puffin code, to solve other radiation-electron interactions in static magnetic fields.

This general description is then used to implement both a generic plane pole and curved (canted) pole undulator FEL. Results are presented to demonstrate the correct electron motion and radiation characteristics are being solved.

MODIFIED MATHEMATICAL MODEL

The derivation of the FEL system of equations modelled by Puffin is given in [1], using a magnetic undulator field $\mathbf{B}_u = \frac{B_u}{2}(\mathbf{u}e^{ik_u z} + c.c.)$, where $\mathbf{u} = u_x\hat{\mathbf{x}} + iu_y\hat{\mathbf{y}}$ defines the polarization of the undulator. Following the same derivation, but using a general 3D magnetic field of the form $\mathbf{B} = B_x\hat{\mathbf{x}} + B_y\hat{\mathbf{y}} + B_z\hat{\mathbf{z}}$, one obtains the following system of equations:

$$\Big[\frac{1}{2}\Big(\frac{\partial^2}{\partial\bar{x}^2} + \frac{\partial^2}{\partial\bar{y}^2}\Big) - \frac{\partial^2}{\partial\bar{z}\partial\bar{z}_2}\Big]A_\perp = -\frac{1}{\bar{n}_p}\frac{\partial}{\partial\bar{z}_2}\sum_{j=1}^{N}\bar{p}_{\perp j}L_j\delta^3(\bar{x}_j,\bar{y}_j,\bar{z}_{2j}) \quad (1)$$

$$\frac{d\bar{p}_{\perp j}}{d\bar{z}} = \frac{1}{2\rho}\Big[ib_\perp - \frac{\eta p_{2j}}{\alpha^2}A_\perp\Big] - i\alpha\bar{p}_{\perp j}L_j b_z \quad (2)$$

$$\frac{dp_{2j}}{d\bar{z}} = \frac{\rho}{\eta}L_j^2\Big[\eta p_{2j}(\bar{p}_{\perp j}A^*_{\perp j} + c.c.) - i(1+\eta p_{2j})\alpha^2(\bar{p}_{\perp j}b^*_{\perp j} - c.c.)\Big] \quad (3)$$

$$\frac{d\bar{z}_{2j}}{d\bar{z}} = p_{2j} \quad (4)$$

$$\frac{d\bar{x}_j}{d\bar{z}} = \frac{2\rho\alpha}{\sqrt{\eta}}L_j\Re(\bar{p}_{\perp j}) \quad (5)$$

$$\frac{d\bar{y}_j}{d\bar{z}} = -\frac{2\rho\alpha}{\sqrt{\eta}}L_j\Im(\bar{p}_{\perp j}). \quad (6)$$

where

$$\bar{p}_\perp = \frac{p_\perp}{mca_u}, \qquad A_\perp = \frac{eua_u l_g}{2\sqrt{2}\gamma_r^2 mc^2\rho}E_\perp,$$
$$\rho = \frac{1}{\gamma_r}\left(\frac{a_u\omega_p}{4ck_u}\right)^{2/3}, \qquad a_u = \frac{eB_0}{mck_u},$$
$$\alpha = \frac{a_u}{2\rho\gamma_r}, \qquad b_\perp = b_x - ib_y, \quad (7)$$

and $b_{x,y,z} = B_{x,y,z}/B_0$ are the scaled magnetic fields in x, y and z, respectively, and B_0 is the peak on-axis magnetic field. Other parameters remain as defined in [1]. The FEL parameter ρ above is defined using the peak undulator parameter, rather than the *r.m.s.* undulator parameter.

ISBN 978-3-95450-133-5

Using the above system of equations, one may use b_x, b_y and b_z to define a static 3D magnetic field with which to simulate the energy exchange between a co-propagating electron beam and radiation field. The model is still subject to the same limitations as in [1], *i.e.* the paraxial approximation and the neglect of the backwards propagating wave.

Currently, two 3D undulator fields have been implemented in Puffin using this model, both derived from [3, 4]. The first is an undulator field with canted, or curved, pole faces, providing beam focusing in both transverse dimensions:

$$\begin{aligned} b_x &= \frac{\bar{k}_x}{\bar{k}_y} \sinh(\bar{k}_x \bar{x}) \sinh(\bar{k}_y \bar{y}) \sin(\bar{z}/2\rho), \\ b_y &= \cosh(\bar{k}_x \bar{x}) \cosh(\bar{k}_y \bar{y}) \sin(\bar{z}/2\rho), \\ b_z &= \frac{\sqrt{\eta}}{2\rho \bar{k}_x} \cosh(\bar{k}_x \bar{x}) \sinh(\bar{k}_y \bar{y}) \cos(\bar{z}/2\rho), \end{aligned} \tag{8}$$

where $\bar{k}_{x,y}$ give the hyperbolic variation of the magnetic field in $\bar{x}, \bar{y}$, and must satisfy

$$\bar{k}_x^2 + \bar{k}_y^2 = \frac{\eta}{4\rho^2}. \tag{9}$$

The second undulator type is a planar undulator with plane pole faces, described by:

$$\begin{aligned} b_x &= 0, \\ b_y &= \cosh(\sqrt{\eta}\bar{y}/2\rho) \sin(\bar{z}/2\rho), \\ b_z &= \sinh(\sqrt{\eta}\bar{y}/2\rho) \cos(\bar{z}/2\rho). \end{aligned} \tag{10}$$

SIMULATIONS

The electron transport through both of these undulator types is well known. Some simple tests can therefore be designed to see if the electron motion in Puffin exhibits the correct behaviour.

As described in [3], a natural focusing channel arises from the off-axis variation of the magnetic field in the curved-pole undulator. From this so-called 'natural' focusing, one expects a slow oscillation characterised by betatron wavenumbers and corresponding matched beam radii in $\bar{x}$ and $\bar{y}$, given, in the scaled notation, as:

$$\bar{k}_{\beta x} = \frac{a_u \bar{k}_x}{\sqrt{2\eta}\gamma_r}, \qquad \bar{k}_{\beta y} = \frac{a_u \bar{k}_y}{\sqrt{2\eta}\gamma_r}, \tag{11}$$

$$\bar{\sigma}_x = \sqrt{\frac{\rho\bar{\epsilon}_x}{\bar{k}_{\beta x}}}, \qquad \bar{\sigma}_y = \sqrt{\frac{\rho\bar{\epsilon}_y}{\bar{k}_{\beta y}}}. \tag{12}$$

respectively.

For the curved pole simulation, $\rho = 0.0017$, $a_u = 4.404$, $\bar{\epsilon}_{x,y} = 1$ and $\gamma_r = 575.63$. A small electron pulse is used to generate a significant amount of coherent spontaneous emission (CSE) [5], to avoid a noisy transverse intensity distribution, allowing an simple check of the emitted radiation properties.

The radii in $\bar{x}$ and $\bar{y}$, matched at injection, are are seen to be constant throughout propagation. $\bar{\sigma}_x$ is plotted against $\bar{z}$ in Figure 1. In this case, $\bar{k}_x = \bar{k}_y$, which, from condition (9) and equation (11), results in

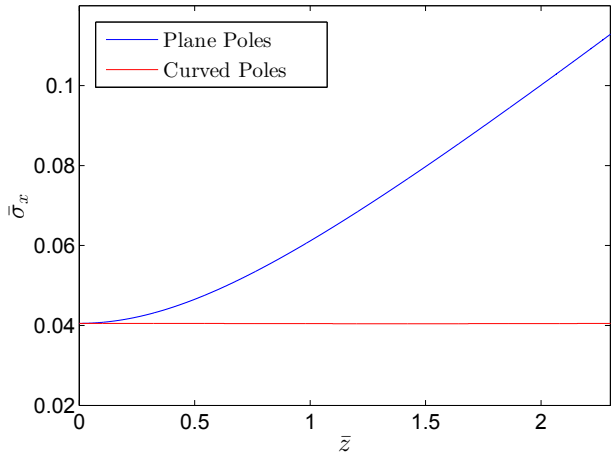

Figure 1: The electron pulse radius $\bar{\sigma}_x$ plotted as a function of distance through the undulator.

$$\bar{k}_{\beta x} = \bar{k}_{\beta y} = \frac{a_u}{4\rho\gamma_r}, \tag{13}$$

and, from (12), matched beam radii of $\bar{\sigma}_{x,y} = 0.039$, giving good agreement with Figure 1.

Similar to the curved-pole undulator, a natural focusing channel also arises in the plane-pole undulator, this time exclusively in the $\bar{y}$ direction. For this simulation, the parameters used are identical to the curved pole case, except the beam energy and the undulator parameter are adjusted to $\gamma_r = 238.04$ and $a_u = 1.2876$, to give the same betatron wavelength and transverse radii for comparison to the curved pole case.

The betatron period and matched beam radius in $\bar{y}$ are now:

$$\bar{k}_{\beta y} = \frac{a_u}{2\sqrt{2}\rho\gamma_r}, \tag{14}$$

$$\bar{\sigma}_y = \sqrt{\frac{\rho\bar{\epsilon}_y}{\bar{k}_{\beta y}}}, \tag{15}$$

and electron motion in the $(\bar{x}, \bar{p}_x)$ dimension should undergo free space dispersion when averaged over an undulator period, resulting in an expansion of the beam in the $\bar{x}$ dimension.

The radius in $\bar{x}$ during propagation is plotted in Figure 1, showing the beam expansion. The initial radius in $\bar{x}$ is here set to the matched radius in $\bar{y}$, so $\bar{\sigma}_x = \bar{\sigma}_y = 0.0327$. The radius in $\bar{y}$ remains constant, as expected.

Another test which can be made on the electron motion is that, again from [4], $|\bar{p}_\perp|^2 = 0.5$ remains constant for all electrons when averaged over an undulator period, which maintains a constant resonance condition throughout their betatron oscillations. This condition is seen to be satisfied in Puffin.

ISBN 978-3-95450-133-5

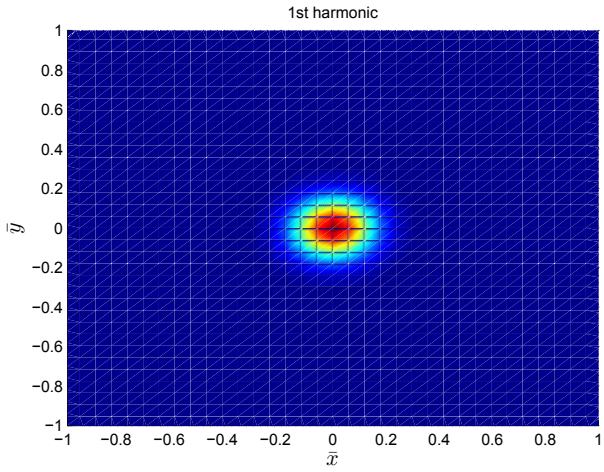

Figure 2: Transverse intensity profile of the 1^{st} harmonic.

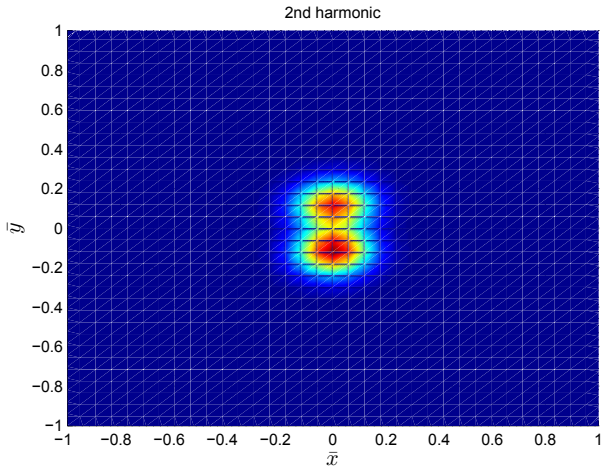

Figure 3: Transverse intensity profile of the 2^{nd} harmonic.

Puffin, being and unaveraged, non-SVEA code, is capable of the self-consistent simulation of the full radiation field spectrum in the FEL. The transverse intensity distributions of the first 2 harmonics in the plane-pole case from CSE is shown in Figures 2 and 3, showing the expected on-axis emission for the first harmonic and the off-axis emission for the second harmonic [6].

CONCLUSION

The system of equations (1 - 6) have been derived in order to implement more realistic 3D undulators in Puffin, increasing the scope of the code.

The betatron oscillation of each electron arises naturally and self-consistently from the motion of the electrons in the specified undulator fields - it is not an approximation of the motion, which would only be valid for electrons close to a given energy, super-imposed on top of another system of equations. Consequently, the functionality reported here will allow the simulation of broadband electron beams transported correctly through the FEL.

The work here may be combined with the model presented in [7], which describes how to employ a taper in the equations, to taper an undulator module's magnetic fields to and from zero over the first and last few undulator periods in each module. As well as more closely modelling a 'realistic' undulator, this avoids the task of calculating the correct initial conditions of the electron beam macroparticles that ensures a stable propagation along the undulator. This calculation can non-trivial, particularly for beams with a large energy spread.

Other static magnetic fields, such as quadrupoles, may be added to the equations. They would be subject to the same scalings presented here, which are specific to the FEL - for example, z is scaled to l_g, the FEL gain length. It is intended this will be done in the future.

ACKNOWLEDGMENTS

We gratefully acknowledge the computing time granted by the John von Neumann Institute for Computing (NIC) and provided on the supercomputer JUROPA at Julich Supercomputing Centre (JSC), under project HHH20; Science and Technology Facilities Council Agreement Number 4163192 Release #3; and ARCHIE-WeSt High Performance Computer, EPSRC grant no. EP/K000586/1

REFERENCES

[1] L.T. Campbell and B.W.J. McNeil, Physics of Plasmas **19**, 093119 (2012)

[2] R. Bonifacio, L. De Salvo Souza, and B.W.J. McNeil, Opt. Commun. **93**, 179-185 (1992)

[3] E.T. Scharlemann, J. Appl. Phys. **58**, 2154 (1985)

[4] E.T. Scharlemann, in High Gain, High Power FELï£¡s (edited by R. Bonifacio et al) (1989)

[5] N. Piovella, Phys. of Plasmas **6**, 3358 (1999)

[6] J.A. Clarke, The Science and Technology of Undulators and Wigglers, Oxford University Press (2004)

[7] L.T. Campbell, B.W.J. McNeil and S. Reiche, Investigation of a 2-Colour Undulator FEL Using Puffin, MOPSO09, Proceedings of FEL 2013

ISBN 978-3-95450-133-5

CHIRPED AND MODULATED ELECTRON PULSE FREE ELECTRON LASER TECHNIQUES

J. R. Henderson[1], L.T. Campbell[1,2,3,4], and B.W.J. McNeil[1]
[1]SUPA, Department of Physics, University of Strathclyde, Glasgow, UK
[2]ASTeC, STFC Daresbury Laboratory and Cockcroft Institute, Warrington, UK
[3]Center for Free-Electron Laser Science, Notkestrasse 85, Hamburg, Germany
[4]Institut für Experimentalphysik, Universität Hamburg, Hamburg, Germany

ABSTRACT

A potential method to improve the free electron laser's output when the electron pulse has a large energy spread is investigate and results presented. A simplified model is the first given, in which there are a number of linearly chirped beamlets equally separated in energy and time. By using chicanes, radiation from one chirped beamlet is passed to the next, helping to negate the effect of the beamlet chirps and maintaining resonant interactions. Hence the addition of chicane allow the electrons to interact with a smaller range of frequencies ($\Delta\omega < 2\rho\gamma_r$), sustaining the FEL interaction. One method to generate such a beamlet structure is presented and is shown to increase FEL performance by two orders of magnitude.

INTRODUCTION

Free Electron Lasers are already important research tools and have started to unlock many new areas of science in diverse fields such as; Warm-Dense matter studies, short pulse protein diffraction and medicine/surgery. Current Free Electron Lasers rely on linear accelerators to provide the electron bunch, for an x-ray FEL the accelerator can be kilometres long. The potential for plasma-wakefield accelerators to drive the Free Electron Laser has been of theoretical and experimental interest for many years. Plasma accelerators generate accelerating gradients on the order of 10^3 times greater traditional linear accelerators, which offers the potential to reduce the total length of the FEL. Electron pulses used in free electron lasers can exhibit a large energy chirp (greater than 1 % of mean electron beam energy) which can degrade the FEL interaction. Linear energy chirps have been previously studied in [1] the results of this work have been recreated here using Puffin [2] an unaveraged 3D parallel FEL simulator. The results of these chirped pulse simulations are in good agreement with [1] showing the flexibility of Puffin. Electron pulses from plasma accelerators are limited by a large energy spread, this is also issue with older accelerators were energy spread is sacrificed for a larger rho (a measure of FEL efficiency) and higher pulse energies. A method that may allow the free electron laser to operate with a large energy spread is proposed, simulations were performed using Puffin. In this method a chirped electron pulse is split in a number of chirped electron beams or beamlets. To sustain the FEL interaction radiation is passed from beamlet to beamlet by applying a series of chicane slippage sections. By making the slippage in undulator-chicane module equal the beam separation the radiation pulse will continuously interact with electrons within the same energy range. One method to generate a similar beamlet structure, the beamlet method, is presented. In the beamlet method a modulator-chicane section is used to generate a set of beamlets which have a smaller local (slice) energy spread than the initial electron pulse. Radiation is then passed from these areas of reduced energy spreads to sustain the FEL interaction. This method shows an approximate two-fold improvement in the radiation field intensity and a four-fold improvement when the radiation field is filtered around the resonant frequency.

SINGLE CHIRPED PULSE

When an electron pulse is given an energy chirp, the effects can be both beneficial and detrimental to the FEL interaction depending upon the gradient of the chirp [1].

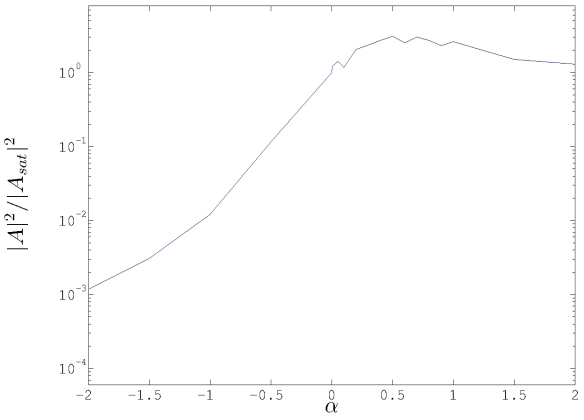

Figure 1: Chirped electron pulse: the scaled saturation power $|A|^2$ is plotted as a function of the energy chirp, the energy chirp parameter [1] is given by $\hat{\alpha} = -\frac{2}{\rho\gamma_r}\frac{d\gamma}{d\bar{z}_2}$, were $|A_{sat}|^2$ is the saturation intensity at $\hat{\alpha} = 0$. This agrees with Figure 2 of [1] where matching parameters parameters have been used. $|A|^2/|A_{sat}|^2$ is equivalent to η from [1].

The results of [1] are reproduced using Puffin. Puffin uses the scaled notation of [3, 4],were $\bar{z}_2$ defines a position in the electron bunch and is given by $\bar{z}_2 = (ct - z)/l_c$ where the cooperation length is defined as $l_c = \lambda_r/4\pi\rho$. The scaled radiation is field is given by, $A_\perp = \frac{eu\bar{a}_u l_g}{2\sqrt{2}\gamma_r^2 mc^2\rho}E_\perp$, where u

ISBN 978-3-95450-133-5

describes the undulator polarization (i.e. $u = 1$ planar or $u = \sqrt{2}$ helical), which in this case is helical. At saturation in the free electron laser exhibits temporal spikes of the order $A_\perp A_\perp^* = |A|^2 = 1$.

Figure 1 shows the normalised saturation power ($|A|^2/|A_{sat}|^2$) against energy chirp parameter $\hat{\alpha}$, where $|A_{sat}|^2$ is the average radiation field at saturation for the unchirped electron pulse. The resonant energy is defined as the initial average energy $\gamma_r =< \gamma_j >|_{\bar{z}=0}$ and the gain length is defined as $l_g = \lambda_u/4\pi\rho$. The saturation length for various chirps was estimated from Figure 1 of [1]. It should be noted that extending the simulation along a long undulator can generate large power spikes of $|A|^2 = 25$ (see Figure 2). This result was not included in [1]. The electron pulse's energy chirp is beneficial, with a flat-top (non-chirped) electron pulse, the electron pulse loses energy as the radiation field grows after a number of undulator periods the electrons are no longer resonant with the initial radiation field (i.e. the electron pulse can now only amplify radiation at a lower frequency). With a chirped pulse the interaction can be sustained, when the radiation pulse propagates through the electron pulse it will find electrons at a higher energy (which are not resonant with it) and electrons that have lost energy which are now resonant with this radiation pulse. This technique is similar to undulator tapering, wherein the undulator's magnetic field is longitudinally tapered to maintain a resonant interaction along the undulator. The resonant FEL interaction continues as the radiation pulse propagates through the electron pulse allowing the generation of large radiation spikes.

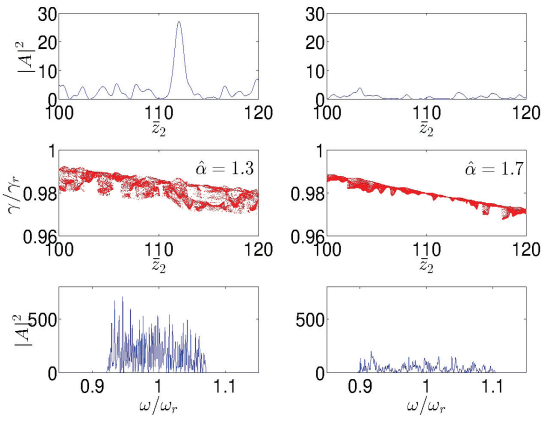

Figure 2: Comparison of chirped electron pulses with different gradients at $\bar{z} = 25$, for $\hat{\alpha} = 1.3$ larger radiation spikes are generated. The energy chirp is beneficial to the FEL interaction because the energy chirp is matched to the rate of energy loss by the electrons so maintaining resonance as the spike propagates through the electron pulse. Larger radiation spikes are present when $\hat{\alpha} = 1.3$ because as the radiation pulse as propagates through the electron pulse it will interact with more electrons within it's FEL bandwidth than it will with a larger energy chirp.

MULTIPLE CHIRPED PULSES - BEAMLETS

In this Section multiple chirped pulses equally spaced in energy are presented. We call this a system of 'beamlets'. Five beamlets are linearly chirped in energy and then equispaced in energy. A schematic of the chirped beamlets is shown in Figure 3 The energy separation of $\Delta\gamma = 2.5\rho\gamma_r$ with a gradient $\frac{d\gamma}{d\bar{z}_2} = \rho\gamma_r$.

In Puffin each macroparticle is given a macroparticle charge weight χ_j defined as $\chi_j = n_j/n_p$ [2], n_j is the macroparticle charge density and n_p is peak macroparticle density of the electron beam. In the beamlet model here, the chi-value of each macroparticle is given by $\chi_n = \chi_j/N_b$ where N_b is the number of electron beams and χ_j is the chi-value if only one beam were modelled. Therefore if all the electron pulses have the same resonant energy (i.e. $\Delta\gamma = 0$) and then the pulses would be indistinguishable.

Table 1 lists all the relevant simulation parameters.

The Model - Multiple Chirped Pulses

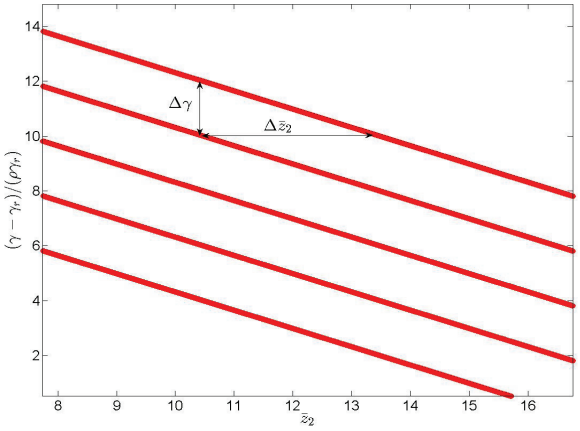

Figure 3: This diagram shows the initial electron pulse phase space. Five cold electron pulses with a linear energy chirp are overlapped and separated in energy by $2.5\rho\gamma_r$. The chirp gradient is $\frac{d\gamma}{d\bar{z}_2} = \gamma_r\rho$ and the temporal separation is 2.5 l_g.

The basic principle of this model is to pass radiation from beamlet to beamlet. This is achieved by using a undulator-chicane lattice, the range of electron energies experienced by a radiation pulse can be controlled by changing number of undulator periods per undulator-chicane module.

Standard mode-locking free electron laser theory [5, 6] states that an undulator-chicane lattice will amplify modes which are separated by $\Delta\omega/\omega_r = 4\pi\rho/\bar{s}$, where $\bar{s}$ is the scaled slippage in an undulator-chicane module $\bar{s} = s/l_c$. The undulator-chicane slippage is the sum of slippages in the undulator $\bar{l}$ and chicane $\bar{\delta}$ i.e $\bar{s} = \bar{l} + \bar{\delta}$. The beamlets are are separated by $\Delta\gamma$ in energy which can be rewritten as a frequency difference of $\Delta\omega/\omega_r \approx 2\Delta\gamma\gamma_r$ using the resonance condition. To lock the modes these two frequencies are equated; $2\Delta\gamma/\gamma_r \approx 4\pi\rho/\bar{s}$. The chirp gradient is given

ISBN 978-3-95450-133-5

by the ratio of the beamlets energy and temporal separation. In this case the temporal separation is given by $\bar{s}$ to ensure that the radiation always interacts with electrons of the same energy range. Therefore the electron chirp gradient is given as,

$$\frac{d\gamma}{d\bar{z}_2} = \frac{\Delta\gamma}{\Delta\bar{z}_2} = \frac{4\pi\rho\gamma_r}{2\bar{s}}\frac{1}{\bar{s}}$$
$$\frac{d\gamma}{d\bar{z}_2} = \frac{2\pi\rho\gamma_r}{\bar{s}^2}. \quad (1)$$

In Figure 3 the initial electron pulse phase space is shown, the cold beam approximation is made, the beamlets are separated by $2.5\rho\gamma_r$ and have energy chirp such that $\frac{d\gamma}{d\bar{z}_2} \leq \rho\gamma_r$. This condition ensures that for $1l_g$ (gain-length) of interaction the radiation field only interacts with electrons within the FEL bandwidth, a value of $\frac{d\gamma}{d\bar{z}_2} = \rho\gamma_r$ was chosen. Temporally the beams are now separated by $2.5l_c$. By using an undulator-chicane lattice radiation can be passed from one beamlet to the next. The undulator-chicane slippage is set equal to the temporal separation of the beamlets, by doing so the radiation pulse at the start of each undulator module can interact with electrons of the same energy. This allows the radiation field to continuously interact with electrons of the same energies sustaining the FEL interaction.

An electron pulse with a linear energy chirp will have an energy dependent slippage length, s_γ, because electrons travelling at different speeds will arrive at the end of the undulator at different times. Therefore the separation of the modes amplified by an undulator-chicane lattice will be energy dependent $\Delta\omega/\omega_r = 4\pi\rho/\bar{s}_\gamma$, where $\bar{s}_\gamma = \bar{l}_\gamma + \bar{\delta}_\gamma$. Here $\bar{l}_\gamma$ and $\bar{\delta}_\gamma$ are the energy dependent slippages in the undulator and chicane respectively. The energy dependent slippage can be written as,

$$\bar{s}_\gamma = (\bar{l} + D)p_{2j} - D + \bar{\delta} \quad (2)$$

were $p_{2j} \approx 1 - 2(\gamma_j - \gamma_r)/\gamma_r$, or in terms of γ_j,

$$\bar{s}_\gamma = 2\left(\frac{\gamma_r - \gamma_j}{\gamma_r}\right)(\bar{l} + D) + \bar{s} \quad (3)$$

.

As the modal separation of the undulator-chicane modes is now energy dependent this can reduce the mode visibility for large energy chirps and long undulators. It is possible to overcome this by applying a negative dispersion in the chicane , when $D = -\bar{l}$ the effect of the energy dependent slippage is negated (i.e. $\bar{s}_\gamma = \bar{s}$). Equation 3 also explains why using a long undulator (large $\bar{l}$) can destroy the mode-locking by increasing the energy dependence of the slippage length. Similarly a large dispersion D also increases the effect of the energy dependent slippage.

Results - Multiple Chirped Pulses

The simulations that follow were performed using Puffin with the parameters stated in Table 1. Numerous simulations were performed to demonstrate the effects of changing the undulator-chicane configuration. The effect of the energy dependent slippage is demonstrated, by destruction of the modes when increasing $\bar{l}$ and D (see equation 3). It is will also be shown that modes normally destroyed by a long undulator (large $\bar{l}$) can be recovered by applying a negative dispersion such that each undulator-chicane module has zero dispersion, i.e. $D = -\bar{l}$, in accordance with equation 3. In addition to this previous unknown chicane modes are generated after the undulator-chicane modes are destroyed. The additional modes are generated by a slippage only chicane.

Table 1: Simulation Parameters for Multiple Chirped Pulses

Parameter	Value	description
Q	3E-12 C	charge per electron pulse
ρ	0.001	FEL parameter
γ_r	176.2	mean energy of beamlets
l_b	80 l_c	bunch length
a_w	0.511	undulator parameter
$\Delta\gamma$	2.5 $\rho\gamma_r$	beam separation in energy
$\Delta\bar{z}_2$	2.5	beam separation in time
$\frac{d\gamma}{dz_2}$	$-\rho\gamma_r$	linear electron pulse chirp
α	2	Saldin chirp parameter

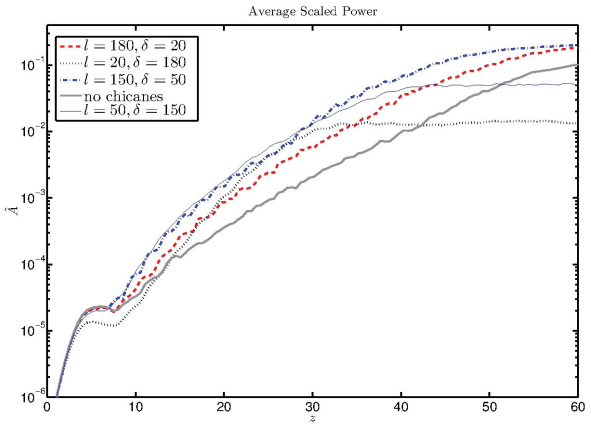

Figure 4: Comparison of a simulation using chicane slippage sections to a simulation without chicane sections. The average radiation power is plotted against $\bar{z}$ (i.e. undulator position). For a large section of the FEL interaction the average radiation power is a factor of ten greater when chicane slippage sections are used.

Figure 4 shows that the average power from beamlets is dependent on the undulator-chicane lattice step-up, increasing the undulator length (while decreasing the chicane slippage) produces higher radiation powers, as happens in normal mode-locking free electron lasers.

In Figure 5 five beamlets are sent through an undulator-chicane lattice. This lattice amplifies modes that are separated by $\Delta\omega/\omega_r = 4\pi\rho/\bar{s} = 0.005$ where $\bar{s}$ is the scaled slippage in an undulator-chicane module. Electron pulses with an energy chirp have an energy dependent slippage (equation 3), i.e. higher energy electrons slip less than low

ISBN 978-3-95450-133-5

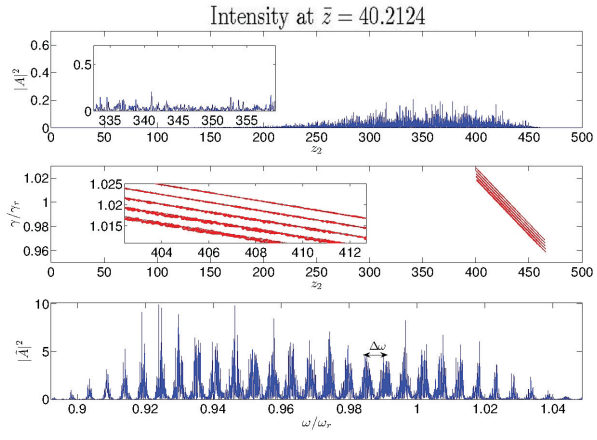

Figure 5: At $\bar{z} = 40$ the radiation is high (top panel), electron microbunching is well developed (middle), the spectrum of the field is shown in the bottom panel. In this case $\bar{l} = 0.2513, \bar{\delta} = 2.2619$. Giving a modal separation is given by $\Delta\omega/\omega_r = 4\pi\rho/\bar{s} = 0.005$, which matches the numerical result well.

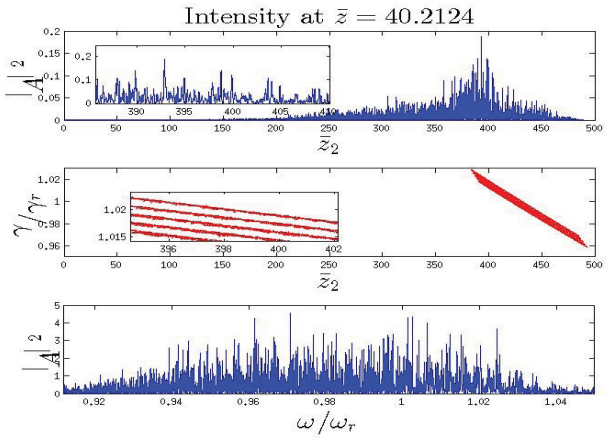

Figure 6: This simulation is identical to Figure 5 , expect that the chicanes now apply a small dispersion to the electron pulse which disrupts mode formation. The reason for this is that an electron pulse with such a large energy chirp will have an energy dependent slippage length. For example the slippage of a low energy electron will be greater than that of a higher energy electron. Using a dispersive chicane will increase the difference in slippage lengths between high and low energy electrons. Therefore modes generate at the head of the pulse will have different $\bar{s}$ than at the tail and hence a different $\Delta\omega_\gamma/\omega_r = 4\pi\rho/\bar{s}$ (see Eq. 3), such that the modes start overlapping each other. However using a non-dispersive chicane means that the difference in modal separation is due solely to undulator dispersion, which is small enough to allow the modes to form.

energy electrons. The result of this is that any mode-locking that occurs at the high energy part of the pulse will involve a different set of modes than low energy part of the pulse. The energy dependent slippage (equation 3) can counteracted by using a short-undulator and a slippage only chicane as is seen Figure 5. However using a dispersive chicane will increase the effect of this energy slippage (equation 3), as higher higher electrons will propagate more than low energy electrons increasing the difference in their slippage lengths. This difference in slippage lengths means that radiation field cannot be passed to the same energy range from one electron pulse to the next. The combination of these effects destroys the modes as is shown in Figure 6. The modes are also destroyed when using a long undulator (Figure 7), as the undulator dispersion over a large number of periods is significant enough to disrupt the mode formation.

In Figure 7 a dispersionless chicane generates an extra set of modes separated by $\delta\omega = 4\pi\rho/\bar{\delta} = 0.02$, these modes are generated because the beamlets will produce a radiation pulse before and after the dispersionless chicane that are similar (nearly identical), therefore the only modes

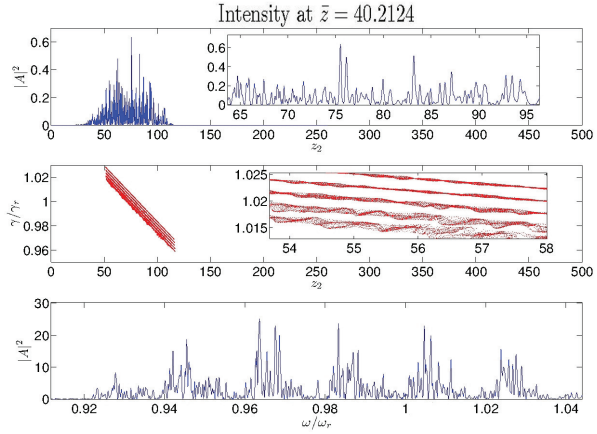

Figure 7: In this simulation longer undulator modules are used, $\bar{l} = 1.885, \bar{\delta} = 0.6283$ and slippage only chicanes. Using a longer undulator will produce more dispersion in the electron pulse, this makes the energy dependent slippage between electron of various energies greater. Therefore the radiation modes now overlap. However the slippage only chicanes will produce modes separated $\delta\omega/\omega_r = 4\pi\rho/\bar{\delta}$, this because the electron pulse will produce similar (nearly identical) radiation pulse before and after the slippage only chicane. Therefore the only modes that can survive the U-CS-U section are given by $\delta\omega/\omega_r = 4\pi\rho/\bar{\delta} = 0.02$.

that can survive this chicane slip are those separated by $\delta\omega = 4\pi\rho/\bar{\delta} = 0.02$. These modes can be replaced by the original modes by applying a negative dispersion in the chicanes (Figure 8), the dispersion is in a chicane is such that the total dispersion by an undulator-chicane module is now zero. Having zero-dispersion undulator-chicane modules negates the effects of the energy dependent slippage (see equation 3); as energy dependent slippage and dispersion are the same thing. Using zero-dispersion undulator-chicane modules hinders the development of the bunching, reducing the radiation intensity. The modes of Figure 7 can also be generated by using a short undulator (U), a dispersion only

ISBN 978-3-95450-133-5

chicane (CD) and a slippage only (dispersionless) chicane (CS). For this simulation (Figure 9) of an undulator-chicane lattice was constructed from modules of U-CD-U-CS, where each undulator has half the number of periods (10 periods) of the undulator used in Figure 5. The dispersion only chicane will supply the equivalent of 130 periods of undulator dispersion. This gives a total dispersion of 150 periods per module just as in Figure 7 and then the slippage only chicane generates modes separated by $\delta\omega = 4\pi\rho/\bar{\delta} = 0.02$.

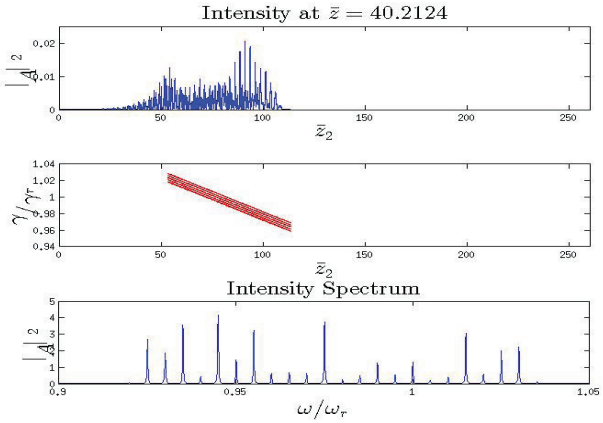

Figure 8: The modes that where destroyed in Figure 7, can be restored by using a chicane that applies a negative dispersion. The magnitude of dispersion applied is equal to the amount dispersion experienced in the preceding undulator section, therefore in an undulator-chicane module there is effectively zero dispersion. In this simulation $\bar{l} = 1.885, \bar{\delta} = 0.6283$. The modes are more clear in this case because of the zero dispersion undulator-chicane modules, where as in Figure 7 the undulator dispersion causes a differential slippage whereby the mode separation varies with energy. Note the reduced radiation intensities, which is due to the negative dispersion chicanes that prevents the formation of microbunches.

A full understanding of the interaction of multiple electron pulses (beamlets) is important when modelling more advanced 'novel' FEL schemes. The effect of undulator length, energy dependent slippage and dispersion has been analysed, and will impact different FEL schemes where large variation in electron energies are present.

BEAMLETS

In this section a technique to generate chirped electron pulses from a single electron pulse is presented. The beamlet technique is a two stage method which involves an undulator and a chicane. The electron pulse is modulated in energy and then dispersed. This generates a series of beamlets with reduced local energy spreads, passing radiation from beamlet to beamlet can sustain the FEL interaction.

The Model - Beamlets

The electron pulse is first modulated in an undulator and then dispersed by a chicane section, these transformations

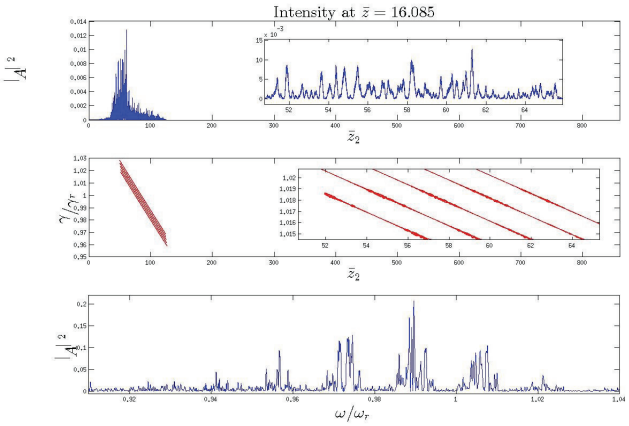

Figure 9: Using a unique undulator-chicane lattice, consisting of dispersion only chicanes (CD) and slippage only chicanes (CS). The lattice is constructed from blocks of U-CD-U-CS arranged in series. In the undulator $\bar{l} = 0.1257$ (10 periods), in the dispersion only chicane (CD) the equivalent of $\bar{\delta} = 1.6336$ (130 periods) of dispersion is applied and in the slippage only chicane (CS) a slippage of $\bar{\delta} = 0.6283$ (50 periods) is used. Therefore the dispersion is the same per module as it is in Figure 7. As in Figure 7 the slippage only chicane generates modes given by $\delta\omega/\omega_r = 4\pi\rho/\bar{\delta} = 0.02$.

are performed by applying the point-transforms given below,

$$\gamma_j = \gamma_j + \gamma_m \sin\left(\frac{\bar{z}_{2j}}{2\rho}\right) \quad (4)$$

$$\bar{z}_{2j} = \bar{z}_{2j} + 2D\left(\frac{\gamma_j - \gamma_r}{\gamma_r}\right). \quad (5)$$

Upon exiting the chicane the electron pulse has a unique phase-space structure. In Figure 10 this phase space structure is shown and is similar to series of chirped electron pulse or beamlets. After the undulator-chicane section the beamlets are passed through an undulator-chicane lattice, this allows radiation to be passed from beamlet to beamlet, similar to the chirped electron pulses method present earlier, sustaining the FEL interaction throughout the electron pulse. The slippage in a undulator-chicane module is therefore equal to the period of energy modulation. A modulation amplitude of $\gamma_m = 0.04\gamma_r$ and dispersion of $D = 200$ was selected.

Results - Beamlets

An electron pulse with a large energy spread and Gaussian current profile is initially generated ($\sigma_\gamma \approx 2.5\gamma_r\rho$, were $\rho = 0.01$). Applying a Gaussian distribution in energy and space will reduce the charge density at the electron pulse corners (in phase space) see Figure 10. Macroparticles with such a low weight are eliminated by Puffin, consequently the electron pulse's phase space is rounded. The electron pulse's Gaussian current profile generates coherent emission at the lower frequencies consequently this radiation has been filtered out. Due to the electron pulse's large energy spread

ISBN 978-3-95450-133-5

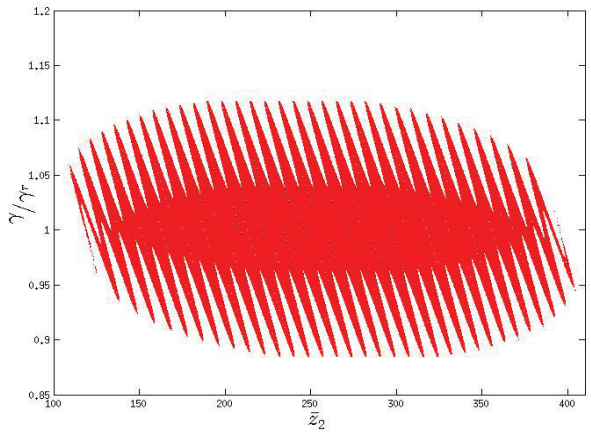

Figure 10: The EEHG beamlet scheme, an electron pusle of a large energy spread is energy modulated ($\gamma_m = 0.04\gamma_r$) and dispersed ($D = 200$) by applying transform 4 and 5. This results in the formation of beamlets with a reduced local energy spread. Radiation can then be passed from beamlet to beamlet sustaining the FEL interaction. The electron pulse was given gaussian distribution in space to cut down on coherent emission from the pulse edges. The macroparticle model of Puffin eliminates marcoparticles whose weight is below a certain threshold, as such the particles at the corners of the pulse (in phase space) have the lowest weight and are eliminated. This leaves the outer beamlets less dense and therefore less able to contribute to the FEL interaction.

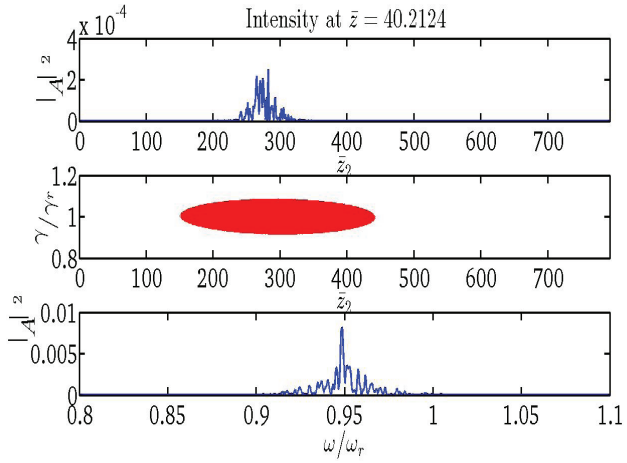

Figure 11: An electron pulse with a large energy spread that exceeds the FEL operational range. This pulse also has a gaussian distribution in space, this was done to minimize coherent spontaneous from the pulse edges.

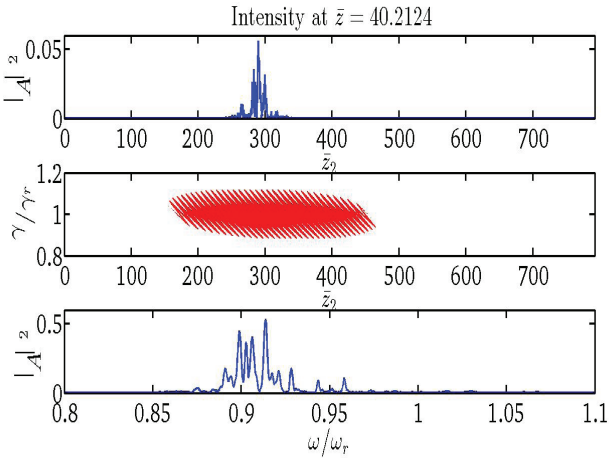

Figure 12: Beamlets near saturation, the radiation field is approaching saturation and the electron microbunching highly developed. Comparing with Figure 11 shows an increase in peak field intensity of 200.

it cannot produce and amplify FEL radiation to useful intensities, at $\bar{z} = 40$ generally consider to beyond saturation significant radiation is not present (Figure 11). However by applying equations 4 and 5 the electron pulse is transformed into beamlets. These beamlets (at $\bar{z} = 40$) show an approximately two-orders of magnitude improvement as can be seen in Figures 12 and 11. For these simulations $\rho = 0.01$ and the undulator-chicane lattice had 50 undulator periods per module ($\bar{l} = 6.2832$) and 18 chicane ($\bar{\delta} = 2.2619$) slippage periods. In Figure 13 a comparison is made between the beamlet case and the original beam, the radiation field has been filtered around the resonant frequency $0.8 < \omega/\omega_r < 1.2$.

CONCLUSION

The interaction of multiple electron pulses has been analysed and this understanding should prove useful when designing more novel FEL techniques. A potential scheme for generating radiation from an electron pulse of large energy spread has been demonstrated. However many improvement (optimisations) should be possible. Using dispersive chicanes further along the undulator-chicane lattice may help improve the FEL interaction. Due the energy dependent slippage of the beamlets, it may be useful (when using large undulator sections) to match the slippage of various sections of the beam. For example decreasing the slippage per module to counteract the increased slippage for lower energy electrons may prove beneficial. The modulation and dispersion parameters of the beamlets scheme can also be optimised and requires further study. The use of the two-colour FEL technique to preferentially amplify modes from the high and low energy regions of the pulse may produce higher radiation powers.

ACKNOWLEDGEMENTS

We gratefully acknowledge suport of Science and Technology Facilities Council Agreement Number 4163192 Release #3; ARCHIE-WeSt HPC, EPSRC grant EP/K000586/1; John von Neumann Institute for Computing (NIC) on JUROPA at Jlich Supercomputing Centre (JSC), under project HHH20.

ISBN 978-3-95450-133-5

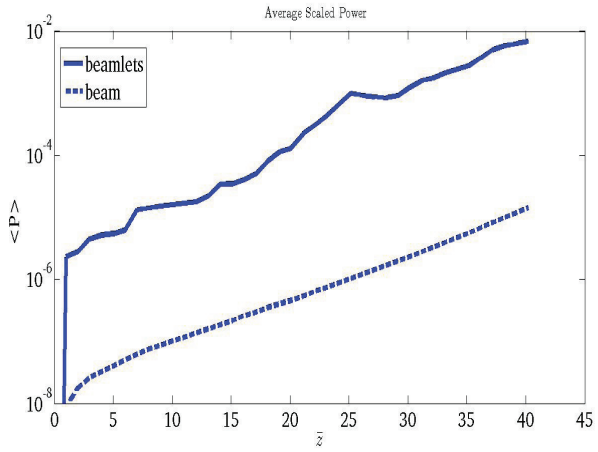

Figure 13: A comparison of the average filtered power of beamlet and original beam is given above. The radiation is filtered around the resonant frequency, $0.8 < \omega/\omega_r < 1.2$. Around 2-3 orders of magnitude improvement has been achieved and may be further optimized.

REFERENCES

[1] Saldin, E., Schneidmiller, E., and Yurkov, M. (2006). Self-amplified spontaneous emission FEL with energy-chirped electron beam and its application for generation of attosecond x-ray pulses. Physical Review Special Topics - Accelerators and Beams, 9(5), 050702.

[2] Campbell, L. T., and McNeil, B. W. J. (2012). Puffin: A three dimensional, unaveraged free electron laser simulation code. Physics of Plasmas, 19(9), 093119. doi:10.1063/1.4752743.

[3] R. Bonifacio et. el. Physics of the High-Gain FEL and Superradiance (1990).

[4] R. Bonifacio et. el. New Effects in the Physics of High-Gain Free-Electron Laser (1992).

[5] N. R. Thompson and B. W. J. McNeil Phys Rev Let, **100** 203901 (2008).

[6] B. W. J. McNeil, N. R. Thompson D. J. Dunniing and B. Sheehy J. Phys. B: At. Mol. Opt. Phys. **44** (2001) 065404.

ISBN 978-3-95450-133-5

epl A Letters Journal Exploring the Frontiers of Physics

December 2012

EPL, **100** (2012) 64001
doi: 10.1209/0295-5075/100/64001

www.epljournal.org

Echo enabled harmonic generation free electron laser in a mode-locked configuration

J. R. Henderson[1,2] and B. W. J. McNeil[1]

[1] *SUPA, Department of Physics, University of Strathclyde - Glasgow, G4 0NG, UK, EU*
[2] *ASTeC, STFC Daresbury Laboratory and Cockcroft Institute - Warrington, WA4 4AD, UK, EU*

received 8 October 2012; accepted in final form 27 November 2012
published online 3 January 2013

PACS 41.60.Cr – Free-electron lasers
PACS 42.55.Vc – X- and γ-ray lasers
PACS 42.65.Re – Ultrafast processes; optical pulse generation and pulse compression

Abstract – Echo Enabled Harmonic Generation (EEHG) is a method of harmonic up-shifting proposed to extend the temporal coherence properties of Free Electron Lasers (FEL) at shorter wavelengths where coherent laser seed fields are not available. Previous theoretical studies of EEHG have applied periodic boundary conditions to the electron distribution in phase space. It is shown that when these periodic boundary conditions are removed a temporal comb of enhanced electron microbunching is revealed. By matching this comb structure in the electron microbunching to the radiation modes that are generated in a Mode-Locked Optical Klystron (MLOK) FEL configuration, a train of short radiation pulses can be generated.

Introduction. – X-ray Free Electrons Lasers [1] (FEL) are now generating high-brightness, X-ray pulses that are opening up many new areas of science in fields as diverse as the creation of warm dense matter [2], high energy pumping of atoms to population inversion to create an atomic X-ray laser [3] and the making of "molecular movies" of biological processes [4]. The latter processes require femtosecond timescale pulses to investigate transient molecular structure in, *e.g.* protein nanocrystallography [5] and single virus imaging [6], succinctly described as "dynamic biology" [4].

The general capability of capturing and possibly altering faster electronic processes that guide chemical pathways in the attosecond regime, would help further transform this research area to include imaging of catalysis, graphene, carbon nanotechnology and nanostructure development [7] and the nascent field of quantum biology [8]. This imaging of the faster electronic motion at the quantum level is ultimately the key to a more complete understanding of the functioning of complex molecular and biological systems [9]. There is therefore considerable interest in developing high-brightness, X-ray attosecond duration pulses that would allow the study of these ultra-fast atomic and molecular processes. This letter proposes a method of achieving this by combining the two previously unrelated FEL methods of Echo Enabled Harmonic Generation (EEHG) [10,11] and the Mode-Locked Optical Klystron (MLOK) [12].

The method of EEHG manipulates electron pulse phase space using two temporally coherent, long wavelength seed lasers and two dispersive chicanes. The electrons are first modulated by a seed laser in an undulator and then dispersed in a chicane. This process is then repeated and a fine microbunching of the electron beam is created at a shorter wavelength while retaining a high level of the temporal coherence from the long wavelength lasers. When propagated through a final radiator undulator, the electron beam emits X-rays at the shorter wavelength of the electron microbunching and with an improved temporal coherence over that generated by self-amplified spontaneous emission which starts from intrinsic shot-noise in the electron beam [13]. Previous models of EEHG have used periodic boundary conditions applied to the electron phase space and simulation codes that average the electron and radiation properties over a radiation wavelength.

In this letter, these limiting assumptions are removed by using the unaveraged FEL simulation code of [14] with the macroparticle loading algorithm of [15]. Using this model, simulations of EEHG up to before the final undulator reveal a frequency comb of modes in the electron microbunching parameter, with adjacent modes

being separated by the second seed laser frequency. This frequency comb may then be matched to and seed a MLOK undulator-chicane lattice as the final radiator stage of the process to generate a seeded Attosecond Pulse Train (APT).

EEHG pre-radiator stage. – To demonstrate the process, EEHG was simulated with the following parameters for a cold beam with no intrinsic shot-noise. A uniform "flat top" current profile electron pulse was used with electron energy $E_r = 1.2\,\mathrm{GeV}$, charge $Q = 100\,\mathrm{pC}$ and initial pulse length of $12\,\mu\mathrm{m}$ (which is equivalent to a current of 2.5 kA). The first and second seed laser wavelengths are $\lambda_{1,2} = 240\,\mathrm{nm}$ with the final radiating resonant wavelength $\lambda_r = 10\,\mathrm{nm}$. The electron energy modulation in the first and second modulating stages are $\Delta E_1 = 750$ keV ($\Delta E_1/\rho E_r = 0.625$) and $\Delta E_2 = 150$ keV ($\Delta E_2/\rho E_r = 0.125$) respectively, where the bracketed terms are scaled with respect to the FEL ρ-parameter [1] of the final radiator stage. The dispersive strength of the corresponding chicanes are $R_{56}^{(1)} = 8.25$ mm and $R_{56}^{(2)} = 0.34$ mm. The electrons are modelled by macroparticles [15] each assigned a weight N_j corresponding to the number of electrons the macroparticle represents. A FEL parameter of $\rho = 10^{-3}$ was used as a typical value for the simulations at this resonant wavelength.

Each of the two modulation-dispersion processes of EEHG prior to the radiator stage were simulated by applying an energy modulation to the electron distribution and then dispersing the distribution using the following transformations applied to the initial distribution:

$$\gamma_j^{(n+1)} = \gamma_j^{(n)} + \Delta\gamma_{n+1}\sin(z_j^{(n)}k_{n+1}), \tag{1}$$

$$z_j^{(n+1)} = z_j^{(n)} + R_{56}^{(n+1)}\left[\frac{\gamma_j^{(n+1)} - \gamma_r}{\gamma_r}\right], \tag{2}$$

where $n = 0, 1$, and bracketed superscripts $(0, 1, 2)$ referring to the initial conditions, and to the exit from the first and second modulation/dispersive stages, respectively; γ is the electron energy in units of the electron rest-mass energy and $\Delta\gamma$ is the energy modulation.

Applying the four transforms of eqs. (1) and (2) develops a microstructure in the electron pulse that contains significant microbunching at higher harmonics of the seed radiation fields used to modulate the electron beam energy.

In demonstrating the principle of EEHG, the work of [10,11] applied periodic boundary conditions in the position of the electrons across a region of the longitudinal z-axis. Here, no such boundary conditions are applied and the electron positions are transformed according to (2). The removal of the boundary condition has little effect around the centre of the electron pulse where the dispersive effects are symmetric. The effects of the two modulation and dispersive sections are seen in fig. 1 and result in a phase space that is very similar to that of reported

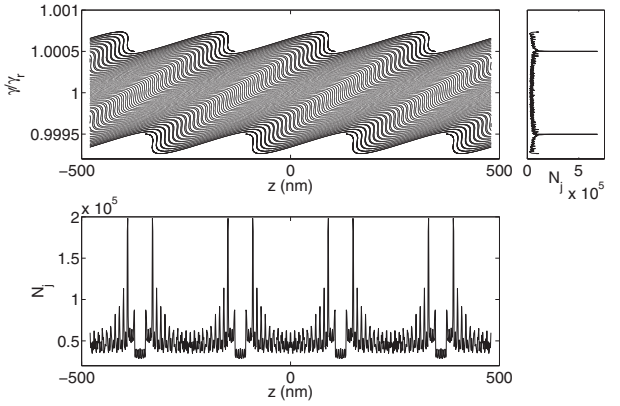

Fig. 1: Electron phase space (top) and histogram of electron numbers (bottom) about the centre of the electron pulse at $z = 0$. The particle density is increased for the high and low energy electrons as is indicated by the top right plot.

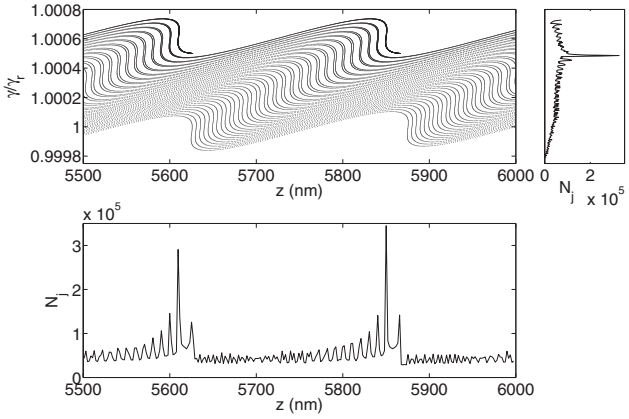

Fig. 2: Electron phase space (top) and histogram of electron numbers (bottom) at the head of the electron pulse. The particle density is increased for the higher energy electrons as is indicated by the top right plot. Single current bands can be seen in the region around $z = 5600$–$5615\,\mathrm{nm}$ with double current bands around $z = 5620$–$5830\,\mathrm{nm}$.

in [10,11]. The higher and lower energy electrons, from the extrema of the energy modulated beam, form tight (single) "current bands", whereas electrons close to the initially unmodulated beam energy form a looser (double) current band structure. This is not the case towards the head and tail of the electron pulse where dispersion causes predominantly single current bands formed by the higher and lower energy electrons, respectively. This effect is seen for the case of the head of the electron pulse in fig. 2.

The underlying process is detailed in fig. 3 which shows the effects of the EEHG process upon the higher energy electrons of the initially modulated beam. The higher energy electrons are seen to form relatively tight energy bands which are then transformed into single current bands around the maxima following the second energy modulation. This creates a series of higher energy current

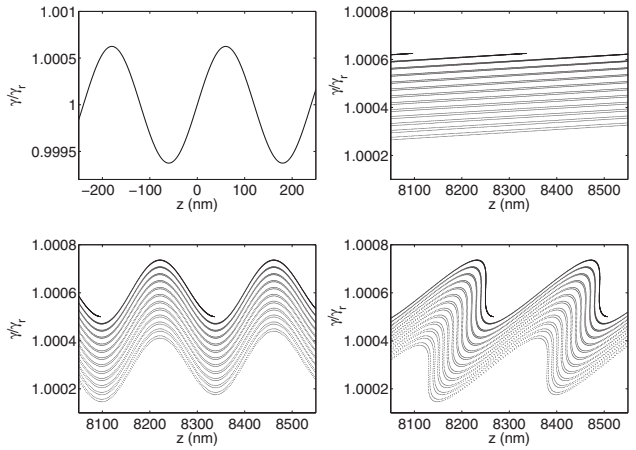

Fig. 3: Both single and double current-bands can be seen to evolve during the pre-radiator EEHG process (left-to-right, top-to-bottom): 1) first beam energy modulation, 2) first chicane dispersion, 3) second beam energy modulation, 4) second chicane dispersion. Notice the relatively large shift in the electron positions in z due to the first chicane.

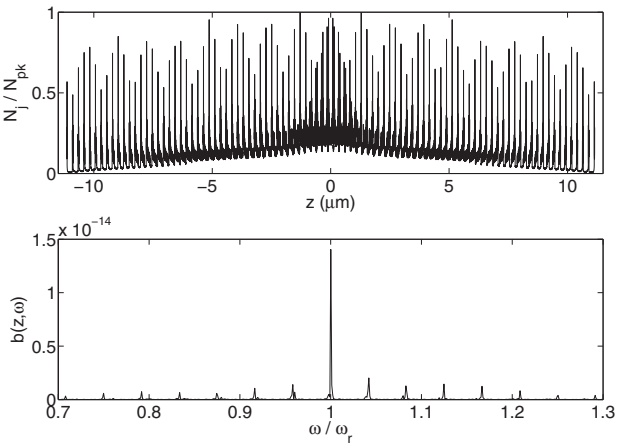

Fig. 4: Histogram of electron numbers (top) normalised with respect to the peak, and the Fourier transform of the bunching parameter $b(z,\omega)$ for the full electron beam distribution showing the modal structure at the end of the EEHG pre-bunching process.

bands at the head of the electron pulse separated by the wavelength of the second seed laser. At the tail of the electron pulse, the EEHG process causes similar single current bands to be formed, but around the minima of the second energy modulation. Thus, dispersion causes the high (low) energy electrons to be dispersed to the head (tail) of the pulse and also a phase difference of $\pi(\lambda_2/2)$ between the current bands at the head and tail.

A histogram of the full electron number distribution is shown in fig. 4 together with a (unitary) Fourier transform of the electron bunching parameter about the resonant frequency ω_r of the final radiator stage. The Fourier bunching parameter is simply derived from the driving term of the scaled wave equation of [15] and may be written as

$$b(z,\omega) = \frac{1}{\sqrt{2\pi}} \frac{1}{n_{p\|}} \sum_{j=1}^{N_m} N_j e^{-iz(k_r+k_u)} e^{i(\omega_r-\omega)t_j}, \qquad (3)$$

where $n_{p\|}$ is the peak linear electron density, N_m is the total number of macroparticles used in the simulation, k_u is the undulator wavenumber, $t_j = -z_j/c\beta_\|$ is the arrival time of the macroparticle at the undulator entrance at $z=0$ and $\beta_\| = v_z/c$ is the mean scaled speed of the electron pulse along the undulator z-axis. It is seen that a well-defined modal structure is present in the electron bunching parameter with mode separation given of $\Delta\omega/\omega_r = 10/240 \approx 0.042$ corresponding to the seed modulation frequency. The modes are relatively well phase-matched as seen from the well-defined peaked periodic microstructure in the electron density histogram.

EEHG radiator. – The pre-bunched electron distribution above was propagated through two different undulator systems, a simple undulator and an undulator-chicane system of the MLOK type, both tuned to the resonant frequency ω_r using the unaveraged simulation code of [14]. The transformations of (1,2) may be rewritten in the universal scaling of [16] as used in the simulations as

$$p_j^{(n+1)} = p_j^{(n)} + \Delta p^{(n+1)} \sin\left(\frac{\bar{z}_{1j}^{(n)}}{2\rho h_{n+1}}\right), \qquad (4)$$

$$\bar{z}_{1j}^{(n+1)} = \bar{z}_{1j}^{(n)} + 2\rho D^{(n+1)} p_j^{(n+1)}, \qquad (5)$$

where $\Delta p^{(1,2)} = \Delta\gamma^{(1,2)}/\rho\gamma_r$; $D^{(1,2)} = k_r\rho R_{56}^{(1,2)}$; $h_{1,2} = \omega_r/\omega_{1,2}$ and $\beta_\| \approx 1$ is assumed. At the beginning of the undulator: $\bar{z} \equiv 2\rho k_u z = 0$; $\bar{z}_{1j} = -2k_r\rho c t_j$ and $p_j = (\gamma_j - \gamma_r)/\rho\gamma_r$.

Performing the Fourier transform with respect to $\bar{z}_1$ defines the scaled frequency as $\bar{\omega} = -\omega/2\rho\omega_r$ so that

$$b(\bar{z},\bar{\omega}) = b(z,\omega)\frac{c}{l_c}\exp\left(i\frac{\omega z}{c}\right), \qquad (6)$$

where $l_c = \lambda_r/4\pi\rho$ is the cooperation length [16].

Simple undulator. EEHG was first simulated in a simple undulator configuration of scaled length $\bar{z} = 1.1$. The scaled radiation and electron pulse parameters are plotted in fig. 5. It is seen that while the radiation generated had some temporal structure, no modal structure is present in Fourier space with emission confined to the resonant frequency. This is consistent with the previous results of [10,11].

MLOK undulator. Here an MLOK undulator-chicane lattice is constructed so that the radiation modes will match the properties of the electron bunching above. Using the notation of [12], each undulator has four periods so that a radiation wavefront will propagate four resonant

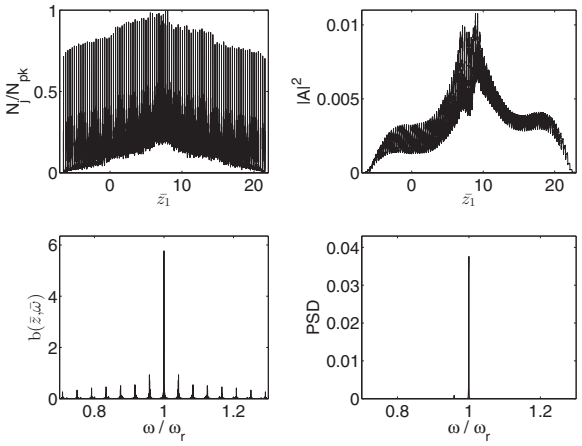

Fig. 5: Electron and radiation pulse at saturation in a simple undulator at $\bar{z} \approx 1.1$ for the normal EEHG case. Plots on the left are: top, normalised electron number histogram (bin size = $\lambda_r/5$); bottom, Fourier transform of bunching $b(\bar{z}, \bar{\omega})$. On the right: top, radiation field amplitude $|A|^2$ as a function of $\bar{z}_1$; bottom, scaled Power Spectral Density (PSD) showing that emission at resonance dominates.

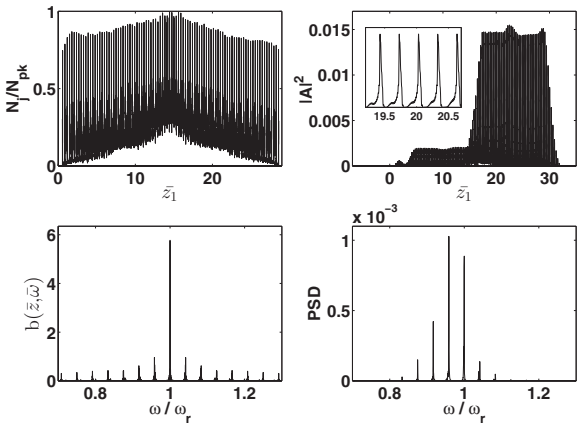

Fig. 6: As fig. 5, but for the MLOK undulator at saturation ($\bar{z} \approx 0.6$). The inset (top, right) shows more detail expanded in $\bar{z}_1$. A well-defined set of phase-matched radiation modes has developed resulting in a train of short radiation pulses. In unscaled units the individual pulse widths are ∼106 attoseconds (FWHM) and separated by ∼ 0.8 femtoseconds corresponding to $\bar{s} = 0.3$ in scaled units of $\bar{z}_1$.

wavelengths through the electron pulse in each undulator. Each chicane delays the electron pulse by a further twenty wavelengths so that the total slippage of a resonant wavefront in traversing one undulator-chicane module is $s = (4 + 20)\lambda_r = 240\,\text{nm}$, which is equal to the second seed laser wavelength, λ_2. In the scaled units of $\bar{z}_1$ this corresponds to $\bar{s} = s/l_c \approx 0.3$. In this way the relative slippage between radiation and electrons in each undulator-chicane module matches the strong periodic electron microbunching. It is seen from the inset of fig. 6 that this matching generates a periodic train of short radiation pulses (corresponding to full width half-maximum duration of ∼106 as) separated by the second seed laser wavelength. This pulse train is equivalent in frequency space to the observed set of modes equally spaced by the frequency of the second seed laser, $\Delta\omega/\omega_r \approx 0.042$. It is easily shown from the FEL resonance relation [1] that the frequency range of radiation emission due to the electron energy modulations $\Delta\gamma_{1,2}$ is negligible in comparison with the mode spacing when $(\Delta\gamma_1 + \Delta\gamma_2)/\gamma_r \ll \Delta\omega/2\omega_r$. Here, this condition is satisfied as $(\Delta\gamma_1 + \Delta\gamma_2)/\gamma_r \approx 4 \times 10^{-2}\Delta\omega/2\omega_r$. Note that peak powers generated by the higher energy electrons at the head of the radiation pulse train envelope are greater than those generated at the tail by the lower energy electrons. While the higher energy electrons lose energy and fall into resonance to emit strongly, those at lower energies continually fall away from resonance and strong radiation emission. The visibility of radiation pulse train structure is defined as $V = (|A|^2_{max} - |A|^2_{min})/(|A|^2_{max} + |A|^2_{min})$, were the maximum and minimum values are defined between two adjacent peaks. The effect of introducing an energy spread σ_E in the initial electron pulse energy decreases the visibility gradually from $V = 0.93$ at 1 keV ($\sigma_E/\rho E_r = 0.0008$) to $V = 0.78$ at 150 keV ($\sigma_E/\rho E_r = 0.125$).

Conclusions. – By removing previous simplifying assumptions in EEHG modelling, a previously unreported temporal structure in the electron pulse microbunching was revealed. This structure can be matched to a mode-lock FEL (MLOK) configuration which can generate trains of ∼106 attosecond (FWHM) duration pulses at 10 nm wavelength. The parameters used here are similar to those used previously to demonstrate EEHG. However, there are no intrinsic reasons why the resonant wavelength and pulse durations cannot be scaled down further into the hard X-ray.

* * *

The authors would like to thank Lawrence Campbell and David Dunning for helpful discussions. This work received support from STFC Memorandum Of Agreement No. 4163192.

REFERENCES

[1] McNeil Brian W. J. and Thompson Neil R., *Nat. Photon.*, **4** (2010) 814.
[2] Vinko S. M. *et al.*, *Nature*, **482** (2012) 59.
[3] Rohringer N. *et al.*, *Nature*, **481** (2012) 488.
[4] Spence J. C. H., Weierstall U. and Chapman H. N., *Rep. Prog. Phys.*, **75** (2012) 102601.
[5] Chapman H. N. *et al.*, *Nature*, **470** (2011) 73.
[6] Seibert M. M. *et al.*, *Nature*, **470** (2011) 78.
[7] Flavell W. R., *Proceedings of IPAC2012, New Orleans, U.S.A.* (Joint Accelerator Conferences Website (JACoW)) 2012, paper WEI04.
[8] Olaya-Castro A., Nazir A. and Fleming G. R., *Philos. Trans. R. Soc. A*, **370** (2012) 3613.

[9] Dixit Gopal, Vendrell Oriol and Santra Robin, *Proc. Natl. Acad. Sci. U.S.A.*, **109** (2012) 1636.
[10] Xiang D. and Stupakov G., *Phys. Rev. ST Accel. Beams*, **12** (2009) 030702.
[11] Xiang D., Huang Z. and Stupakov G., *Phys. Rev. ST Accel. Beams*, **12** (2009) 060703.
[12] Thompson N. R. and McNeil B. W. J., *Phys. Rev. Lett.*, **100** (2008) 203901.
[13] Bonifacio R., De Salvo L., Pierini P., Piovella N. and Pellegrini C., *Phys. Rev. Lett.*, **73** (1994) 1.
[14] McNeil B. W. J., Robb G. R. M. and Jaroszynski D. A., *Opt. Commun.*, **165** (1999) 65.
[15] McNeil B. W. J., Poole M. W. and Robb G. R. M., *Phys. Rev. ST Accel. Beams*, **6** (2003) 070701.
[16] Bonifacio R., McNeil B. W. J. and Pierini P., *Phys. Rev. A*, **40** (1989) 4467.